Structural and Functional Studies of K2P Channels

Submitted in partial fulfilment of the requirements for the degree of Doctor of Philosophy

Alexandra Mackenzie

Keble College, University of Oxford

Trinity 2015

Authorship Declaration

This thesis and the work presented in it were completed at the University of Oxford (Nuffield Department of Medicine and Department of Physics) between October 2011 and October 2015, under the supervision of Prof. Liz Carpenter and Prof. Stephen Tucker. All contributions made by others have been stated clearly in the text. This work has not been submitted in full or partial fulfilment of any other degree.

Alexandra Mackenzie

October 2015

Abstract: Structural and Functional Studies of K2P Channels

Two-pore domain potassium channels (K2Ps) are a family of dimeric potassium channels responsible for regulation of cellular excitability. In 2012, crystal structures of TREK-2 were solved revealing this channel in two different conformational states. In the down state, transmembrane helices M2, 3 and 4 descend further into the cytoplasm than in the up state. This reveals two gaps (fenestrations) that link the membrane directly to the ion conduction pathway. However, the functional relevance of these two states was not known.

In this work, I use state-dependent modulators of TREK-2 to investigate the functional relevance of helical movement in K2P channels. By solving the co-crystal structures of these modulators with TREK-2, I aimed to uncover which states these modulators bind to and how this modifies potassium conductance through the channel. As small molecule binders have weak affinities for TREK-2, brominated ligand derivatives were used to increase sensitivity and specificity of ligand detection.

The co-crystal structures of TREK-2 with brominated fluoxetine (Prozac) derivatives revealed functionally inhibited down states with reduced occupancy in the selectivity filter. These inhibitors bind within the fenestration of TREK-2. Since the fenestration is absent in the up state, inhibition must work by stabilising the down state of the protein. This finding supports a gating mechanism of TREK-2 that links movement of the M2-4 helices with gating at the channel filter.

TREK-2 was also co-crystallised with derivatives of the small molecule activator BL-1249. Crystals of this complex were produced using both vapour diffusion and lipidic cubic phase. These crystals produced diffraction at both synchrotron and free electron laser sources. Initial low-resolution structures provide the first insight into where BL-1249 may bind to TREK-2.

Alexandra Mackenzie, Trinity 2015

Submitted in partial fulfilment of the requirements for the degree of Doctor of Philosophy

Acknowledgements

This work would not have been possible without the help of a great many colleagues and friends; first and foremost my supervisors. I would like to thank Prof. Liz Carpenter for her advice and support, and for agreeing to take on a physicist and turn her into a biochemist. I would also like to thank Prof. Stephen Tucker for his supervision and enthusiasm that has kept me motivated throughout my D.Phil. I am extremely fortunate to have studied under these two renowned professors who are nonetheless always able to find time to teach me.

I would like to thank all my colleagues for their support. In particular Yin Dong who persevered in teaching me everything I know about protein purification and Ashley Pike who, in teaching me crystallography, has remained patient through my many questions (and mistakes!). For keeping the lab running I would like to thank Andy Quigley, Shubhash Mukhopadhyay, Kasia Kupinska, Katie Ellis, Dong Wang, Gavin McKinley, Frank Waters, Leela Shrestha, Annamaria Tessitore, Amy Chu and Bérénice Rotty. For cloning and pipeline support I would like to thank Claire Strain-Damerell and Nicola Burgess-Brown. For help with functional tests I would like to thank Conor McClenaghan, Micheal Clausen and Jackie Ang. For synthesising compounds I would like to thank Paul Brennan's group (Gian Filippo Ruda and Melissa D'Ascenzio) at the TDI Oxford, and David Pryde at Pfizer.

Finally, thank you to my friends, family and Hector.

My D.Phil. has been generously supported by the E.P.S.R.C. through the Life Sciences Interface Doctoral Training Centre.

For Daddy

Chapter 1 Introduction

1.1 Ion Channels

1.1.1 Function of ion channels

The cell membrane presents a formidable barrier separating the cytoplasm from the extracellular milieu. This ≈50Å thick lipid bilayer inhibits passage of the water-soluble compounds necessary for life: from sugars to amino acids, peptides to ions[1]. It is often described as a fluid mosaic, a lipid sea studded with integral membrane proteins (IMPS). These proteins constitute up to 75% of the cell membrane and allow both signals and polar nutrients to pass in and out of the cell[2]. IMPS constitute 30%[3] of the human genome and represent a disproportionately large percentage of drug targets (50%[4]). They can be broadly classified by their function: signal transducers, enzymes, transporters or ion channels[2].

Ion channels are membrane-spanning proteins that allow ions to overcome the hydrophobic barrier of the membrane. They achieve this by creating a hole known as a pore through which ion can freely pass. Ions then flow down the electrochemical gradients across the membrane at near-diffusion limited rates (≈10^7 ions per second). This is in contrast with ion pumps such as Na^+-K^+ ATPase that require energy to transport ions against the electrochemical gradient. Transport is typically associated with a large conformational shift in the protein, limiting ion flux to ≈10^2 ions per second[5].

The large currents supported by ion channels can be rapidly turned on or off through structural changes in the protein, a process known as gating. Gating can be triggered by ligand binding[6,7] or by changes in the cellular environment, for example membrane stretch[8,9], voltage[10], pH[11,12], light intensity[7,13], ion concentration[14] and temperature[15]. Specialised domains such as voltage sensing domains are often tethered to the channel to couple these changes in environment with changes in their membrane permeability.

Ion channels can be classified based on the type of permeant ions they allow across the membrane. Evolution of physiochemical properties within channel pores has limited which ions can pass through a given channel- this is known as selectivity. Ion channels can be highly selective for certain ions e.g. sodium channels[16], or allow multiple different types of ions to pass through the membrane (e.g. certain Transient Receptor Potential cation channels allow sodium, potassium and calcium[17]).

As ion channels equip cells with a means to rapidly, precisely and selectively control ion flux in response to the environment, they have evolved roles in physiological processes as diverse as signal transduction[18], osmotic regulation[19] and cell migration[20].

1.2 Structural Biology of Ion Channels

1.2.1 The first structure of an ion channel was solved by X-ray crystallography

The first structure of an ion channel was published in 1998[21] by Rod MacKinnon and Declan Doyle, a feat that would later earn MacKinnon the 2003 Nobel Prize in chemistry. This structure was solved using X-ray crystallography. X-ray crystallography is a technique for determining the atomic structures of molecules. The technique requires growth of crystals of the molecule (in this case protein crystals), which are then exposed to intense X-ray beams. The X-rays elastically scatter from the electrons in the crystal altering their direction of travel; this phenomenon is known as diffraction. The diffracted X-rays then interfere with each other before being detected. The readout of X-ray intensities at the detector is known as the diffraction pattern[22,23].

Obtaining the structure of a protein from the diffraction pattern is non trivial. This is because information is lost during the experiment; the detector is incapable of measuring the phase of the waves it detects. If a lens were available to focus the diffracted X-rays, an image of

protein molecules would appear on the detector. However, due to the similarity of the refractive indices of X-rays in air and in common lens materials, this is not possible. This problem is known as the phase problem, and if it is solved then the structure of the protein within the crystal can be determined[24].

Since the diffraction pattern arises from the scattering of X-rays from electrons within the crystal, the information obtained from it is the location of electrons within the crystal. All atoms contain electrons, and the number of electrons and thus the scattering from an uncharged atom is proportional to its atomic number. Solving the crystal structure of a protein entails producing electron density maps- the density of electrons within three-dimensional space. A model of the protein structure can then be built which agrees with this electron density[24] (The mathematical basis of crystallography is further discussed in Section 1.11).

1.2.2 The first ion channel structure revealed a re-entrant loop forming a pore

The structure solved by MacKinnon in 1998 was that of a potassium selective channel (the potassium crystallographically-sited activation channel or KcsA) [21]. This structure revealed how a protein can form an ion-selective pore in the membrane (Figure 1-1).

KcsA is a prototypical tetrameric K^+-channel with each subunit containing a pore forming or P-domain flanked by two trans-membrane helices (M1-P-M2). The transmembrane (TM) helices (M) cluster around a central water filled cavity, forming an ion conduction pathway. Four shorter, tilted pore helices form from the P-domains of each subunit create a narrowing within the extracellular leaflet of the membrane. This narrowing, roughly 12Å in length and just 2.5Å in diameter is lined by a loop that projects from the C-terminus of the pore-helix. The amino acids on this loop form the selectivity filter of the channel. Thus the re-entrant loop structure formed by the P-domain and supported by the TM helices is responsible for ion channel selectivity (Figure 1-1A, light grey). Beneath this, a large (~10Å diameter) water

filled cavity lies within the inner leaflet of the membrane. The structure shows a four-fold symmetry around the selectivity filter[21].

Subsequent structures including MthK[25] (1LNQ, 2002), KvAP[26] (1ORQ, 2003), KirBac 1.1[27] (1P7B, 2003), KirBac 3.1 (1XL4), GIRK1[28] (1N9P, 2002) demonstrated that this architecture is conserved among potassium channels irrespective of additional domains such as voltage sensing domains.

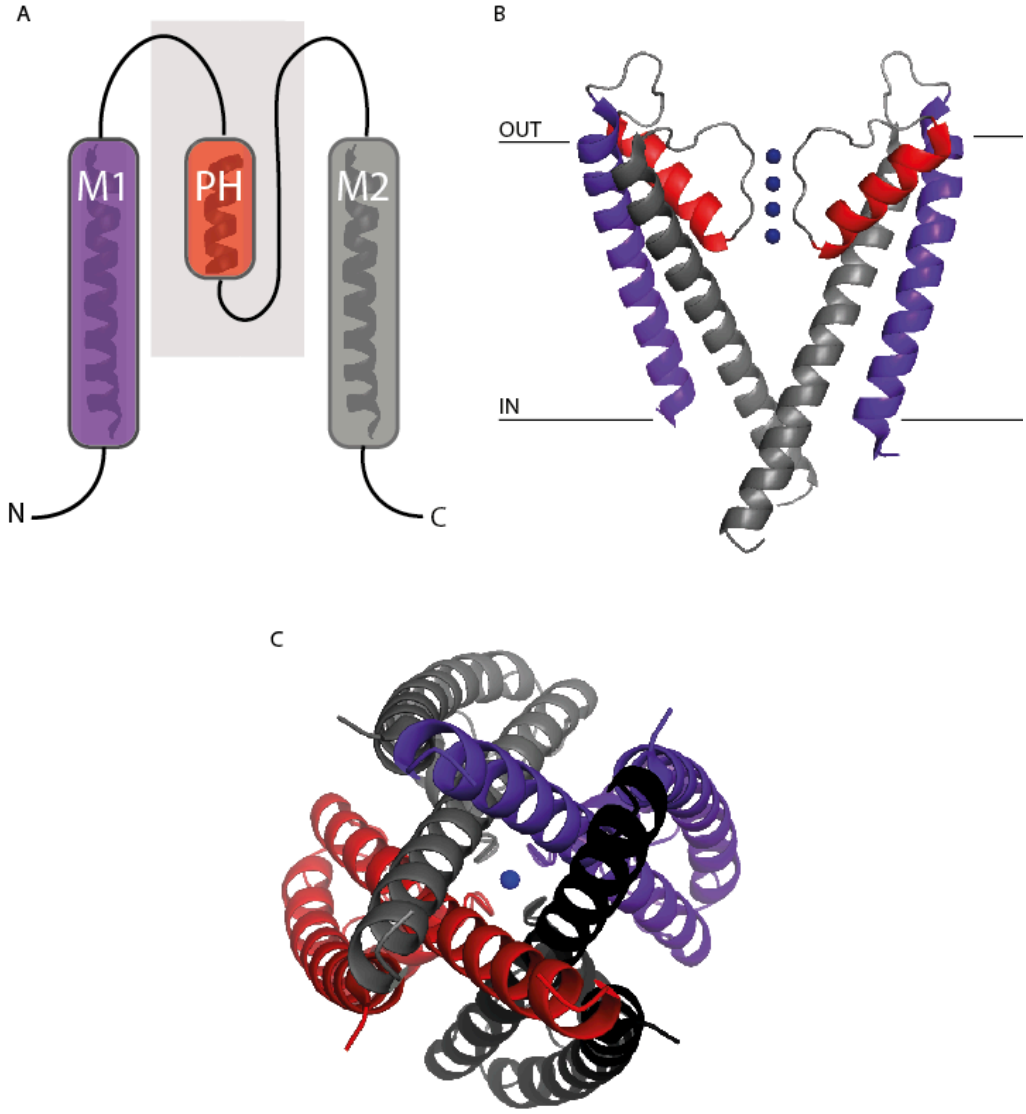

Figure 1-1 The core structure of a K^+ channel demonstrated by KcsA.

A single subunit of KcsA has a pore-forming domain sandwiched between two transmembrane helices (A). Four of these subunits combine to form a complete channel. The P-domain that forms the re-entrant loop of the channel is highlighted in light grey. B) The 3-dimensional structure of two subunits of KcsA. The structure forms a hole in the membrane through which potassium ions (blue) can pass. C) Coloured by subunit, this view of KcsA from the intracellular side shows the four-fold symmetry of the channel. PDB: 1K4C[29]. Images produced with PYMOL and Adobe Illustrator.

1.3 Subsequent structures show a conserved fold in most channels

Subsequent protein structures reveal this fold is not unique to potassium channels, but is formed by other channels with re-entrant loops (M-P-M channels). Between 2011 and 2012 two groups determined the first crystal structures of prokaryotic sodium channels, both containing re-entrant loops (Payandeh *et al.* 2011[30], McCusker *et al.* 2012[31]) . These channels consist of a single subunit, with four repeated domains. Each domain has 6 TM helices; 4 form a voltage-gating domain, while the remaining two (S5-S6) contribute to pore formation. The structures reveal a four-fold symmetrical pore lined by pore-forming loops. These loops are supported by four tilted pore-lining helices. This is surrounded by an inner cone of four S6 helices, and an outer cone of a further four S5 helices; analogous to a K^+ channel structure. This three-dimensional architecture has also been observed for NaK channels, that facilitate both Na^+ and K^+ currents[32].

The determination of the structure of TRPV1[33] (3.4Å resolution) , a non-selective cation channel, by electron microscopy revealed yet another channel with this structure. This channel has six transmembrane segments S1-S6, with a short pore-helix and loop between S5 and S6. The S5-S6 regions, analogous to a single subunit of a KcsA K^+ channel, tetramerise to form a four-fold symmetrical ion channel pore.

Multiple types of ion channels including voltage gated sodium (Na_V), potassium (K_v) and calcium channels (Ca_v), transient receptor potential (TRP) channels, Inwardly rectifying potassium channels (K_{IR}) and ATP stimulated potassium channels (K_{ATP}) share this three-dimensional M-P-M architecture, but have vastly different ion selectivity. While the architecture serves to create a pore lined by residues on the re-entrant loop, selectivity is achieved by fine-tuning of the amino acid sequence of this loop and those of the pore helix that support it's structure. Ion channels can therefore maintain an overall structure conducive to ion flow through the membrane, while fine-tuning selectivity.

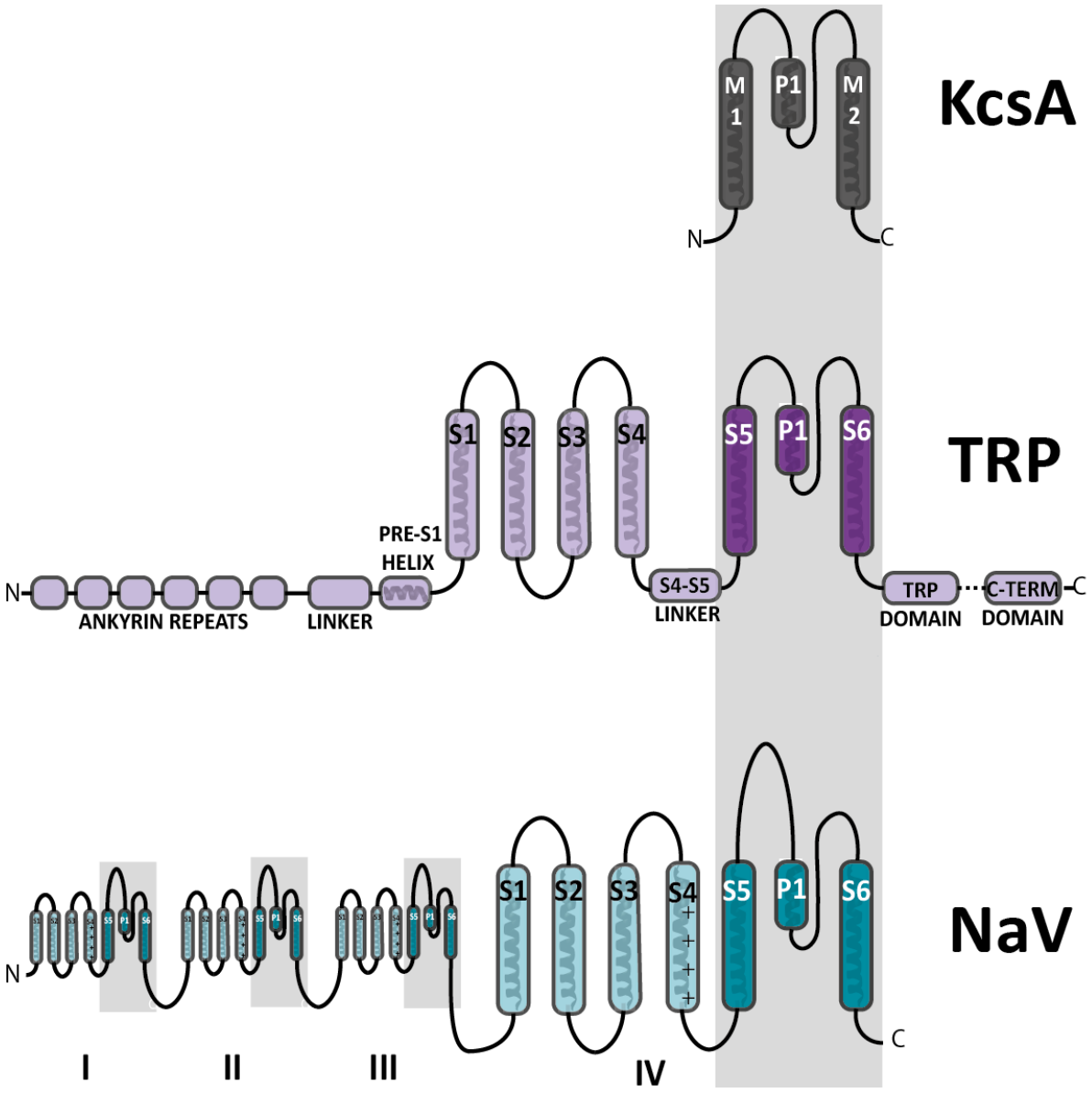

Figure 1-2 The re-entrant pore loop of ion channels

For illustrative purposes, the subunits of three representative channels KcsA, TRPV1 and NaV are shown compared to one another. S5-P1-S6 or M1-P1-M2 comprises the transmembrane helix - re-entrant loop - transmembrane helix domain found in many ion channels (highlighted in grey). KcsA and TRP channels tetramerise to form a functional channel with four TM-P-TM domains, while NaV contains four such domains within a single unit (shown smaller for illustrative purposes). Image produced in Adobe Illustrator.

Although not discussed in this thesis, there are ion channels that do not contain re-entrant loops. Such channels include calcium activated chloride channels (CLC), cys-loop receptors and P2X receptors[34]. These structures are exemplified by the human GABA-receptor, a pentameric ligand-gated chloride channel solved by Miller and Aricescu in 2014[6]. Rather than being lined by residues from a loop, the pore is instead lined by side-chains of trans-membrane helices. The physiochemical properties of these side chains confer selectivity to

the channel. The diameter of the ion conduction pathway (~10Å) is larger than is observed for M-P-M ion channels (~2.5Å in the selectivity filter of a potassium channel).

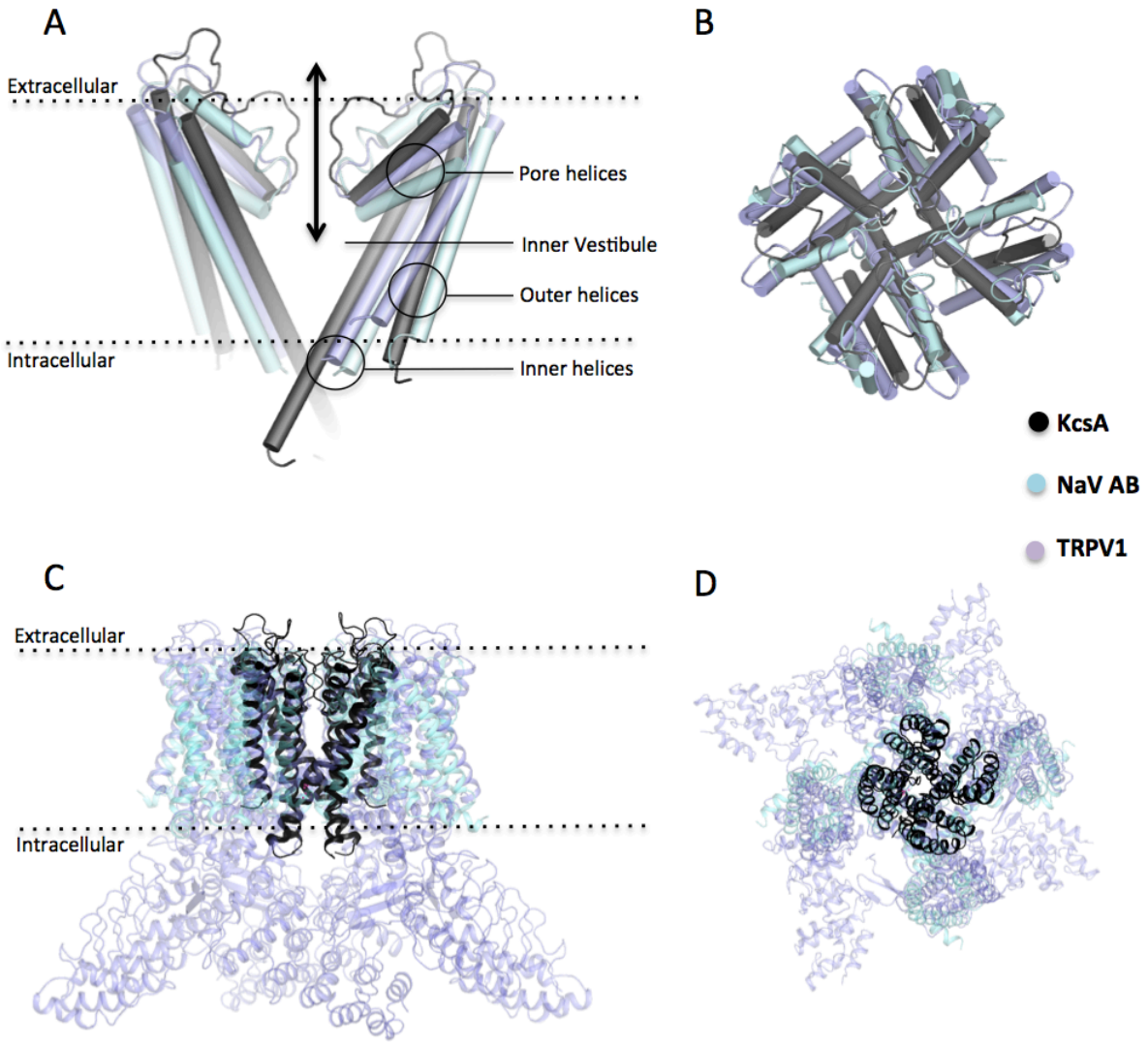

Figure 1-3 Structural comparison of re-entrant loop ion channels

Shown are structural super-positions of atomic structures of KcsA (1K4C), NavAB (4EKW) and TRPV1 (3J5P). A cutaway of the M-P-M domains (A) shows that the ion channel selectivity filter is lined by a re-entrant loop, supported by pore helices. A water-filled inner vestibule is formed by the TM helices within the intracellular leaflet of the membrane. A top view (B) demonstrates the cyclical symmetry around the pore. Complete structures of the three channels (side view C and top view D) show that while additional domains have been added to the M-P-M domain, it remains present in all the structures (as highlighted by KcsA in black). Image produced in PYMOL and edited in Adobe Illustrator.

1.4 Potassium Channels

Potassium selective ion channels (K^+ channels) are the largest family (70 genes, which are often multiply spliced[35]) of ion channels. They are present in all kingdoms of life, and at least one K-channel is present in every fully sequenced genome[36]. K^+ channels all share a basic common function: allowing K^+ to flow down an electrochemical gradient. Since cells typically maintain elevated potassium levels within their cytoplasm, opening a potassium channel means allowing potassium to flow out of the cell. This results in the build up of negative charge in the inner leaflet of the cell (hyperpolarisation)[37]. By controlling membrane polarisation, K^+ channels can modulate action potentials[38,39], mediate apoptosis[40] and even trigger cell proliferation in the immune system[41]. To fulfil this common function, all potassium channels share a core structural component: a potassium selectivity filter.

1.4.1 Selectivity in potassium channels

K^+-channels have a striking selectivity for K^+ ions, allowing 100x more K^+ ions through than Na^+ ions despite their similar atomic radii (K^+ 1.33Å; Na^+ 0.95Å) This is due to the highly conserved sequence of amino acids Thr–X–Gly–Tyr–Gly (X = hydrophobic residue) of the amino acids lining the narrowest section of the ion conduction pathway. The alternating left and right handed helical dihedral angles they adopt forces their backbone carbonyls, and the side chain oxygen of the threonine, to face out into the pore of the channel. This creates five regularly spaced tiers of electronegative oxygen atoms. The spacing between these tiers is ideal to fit a de-solvated K^+ ion, meaning there are four equally spaced K^+ binding sites (S1-S4) within the filter. The snug fit model suggests that when a smaller Na^+ ion enters the pore the oxygen atoms are too far apart to mimic it's hydration shell and the filter collapses. In this way, the selectivity filter can prevent the flow of sodium ions while permitting potassium ions[29].

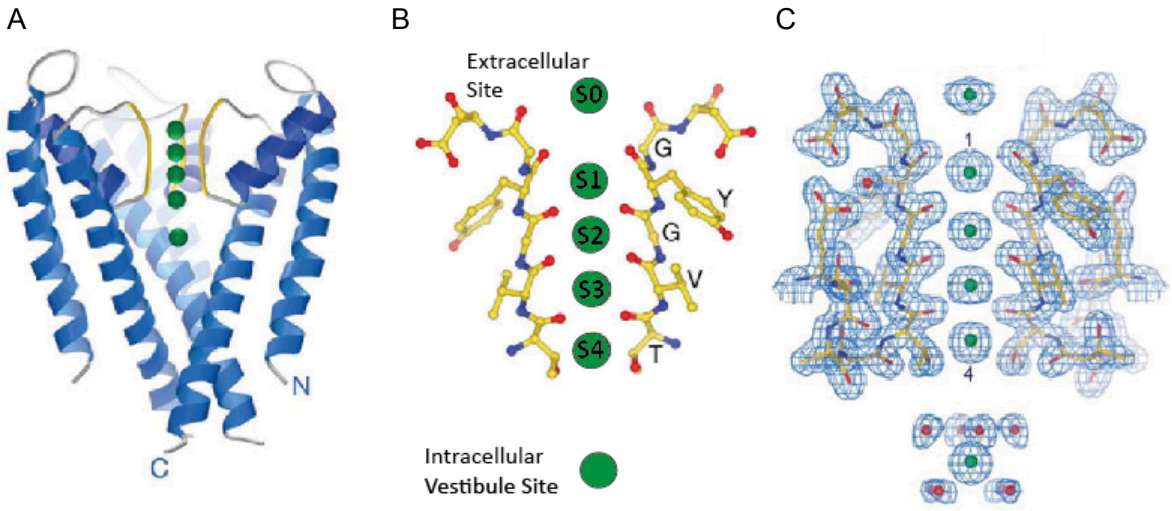

Figure 1-4 The K^+ channel selectivity filter

The selectivity filter (yellow) lines the pore of the potassium channel KcsA, making it selective for potassium ions (green) (A). The filter consists of the conserved amino acid sequence TVGYG that results in five regularly spaced tiers of oxygen atoms that mimic the K^+ hydration shell. This creates four K^+ binding sites (B; two of four subunits shown). Extracellular and intracellular sites feed ions into the filter. C) The $2F_o$-F_c density map (2σ) shows the presence of potassium within the filter. In the intracellular vestibule, the potassium ion is coordinated with eight water atoms. Images reproduced from Zhou *et. Al.*[29] and Joao *et. Al.*[42] with permission from Nature.

However, the snug fit of potassium ions does not entirely account for potassium selectivity. It is thought that the number of contiguous potassium sites in the filter is also important. Publication of the crystal structure of NaK channel revealed that it has two binding sites chemically identical to S3 and S4 within K^+ channels[32] (Figure 1-5). However these channels can conduct both sodium and potassium ions at equal rates. This may be due to the reduced number of contiguous K^+ sites in the filter. Mutation of a NaK channel to contain three binding sites equivalent to S2-S4 (TVGDGNFS to TVGDTPP, NaK-CNG) did not enforce K^+ selectivity[43]. A further mutation restores S1, and the resulting four contiguous binding sites (S1-S4) impart K^+ selectivity to the channel (P_{Na}/P_K ~0.04).

Molecular dynamics simulations of the 3 (NaK-CNG) and 4 (KcsA) site channel structures provide an energetic explanation of why the number of contiguous binding sites is important for selectivity. In these simulations, potassium ions are placed at the S2/S4 or S1/S3 positions, consistent with the soft knock-on mechanism discussed in 1.4.2. Sodium ions introduced at the intracellular vestibule can bind within this selectivity filter, occupying the

space between potassium sites (S0-S1 or S3-S4)[44,45]. Four protein carbonyls and two water molecules coordinate them. These atoms form an octahedron reminiscent of the Na^+ hydration shell. An energy barrier of >10 kCal mol^{-1} at the S2-S3 site prevents them from completely traversing the filter. However in NaK-CNG this barrier lowers to 6 kCal mol^{-1} [46] . This may allow sodium through the filter.

Two reasons are proposed for the difference in energy barriers experienced by Na^+ ions passing through the 3 and 4 site channels. The first is based on restraints arising from an S0 potassium ion. In a four-site channel the S0 ion constricts movement of the S1 potassium, imposing an energy barrier to sodium binding at the S2-S3 site. The relatively high freedom of movement of the S1 ion in a three-site channel, this energy barrier is dramatically reduced. Alternatively, the increased water density at S1 in the NaK-CNG protein could reduce the S2-S3 sodium energy barrier. The two site protein (NaK) has a water-filled cavity in lieu of S2, thus no S2-S3 barrier would exist[44].

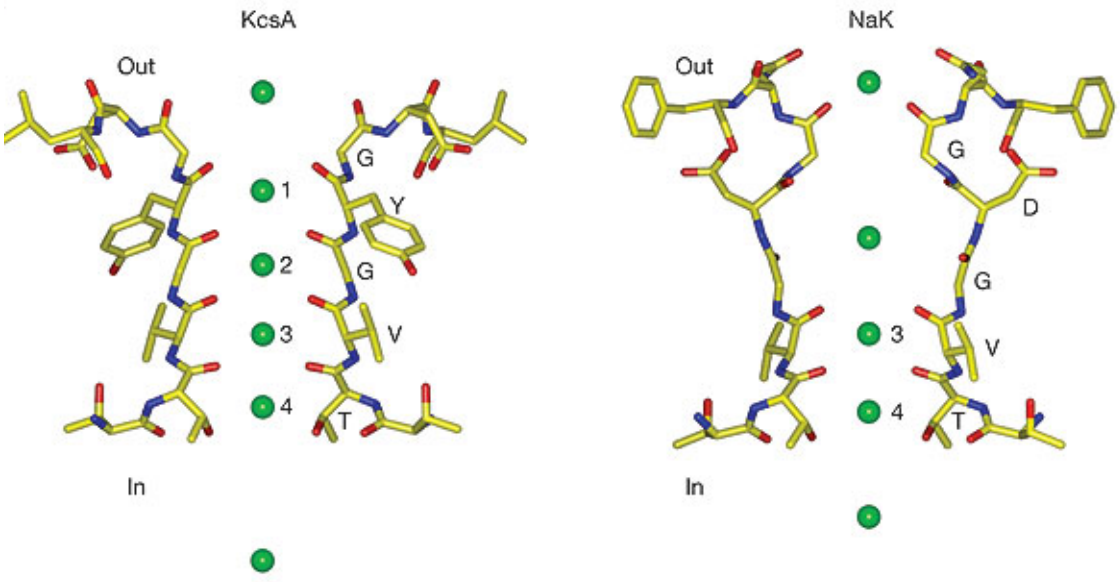

Figure 1-5 Structure of the KcsA and NaK selectivity filters

There are four potassium-binding sites within a potassium selectivity filter (S1-S4, green spheres, shown left for KcsA). By contrast, a selectivity filter which is unable to distinguish sodium from potassium (NaK channel, right) has just two sites (S3-S4) which are chemically identical to those observed in potassium channels. The number of contiguous potassium sites may therefore be an important factor in determining potassium selectivity. Figure from Shi *et al.* 2006[32] with permission from nature.

Consistent with this, the TRPV1[33] and NaV [30,31] structures (both Na^+ permeable) have shorter narrow selectivity filters than K^+ channels, accompanied with wide outer pores (Figure 1-3 A). Although the structures do not indicate the number of binding sites within the filter (this may be due to the low resolution or the relatively weak affinity of ions for the filters), structural inference combined with molecular simulations indicate there are two or three ion-binding sites within the TRPV1[47] and NaV[30,48] Channels. The NaV channel has a wider selectivity filter than KcsA, as is expected due to the larger radius of the partially hydrated ions that pass through it.

1.4.2 Mechanisms for high-flux potassium conduction

The potassium selectivity filter provides a specialised binding site for dehydrated potassium ions. However, selectivity is one of two necessary properties for an ideal K^+-channel. The pore must also support high potassium fluxes at near diffusion-limited rates. This means that K^+ cannot bind to strongly within the channel, or it will not move through. To that end, the filter undergoes a conformational change on potassium binding. In low potassium concentrations the filter collapses becoming non-conductive. When potassium concentration increases, a conformational change moves the channel to a conductive state. This takes up some of the binding energy of the ion making it less stable and facilitating high flux through the channel[49].

High potassium flux is also maintained by a fine-tuned mechanism of knock-on conduction through the pore. A long held mechanism for conduction involves K^+ ions occupying the pore in one of two configurations, either S1/S3 or S2/S4. This is consistent crystallographic occupancy of 0.5 that has been observed in each site in KcsA (using Tl^+ ions as a K^+ analogue)[49]. The remaining sites contain water molecules that are thought to be necessary to shield the repulsion between two K^+ ions. A potassium ion enters the filter either from the intracellular vestibule or from the extracellular K^+ binding site (S0). In a concerted process, the ions in the filter move between the S1/S3 and S2/S4 configurations to expel K^+ from the

opposite end of the filter. The S1/S3 and S2/S4 configurations are energetically equivalent to one another; simulations have demonstrated that this is required to maximise ion flux through the channel[49–51]. Since the K^+ ions do not directly contact each other, this is known as the soft knock on mechanism[52].

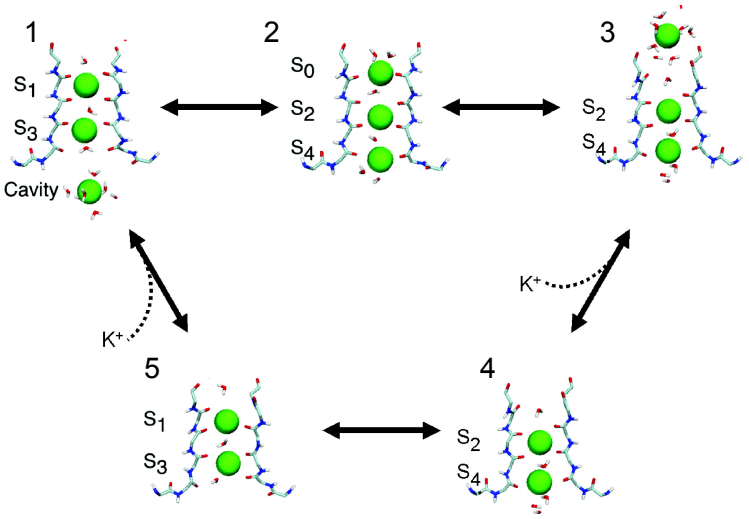

Figure 1-6 Soft known-on mechanism of potassium conduction
A potassium ion enters the filter from the cavity while two other ions occupy sites S1/S3 (1). In a concerted movement, all the ions move up a position (2). An ion is expelled to the extracellular site S0, and the ions in the filter move to configuration S2/S4 (2-4). Since S1/S3 is readily interchangeable with S2/S4, the process begins again (5). Figure from Roux *et. Al.*[51] with permission from Nature.

However, recent computational simulations challenge the soft knock on mechanism. Köpfer *et al.* suggest that the lack of potential difference and bias in restraints in previous simulations may have led to erroneous results[53]. Instead a mechanism is proposed that involves neighboring sites S2 and S3 to be simultaneously occupied. This mechanism would use direct coulomb repulsion between the K^+ ions through the filter and maintain a high flux. Such a mechanism would explain why large volumes of water do not co-translocate through potassium channels. The authors also re-analysed the KcsA Tl^+ soak X-ray crystallography data, finding that all sites have occupancies close to 1. This is in contrast with the original analysis by Zhou *et al. in 2003* [49], that suggested all sites have an occupancy of 0.5, and supports the direct coulomb knock on mechanism of potassium conduction. Since this mechanism involves direct contact between K^+ ions, it is known as the hard knock-on mechanism[52].

Whichever mechanism potassium uses to transverse the filter, the importance of filter structure in maintaining rapid potassium flow is evident. Changes in the structure of the pore would therefore have a dramatic effect on potassium flow. Indeed, such changes can

underlie gating in potassium channels. This type of gating is known as C-type inactivation. In KcsA, structures of C-type inactivated channels have potassium occupancy only at the S1 and S4 sites[54].

1.5 Two Pore Domain Potassium Channels

While all K^+ channels share the same pore architecture, addition of domains to the subunits has allowed them to evolve specific functions. K^+ channels are therefore classified based on the subunits they contain (Figure 1-7). 2M/P are the prototypical K^+-channel subunits and include K_{ir} channels. Addition of a further four TM helices allow channels to become voltage sensing or ligand gated. Finally, two prototypical subunits are sometimes fused to form a 4M/2P subunit. These atypical channels are dimeric, and include two-pore-domain (K2P) potassium channels[55].

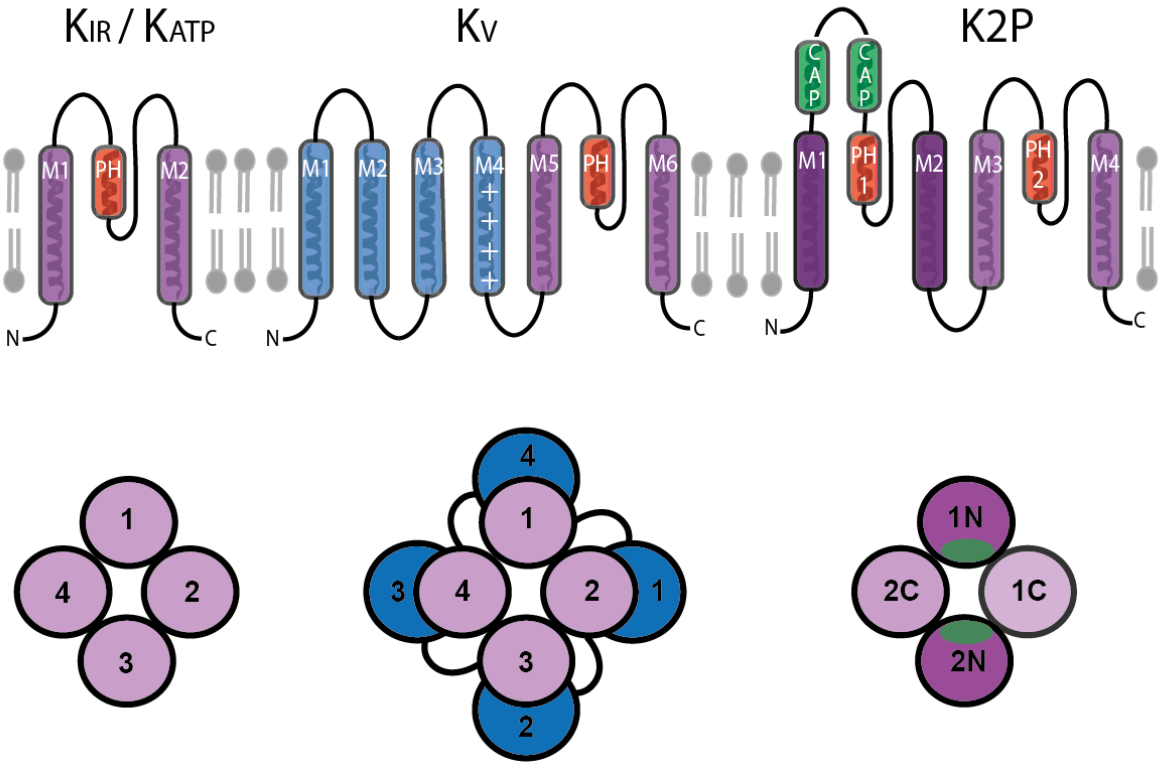

Figure 1-7 Potassium channel families

Top: Schematic of a single subunit of a potassium channel. Bottom: Schematic of an assembled channel numbered by subunit. There are three main types of potassium channel. The canonical voltage gated K_{IR} subunit contains 2 transmembrane helices (purple) and one pore-forming domain (red) per subunit and assemble as tetramers. Voltage gated channels K_v contain an extra 4 transmembrane helices (blue) and are also tetramers. The voltage sensing domains (blue) interact with the M5-PM6 domains (purple) of the clockwise subunit. The two-pore domain K2P channels contain 4 transmembrane helices and two pore forming domains per subunit, so assemble as dimers. These dimers are labelled by subunit (1 and 2) and the N and C terminus of the subunit is also labelled (1N, 1C, 2N, 2C). They also contain an extracellular cap domain (green). Figure based on Sharma 2012[56] and produced in Adobe Illustrator.

K2Ps are a family of K^+ channels whose function is to maintain the resting potential of cells and thus modify cellular excitability[57,58]. This control of membrane potential is linked to excitability, as it determines the magnitude of excitation required for action potential initiation[59].

K2Ps have several unique features that are evident from their amino acid sequence. Perhaps most striking is that they are dimeric, while most K^+-channels function as tetramers. The first dimeric potassium channel (TOK-1 channel in *Saccharomyces cerevisiae*) was identified in 1995 from genome mining in yeast[60]. Subsequently, K2P channels have been cloned from plants[61], naematodes[62], insects[63] and mammals[64]. Each K2P subunit consists of two potassium channel domains (outer helix, inner helix, and pore forming domain "P"). Dimerization provides the four pore-forming domains necessary to create a K^+ selectivity filter without the need for four subunits[65,66]. Mammalian subunits also contain an extra cellular cap domain of unknown function (Figure 1-8).

The highly conserved four-fold symmetrical selectivity filter sequence T–X–G–Y–G appears less conserved in K2Ps than among tetrameric potassium channels (Table 1-1). These channels instead encode a two-fold symmetrical pore; the first pore-forming domain P1 has the sequence T-I/T/V-G-Y/F-G, while P2 has T-I/V-G-F/L-G. This is thought to reduce the selectivity of the channels; K2P channels have a P_{Na}/P_K ten fold higher than for other K^+-channel classes. K2Ps can still effectively select for potassium over sodium, allowing just 3 Na^+ ions for every 100 K^+ ions that permeate the membrane[57]. However the relatively high Na^+ permeability is thought to be of particular

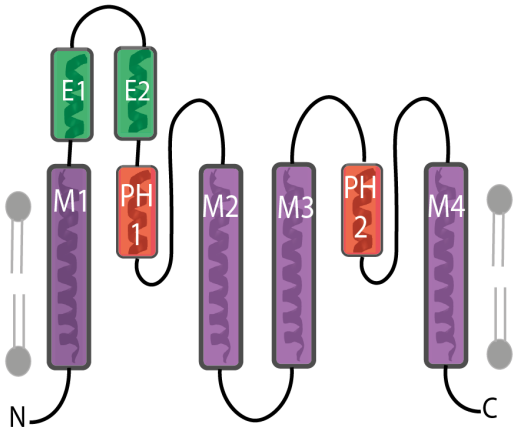

Figure 1-8 Subunit Structure of K2Ps
The subunit contains two pore-forming domains: P1 (M1→M2) and P2 (M3→M4). The extracellular cap is shown in green, and has two helices E1 and E2.

significance in pathological states, where the P_{Na}/P_K may increase further. For example the K2P channel TWIK-1 becomes more sodium permeable at low extracellular potassium concentrations. This is thought to contribute to cardiac arrhythmias during pathological hypokalemia[67].

	Pore 1	Pore 2
TWIK-1	TTGYG	TIGLG
TWIK-2	TVGYG	TIGLG
KCNK7	TTGYG	TIGLE
TRAAK	TIGYG	TVGFG
TREK-1	TIGFG	TIGFG
TREK-2	TIGYG	TVGFG
THIK-1	TIGFG	TIGFG
THIK-2	TIGFG	TIGFG
TALK-1	TIGFG	TIGFG
TALK-2	TIGYG	TVGFG
TASK-2	TIGYG	TIGFG
TASK-1	TIGYG	TIGFG
TASK-3	TIGYG	TIGFG
TASK-5	TIEYG	TIGFG
TRESK	TVGYG	TIGFG

	Pore 1
HUMAN	
Kv 1.1	TVGYG
Kv 1.2	TVGYG
Kv 2.1	TVGYG
Kv 3.1	TLGYG
Kv 4.1	TLGYG
Kv 7.1	TIGYG
Kv 11.1	SVGFG
PROKARYOTE	
SHAKER	TVGYG
KvaP	TVGYG
ROMK-1	TIGYG
IRK-1	TIGYG
GIRK-1	TIGYG
KcsA	TVGYG

Table 1-1 Selectivity filter sequences in potassium channels
The selectivity filter sequences for the two pore loops in K2P channel subunits (left) and the one pore loop in tetrameric potassium channels (right) are shown. Highlighted in red are residues that deviate from the canonical selectivity filter sequence TXGYG, where X is a hydrophobic residue.

In humans, there are 15 different K2Ps, divided into six diverse subfamilies based on sequence identity and functional similarity: TWIK (**T**andem of pore-forming domains in a **W**eakly **I**nwardly rectifying $\mathbf{K^+}$ channel), TREK (**T**WIK **Re**lated $\mathbf{K^+}$ channel), TASK (**T**WIK related **A**cid **S**ensitive $\mathbf{K^+}$ channel), TALK (**T**WIK- related **Al**kaline pH-activated $\mathbf{K^+}$ channel), THIK (**T**andem pore domain **H**alothane-**I**nhibited $\mathbf{K^+}$ channel) and TRESK (**T**WIK **Re**lated **S**pinal chord $\mathbf{K^+}$ channel)[68]. Crystal structures have been published for members of the TREK[66] and TWIK[65] subfamily. The sequence variation between K2P subfamilies is large. For example TWIK-1 and TREK-1 display only 28% identity; this almost as high as the variation between K^+ channel families[69].

The 15 K2P subunits have largely been studied as homodimers, formed of two identical K2P subunits. However, as K2P channels show overlapping expression patterns within tissues, K2P heterodimers may also form. As is the case in both voltage-dependent[26] and inwardly rectifying[27] K^+ channels, hetero-multimerisation may further increase the functional diversity of K2P channels. Indeed, functional heterodimers have been proposed for TWIK-1/TASK-3[70], TASK-3/TASK-1[70] and TWIK-1/TREK-1[71]. However, the physiological relevance of these heterodimers has yet to be demonstrated.

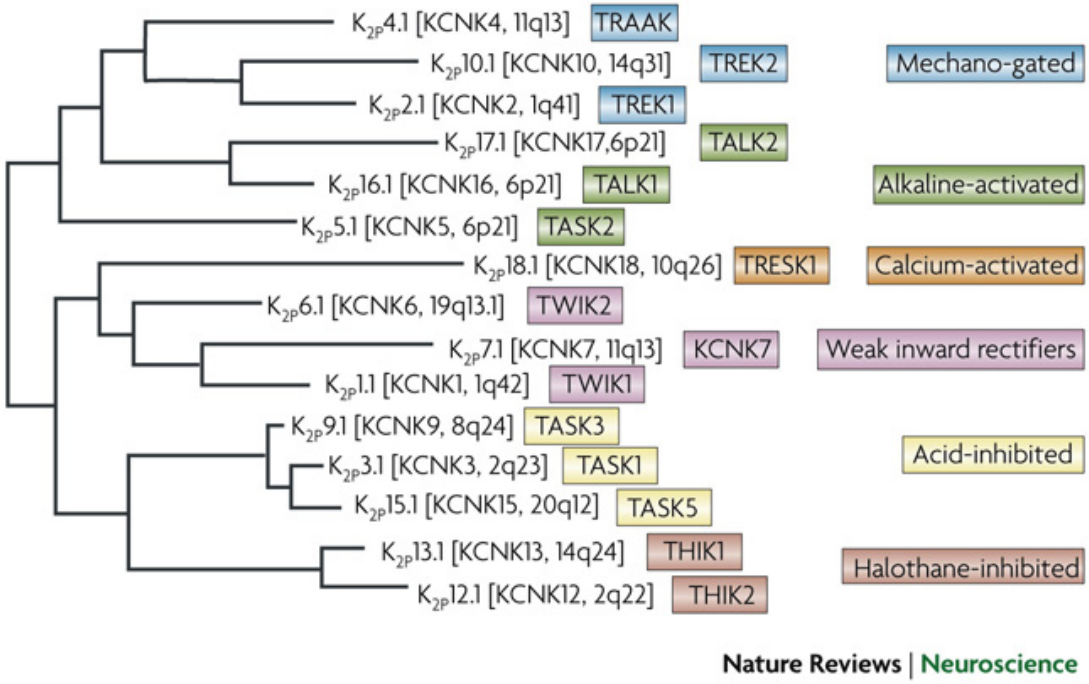

Figure 1-9 Sub-families of human two-pore-domain potassium channels

There are 15 K2P channels, split into six sub-families based on sequence identity and functional similarities. This diagram shows the phylogenetic tree for the K2P channels. Diagram from Honoré 2007[57] with permission from Nature. KCNK8, KCNK11 and KCNK14 are absent as they do not exist. The gene names and chromosome locations are given in square brackets.

1.6 Structure of K2P channels

The first structures of the K2P channels TWIK-1 (3.4Å, PDB ID 3UKM) and TRAAK (3.31Å, PDB ID 3UM7) were solved in 2012[65,66]. As expected, they had the overall transmembrane architecture conserved among K^+ channels. The M1 and M3 helices line the pore analogous to the inner helices in an open state tetrameric potassium channel. The M2 and M4 helices pack around M1 and M2 analogous to the outer helices. The pore-forming loop and helix create a selectivity filter with four potassium sites. Despite the altered selectivity sequences (TWIK-1: TTGYGH and TIGLGD, TRAAK: TVGTG and TIGPG, canonical: TXGYG), there are no observable changes in selectivity filter structure.

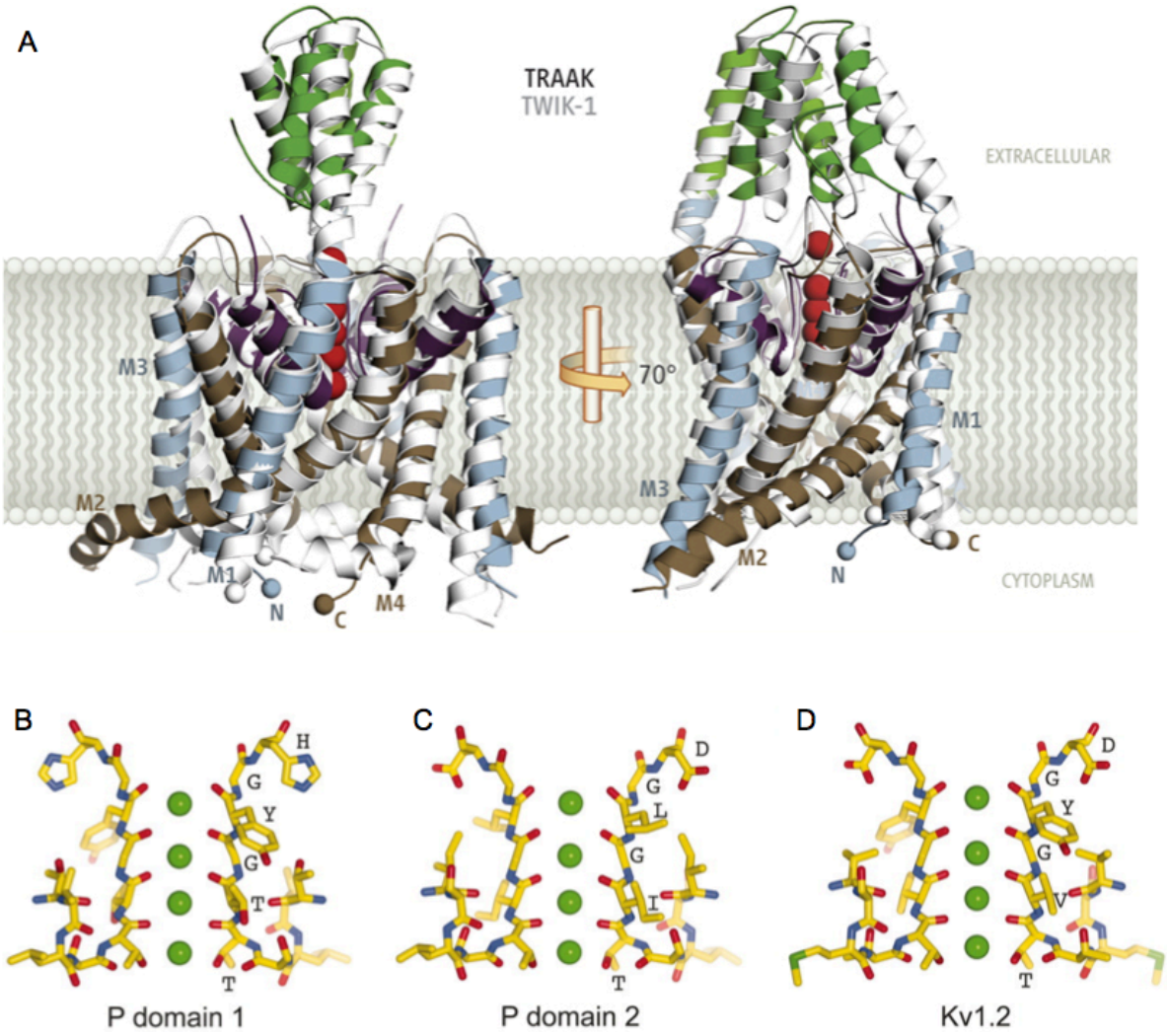

Figure 1-10 The crystal structures of TWIK-1 and TRAAK

The structures of TWIK and TRAAK have a similar overall architecture (A, TWIK-1 3UKM Grey cartoon. TRAAK 3UM7 cyan/brown/green cartoon). The structure of the selectivity filter in TWIK-1 (Figures B, C) is indistinguishable from that observed in $K_v1.2$ (PDB 2R9R, D), despite the change is amino acid sequence. Figure A reproduced from Poulsen and Nissen 2012[72].Figures B-D reproduced from Miller and Long 2012[65] . Reprinted with permission from AAAS.

However, these structures revealed key differences between K2Ps and other potassium channels. A helical extracellular cap domain was present in each subunit. Each subunit provides an ascending (E1) and descending (E2) helix forming a two-helix hairpin. A disulphide bond links the two subunits at the apex of the cap domain (TWIK-1 Cys[69], TRAAK Cys[52] between E1 and E2) about 35Å above the membrane, stabilising the dimer. The electronegative C-terminus of the E2 helix is positioned above the selectivity filter, supporting an extra binding site for partially hydrated K^+ ion. The function of this cap domain is unknown, and while it is present in all K2P channels it is absent in all other K^+-channel classes[58].

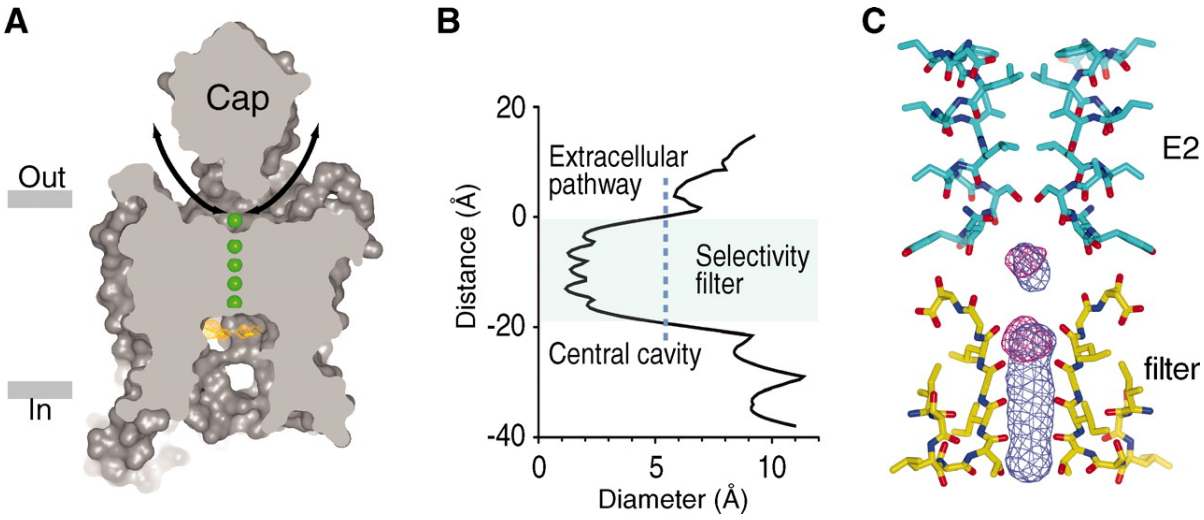

Figure 1-11 Ion conduction in TWIK-1

An extracellular cap, present in all K2P channels, is observed in the TWIK-1 structure (A). This extends the extracellular ion conduction pathway through two portals beneath the cap domain. The extracellular ion conduction pathway can be seen as a constriction in diameter above the selectivity filter (B). The dashed line represents the diameter of hydrated K^+ ions. The descending extracellular cap helices E2 (cyan) point their electronegative dipole towards the selectivity filter (yellow) (C). This creates an extra potassium ion binding site, as seen in the electron density maps (blue mesh F_o-F_c map contoured at 4σ, red mesh Tl^+ isomorphous difference Fourier map contoured at 4σ). Figure reproduced from Miller and Long 2012[65]. Reprinted with permission from AAAS.

The cap also serves to extend the extracellular ion pathway in the channel. Access between the extracellular milieu and the selectivity filter is restricted to two side portals, lined with negatively charged side chains, that are created by the cap domain. These portals are wide enough to support the flow of fully hydrated potassium ions, but may prevent access of larger ions or ligands to the selectivity filter[65].

In both channels two fenestrations are visible. These fenestrations lie between M4 and M2, connecting the inner vestibule of the chanel with the hydrophobic region of the cell membrane. Such fenestrations have been observed for other ion channels (tetrameric NaV for example has four fenestrations[30]), and may be binding sites for ligands. Electron density was visible in these sites, and the authors of TWIK-1 have modelled this density as a lipid chain[65].

Both K2P channels have an ampipathic helix which may be involved in gating. This is particularly striking in TWIK-1 where a almost 90° bend in the M4 helix creates a "C-Helix" that runs parallel to the (modelled) intracellular leaflet of the membrane. This helix does not appear to be involved in a crystal contacts. In $K_v1.2$ an intracellular amphipathic helix couples the S4 and S5 helices. This connects the voltage sensing domain (S1-S4) with the channel domain (S5-S6), allowing it to gate the channel[73]. Such a helix also exists in voltage gated sodium channels[30]. This suggests that movement of an interfacial helix may gate K2P channels.

The next K2P publication, in early 2013, revealed a domain-swap in TRAAK channels[74] (Figure 1-12). The authors used an antibody fragment to increase the resolution of TRAAK crystals to 2.75Å (PDB ID 4I9W). This higher resolution data demonstrated that an error might have occurred in chain tracing for the first two published K2P structures. The subunits in in the higher resolution TRAAK structure (4I9W) have a domain swap at the disulphide bond; the inner helix in one subunit interacts with the outer helix of another subunit[74]. This had not been seen in other potassium channels of known structure.

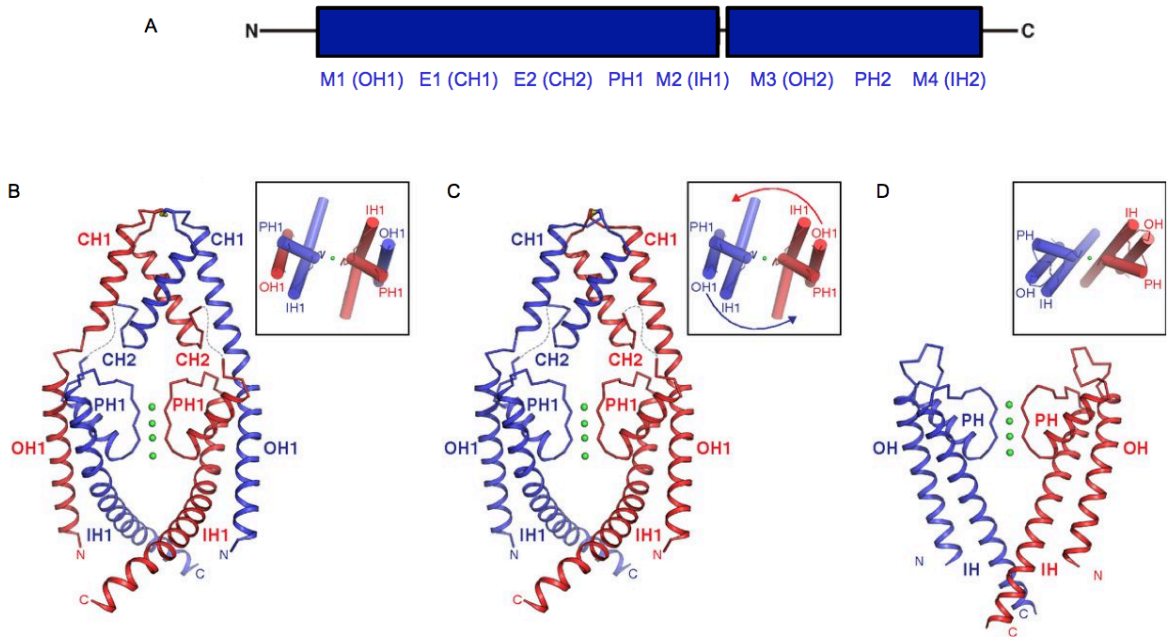

Figure 1-12 Domain swap in TRAAK

Figure A shows the subunit structure of TRAAK. In blue is one subunit, and in red the second. The names of the helices are given both how they are presented in this thesis (M1-M4) and how they are presented in the TRAAK domain swap publication (Inner Helix IH, outer helix OH). Figures B-D show the domain swap in 4I9W (B), the original lower resolution TRAAK model 3UM7(C) and K_v 1.2 for comparison. Images B-D are reproduced from Brohawn *et al.* 2013[74]. Reproduced with permission from PNAS.

This structure also differed in that it had just one fenestration- the second fenestration had been closed by the upward movement of M4 around the glycine hinge Gly[268]. M4 residues Phe[272], Val[275], Ile[279] and Leu[283] were packed against M2, resulting in closure of the fenestration. This compared with the M4 state observed in the other chain where a gap between M2 and M4 resulted in a fenestration. This structure provided the first evidence that M4 could move.

TREK-2 was the first K2P to be solved in two completely different states[75]: with both M4 helices down (4XDJ, “down state”) and with both up (4BW5, “up state”) (Figure 1-13). The authors also observe movement of the M2-M3 helices between the two states that had not yet been noted in other K2Ps. In the down state, the M2/M3 helices move downwards into the cytoplasm while simultaneously rotating clockwise (when viewed from the cytoplasm). At this time the functional relevance of these two states was not known. However, the down state has reduced ion occupancy in the filter (only S2-S4 sites were occupied), indicating that this may be a less conductive state.

While the data presented here were being solved and published, a further two high-resolution TRAAK structures were published by Brohawn *et al.*[76]. These structures had TRAAK in dual M4 down and dual M4 up states. The functional implications of these states were investigated using thallium soaks as a potassium analogue. The functional implications of M4 movement were also studied in TRAAK by Lolicato *et al.*[77]. This work is discussed in more detail in Chapter 3, in the context of the results generated in this thesis.

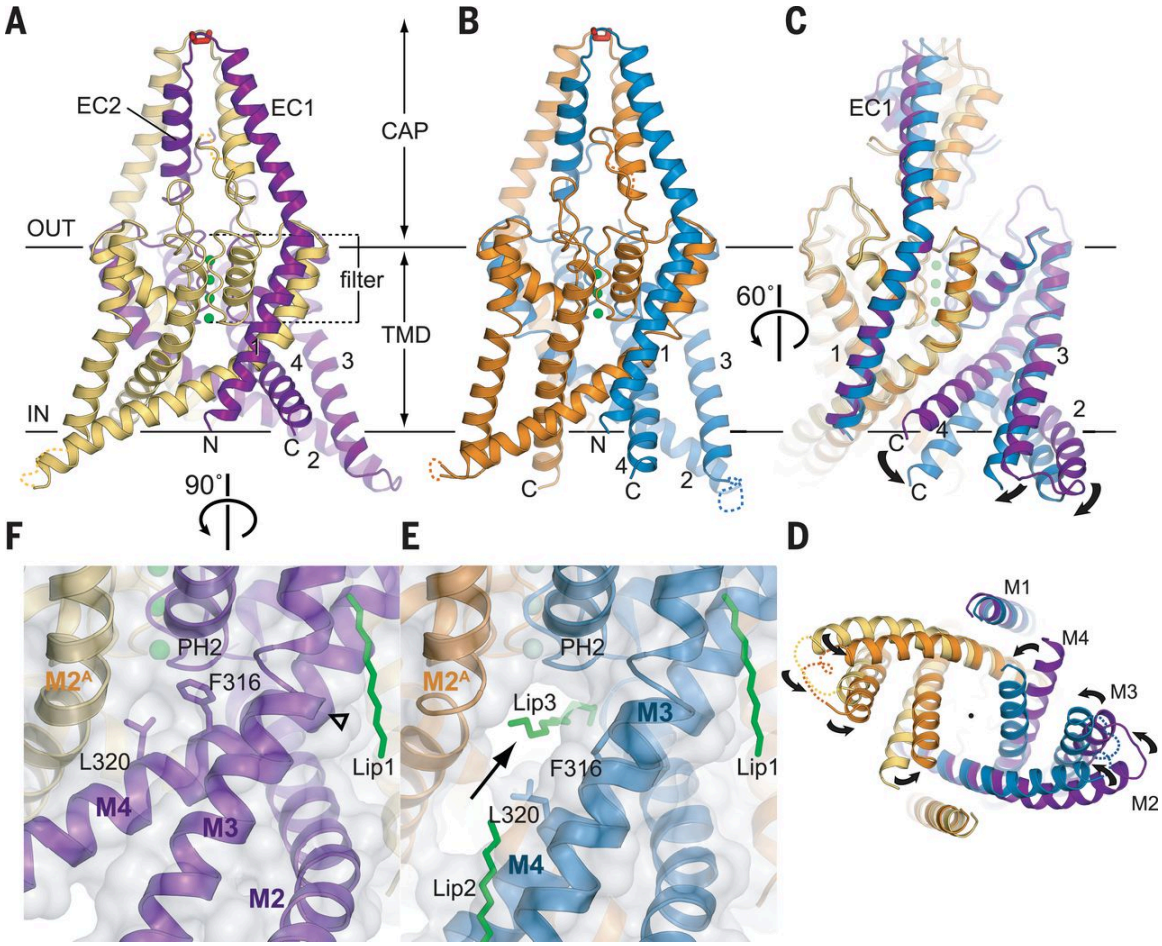

Figure 1-13 Movement of M2-M4 in TREK-2 seals a fenestration

TREK-2 structures are shown in the up state (4BW5, purple/yellow, A) and the down state (4XDJ, orange/blue, B) and overlaid in C. Figure D shows the overlaid structures viewed from the intracellular leaflet of the membrane. These figures demonstrate that helices M2-M4 are in different conformations in the two states. In the down state, M2-M4 move down to project further into the cytoplasm. There is also a clockwise rotation of the helices (when viewed from the cytoplasm). In the down state two lateral fenestrations connect the lipid membrane with the inner vestibule of the channel (E). These fenestrations contain elongated density that has been modelled as a lipid molecule. In the up state the fenestrations are blocked by Phe^{316} and Leu^{320} (F). Figure reproduced from Dong *et al.* 2015[75]. Reprinted with permission from AAAS.

1.7 Function of K2P Channels

Electrical signalling in cells originates from the underlying potential difference across the cell membrane (E_m) during quiescence; this is known as the resting potential. By maintaining a negative potential, voltage-dependent processes such as action potential initiation can be dormant until activated by a suitably large excitatory input; the more negative the resting potential, the larger the excitatory input required. Regulation of V_{rest} can therefore regulate cell excitability[1].

E_m is determined by two factors; firstly the relative concentration of intra and extra cellular ions. In animal cells, the ATP-driven Na^+-K^+ ATPase ensures that the intra-cellular concentration of K^+ is high while the intracellular Na^+ concentration is low, leading to high concentration gradients across the cellular membrane. The concentration gradient influences the reversal (Nernst) potential of the ion; the membrane potential at which the net flux across the membrane is zero for a given ion (i.e. electrochemical equilibrium is satisfied). Secondly, E_m is determined by the relative permeability of the membrane to these ions. If the membrane permeability to a particular ion is high, that ion will flow through the membrane towards equilibrium. As it flows, the resting potential of the cell is driven towards the Nernst potential for that particular ion. This is described by the Goldman-Hodgkin-Katz (GHK) voltage equation;

$$E_m = \frac{RT}{F}\ln\left(\frac{P_{Na^+}[Na^+]_{out} + P_{K^+}[K^+]_{out} + P_{Cl^-}[Cl^-]_{out}}{P_{Na^+}[Na^+]_{in} + P_{K^+}[K^+]_{in} + P_{Cl^-}[Cl^-]_{in}}\right)$$

where E_m is the membrane potential (Volts), R the ideal gas constant (joules/kelvin), F the Faraday constant(coulombs/mole), T the temperature (Kelvin), $[ion]_{out}$ the extracellular concentration, $[ion]_{in}$ the intracellular ion concentration and P_x the permeability of the ion across the membrane. In effect the resting potential represents an average of the Nernst potentials of permeant ions, weighted by their relative permeabilities.

The resting potential of most cells is close to the reversal potential for K^+ (-40 to -70mV is typical), indicating that the membrane is highly permeable to potassium during quiescence. Therefore K^+ permeability, which gives rise to K^+ current across the membrane, largely determines the resting potential of the cell. This phenomena was first observed as a "leak" current by Hodgkin and Huxley, and the K^+ channels ("leak" channels) which facilitate it can control cellular excitability via control of E_m[37].

Any K^+ channel that is active near the resting potential can constitute a leak channel, and two main families of potassium channels exist that fulfil this requirement. The first are inwardly rectifying channels, which are reviewed extensively elsewhere[37]. The second are the two-pore-domain potassium channels (K2Ps), which are the focus of this work.

K2Ps facilitate K^+ currents that have been traditionally described as time independent (slowly or non-inactivating) and not voltage gated; ideal properties for leak channels (Figure 1-14). However, voltage-dependent rectification has since been reported. This is partially due to the voltage dependence of the current in the presence of external Mg^{2+} ions[78] (although the how Mg^{2+} influences channel function is unclear). Additionally, studies by the Baukrowitz group (Physiological Institute; Christian-Albrechts University) suggest intrinsic voltage dependent C-type gating within the filter of K2P channels (under review). This conformational change may allow the filter to act as a one-way value at certain E_m values.

Despite the name "leak ", K2Ps are not constitutively active. K2P function is regulated by a number of physical and chemical factors including membrane stretch, volatile anaesthetics and pH. K2Ps therefore act to respond to environmental changes by modifying cellular excitability[68].

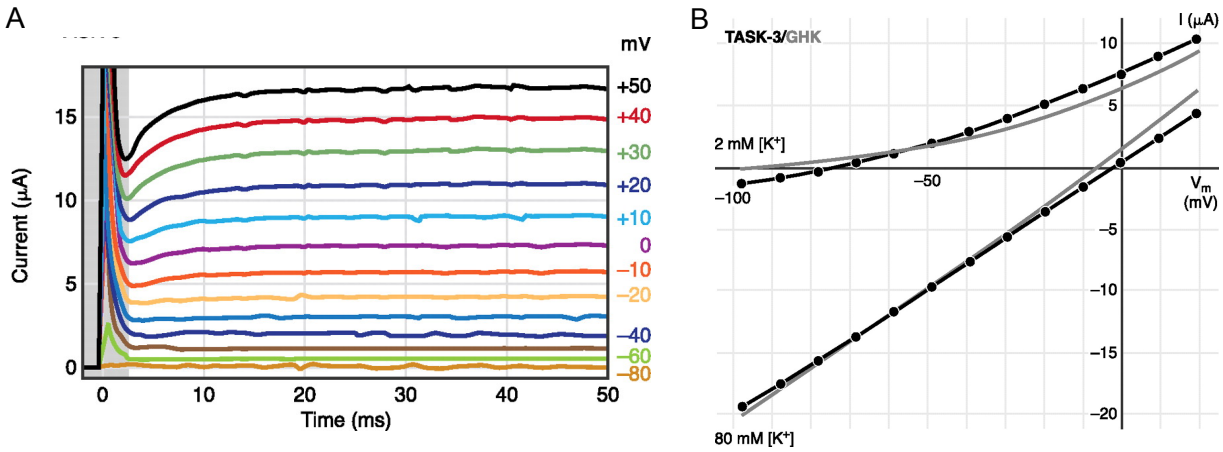

Figure 1-14 Current-Voltage Relationships in K2P Channels

K2P channels can be thought of as leak channels, since the current through them is related to the voltage across them, like a simple resistor. Here, the human TASK-3 channel is expressed in *Xenopus* Oocytes. The membrane is then clamped from -80mV to +50mV in 10mV increments, with a holding potential of -80mV. The current resulting from the voltage step is recorded (A). After the capacitative transient (grey shaded), the current through TASK-3 increases with increased membrane depolarisation, as is expected with a leak channel. B) Compares the current (at 2.4ms) / voltage (-80 to 20mV; 1mV steps) profile of TASK-3 in symmetric (80mM) and physiological (2mM) K^+. Drawn in grey is the current that would be observed through a perfect leak channel according to the GHK current equation. K2P channels are therefore a good approximation to a GHK open rectifier or leak channel. Image reproduced from Czirjak and Enyedi 2010[79]. Reprinted with permission from the American Physiological Society.

1.8 TREK K2P Channels

First discovered in 1996[69], the **T**WIK-**Re**lated-**K**$^+$-Channel (TREK) K2P subfamily has three members: TREK-1 encoded by KCNK2[69], TREK-2 encoded by KCNK10[80,81] and TRAAK (**T**WIK-Related-**A**rachadonic-**A**cid-sensitive-**K**$^+$-Channel) encoded by KCNK4[82]. TREK-1 and TREK-2 share 63% of identical residues and 78% of homologous residues. TRAAK is less similar to the other TREK channels, sharing 45% identity and 69% homology with TREK-1[83]. TREK channels are distributed in the central and peripheral nervous system, pointing to their importance in neurophysiology. TREK-1 and TREK-2 can also be found in the heart and other visceral organs[84].

1.8.1 Diversity of TREK channels

TREK channels are encoded by single genes with seven exons per gene[81]. However these genes do not produce a single protein product. The diversity of TREK channels is increased through alternative splicing in exon 1[81], which produces functional proteins with amino-terminal variants[85]. Splice variation does not appear to alter the biophysical properties of the channel[86,87], however relative expression of the splice variants is tissue dependant.

Heterogeneity is further increased through alternative translation initiation. TREK-1 and TREK-2 have weak kozak sequences and possess downstream in-frame AUGs that may initiate translation. This results in channels with large truncations in the amino-terminal intracellular tail (TREK-1Δ1-56[88]; TREK-2Δ1-55; TREK-2Δ1-67[89]). These variants have reduced potassium selectivity in TREK-1 (P_{Na}/P_K = 0.18[88]) , and modify unitary conductance in both TREK-1 and TREK-2. The relative abundance of these isoforms is tissue specific.

Although TREK channels have mostly been studied as homodimers, they may also function as heterodimers. Indeed, TREK-1 covalent heterodimers with TWIK-1 have been proposed,

and may be important in electrical signalling in astrocytes[71]. Functional heterodimers may also exist between different isoforms of the same TREK subunit. This would explain the observation of intermediate conductance channels when the isoforms are co-expressed[89].

The functional diversity of TREK isoforms together with the tissue specific distributions points to highly specialised physiological roles for these channels.

1.8.2 Regulation of TREK channels

TREK channels are modulated by a diverse range of stimuli including stretch, heat, membrane stretch, pH, membrane voltage, phosphorylation, lipids and interacting partner proteins. Although the exact mechanism by which these diverse stimuli alter channel gating is unknown, mutagenesis and chimera studies determined a ~30 amino-acid section of the intracellular C-terminus as important for the gating response. This C-terminal regulatory domain (CTD) lies at the end of M4, from Val^{298}-Thr^{322} for TREK-1 and Val^{324}-Thr^{348} for TREK-2. This highly charged regulatory domain (TREK-1 297**R**VIS**KK**T**KEE**306) is thought to interact with the negatively charged phosphate head groups within the inner leaflet of the lipid bilayer (for example the negatively charged head group of phosphatidylinositol-4,5-bisphosphate (PIP_2). Modifications to this domain could inhibit this electrostatic interaction, causing it to move away from the bilayer. This movement may be linked to changes in protein confirmation that cause channel activation (Section 1.10)[68]. A homologous region has been shown to be important in the regulation of TASK channels[90], indicating this may be a common gating mechanism in K2Ps.

However, not all TREK channel gating is mediated by the CTD. Extracellular acidification for example is known to modify TREK- channel function; it is clear that this would not have a direct effect on intracellular domains of the protein.

1.8.3 Physiological Roles for TREK channels

TREK knock out mice have highlighted some of the possible physiological roles for these channels. The most well studied knockouts are TREK-1 double knock out (TREK-1$^{-/-}$) mice, which are overall healthy and normal. However, they display increased resistance to depression pointing to a potential therapeutic role for TREK-1[91]. These mice are also more sensitive to ischemia and epilepsy than the wild type (WT). This role of TREK-1 in neuroprotection is thought to be mediated by poly-unsaturated fatty acids (PUFAS) such as arachidonic acid which are released during brain ischemia, and lead to activation of TREK channels[92].TREK-1$^{-/-}$ mice are more sensitive to painful heat and mechanical stimuli than WT. This is a result that has been mirrored in TRAAK $^{-/-}$ [93], TREK-2 $^{-/-}$, and TREK-1 $^{-/-}$ TREK-2 $^{-/-}$ TRAAK $^{-/-}$ triple knockdown mice[94]. TREK channels are expressed in dorsal root ganglion neurons (DRGN) along with polymodal TRP channels. TREK-1 is thought to oppose the effect of TRP channel, reducing the magnitude of depolarisation resulting from the heat or pressure induced opening of TRP channels such as TRPV1[95]. In addition, TREK-1$^{-/-}$ mice have abolished sensitivity to inhalational anaesthetics such as chloroform and halothane[92]. This points to a role for TREK-1 in anaesthesia.

1.9 TASK K2P Channels

First cloned in 1997[96], the **T**WIK-related-**A**cid-**S**ensitive-**K**$^{+}$-Channel (TASK) K2P subfamily has three members: TASK-1 encoded by KCNK3, TASK-3 encoded by KCNK9 and TASK-5 encoded by KCNK15[97]. The evidence for TASK-5 is on a transcript only level; no functional TASK-5 protein has been discovered. TASK-3 and TASK-1 share high sequence identity of 54%. However, they share less than 30% identity with TASK-2 (KCNK5) and TASK-4 (TALK-2), which is reflected in their different biophysical characteristics. TASK-2 and TASK-4 have therefore been reclassified as TALK channels[98]. In humans, TASK channels are highly expressed in cerebellum[99], while evidence of a wider tissue distribution has been

found in rats[96]. TASK-3 channels are also overexpressed in human cancers including breast lung and colorectal cancer[100,101].

1.9.1 Regulation of TASK channels

TASK channels are named after their sensitivity to extracellular pH variations within physiological ranges. Channel inhibition arises from protonation of a histidine (TASK-1 and TASK-3 His[98]) residue in the P1 domain, following the GYG selectivity motif[102]. In most other K2Ps, this amino acid is an aspartic acid. As well as reduced K^+ currents, TASK channels demonstrate increased Na^+ permeability in response to extracellular (EC) acidification[103]. Neither channel is sensitive to intracellular pH. TASK channels therefore respond to EC acidification by reducing potassium current and increasing sodium permeability across the membrane.

TASK channels are also characterised by their response to inhalational anaesthetics. A VLRF(M/L)T sequence in the proximal C-terminal domain (equivalent to the TREK CTD) is necessary for this activation. Interestingly, this region was also found to be vital for inhibition by neurotransmitters (an indirect affect), indicating that the same region of the protein can be involved in both activation and inhibition[104].

The functional diversity of TASK channels is increased through heterodimerisation between members of the TASK subfamily. These channels are highly homologous and have overlapping tissue distributions, which means they can form functional heterodimers[70]. Indeed, these heterodimers can constitute between up to 75% of pH sensitive background currents in certain cell lines[105].

1.9.2 Physiological roles for TASK channels

Due to the ability of TASK channels to couple changes in pH to changes in cell excitability, they have physiological roles in acid sensing processes such as sensing hypoxia in the carotid body[106] and vasoconstriction in response to reduced PO_2 levels in pulmonary arteries[107].

Knockout mice have provided evidence for further physiological roles of TASK channels. Double knock outs (TASK3$^{-/-}$/TASK1$^{-/-}$) show characteristics of low renin hypertension[108] and hyperaldosteronism[109]. TASK-1 knockouts show significant changes in electrical function of the heart, including modified ECG traces (prolonged QT intervals and repolarisation)[110,111]. Indeed, TASK channels are modulated by several antiarrhythmic drugs[112,113]. Meanwhile TASK-3 knockouts have reduced sensitivity to inhalational anaesthetics, impaired cognitive abilities and nocturnal arousal.[114]

TASK-3 is unique amongst the K2P channels in that it is only expressed from the maternal allele[19]. In humans, a TASK-3 mutation is associated with maternally inherited disease with mental retardation and characteristic dysmorphism[20]. This correlates well with evidence from TASK-3 knockout mice, which have impaired cognitive abilities.

1.10 K2P Channel Gating

KcsA was first solved in a closed state in 1998[21]. This structure demonstrated gating of the channel at the helical bundle crossing; gathering of the helices near the intracellular leaflet of the membrane provided a physical blockade to ion flow. It would take another 5 years before the first structure of a open-state potassium channel would be published[27]. In the open state, bending of the TM2 helices at a conserved glycine hinge[115] forces them rotate and pivot away from the symmetry axis of the pore. This opens a 12Å aperture at the

intracellular gate, removing the physical blockade to ion flow. This bundle-crossing gate is thought to be the primary gating mechanism of most potassium channels.

Figure 1-15 Conserved glycine hinge in potassium channels
KcsA and MthK have been aligned (Clustal Omega) with the P1-TM2 and P2-TM4 domains of TREK-1 and TREK-2. In grey, the filter sequences are well aligned. Highlighted in red is the conserved hinge glycine.

Since the glycine hinge is conserved in K2P channels, they could also gate through this mechanism (Figure 1-15). The role of he bundle-crossing gate in K2Ps was investigated using Quaternary Ammonium ions (QA), high affinity blockers which access the pore from the intracellular vestibule and lodge beneath the selectivity filter. This results in a physical blockade to ion flow. It was found that QA ions could access this binding site equally well in both the conductive and non-conductive states. This indicates K2P channels have a constitutively open intracellular bundle-crossing gate[116]. Therefore the gate in K2P channels must lie further up in the channel; either within or close to the selectivity filter.

More than ten years after the structure of KcsA was published, the first structures of K2P channels were solved; TRAAK[66] and TWIK-1[65]. Both channels had 3-dimensional structures closely resembling classical potassium channels; four outer and four inner helices supported a 4-fold pseudo symmetric selectivity filter. In both structures the helical bundle-crossing gate was clearly open. Consequently, all nine deposited structures of K2P channels have open bundle crossings. The M2-M3 linker present in all of these channels may impose a structural constraint on closure of this bundle crossing.

However, structural evidence suggested these helices could move. A high resolution TRAAK-Fab structure was soon published[74], which demonstrated the domain-swapped nature of K2P channel subunit interactions. While one M4 helix was straight, the second M4 helix was kinked at the conserved glycine hinge. Rather than obstructing the ion conduction

pathway, bending of the M4 helix instead lead to closing of the corresponding fenestration. This provided a mechanistic explanation for electrophysiological data suggesting that changes in the CTD could affect M4 and in turn this could affect C-type gating in the pore[117].

Integration of this data allowed a structural model of K2P channel gating to be hypothesised. Changes in the CTD cause it to associate or dissociate from the inner leaflet of the membrane. This is tightly coupled with movement of M4, and this movement is coupled with structural changes in the filter that lead to channel gating[56]. However, the exact changes within or close to the filter that lead to gating are unknown.

1.11 An introduction to crystallography

In what follows below, I will briefly describe the fundamental mathematical aspects of crystallography. I will start by describing diffraction from a set of parallel planes, and how this can be used to determine data collection strategies. I will then go on to describe scattering as mathematically equivalent to a Fourier transform, and thus the mathematical basis of structure determination. Finally I will describe how electron density maps can be generated from diffraction data and used to build an accurate protein model.

1.11.1 Crystallography shows the average structure of a protein in a crystal

Of course, a single molecule can give rise to diffraction. If this is the case then why must we grow a crystal containing ~10^{13}-10^{15} molecules? This is because diffraction from a single molecule is very weak; the intensity of the pattern on the detector would be indistinguishable from noise. It is therefore necessary to sum the scattering effects of many molecules aligned within the crystal[24].

It is therefore important to realize that crystallography is not a single-molecule technique. Although a single model of the protein is produced, this model represents the average structure of all of the 10^{15} proteins within the crystal. Furthermore, the non-zero time duration of the experiment means that the result is also a time-averaged structure of the average protein within the crystal[24].

1.11.2 Diffraction from a set of planes

A crystal can be described as a repeating motif of proteins. This repeating array of proteins can be described as a minimum crystallographic unit known as the asymmetric unit along with the symmetry of the crystal. Combining the asymmetric unit with this symmetry produces a unit cell. The unit cell is described by its dimensions a,b,c and by the angles between these dimensions α, β, γ The unit cell is repeated to fill space[23].

Bragg's law defines how scattering (diffraction) occurs from within the unit cell. The unit cell can be described by sets of parallel planes. The number of times each set of planes intersect the crystallographic axis defines their Miller indices, given in parenthesis as (h k l). For example, a set of planes that intersects the a axis once, the b axis twice and the c axis three times are known as the (1 2 3) planes. Higher frequency information, in other words finer detail, is encoded in planes that intersect the unit cell axis with a higher frequency and therefore have larger Miller indicies[22,24].

Bragg's law states that constructive interference of diffracted waves (I.e. maxima on the detector, also known as Bragg peaks or reflections) occurs only when experimental geometry fulfills the condition;

$$2\, d_{hkl} \sin(\theta) = n\lambda \qquad \textbf{Equation 1-1}$$

where d_{hkl} is the perpendicular distance between the set of plane with Miller indices (h k l), θ the angle between the X-ray beam and the planes (or half the angle between the incident

and reflected beams), n is any integer number and λ is the wavelength of the incident beam. Therefore, to measure reflections for all sets of Bragg planes the angle θ must be varied; that is to say the crystal must be rotated in the beam[22,24].

To understand how to define the geometry of the experiment such that the maximum number of Bragg peaks are detected, we must consider the experiment from the view of the reflections themselves; in reciprocal space. The reciprocal space lattice is a lattice where each reflection lies on a lattice point. It is related to the real space lattice (the lattice of the crystal) by drawing lines normal to the real space planes, of a length equal to $1/d_{hkl}$. The resulting lattice points are named after the set of planes from which they arise (e.g. the (1 2 3) planes produce the 1,2,3 reflection), demonstrating that set of parallel planes produces a single diffraction peak. Only the reciprocal lattice points which obey Bragg's law at that specific geometry will appear on the detector[22–24].

To determine which reflections obey Bragg's law for a defined incident beam vector, beam wavelength and reciprocal lattice the Ewald sphere can be used. The sphere is centered on the crystal and has a radius equal to 1/λ. Reciprocal lattice points in contact with the Ewald sphere fulfill Bragg's law and produce a maxima on the detector. Rotation of the crystal at the centre of Ewald sphere rotates the reciprocal lattice through the sphere, allowing new reciprocal lattice points to obey Bragg's law and a different set of reflections to be measured. In order to sample all possible reflections it is therefore necessary to rotate the crystal such that each reciprocal lattice point comes into contact with the Ewald sphere. However, since the Ewald sphere is finite (it's radius dependent on the wavelength of the beam), the number of measurable reflections is also finite, and is bounded by a limiting sphere. This determines the maximum resolution that is theoretically achievable for a given crystal at a given wavelength[22–24].

1.11.3 Diffraction as a Fourier transform

The diffraction pattern is a Fourier transform of the electron density

While it is conceptually helpful to consider the crystal as being made up of sets of planes, in fact the crystal is made up of atoms containing electrons. When elastic scattering (diffraction) of X-rays occurs from these electrons, the resulting wave can be described mathematically as the Fourier transform T of the crystal of volume V;

$$F(\boldsymbol{r}^*) = \int_V \rho(\boldsymbol{r})\, e^{2\pi i\, \boldsymbol{r}^*.\boldsymbol{r}}\, d\boldsymbol{r} = T[\rho_M] \qquad \textbf{Equation 1-2}$$

where $F(\boldsymbol{r}^*)$ is the amplitude of diffraction from the crystal at the point in reciprocal space $\boldsymbol{r}^*$, $\boldsymbol{r}$ is the real space vector of the diffracting electron density and $\rho(\boldsymbol{r})$ is the electron density of the molecule in real space. Note that $F(\boldsymbol{r}^*)$ is a **c**omplex function that has both amplitude and phase[23]**.**

As a side note: since $\rho(\boldsymbol{r})$ is a combination of electron densities from individual atoms, and atomic electrons undergo thermal motion. Therefore $\rho(\boldsymbol{r})$ must contain a Gaussian blurring term to take motion into account. The blurring induced in the diffraction pattern is highly dependent on the angle of the diffraction, and thus the resolution of the reflection. The intensity of high-resolution reflections decreases when the structure has high overall thermal motion. This limits the achievable resolution of structures with high thermal motion. The scale of this blurring is known as the atomic temperature factor, denoted as B and measured in Å^2. In reciprocal space;

$$f_{at}(\boldsymbol{r}^*) = f_a(\boldsymbol{r}^*).\, e^{-\frac{B\boldsymbol{r}^{*2}}{4}} \qquad \textbf{Equation 1-3}$$

where $f_{at}(\boldsymbol{r}^*)$ is the scattered wave arising from a thermally agitated atom, $f_a(\boldsymbol{r}^*)$ the amplitude from a stationary atom and $\boldsymbol{r}^*$ the vector location in reciprocal space. Therefore as $\boldsymbol{r}^*$ increases, $f_{at}(\boldsymbol{r}^*)$ decreases; scattering amplitude decreases with higher angle reflections[22,23].

The diffraction pattern of an infinite crystal is the diffraction pattern of a single diffracting unit sampled at reciprocal lattice points

In its simplest form (P1, one molecule per unit cell), the crystal is a motif of this molecule, repeated at each lattice point. Mathematically this can be described as a convolution of an infinite lattice with the structure of the molecule. Thus the electron density ρ(r) at a position **r** within the infinite crystal is given as;

$$\rho(\boldsymbol{r}) = \rho_M(\boldsymbol{r}) * L(\boldsymbol{r}) \qquad \textbf{Equation 1-4}$$

where $\rho_M(\boldsymbol{r})$ is the electron density of the individual molecule, $*$ the mathematical symbol for convolution and $L(\boldsymbol{r})$ an infinite lattice of delta functions δ centered at the lattice points of the crystal ($\boldsymbol{r}_{\boldsymbol{u,v,w}} = u\boldsymbol{a} + v\boldsymbol{b} + w\boldsymbol{c}$);

$$L(\boldsymbol{r}) = \sum_{-\infty}^{\infty} \delta\,(\boldsymbol{r} - \boldsymbol{r}_{\boldsymbol{u,v,w}}) \qquad \textbf{Equation 1-5}$$

The diffracted wave is therefore a Fourier transform of the crystal;

$$F(\boldsymbol{r}^*) = T[\rho_M(\boldsymbol{r}) * L(\boldsymbol{r})] = T[\rho_M(\boldsymbol{r})]\,.\,T[L(\boldsymbol{r})] \qquad \textbf{Equation 1-6}$$

where $F(\boldsymbol{r}^*)$ is the amplitude of the diffracted wave at the location $\boldsymbol{r}^*$ in reciprocal space (denoted by the *) and T is the Fourier transform operator. The second step utilizes the

mathematical principle that the transform of convoluted functions is the multiple of their individual transforms. $T[\rho_M(\boldsymbol{r})]$ is therefore the Fourier transform of the molecule itself, while $T[L(\boldsymbol{r})]$ is the transform of the real space lattice. Fourier transforms of real space lattices are themselves lattices, with spacing equal to the inverse of that in real space. That is to say that $T[L(\boldsymbol{r})]$ is an infinite series of delta functions centered on reciprocal lattice points[23].

Therefore the Fourier transform of the crystal is the Fourier transform of the single molecule (P1, one molecule per ASU) sampled at the location of reciprocal lattice points. This gives rise to specific localized reflections or Bragg peaks within the diffraction pattern of an infinite crystal, denoted as F_{hkl} with hkl representing the Miller indices of the reciprocal lattice point of the individual reflection. Because F_{hkl} arise from $F(\boldsymbol{r}^*)$, they too are complex functions that have both amplitude and phase. F_{hkl} are also known as structure factors. The structure factors can be written as:

$$F_{hkl} = |F_{hkl}|\mathrm{e}^{i\emptyset} \qquad \textbf{Equation 1-7}$$

where $|F_{hkl}|$ is the structure factor amplitude and ϕ is the relative phase of the structure factor. Since $F(\boldsymbol{r}^*)$ is derived from the electron density of the whole molecule, every atom in the structure contributes to each structure factor[23].

<u>To discover the electron density from the diffraction pattern we must use an inverse Fourier transform</u>

If the diffraction pattern is a Fourier transform of the electron density, then to extract the electron density from the diffraction pattern we must simply subject it to an inverse Fourier transform T^{-1} (the inverse of a fourier transform is another fourier transform);

$$\rho(\boldsymbol{r}) = T^{-1}\left[T[\rho(\boldsymbol{r})]\right] = \int_{V^*} F(\boldsymbol{r}^*)\ e^{-2\pi i\, \boldsymbol{r}^*.\boldsymbol{r}}\ \ d\boldsymbol{r}^* \qquad \textbf{Equation 1-8}$$

Since the diffraction pattern only exists at discrete points in reciprocal space (the reciprocal lattice points with indices hkl) this can be turned into a Fourier sum;

$$\rho(\boldsymbol{r}) = \frac{1}{V} \sum_h \sum_k \sum_l\ F_{hkl}\ e^{-2\pi i\, \boldsymbol{r}_H{}^*.\boldsymbol{r}} \qquad \textbf{Equation 1-9}$$

To solve the electron density within a crystal amounts to determining F_{hkl} and then applying an inverse Fourier transform to this set of complex functions. We measure the intensity of individual structure factors F_{hkl} by recording the diffraction pattern. We can calculate the structure factor amplitude $|F_{hkl}|$[22–24].

However, the detector does not give us information on the phase ϕ of F_{hkl}. This is an unknown in a typical diffraction experiment and is the mathematical basis of the phase problem. Since phase information dominates when calculating the inverse Fourier transform, obtaining phases is necessary for structure determination. There are three main methods for solution of the phase problem:

Direct methods - These are used in small molecule crystallography and are not applicable for large molecules such as proteins[23].

Experimental phasing This aims to estimate initial structural phases by modifying scattering factors of specifically located atoms; for example by making heavy metal derivatives. These metals make small changes to the diffraction pattern that can be used to trace their location within the crystal. Bootstrap methods can then be used to refine the phases for the whole structure[22,23].

Molecular replacement Here a molecule with suspected structural similarity is used to search for solutions to the phase problem. The molecule is first rotated to find a best match

with the Patterson function of the data, generating a translation function. The molecule is then translated to match the data itself generating a translation function. At low resolution, it is particularly important to ensure that the input model does not bias the new maps generated. In this thesis, all phases are determined by the Molecular Replacement method[22–24].

1.11.4 Generating maps from experimental electron density

In order to refine a protein model we need to generate electron density maps from the structure factor amplitudes and phase estimates we have. Maps are calculated using the Fourier transform of the structure factors including both amplitudes and phases;

$$\rho(r) = \frac{1}{V} \sum_h \sum_k \sum_l F_{hkl}\, e^{-2\pi i\, \boldsymbol{r_H}^* . \boldsymbol{r}} = \frac{1}{V} \sum_h \sum_k \sum_l |F_{hkl}|\, e^{i\emptyset}\, e^{-2\pi i\, \boldsymbol{r_H}^* . \boldsymbol{r}} \qquad \textbf{Equation 1-10}$$

There are several different types of map that can be generated. The most basic type of map is known as an $F_o\emptyset_c$ map which used observed structure factor amplitudes (F_o) and calculated phases ($\emptyset_c$) that are derived from a model of the structure, for example a molecular replacement solution or a refined protein model[22].

However, $F_o\emptyset_c$ maps are rarely used in structure building. This is in part because they weight density that is missing from the model at roughly half the level of that that is present in the model. It may therefore be difficult to visualize density corresponding atoms that are absent in an incomplete protein model. Instead, composite maps that combine different structure factors and phases are used. These aim to reduce bias, improve quality of electron density and assist model building by reducing the effects of errors. The weighted combinations of structure factor amplitudes are known as map coefficients or Fourier coefficients[22].

One such composite map is the $(F_o - F_c)\emptyset_c$ map. This map uses the observed structure factor amplitudes in combination with those calculated from the current protein model (F_c) to highlight errors in the model. If this map has positive density at a location, the model has insufficient atoms to explain the density. If the density is negative, $F_o < F_c$ and atoms have been placed in a location where there shouldn't be any. However, while these maps serve to highlight model errors they are not used alone for model building[22].

Another commonly used map is the $(2F_o - F_c)\emptyset_c$, which can be thought of as a sum of the $F_o\emptyset_c$ and $(F_o - F_c)\emptyset_c$ maps. This map is used to show the electron density from correctly placed atoms (if $F_o = F_c$ then these maps look like $F_o\emptyset_c$ maps) while weighting missing atom density at normal density levels. This means that a $(2F_o - F_c)\emptyset_c$ map can account for model incompleteness better than an $(F_o - F_c)\emptyset_c$ map which weights them at roughly half the density of correctly placed atoms[22].

It is also possible to modify a $(2F_o - F_c)\emptyset_c$ map to take into account both model coordinate errors and incompleteness. These maps are known as $(2mF_o - DF_c)\emptyset_{wt}$ maps or σ_A weighted $(2F_o - F_c)$ maps[118].Here, the multiplier m represents the figure of merit for the structure factor phases. D (related to σ_A) represents a measure of model structure completeness and error. $\emptyset_{wt}$ is equal to $\emptyset_c$ unless $2mF_o - DF_c < 0$, where $\emptyset_{wt} = \emptyset_c + 2\pi$. The resulting Fourier coefficient is the maximum likelihood estimator of the true structure factor amplitude. This map is used as a standard in model building.

While these maps are the mainstay of model building, several other techniques are routinely used to improve map quality. Density modified maps (for example those produced in PHENIX RESOLVE[119]) modify phase estimates to improve the quality of density. The concept is that phases of a map possessing certain map-like features are more likely to be correct than other phases. For example, solvent flattening works to make solvent regions have a very low electron density compared to the protein. Non-crystallographic symmetry

averaging works in real space to state that the density of two homologous molecules must be similar. Finally histogram matching states that a certain distribution of electron densities within the protein is expected at a set resolution. By restraining the phases to match these expected map properties (i.e. adding information and constraints to the system) phases can be improved[119].

Another type of map that can be calculated is a prime-and-switch (PS) map[120]. The aim of these maps is to reduce the bias imposed by phases of an input model: a map generated by molecular replacement may be unable to diverge from that of search model used to find it. PS estimates the probability that the map looks like that of a protein, using similar metrics as density modification (flat solvent regions and reasonable density distributions within the protein). It then estimates the first and second derivative map-probability function with respect to phase. It uses these derivatives to indicate in which direction the phases should be altered. This is carried out iteratively for ~100 cycles, and at the end of each cycle the knowledge of the previous phases is lost. This means that it is able to remove significant amounts of model bias from the initial phase estimates[121].

The third and final type of map discussed here is the feature-enhanced map[122]. This type of map can be used to reduce noise (such as that seen in lower resolution data) and enhance weak signal (such as that produced by low-occupancy ligands) in σ_A weighted maps. It is calculated in several stages. First a starting map is calculated from the input files. Several new maps are then calculated with induced random errors. By combining these maps to produce a new map, the introduced noise as well as noise in the original map can be averaged out. Finally, weak features are highlighted by increasing their magnitude to be similar to that of the strong features. This is done by modifying the map such that the signal strength is consistent across the entire unit cell. FEM therefore acts to enhance features in the map, as compared with phase improvement techniques that aim to find features that weren't originally present[122].

Finally, model building may be guided by B-factor sharpened maps. Sharpening is a tool used in structures with high overall B-factors to up weight high-resolution reflections. This aims to recover information lost by the blurring present in high B-factor structures. Sharpening works by applying a negative B-factor to the high-resolution shell data. Sharpened maps can be used in combination with other maps to guide model building[123].

1.12 Aim and summary of thesis

The aim of this thesis is to use structural biology to understand how K2P channels gate. This is done by co-crystallising TREK-2 with small molecule inhibitors and activators. These molecules may stabilise the protein in distinct conformational states that correspond to functional states of the protein. The resulting structures may therefore inform on conformational movements involved in channel gating.

To this end, in chapter two I solve the structure of a Prozac (fluoxetine) derivative bound to TREK-2. This provides evidence for how the channel gates, and how ligand binding may influence this gating. I use this to design potential covalent inhibitors for TREK-2. In chapter three I co-crystallise TREK-2 in the presence of small molecule activators of TREK-2 using vapour diffusion and the lipidic cubic phase. Finally in chapter four I use the lipidic cubic phase to produce microcrystals of TREK-2 in the presence of small molecule activators. I then attempt to use serial femtosecond crystallography to produce a structure of this complex.

Chapter 2 Binding of Prozac to TREK-2: insights into K2P channel gating

2.1 Introduction

2.1.1 TREK-2 shows two conformations in crystal structures

TREK-2 was the first K2P to be solved in two completely different states[75]: a down state (4XDJ) with both M4 helices down and M3/M4 moved outwards, and an up state (4BW5) with both helical bundles up and M3/M4 moved inwards. In the down state (4XDJ), two lateral fenestrations connect the lipid membrane with the inner vestibule of the channel. In the up state they are blocked by Phe^{316} and Leu^{320} on M4. The intracellular portions of M2 and M3 have also moved down towards the cytoplasm (around $Gly^{201/206}$ in M2; Gly^{248}in M3). These states have differing ion occupancy in the selectivity filter. The up state has all four sites (S1-S4) occupied, while the down state has just three (S2-S4). This provides the first evidence that the movement of the helical bundle may influence gating at the selectivity filter.

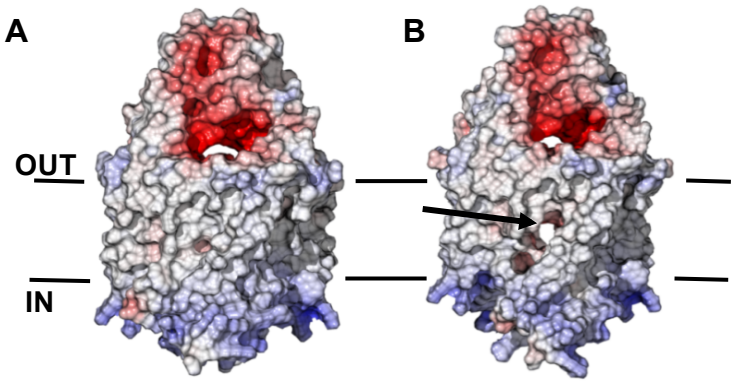

Figure 2-1 Crystal Structures of TREK-2 reveal two conformations
PDB 4BW5 (up state, A) shows a channel with no fenestrations. In PDB 4XDJ (down state, B) TM4 moves down with M2/ M3 reveal a fenestration. Figure drawn by Ashley Pike.

Despite 12 structures deposited in the PDB (Table 2-1), there is no consensus opinion on whether the up or down state represents the more conductive channel. The question remains: what does movement of M2-M4 in TREK-2 represent, and how could channel modulators convert it between these states?

K2P	PDB	Reso-lution (Å)	M4 Conformation (CHAIN: STATE)	Potassium Sites (S0-S4,C)	Lipids in Fenestrations (No. Lipids, No. fenestrations)
TREK-2	4XDJ	3.8	A: Down B: Down	S2- S4	2 Lipids in 2 fen.
	4BW5	3.2	A: Up B: Up	S1- S4	0 lipids 0 fen.
TRAAK	4WFF	2.5	A: Up B: Down	S0-S4	1 Lipid in 1 fen
	4FWH	2.19	A: Up B: Down	S0- S4 (Tl^+)	1 Lipid in 1 fen
	4WFE	2.5	A: Down B: Down	S0-S4, C	0 Lipids in 0 fen.
	4WFG	3.0	A: Down B: Down	S0-S4, C (Tl^+)	0 Lipids in 0 fen.
	4I9W	2.75	A: Up B: Down	S0-S4	1 fen, lipid not modelled
	3UM7	3.31	A: Up B: Down	S0-S4	1 fen, lipid not modelled
	4RUE* (G124I)	3.3	A: Down B: Down	S0-S4, C	2 large fen. (Doors) lipid not modelled
	4RUF* (W262S)	3.4	A: Down B: Down	S0-S4, C	2 large fen. (Doors) lipid not modelled
TWIK-1	3UKM	3.4	A: Down B: Down	S0-S4	2 Lipids in 2 fen.
TREK-1	4TWK$^{\times}$	2.6	A: Up B: Up	S2-S4	0 Lipids in 0 fen.

Table 2-1 Conformational states and potassium occupancies of K2P structures

This table shows all of the K2P structures that have been solved to date, bar those worked on in this thesis. M4 is labelled as down if a fenestration is present; otherwise it is labelled as up. Those with a * next to them have activatory mutations. TREK-1 4TWK ($^{\times}$) is thought to have a distorted pore due to cations present in the mother liquor. Resolution is as quoted on the PDB.

It is possible that crystal structures with small molecules could shed light onto the functional nature of these states. For example, it would be expected that an inhibitor would stabilise a less conductive conformation of the protein. There are numerous small molecules (both

pharmacological and physiological) that modulate TREK channels. A selection of these are summarised in Table 2-2 and Table 2-3. Since it is the most studied channel, some binders have previously been investigated only in TREK-1. However, due to the high sequence identity (65%) binders were predicted to have similar effects on TREK-1 and TREK-2. For all compounds worked on in this thesis, binding and/or functional inhibition has been confirmed in TREK-2. Some of this work was carried out by collaborators and is published (Conor McClenaghan; fluoxetine, brominated fluoxetine[75]) while some is detailed later in this thesis (Sections 3.2.1 and 3.2.6).

In this chapter I focus on solving the co-crystal structure of TREK-2 with the inhibitor fluoxetine (and fluoxetine derivative compounds). The reason for this is two-fold; firstly it has a higher affinity than many other inhibitors (Table 2-2) and secondly because it is more soluble in water than other inhibitors. Note that the inhibitors presented here have all been tried in co-crystallisation but have not produced co-crystal structures (Section 8.1). Table 2-2 shows a selection of relatively high affinity TREK-2 inhibitors.

TREK Inhibitors	**Chemical Structure**	**Solubility (mM,H_2O)**	**IC_{50} (μM)**
Pimozide (Antipsychotic)	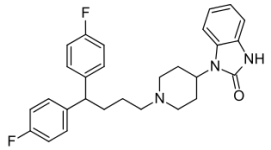	~0	0.4*[124]
Lidocaine (Anaesthetic)	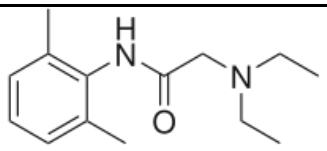	~180	200*[125]
Fluoxetine (Antidepressant)	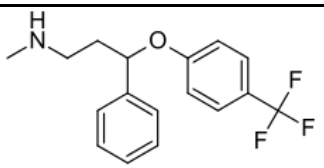	10	20[75]
Penfluridol (Antipsychotic)	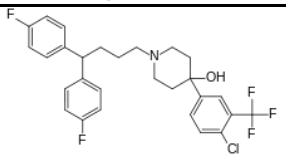	~0	0.2*[124]

Table 2-2 Small molecule inhibitors of TREK Channels

* Indicates that it was measured for TREK-1; others were measured for TREK-2.

TREK Activator	Chemical Structure	Solubility (mM, H_2O)	EC_{50} (μM)
Flufenamic Acid (NSAID)	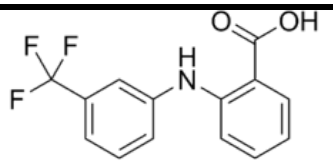	~0	100[126]
Riluzole (Neuroprotectant)	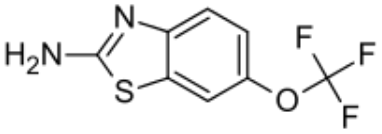	~1	>100*[127]
DCPIB (Neuroprotectant)	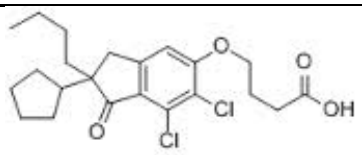	0	100[128]
BL-1249 (Pfizer Probe)	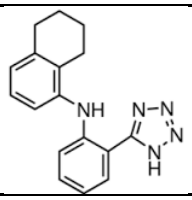	0	8[56]

Table 2-3 Small Molecule Activators of TREK Channels

* Indicates that it was measured for TREK-1; others were measured for TREK-2.

2.1.2 Prozac (Fluoxetine) inhibits TREK channels

Prozac (fluoxetine) is a clinically utilised antidepressant that is prescribed to 20 million people a year in the U.S.A. alone. It inhibits its target protein the SERT (Serotonin Transporter) with an IC_{50} of 17nM. This is thought to treat depression by preventing reuptake of serotonin (5-hydroxytryptamine or 5-HT) from the synapse, increasing synaptic serotonin levels[129]. However the mechanism of action for his drug is not fully understood. In particular, although synaptic serotonin levels peak early in treatment, onset of therapeutic effect can take several weeks. This suggests a potential role for feedback mechanisms or off-target effects[130].

Off target effects may occur because fluoxetine is not a clean drug. Administered as a racemate, it is broken down to norfluoxetine in-vivo (Table 2-2). Fluoxetine and norfluoxetine modulate a wide range of off-target proteins. Some such proteins are the TREK-1 and TREK-2 channels, which are expressed abundantly in the brain. Since

fluoxetine inhibits TREK channels with an IC_{50} of between 9 μM (Norfluoxetine) and 20 μM (Fluoxetine) [75,131], it is unclear whether this interaction is clinically relevant.

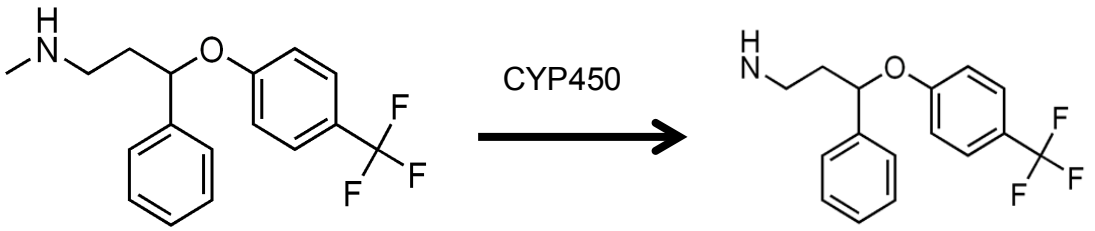

Figure 2-2 Fluoxetine is degraded by CP450 to norfluoxetine

However, evidence from knock out mice indicates a potential role for TREK-1 in prevention of depression. TREK-1 knock out mice are known to be depression resistant, showing decreased response to stress and increased serotonergic neurotransmission[91]. TREK-1 single nucleotide polymorphisms have since been linked to treatment resistance in numerous genome wide annotation studies (GWAS) in humans[132–134]. Although several other studies have failed to find a link between TREK-1 and depression[135,136], it has been suggested that TREK-1 represents a novel target for anti-depressants in its own right[130].

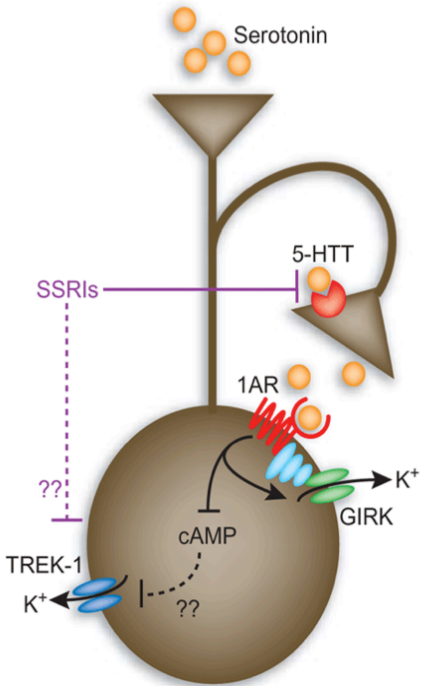

Figure 2-3 Proposed mechanism for involvement of TREK-1 in the fluoxetine (SSRI) therapeutic effect.
Figure from Gordon and Hen 2006[130].

TREK-1 may potentiate therapeutic effects via inhibition of a negative feedback mechanism in serotonergic neurons. In normal function, the serotonin receptor (1AR) is stimulated by synaptic serotonin. This reduces cAMP

levels resulting in TREK channel dis-inhibition, cell hyperpolarisation and action potential inhibition. If Prozac does directly inhibit TREK-1, it may inhibit this negative feedback loop and prevent desensitisation.

Despite the clinical interest in the interaction of Prozac with TREK channels, little is known about its binding site. While one study finds the intracellular N-terminus to be important[137], another study finds the intracellular C-terminus mediates inhibition[138]. It is therefore not possible to speculate how binding of fluoxetine may lead to channel gating.

In this chapter I aim to locate the binding site of Fluoxetine to TREK-2. I am using TREK-2 since it has a high sequence identity to TREK-1 and is known to be inhibited by fluoxetine[75]. It is therefore expected that the binding site would be shared between these two proteins. TREK-2 can be expressed with high yields and has already been crystallised, making the problem tractable. After locating the binding site of fluoxetine to TREK-2, I aim to determine how it modulates potassium flux through the channel. I also aim to design more specific and potent inhibitors for TREK channels to enable further study of their physiological importance.

2.1.3 Anomalous scattering: high signal to noise and specificity

There are currently few high affinity TREK-2 binders known. Combined with the general low solubility of these compounds, occupancy in any crystal structure is likely to be low. Furthermore the optimised resolution of TREK-2 crystals is currently around 3Å in the best direction. This means that small molecule density may not be easily identifiable it may not be distinguishable from other similarly shaped blobs.

To overcome this issue, the anomalous scatter from atoms can be utilised akin to a contrast agent. Covalently binding an atom with an accessible fluorescence edge to a small molecule increases both the sensitivity and the specificity of ligand detection. This strategy

has been used in fragment based drug discovery. In one study, an overall hit rate of 4.4% for 741 screened compounds was much lower than the 24% hit rate found for halogenated compounds[139,140]. This was because weak binding with partial occupancy was to detect and verify by anomalous scattering, even if no ligand electron density was visible.

Below, I discuss the physical nature of anomalous scattering and how it allows sensitive and specific ligand detection. I then describe pertinent examples where anomalous signal has been used to identify low occupancy binding sites in membrane proteins.

2.1.3.1 The physical origin of anomalous scattering

Under most circumstances the energy of X-rays in protein crystallography experiments does not closely match the energy levels of the bound electrons in organic molecules. This means that the electrons can be approximated as free or unbound. The scattering of X-rays from these electrons is known as Thomson Scattering, where electromagnetic radiation interacts with and is elastically scattered by a free charged particle. Therefore the equation for the electromagnetic radiation (E_{0d}^{Th}) resulting from Thompson scattering of an incident wave (E_{0i}) can be derived using assumptions that are only strictly true in unbound electrons[23];

$$\boldsymbol{E_{0d}^{Th}} = \frac{\boldsymbol{e^2}}{\boldsymbol{mrc^2}}\ \boldsymbol{E_{0i}}\ \boldsymbol{e^{i(\omega(t-r/c)+\pi)}} sin\varphi \qquad \textbf{Equation 2-1}$$

where r is the vector describing the point of observation, $sin\boldsymbol{\varphi}$ the polarisation term, e the electronic charge, m the mass of an electron and c the speed of light. It turns out that this is a good approximation for most protein X-ray diffraction. Note the scattered X-rays have the same energy as the incident photons, but have a phase shift of 180 degrees (π). Friedel's law states that the amplitudes of bijovet pairs are equal ($|\mathbf{F_{h,k,l}}| = |\mathbf{F_{-h,-k-l}}|$). This law holds for Thomson scattered X-rays. Because of Friedel's law, $\mathbf{I_{h,k,l} = I_{-h,-k-l}}$; the observed intensity of these two reflections are identical[23].

However, when the energy of the X-Rays is close to the energy of the bound electron resonance occurs. The electrons no longer behave as free electrons, but scatter radiation like bound electrons. To mathematically describe these electrons, they can be imagined as oscillating charged particles that are driven by a periodic force (X-rays), and experience dampening effects (movement of the electron is attenuated). There is a known steady-state solution for the resulting displacement of the electron[23]. It is therefore possible to calculate the electromagnetic field produced by the movement of the charged electron;

$$\boldsymbol{E_d = \frac{\omega^2 e^2}{mrc^2}\, E_{0i}\, \frac{e^{i(\omega t)}}{\omega_0^2 - \omega^2 - ig\omega}} \qquad \textbf{Equation 2-2}$$

where ω is the angular frequency of the incident X-ray, ω_0 the angular frequency of the electron (dependant on which shell it is in) and g is a dampening factor. When g=0 and ω_0 << ω, this is the same as the unbound electron and this equation looks like that of a Thompson scattering. Looking at the ratio of the two scattered waves gives us an electronic scattering factor f_e,

$$\boldsymbol{\frac{E_d}{E_{0d}^{Th}} = f_e = \frac{\omega^2(\omega^2-\omega_0^2)}{(\omega^2-\omega_0^2)^2+g^2\omega^2} + i\frac{g\omega^3}{(\omega^2-\omega_0^2)^2+g^2\omega^2} = f_e' + if_e''} \qquad \textbf{Equation 2-3}$$

that is to say that when the angular frequency of the X-rays ω ≈ the natural angular frequency of the electrons ω_0, the scattering factor has a component which is both in phase (f_e') and not in phase (if_e'') with the Thomson scattered photons[23]. This means that the scattered photon has been retarded with respect to the Thomson photons. Note that if_e'' is always positive and that both terms are wavelength dependent (dispersive). The atomic scattering factor of is thus generally written as:

$$\boldsymbol{f_s(\lambda) = f_s^0 + f_\lambda' + if_\lambda''} \qquad \textbf{Equation 2-4}$$

where f_s^0 is the atomic Thomson scatter factor, f_λ' is the component of the dispersive scatter in phase with f_s^0 and f_λ'' is the component of the dispersive scatter which is not in phase

with f_s^0. Visualising this on an Argand diagram, it is evident that if_λ'' causes Friedel's law to break (Figure 2-4). This means that the intensities of the h,k,l and –h,-k,-l reflections are no longer identical.

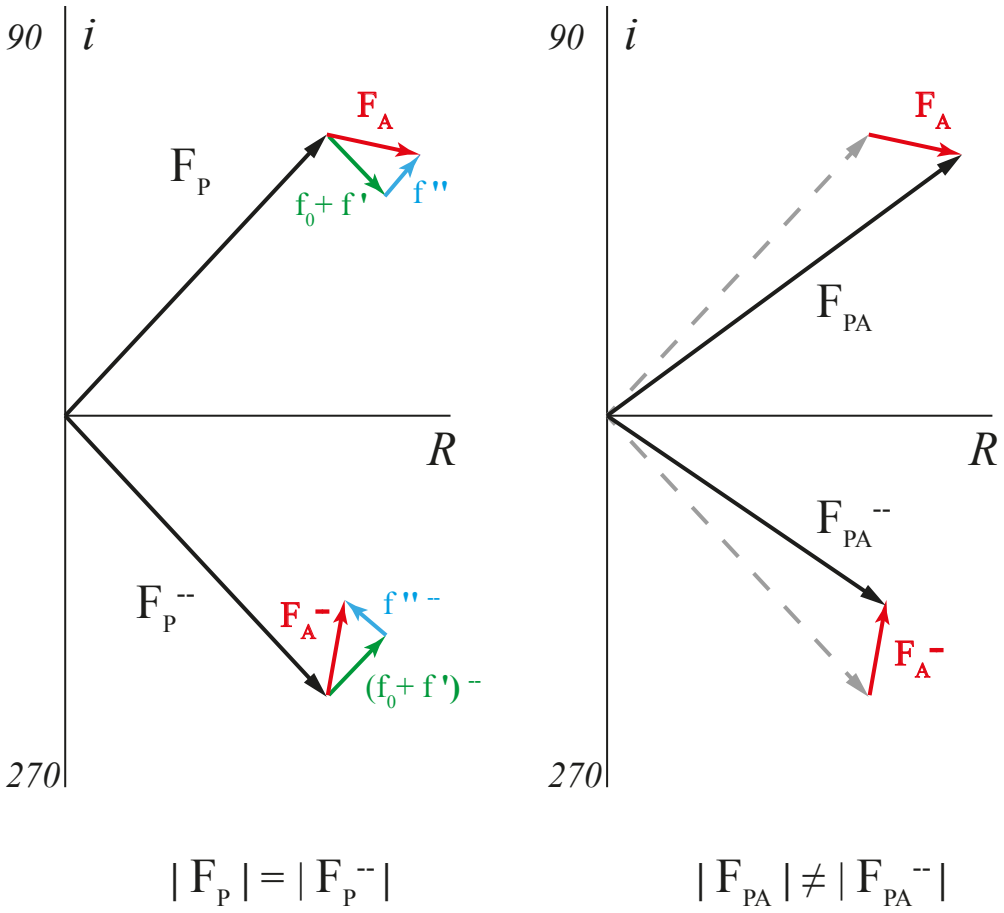

Figure 2-4 Friedel's law and anomalous scattering
Without the heavy atom providing anomalous signal, Friedel's law holds (black lines in diagram A). Addition of the heavy atom adds anomalous scatter (F_A) made up of an in phase (f_0 + f') and an out of phase (f'') component (A), the resulting scattering vectors (F_{PA}) do not obey Friedel's law (B). Based on a diagram in Rupp 2010[22].

Anomalous difference maps can therefore be constructed with amplitudes equal to the anomalous differences observed in Friedel pairs ($F_{h,k,l}$ - $F_{-h,-k-l}$) and with phases that are 90° ahead of those calculated for the scattering in that reflection[141].

It is clear to see how these maps would be highly selective towards certain atoms. f'' is strongly dependant on two things; ω and ω_0. ω_0 is dependent on the energy of the bound electron, and thus on the type of atom. ω is dependent only on the experimental apparatus.

If you select an ω that is close to the ω_0 of the electrons in the atom of interest (for example bromine electrons), only those particular electrons will produce anomalous signal. Thus by tuning the wavelength of the beam, it is possible to produce a signal that is highly specific for certain atoms that are not naturally present in proteins.

Selecting an atom that produces an anomalous signal of large amplitude can increase sensitivity of detection. Furthermore, the strong wavelength dependence of anomalous scattering means that the signal from other atoms should be low, producing anomalous difference maps with high signal to noise ratios.

Anomalous scattering has been effectively used to locate the binding site of inhibitors to a prokaryotic voltage-gated sodium channel (NaVM)[142]. Here, negative cooperativity of binding to four separate sites meant that the expected occupancy of each site was just 0.25. A channel antagonist containing a bromine atom was selected for co-crystallisation studies. The binding site of the antagonist was located by the anomalous signal from this Br despite no visible $2F_o$-F_c density. The binding site of the antagonist was then computationally modelled, based on the fixed pivot point of the bromine atom.

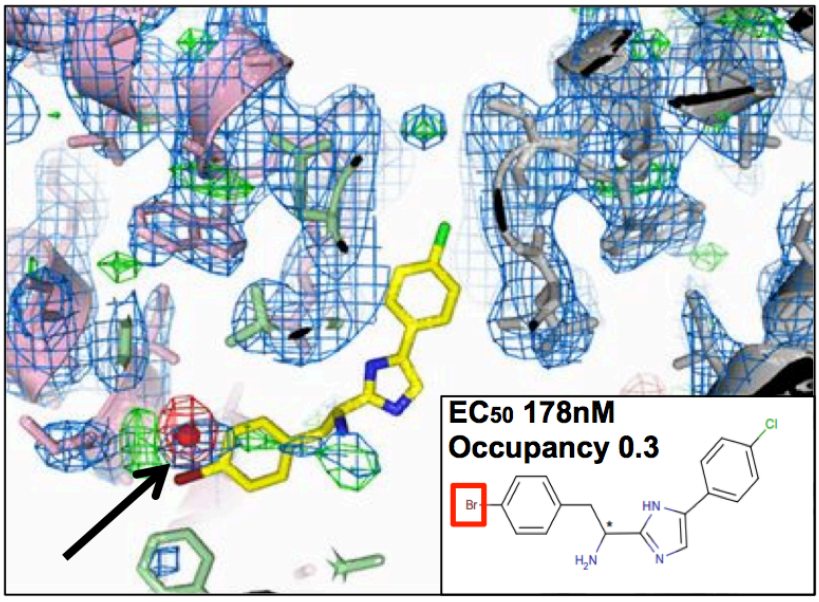

Figure 2-5 Location of Anomalous Signal in NavM
Blue: $2F_o$-F_c 1.5σ, Red: Anomalous Difference map 5σ. Taken from Bagneris *et al.* 2014[142]. Reprinted with permission from PNAS.

2.2 Results

2.2.1 Crystallisation of TREK-2 with fluoxetine derivatives

2.2.1.1 Selection of fluoxetine derivatives

Both fluoxetine and its breakdown product norfluoxetine bind to TREK Channels. These compounds are administered as racemic mixtures. Both the racemic mixtures and the chirally pure compounds were tested in co-crystallisation trials, as there is no evidence that either enantiomer has a higher affinity.

Brominated fluoxetine derivatives were also tested. Three derivatives were used, with the bromine atom in different locations. This was done to reduce the likelihood of Br inhibiting binding. These compounds were designed in collaboration with and synthesised by Gian Filippo Ruda and Paul Brennan from the Target Discovery Institute, Oxford.

	Derivative	Inhibition (%) with 30µM	Solubility mM	Smiles String	Compound Structure
Fluoxetine	R or S Chirally Pure HCL salt	80%	~10 (ddH_2O) <5 (GFB)	**R:**CNCC[C@H](c1ccccc1)Oc1ccc(cc1)C(F)(F)F.[Cl] **S:**CNCC[C@@H](c1ccccc1)Oc1ccc(cc1)C(F)(F)F.[Cl]	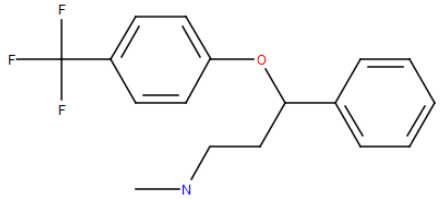
	Racemate HCL Salt			CNCCC(c1ccccc1)Oc1ccc(cc1)C(F)(F)F.[Cl]	
	Br-Fluoxetine 1 (BF-1) (Racemate) HCL salt	80%	<10 (ddH_2O) <5 (GFB)	CNCCC(c1ccccc1)Oc1ccc(cc1[Br])C(F)(F)F.[Cl]	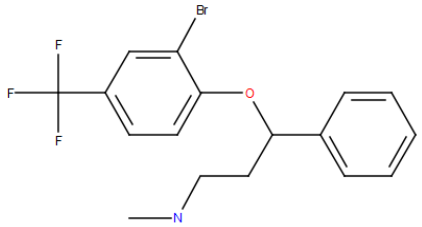
	Br-fluoxetine 2 (BF-2) (Racemate) HCL salt	N/A	<10 (ddH_2O) <5 (GFB)	CNCCC(c1ccccc1)Oc1ccc(c(c1)[Br])C(F)(F)F.[Cl]	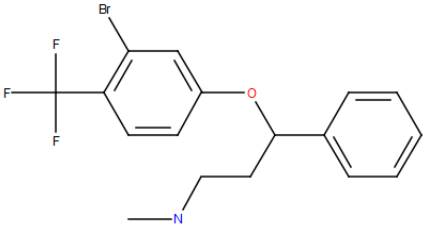

Table 2-4 Fluoxetine derivatives used for TREK-2 co-crystallisation

Saturated suspensions were used for co-crystallisation as solubility in protein purification buffer (GFB) was poor. % inhibition measured by Conor McClenaghan in patches expressing full-length TREK-2 exposed to 30 µM ligand, Brominated fluoxetine have a lower solubility in water and GFB than fluoxetine. N/A is unknown.

All compounds were suspended in ionised water (at an amount of compound equivalent to 50mM). Saturated suspensions were used as the ligand has a low affinity for TREK-2 and most compounds could not completely dissolve even at 10mM in deionised water. Therefore in order to ensure high ligand concentration in crystallisation it was necessary to use saturated stock solutions. Organic solvents were not used in these initial stages, as they may destabilise the protein.

2.2.1.2 Co-crystallisation of fluoxetine derivatives with TREK-2

Compounds were initially added to 10mg/ml TREK-2 protein at ~5mM from the saturated stock in deionised water. The compounds precipitated heavily upon this addition so it is unclear how much remained in solution. Protein did not precipitate (as monitored by 280nm absorbance spectroscopy) in response to addition of compounds. Sample was incubated for three hours at 4°C before crystallisation. The sample was not centrifuged before crystallisation as this may spin out excess compound, which could drive the equilibrium away from binding.

Initial crystal trials were set up in the coarse screens MemGold, MemGold2 and MemSysStart. A third screen was designed around known crystallisation conditions of TREK-2 (KCNK10C-SUPER; Figure 2-27) as determined by Yin Dong. Racemic, R and S fluoxetine all caused heavy protein precipitation in crystal plates, so the concentration used was reduced to 1mM for some crystal trials. In other trials others the protein concentration was reduced and the PEG concentration decreased to reduce precipitation.

Crystals grew with all four compounds across several conditions in the TREK-2 SUPER screen. Initial crystal data sets (Table 2-6, ~4Å resolution, beam energy 12.4keV) could not identify ligand density for R or S fluoxetine. This could be due to low ligand occupancy, or because the crystals were of protein in a conformation that could not bind fluoxetine. However, since anomalous peaks could be identified in structures with BF-1, crystallisation

with this compound could be optimised (Table 2-6, beam energy 13.5keV). Since this optimised crystallisation condition is compatible with ligand binding, it could then be used as a basis for increasing ligand occupancy with R and S fluoxetine.

2.2.1.3 Optimisation of BF-1 / TREK-2 co-crystals

TREK-2 was successfully co-crystallised with bromo-Fluoxetine-1 (BF-1). TREK-SUPER screen produced crystals in 0.1M MES pH 6.5, 0.001M $CdCl_2$, 0.050M $MgCl_2$, 19-21% PEG550MME. To optimise the crystals, crystallisation conditions were fine-screened. Fine screening included variation of salts (magnesium sulphate, magnesium acetate, magnesium chloride, potassium chloride 0-50mM), metal ions (cadmium chloride, nickel chloride) and PEG types (PEG350MME, PEG500MME, PEG500DME, PEG600, PEE15/4). It was determined that while $MgCl_2$ (50-100mM), $CdCl_2$ (1mM) and MES pH 6.5 were necessary for crystallisation, PEG500MME (22-30%) could be exchanged for PEE15/4 (12.5-25%).

After optimisation, two BF-1 crystal morphologies were present: plates and prisms. Screening at Diamond's I24 beam line indicated that the prisms were monoclinic, while the plates were orthorhombic (Table 2-5). However, orthorhombic crystals produced better resolution diffraction. In order to improve data quality, it was therefore necessary to selectively grow the orthorhombic crystals. The crystals could be identified by their morphology and PEG type, PEG concentration, protein concentration, salt type and additive screening did not result in preferential growth of this crystal form.

Lattice	A (Å)	B (Å)	C (Å)	α (°)	β (°)	Y (°)
Orthorhombic	102	112	170	90	90	90
Monoclinic	86	110	105	90	92	90

Table 2-5 Unit cell parameters of TREK2 co-crystals with BF-1.

A seeding strategy was then attempted to promote the growth of orthorhombic crystals. Plate morphology (orthorhombic) nano-crystals were used to seed the previously optimised co-crystallisation conditions. Seeding produced crystals that has both plate and prism morphologies however almost none of the crystals were monoclinic.

The resulting crystals were taken to the Diamond Light Source (DLS) synchrotron for data collection. Fluorescence scans demonstrated a fluorescence edge at (13.47keV). The beam was therefore set >13.5keV for data collection, to maximise anomalous signal. A summary of the datasets collected is provided in Table 2-6 page 67.

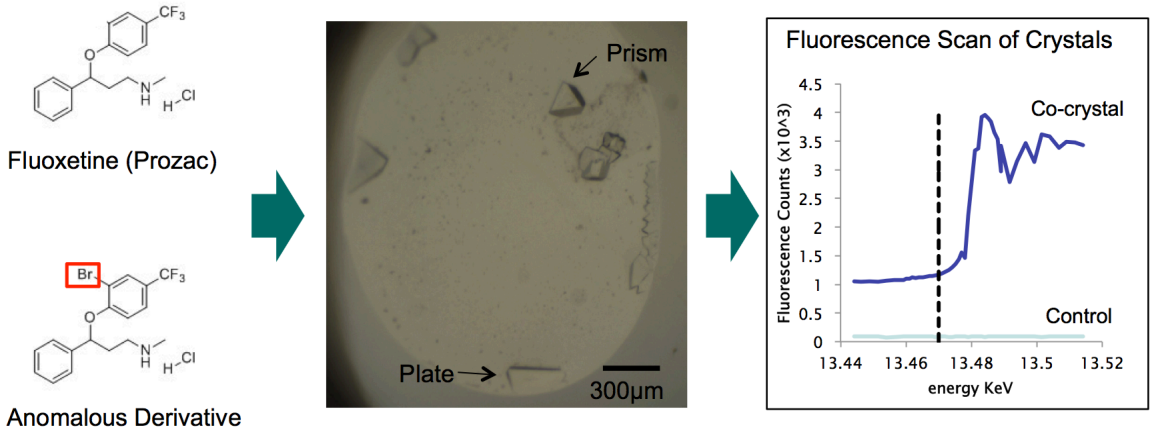

Figure 2-6 Co-crystallisation of TREK-2 with brominated fluoxetine
A bromine atom was covalently bound to the fluoxetine molecule. This was co-crystallised at 5-10mM with 10mg/ml TREK-2. The resulting crystals had two morphologies: prism and plate. Fluorescence scans of these crystals demonstrated an edge at 13.47keV and the resulting data had peaks in anomalous maps - Table 2-6.

2.2.1.4 Optimisation of ligand occupancy in R and S fluoxetine datasets

The crystallisation condition that yielded promising results from BF-1 was used to further investigate the binding of R and S fluoxetine. These were tried both with and without the seeds produced from BF-1. This produced crystals for which diffraction data were collected. However fluoxetine density was not visible. This is possibly due to low ligand occupancy.

In order to improve occupancy in the ligand in the crystals, stock solvents were varied. DMSO, Ethanol and Water were used to make 50mM stock solutions of compounds. While DMSO reduced compound precipitation, it also produced few crystals and they gave split, low resolution (5-8Å) diffraction. Compounds dissolved in Ethanol produced crystals with better resolution diffraction than with DMSO.

Although this strategy appeared to increase ligand solubility, datasets for R/S fluoxetine compounds did not contain definitive ligand density (Table 2-6, Figure 2-7). These datasets were low resolution and had several un-modelled blobs that may have represented ligand density. It is possible either that the ligand was not bound to the protein, or that the occupancy was too low to give clear density. Strategies aimed at improving occupancy, including soaking of crystals with 20mM compound overnight and using organic solvent to increase compound solubility, did not yield improved ligand density.

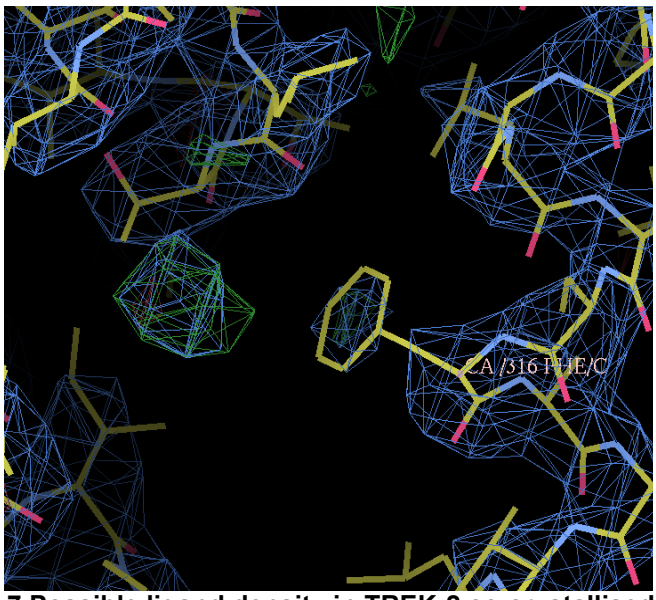

Figure 2-7 Possible ligand density in TREK-2 co-crystallised with R-fluoxetine
Low-resolution datasets (d043) produced with fluoxetine showed some positive F_o-F_c density (Green) in B-Factor Sharpened (-100Å^2) 1.5σ maps. This was insufficient to demonstrate binding.

Ligand	Dataset No.	Maximum Resolution (Å) (h x k x l)	Space Group	State	Electron Density		Crystallisation Conditions and Crystal Mounting
					Ligand	Anom	
R Fluoxetine	43 (5)	$CC_{1/2}$ >0.5 3.8 x 3.7 x 4.2 I/σ >2 3.8 x 3.7 x 4.3	$P2_12_12_1$	Down	No	N/A	**Drop**: 0.1M MES pH 6.5; 50mM $MgCl_2$; 1mM $CdCl_2$; 18% PEE 15/4 **Compound:** 5mM (Ethanol) **Cryo:** 25% PEE15/4 **Seed:** 20nL 1:500 seed stock **Soak:** None
S Fluoxetine	39 (2)	$CC_{1/2}$ >0.5 4.1 x 3.7 x 3.7 I/σ >2 4.6 x 3.7 x 3.7	$P2_1$	Down	No	N/A	**Drop**: 0.1M MES pH 6.5; 200mM $MgCl_2$; 1mM $CdCl_2$; 12.5% PEE 15/4 **Compound:** 1mM (deionised water) **Cryo:** 27% PEE15/4 **Seed:** None **Soak:** 5mM 120 seconds
BF1 (4XDL)	32 (2)	$CC_{1/2}$ >0.5 3.5 x 3.5 x 3.8 I/σ >2 3.6 x 3.5 x 3.9	$P2_12_12_1$	Down	Yes	Yes	**Drop**: 0.1M MES pH 6.5; 50mM $MgCl_2$; 1mM $CdCl_2$; 18% PEG500DME **Compound:** 5mM (deionised water) **Cryo:** PEG escalated to 35% **Seed:** None **Soak:** None
BF2	None	Diffraction quality insufficient for data collection					
4BW5		$CC_{1/2}$ >0.5 3.8 x 3.2 x 3.2 I/σ >2 4.1 x 3.3 x 3.2	$P2_1$	Up	N/A	N/A	(PDB data for reference)
4XDJ		$CC_{1/2}$ >0.5 4.0 x 3.8 x 3.9 I/σ >2 4.1 x 3.8 x 3.8	$P2_12_12_1$	Down	N/A	N/A	(PDB data for reference)

Table 2-6 Dataset Summary: Co-crystals of TREK-2 with fluoxetine derivatives
This table shows the results for the best datasets obtained for each compound in terms of ligand density and resolution. In brackets next to the dataset numbers are the total number of datasets collected for that compound. Resolutions given are calculated from scaled and merged data from the XIA2 pipeline using AIMLESS to 1dp (or from the PDB for 4BW5 and 4XDJ). Soaking was carried out to increase occupancy on crystals grown with low concentration compound (1mM).

2.2.2 Determining the binding site of BF-1 to TREK-2

2.2.2.1 BF-1 binds to the down state of TREK-2

The binding site of fluoxetine was instead determined by location of the anomalous peak from BF-1. This structure was solved with data to a nominal resolution of 3.5 Å (I/σ>2). The model agreed with the data as indicated by a R_{work}/ R_{free} of 23.52 / 26.33. Two dimers were present in each asymmetric unit. Both subunits in these dimers were in a M2-M4 down state, with M4 rotated 3 degrees further around the hinge Gly^{312} down than in the apo down state TREK-2 structure (Figure 2-8). Two fenestrations were therefore present in each

dimer. Both dimers had only three potassium ions present in the filter (S2-S4), with the outer most site S0 being unoccupied. There are no apparent changes in the structure of the filter that would lead to this change in occupancy. However, the resolution of this structure is insufficient to look at small changes in the structure of the filter.

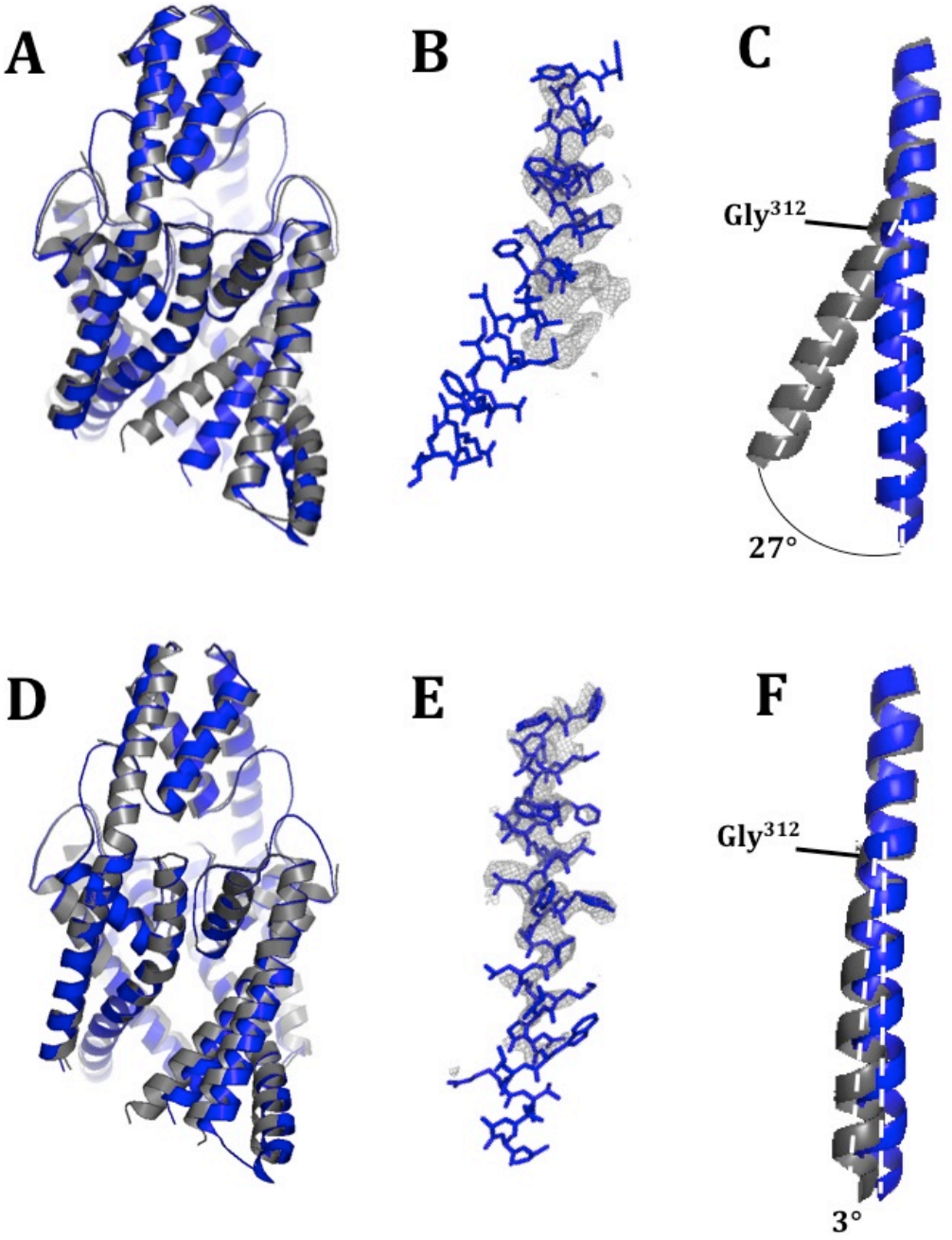

Figure 2-8 TREK-2 co-crystallises with BF-1 in the down state

Prime-and-switch maps (1.5σ) generated using phases from molecular replacement in PHASER show M4 is in the down state when both up state (B) and down state (E) TREK-2 are used MR search models. This indicated that the protein was in the down state. Overlaying the TREK-2 BF-1 structure (blue) with the apo down state (D, grey) and up state (A, grey) show that it is similar to the down state. Comparison of M4 region shows that the helix is straight at the glycine hinge (Gly^{312}). In the BF-1 structure, M4 is separated from the apo upstate M4 by an angle of around 27° (C), but from the apo downstate by just 3° (F).

2.2.2.2 Anomalous peaks reveal that BF-1 binds in the fenestrations of TREK-2

Anomalous difference Fourier maps generated by CCP4's FFT indicated the presence of five peaks in the asymmetric unit. The two largest anomalous peaks (11.8 and 11.5σ at 5Å) corresponded to cadmium atoms, which are present in the crystallisation solution and are known to mediate crystal contacts between helical caps in some crystal forms of TREK-2 (4BW5 for example)[75]. These acted as a positive control for anomalous map generation. The remaining anomalous peaks all lie within the fenestrations of the channels. The peaks assigned as bromines could not be detected in an isomorphous TREK-2 crystal with 100mM potassium bromide. However the cadmium peaks were visible in this control. This demonstrates that the bromine anomalous peaks must have been inserted into the fenestration through binding of BF-1 to the channel. Log likelihood anomalous maps calculated by PHASER showed peaks at locations identical to those observed in FFT maps, further confirming the location of the bromine atoms.

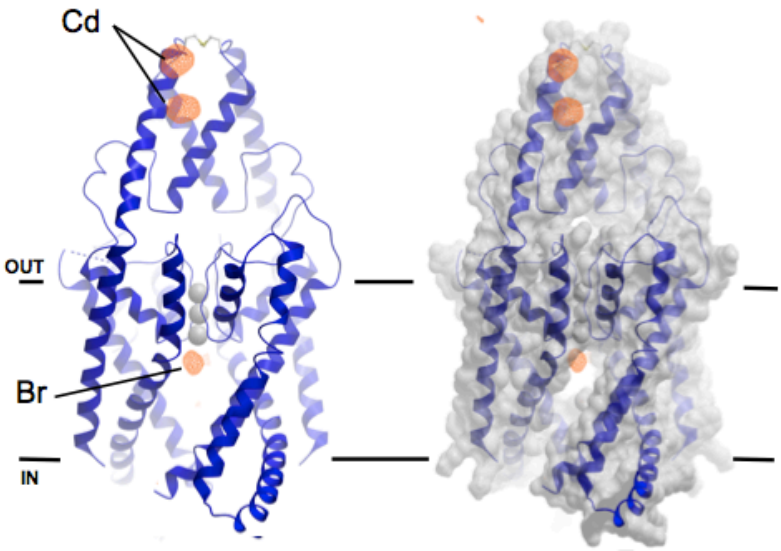

Portal	Anomalous Peak
A	8.7 σ
B	No peak
C	4.6 σ
D	6.30 σ

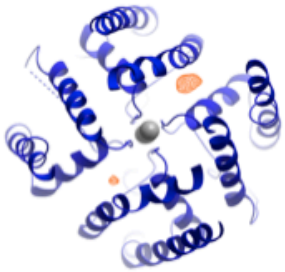

Figure 2-9 Anomalous peaks highlight the binding site of fluoxetine to TREK-2
Cartoon representation of the crystal structure of a brominated fluoxetine derivative bound to TREK-2. Orange mesh: FFT anomalous difference maps calculated to 5Å resolution, contoured at 4.5σ. Two peaks in the cap domain are due to cadmium atoms. Peaks appear in the fenestrations created by the straightening of M4. These are peaks due to bromine atoms. A and B show the protein in the membrane, while C shows the view from the intracellular side. C shows that the occupancy of the ligand in the fenestrations is not equal. The sigma levels of the bromine peaks are given in the table (for maps calculated to a maximum resolution of 5Å). Images produced in ICM Molsoft and Microsoft PowerPoint.

2.2.2.3 BF-1 could bind to TREK-2 in two different poses

Since the location of the brominated ligand had been identified with anomalous peaks, the ligand could be built into $2mF_o$-DF_c density within the fenestration. At 1σ, electron density was evident for the methyl-fluorinated ring of fluoxetine, but not for the aliphatic chain and the pendant phenyl ring. At 0.6σ density appeared for more of the molecule. BF-1 was partially modelled into this density using the location of the anomalous peak as a pivot point.

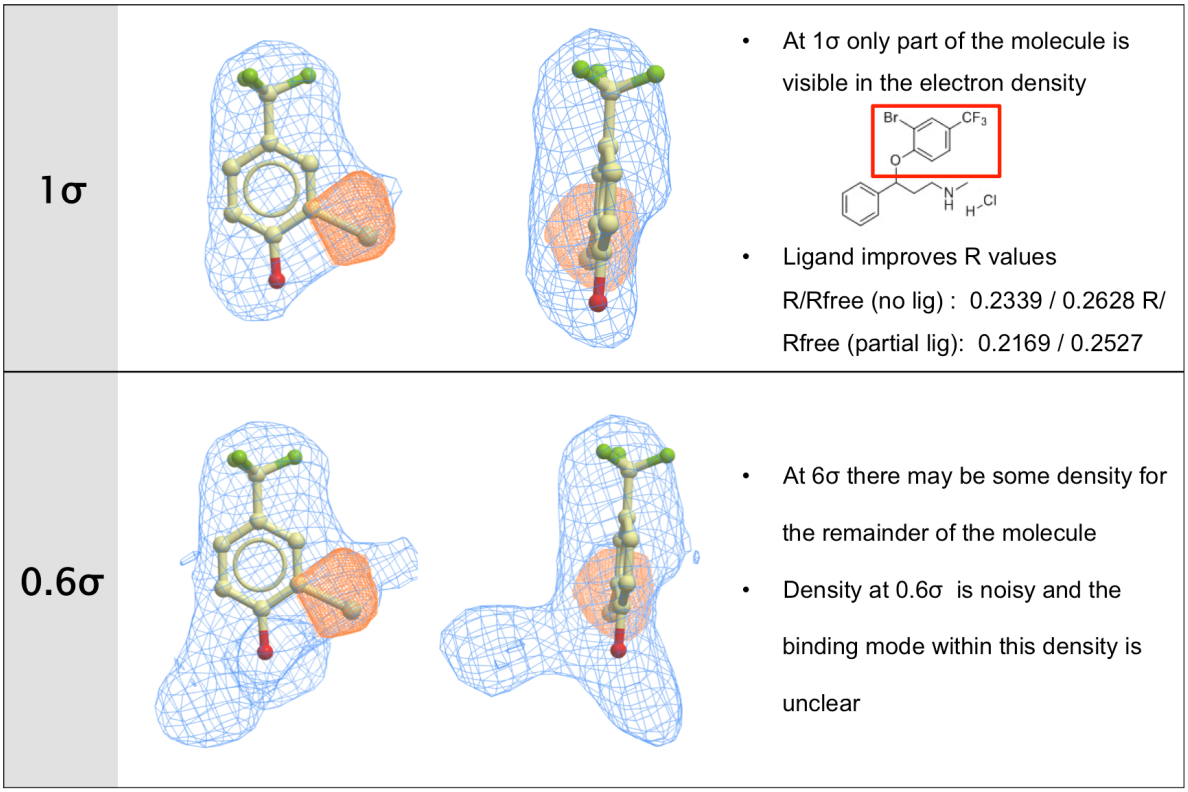

Figure 2-10 Electron density of BF-1 bound to TREK-2

BUSTER $2mF_o$-DF_c maps (blue) are shown, refined without ligand in situ. FFT anomalous difference maps (5Å, 4.5σ, orange mesh) allow the methyl fluorinated ring to be positioned unambiguously.

The remainder of BF-1 was modelled into the 0.6σ density. One branch of this density faces the hydrophilic intracellular vestibule beneath the selectivity filter, while another branch faces the hydrophobic TM helices. BF-1 is a racemic mixture; R and S enantiomers were refined separately as they have different geometric restraints (Figure 2-11). For both enantiomers, it was possible to place the ligand in two alternate poses. One pose had the pendant phenyl ring facing into the pore, while the other had the aliphatic chain facing the pore (Figure 2-12).

For the R-enantiomer, the aliphatic chain facing towards the pore (Pose A) refined to an unstrained geometry, while the pendant ring facing towards the pore (Pose B) refined to a strained geometry. This means that the refined ligand bonds did not agree well with the restraint dictionary. Since this pose is likely to have a higher binding energy than Pose A, Pose A was determined to be the binding mode for R-bromo-fluoxetine-1.

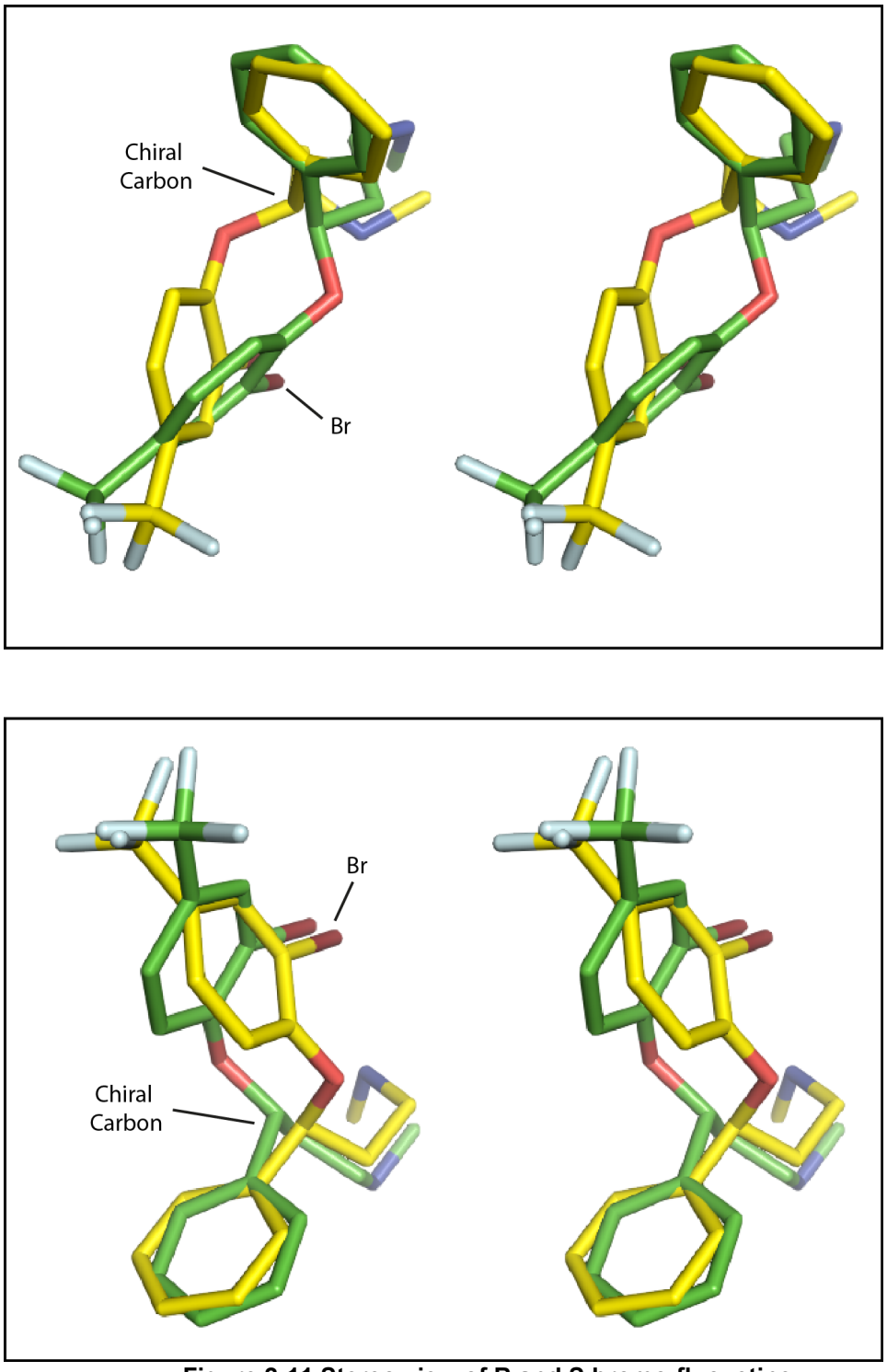

Figure 2-11 Stereo view of R and S bromo-fluoxetine

Stereo views of R (green) and S (yellow) bromo-fluoxetine 1 show that the two enantiomers have different three-dimensional structures; they are mirror images of one another. This means that they need to be modelled into the ligand density independently. Image produced in PYMOL and Adobe Illustrator

However, refinement produced different results for R and S enantiomers. Using the S enantiomer restraint dictionary, pose B was less strained than pose A. It is possible that the two enantiomers bind in different ways, however there is no functional data to support this assertion. It is also possible that both enantiomers can bind in either pose, as the ligand may be able to move around within the pocket. Inspection of the poses indicates that pose A is more likely, as it causes a nitrogen to face towards the hydrophilic pore region, while the aliphatic ring is positioned in contact with the hydrophobic TM helices. This pose has been used to describe ligand binding in the following text.

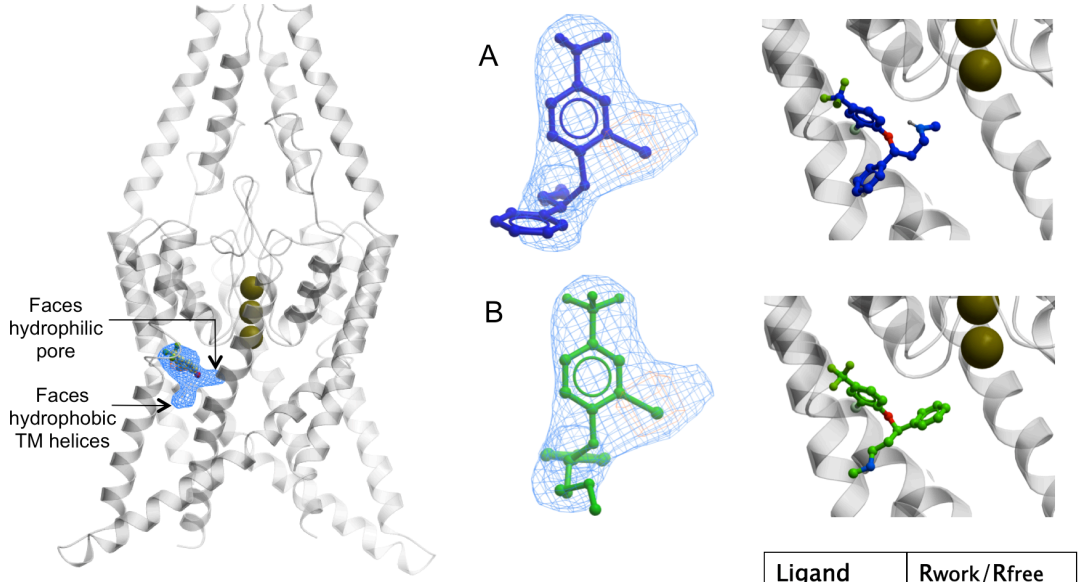

- R-enantiomer used for refinement in all 4 fenestrations
- Modelled into 0.6σ B-factor sharpened density
- Molecule fits density in two distinct positions
- A is more likely as B refines to restrained geometry

Ligand	Rwork/Rfree
None	0.2339/0.2628
Partial	0.2169/0.2527
Complete (A)	0.2170/0.2535
Complete (B)	0.2174/0.2537

Figure 2-12 Modelling of R-bromo-fluoxetine-1 into $2mF_o$-DF_c density
Modelling of BF-1 in two positions using R-enantiomer restraints. The ligand could be modelled in two poses (A and B). However, position B refined to a restrained geometry, indicating this pose is energetically unlikely. The R factors of the refinements without ligand, with the methyl-fluorinated partial ligand, and the complete ligand in two different poses are given in a table. Image produced with ICM Molsoft and Microsoft PowerPoint.

Chain	Partial BF-1		Protein		Phe^{316}	
A	172.53	±1.87	152	±30.92	133.99	±2.62
B	206.11	±2.26	147.71	±27.47	155.1	±4.18
C	229.17	±1.93	169.73	±37.11	186.27	±3.13
D	192.85	±2.05	159.71	±27.32	138.69	±2.52

Table 2-7 B-factors ($Å^2$) of the partially modelled BF-1 in 4XDL
In 4XDL, only the methyl fluorinated ring was modelled as the density uniquely defines it's positioning. These B-factors (±standard deviations) were generated by MOLEMAN2 for ligand (occupancy=1), protein and Phe^{316}. The ligand has higher B-factors than the protein, possibly due to flexible binding or reduced occupancy.

2.2.2.4 The binding site of BF-1 to TREK-2 has few specific interactions

There are few specific interactions between the ligand and the protein; this may explain the low affinity of fluoxetine for TREK-2. The methyl-fluorinated ring forms a π-π stack with Phe^{316}. The nitrogen may also form a hydrogen bond with a backbone carbonyl in pore helix 2 (Val^{276}, Leu^{279}, Thr^{280}). This may link to C-type gating. Other residues involved in van-der-Waals or hydrophobic interactions are Ile^{194} (M2), Val^{253} (M3) and Leu^{320} (M4).

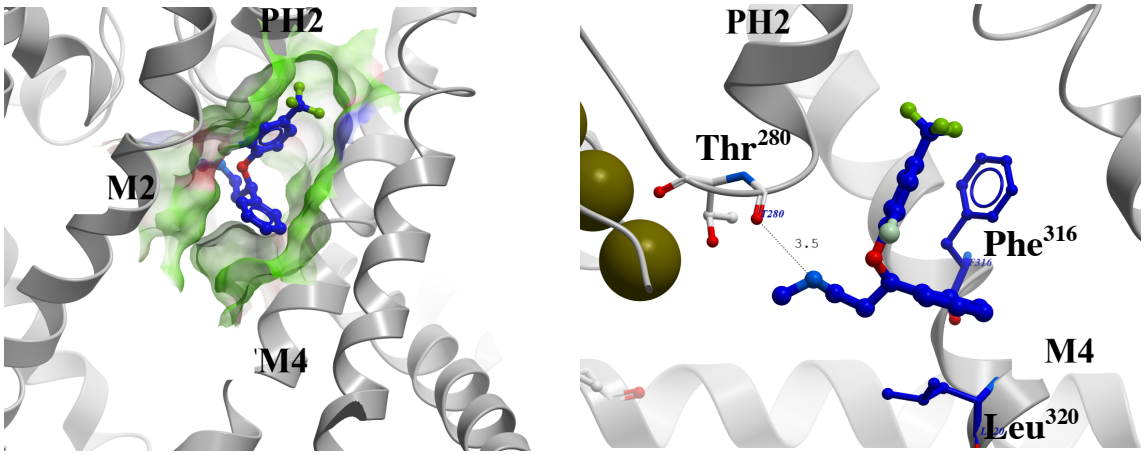

Figure 2-13 The binding site and interactions of BF-1 with TREK-2
Left: The binding site is lined by residues from M2,3,4 and pore helix 2 forming a hydrophobic pocket. A π-π is formed with Phe^{316}, and a weak hydrogen bond may form between the fluoxetine's aliphatic chain and the backbone carbonyl of Thr^{280}. Higher resolution data is necessary to confirm this. Produced with ICM Molsoft.

There are two potential interactions that are not being utilised by BF-1. A free backbone carbonyl in M2 is not hydrogen bonded due to Pro^{198} interrupting the helix. And a free cysteine (Cys^{249}) is present on M3. These binding site characteristics could be utilised to design a more potent or specific inhibitor of TREK-2.

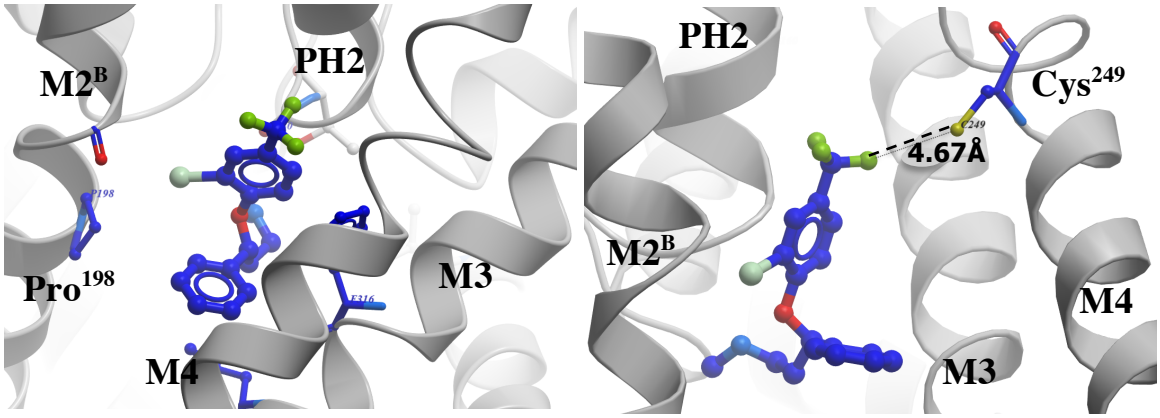

Figure 2-14 Interactions that could be used to design strong binders.
Left: Pro^{198} interrupts M2, leaving a backbone carbonyl free to form hydrogen bonds. Right: Cys^{249} (M3) could be utilised to design a covalent TREK inhibitor. Images produced with ICM Molsoft.

2.2.3 Determining the binding site of BF-3 to TREK-2

2.2.3.1 Selection of fluoxetine derivatives

In order to verify which of pose A and B fluoxetine occupies, it is beneficial to obtain a structure with bromine either on the pendant phenyl ring, or on the aliphatic chain. Since the benzene rings is chemically more accessible this was brominated (Table 2-8, Gian Filippo Ruda and Paul Brennan from the Target Discovery Institute, Oxford). Chiral synthesis was used to enable modelling of a single enantiomer into the resulting electron density.

	Derivative	Smiles String	Compound Structure
Fluoxetine	R or S Chirally Pure	**R:**CNCC[C@H](c1ccccc1)Oc1ccc(cc1)C(F)(F)F.[Cl] **S:**CNCC[C@@H](c1ccccc1)Oc1ccc(cc1)C(F)(F)F.[Cl]	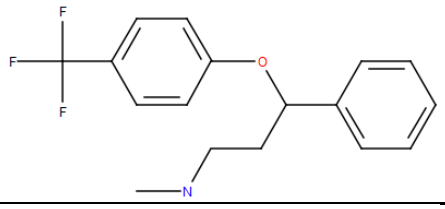
	Br-Fluoxetine 1 BF-1 (Racemate)	CNCCC(c1ccccc1)Oc1ccc(cc1[Br])C(F)(F)F.[Cl]	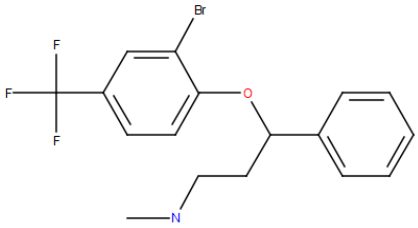
	Br-fluoxetine 3 BF-3 (79%S; 21%R)	[H][N+]([H])(C)CCC(c1ccc(cc1)[Br])Oc1ccc(cc1)C(F)(F)F.[H][Cl]	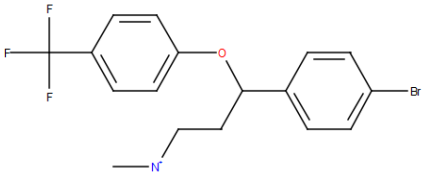

Table 2-8 A third fluoxetine derivative, BF-3, was synthesised to verify the binding mode of Fluoxetine to TREK-2. Relative solubility and affinity are not know for this compound.

BF-3 was co-crystallised with TREK-2 in the same conditions used for BF-1. In order to improve ligand occupancy, a 100mM BF-3 fully solubilised stock was produced in ethanol. Tests indicated that up to 10%v/v ethanol (although much of this may have evaporated during crystallisation) did not prevent crystal growth or decrease diffraction quality so the compound was co-crystallised with TREK-2 at a final concentration of 5-10mM. Soaking into pre-formed crystals with higher ligand concentrations was not possible as it destroyed diffraction. The resulting crystals had the same crystal packing and unit cell constants as the BF-1 dataset.

Derivative/ Enantiomer	Dataset No.	Maximum Resolution (Å)	Space Group	Electron Density		Crystallisation Conditions and Crystal Mounting
				Ligand	Anom	
BF-3	52 (2)	3.5 x 3.5 x 3.9	$P2_12_12_1$	No	Yes	**Drop**: 0.1M MES pH 6.5; 50mM $MgCl_2$; 1mM $CdCl_2$; 17% PEE 15/4 **Compound:** 10mM (Ethanol) **Cryo:** 25% PEE15/4 **Seed:** 20nL 1:500 seed stock **Soak:** None

Table 2-9 Summary of crystal structures of TREK-2 with BF-3

2.2.3.2 Anomalous peaks reveal that BF-3 binds in the fenestrations of the down state

The co-crystal structure is in the down state, with M4 further down than has previously been observed for TREK-2 (Figure 2-15). When compared with the M4 down state of TREK-2, the helix has rotated away from M2 axis by 5° around Gly^{312}. This is two degrees further than the rotation observed in the BF-1 structure. To facilitate this straightening of M4, M2 and M3 move down and away from the central axis of the pore.

Anomalous peaks for cadmium (f'' 1.9e at 13.5keV beam) were present at 12.1 and 11.7σ when anomalous maps were calculated to 5Å resolution, indicating successful anomalous map generation. Anomalous peaks for bromine (f'' 4e at 13.5keV beam) atoms confirmed that the fenestration is indeed the binding site for fluoxetine. The significance of the bromine anomalous peaks was higher than the BF-1 dataset; in fact one of the Br peaks was at a higher significance than the cadmium atoms. This indicates that the compound has a higher occupancy than in the BF-1 structure. This may be due to the increased ligand solubility in the presence of ethanol.

In this structure, the C-D dimer had higher bromine occupancy than in the A-B dimer. Interestingly, the C-D dimer has four potassium ions in the filter (S1-S4), while the A-B dimer has just three (S2-S4). The reason behind this difference is unclear as comparisons of the two dimers indicate there are no helical shift or detectable changes in the selectivity filter (Figure 2-16). Similarly to BF-1, the fenestrations within each dimer have Br peaks with different significance levels. Again, this may indicate negative co-operatively in binding of the ligand.

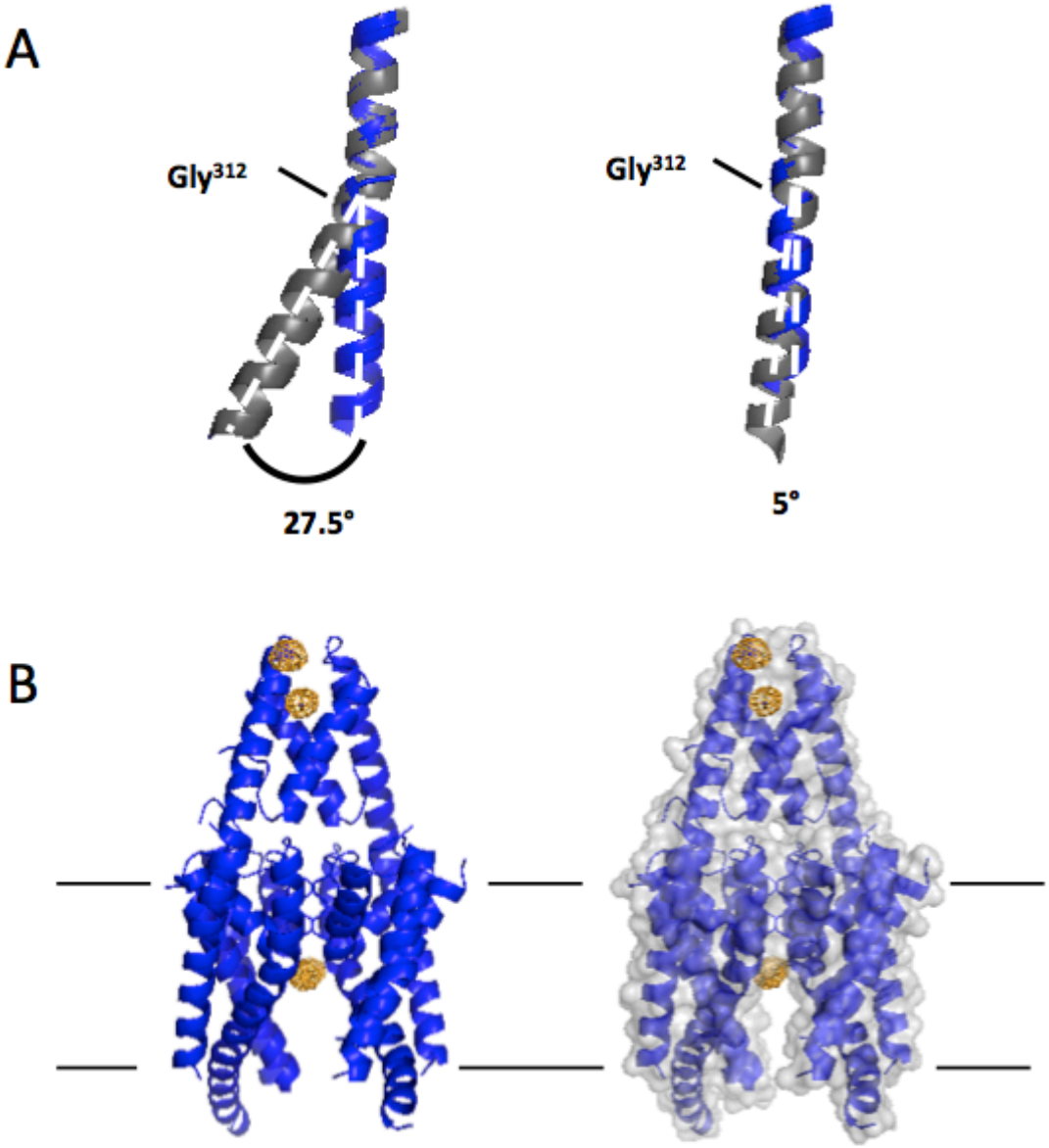

FENESTRATION	ANOMALOUS PEAK (σ)
A	9.60
B	10.27
C	14.80
D	8.78

Figure 2-15 Crystallisation of TREK-2 with a second fluoxetine derivative, BF-3
TREK-2 co-crystallises in a M4 down state, as is shown by comparisons with 4BW5 (A, left) and 4XDL (A, Right). Contoured at 4.5σ, FFT anomalous maps (5Å) demonstrate the presence of two cadmium atoms in the helical cap as well as additional anomalous peaks (bromine atoms) within the fenestrations (B,C). There are two fenestrations in each dimer, and two dimers in the asymmetric unit. The significance level of the bromine peaks in each fenestration are different (C).

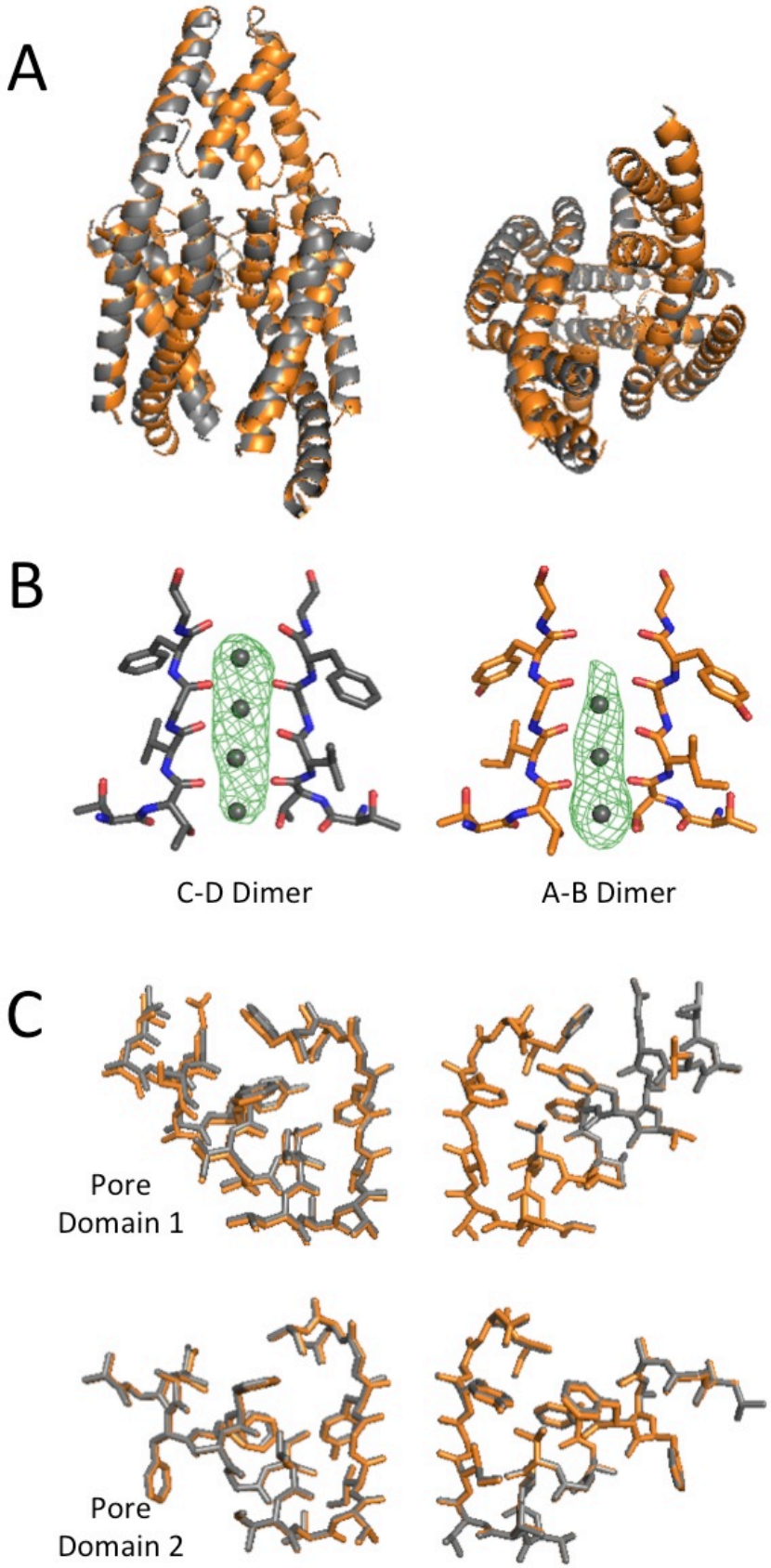

Figure 2-16 Comparison of the two dimers in the structure of TREK-2 with BF-3.
The overall structure is similar for both the C-D dimer (grey) and the A-B dimer (orange) (A). Comparison of the pore-domain (B) shows that the C-D dimer has just 3 potassium sites occupied while the A-B dimer has 4. Buster mF_o-DF_c density contoured at 3σ, refined without potassium present. However, there are no detectable differences in the pore domain structures (overlaid, C) of the two dimers.

2.2.3.3 No unique position for BF-3 could be determined by the electron density

While electron density was present in the fenestration (evident in both BUSTER F_o-F_c maps and RESOLVE 2mF_o-DF_c maps), it was not possible to uniquely build the ligand into the density. B-factor sharpening, density modification with RESOLVE and feature-enhanced maps did not improve the quality of the ligand density. Inspection of the density indicates that this may be due to dual occupancy of the fenestrations, which may contain both lipid and ligand. Alternatively, some of the fenestrations may be occupied by lipid while others are occupied by BF-3. In order to improve the ligand density it may therefore be necessary to remove lipids from the site. Finally the density may represent two different ligand binding modes.

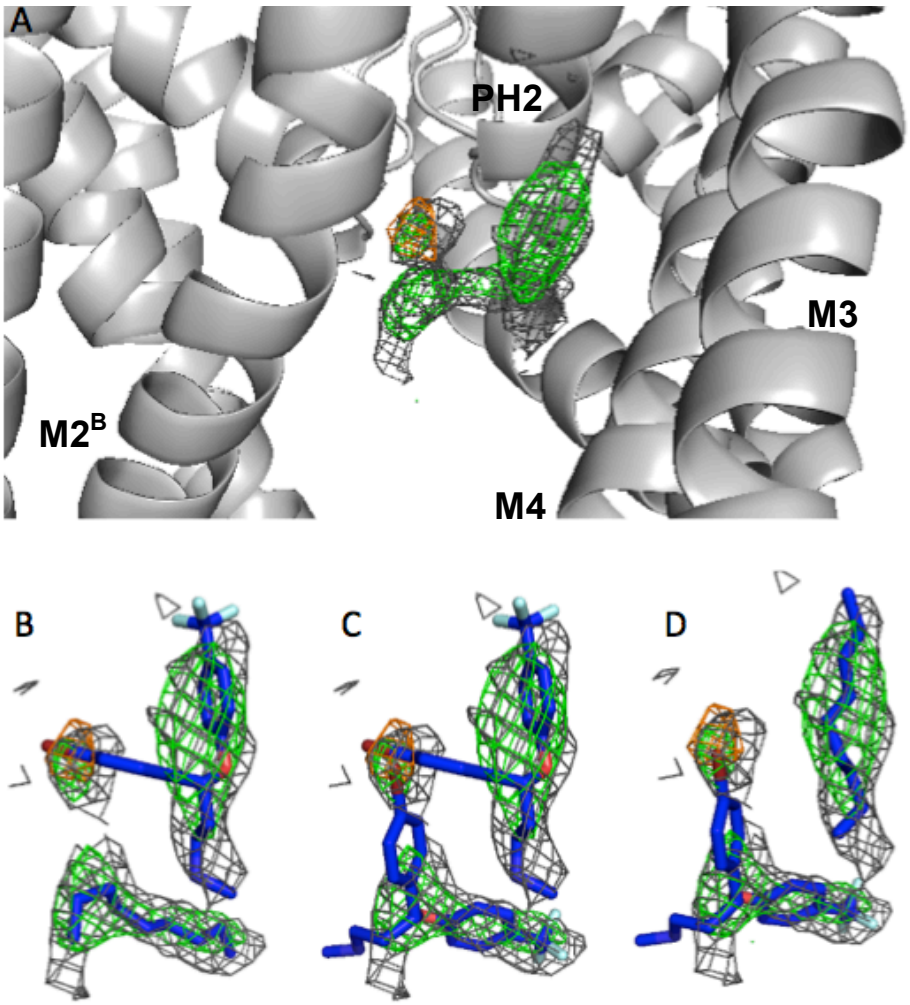

Figure 2-17 Electron density within the TREK-2 fenestration in the presence of BF-3
In grey mesh, the RESOLVE density modified BUSTER 2mF_o-DF_c maps show un-modelled density in the fenestration of a TREK-2 co-crystal structure with BF-3 (1.5σ). In orange, the 5Å anomalous maps are contoured at 8σ. In green, the mF_o-DF_c maps from BUSTER refinement are shown. All maps are from refinement without ligand placed. The location of the ligand density within the fenestration is shown (A). It could be explained using either a combination of two ligand binding modes (C) or ligand binding with lipid (A,B). As the density is not of sufficient quality to determine the true molecular structure within the fenestration, ligand was not modelled.

The location of the anomalous peak within the fluoxetine binding site was the same as for BF-1. This raised the possibility that the peak simply represented free bromide. However, as no free bromide ions were present compound synthesis and co-crystal structures with high concentrations (100mM) of potassium bromide do not display anomalous peaks within the fenestration, this is unlikely to be the case. Instead radiation damage may cause the bromine to separate from the ligand after co-crystal has formed. Alternatively, the binding mode of the ligand may be driven by the bromine. Since bromine is large, and may form an interaction with the free backbone carbonyl, this is indeed a possibility. In order to overcome this it is necessary to produce a crystal structure with a non-brominated fluoxetine derivative for example norfluoxetine.

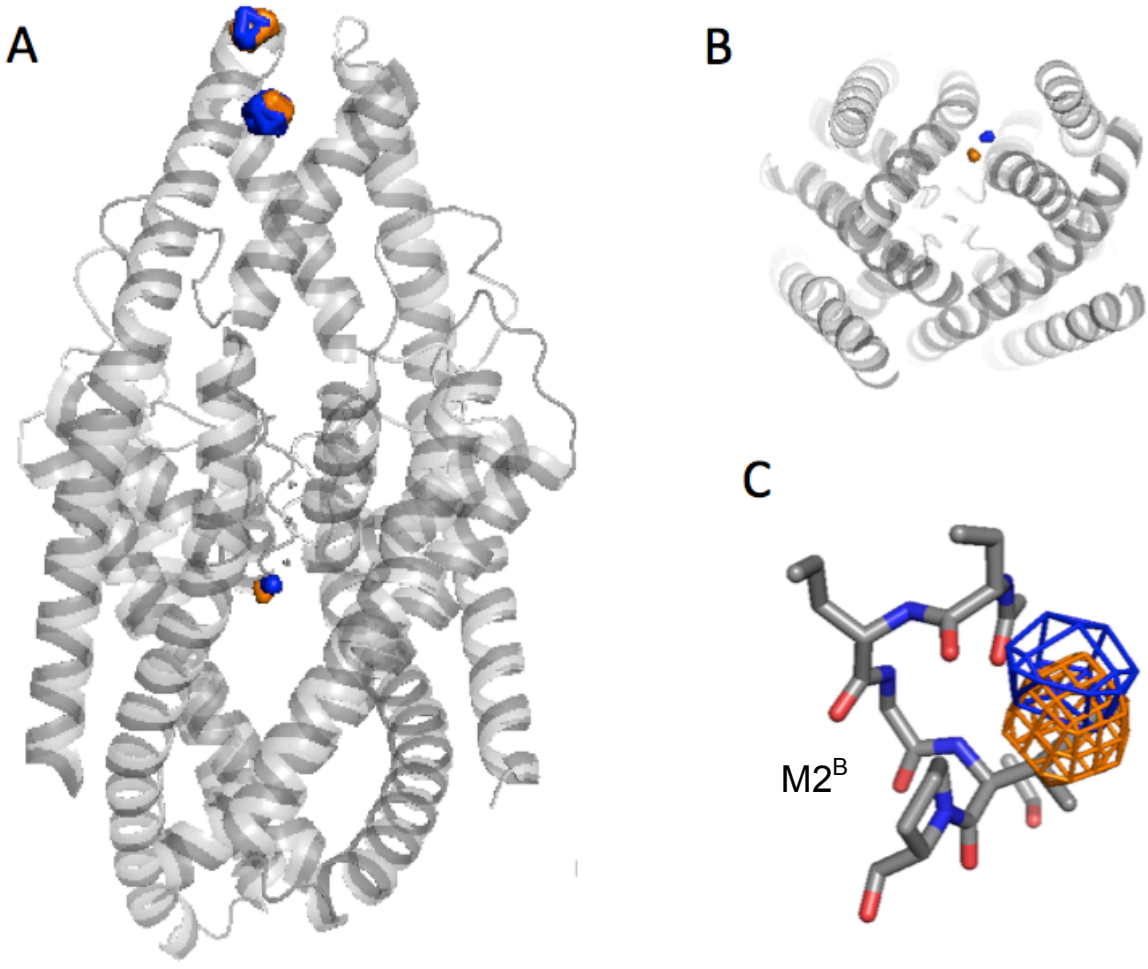

Figure 2-18 Comparison of the locations of BF-1 and BF-3 anomalous peaks
The anomalous FFT map for the BF-1 structure (blue, 7σ) map closely onto the peaks in the BF3 structure (Orange, 9σ) (A,B). The overlapping cadmium peaks in the helical cap (A) demonstrate that this is not due to alignment error. The large bromine atom may be influencing the binding mode of the ligand, since M2 provides a pocket in which the atom can sit. Pro^{198} interrupts the hydrogen-bonding network of M2, and this provides a free carbonyl close to the bromine site. This may form a weak interaction with the bromine, further stabilising its position.

2.2.4 Norfluoxetine density confirms the binding mode of Fluoxetine

The binding site of fluoxetine had been confirmed as the fenestration through co-crystal studies with brominated ligands. It is therefore possible to retrospectively analyse data sets that have been produced with other fluoxetine derivatives. Of particular note, an atomic resolution dataset had been collected by a post-doc in the lab (Yin Dong) in the presence of the racemic fluoxetine breakdown product norfluoxetine. The protein had been modelled in the TREK-2 down state by Ashley Pike, and had filter sites S2-S4 occupied with potassium. Inspection of this dataset demonstrated some potential ligand density within the confirmed fluoxetine binding site. Building norfluoxetine into this density could provide insight to the correct binding pose of fluoxetine without influence from the large bromine atom. I was responsible for completing the structure by building and refining the norfluoxetine ligand (the protein structure was built by Ashley Pike).

Electron density for norfluoxetine had tetrahedral geometry with three substituent parts as expected from the three dimensional structure of this ligand. The fourth atom from the tetrahedral carbon centre is a hydrogen so it is not expected to be visible. However, automated ligand fitting did not work for this dataset. PHENIX ligand fitting toolbox[143,144] produced three separate results with correlation coefficients (correlation of ligand with F_o - F_c density in real space) of 0.62, 0.81 and 0.67. A coefficient > 0.75 indicates correct ligand placement[144]. In all three cases, the ligand was placed in an incorrect binding site. RHOFIT[145] also suggested incorrect binding sites. Seeding the correct binding site into RHOFIT did not assist in the location of the binding site. These techniques fail because they never find the true ligand density, but instead identify sites that are in the bulk solvent. This may be due to a minimum requirement for significance of F_o-F_c and ligand density volume, along with the noise of low-resolution maps. It was therefore decided to position the ligand manually.

To avoid bias in ligand positioning from the BF-1 structure, all six possible poses of norfluoxetine were systematically examined for both enantiomers. Poses which resulted in large sections of the ligand falling outside of the density were rejected. BUSTER was used to refine the remaining poses. These were ranked based on geometric constraints of ligand bonds, clashes with the protein molecule, agreement with electron density and potential for bond formation. The results converged to a single pose for each enantiomer, corresponding to pose A. In both cases, the methyl fluorinated ring stacked against Phe^{316}. This result agrees with the findings for BF-1 binding.

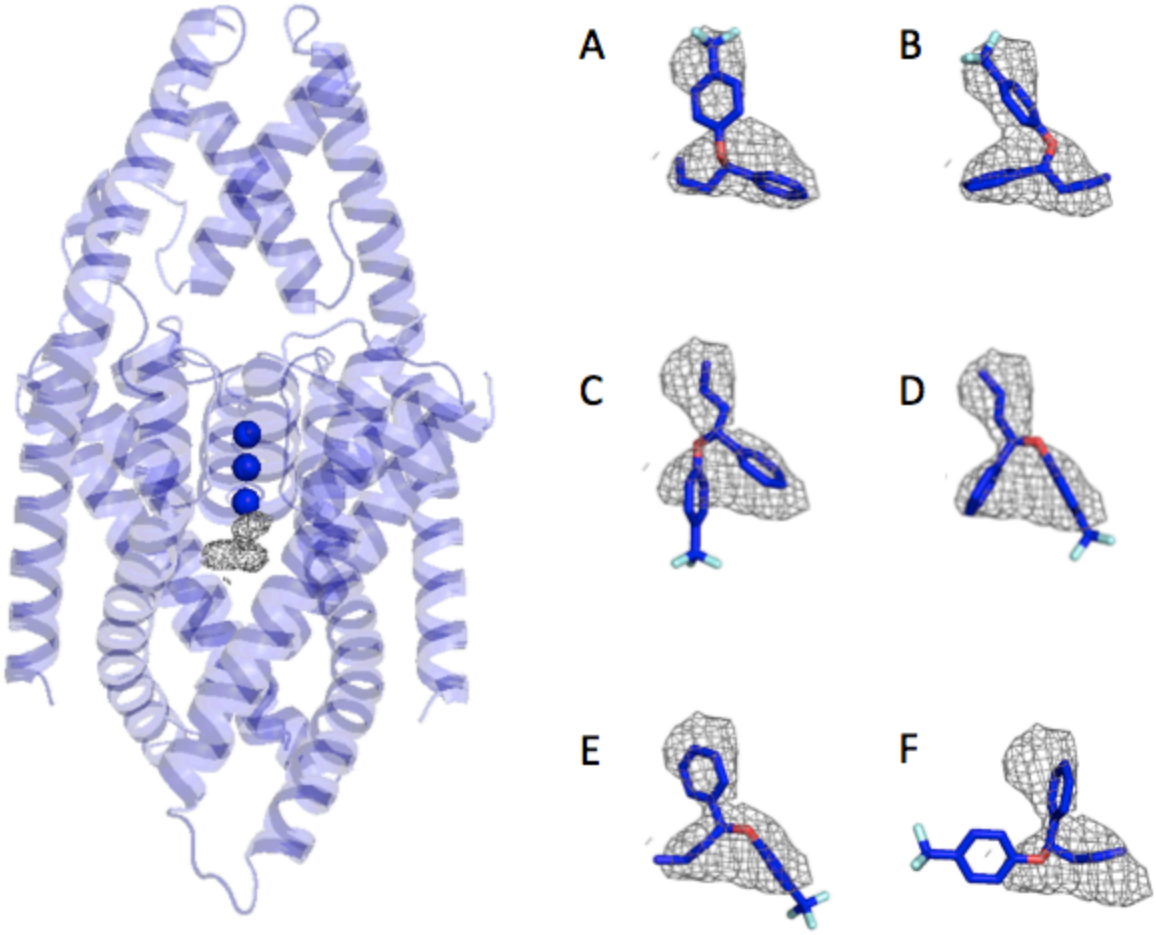

Figure 2-19 Systematic testing of all possible binding modes of norfluoxetine to TREK-2
Electron density (RESOLVE density modified $2mF_o$-DF_c average maps at 1.0σ, grey) for norfluoxetine is visible within the fenestration (Left). The ligand could be modelled into this density in six different ways (A-F), however, most of these poses (C-F) result in parts of the ligand protruding from the density. Here, poses A and B were selected for further investigation, as ligand did not protrude from the density.

Given that there is no data to suggest either enantiomer is a stronger binder, a dual refinement was run. Each enantiomer was positioned in its pose A and given occupancy of 0.5. A dual refinement model is better able to explain the extent of the electron density for the ligand than what is observed for a single enantiomer alone (Figure 2-20).

1	Rfree/Rwork	Density Fit	Bonds	Geometric Restraints	CLASH	Quality
A	0.2471/0.2531	2	H, π- π	0	0	4
B	0.2470/0.2517	1	H, π- π	0	0	3
C	0.2482/0.2506	1	None	0	1	0
D	0.2469/0.2514	0	None	1	0	-1
E	0.2472/0.2508	0	H, π- π	1	0	1
F	0.2481/0.2533	1	H, π- π	1	0	2
2	**Rfree/Rwork**	**Density Fit**	**Bonds**	**Geometric Restraints**	**CLASH**	**Quality**
A	0.2463 / 0.2502	2	H, π- π	0	0	4
B	0.2476/0.2531	2	H, π- π	0	1	3
C	0.2472 / 0.2483	0	π- π	0	2	-1
D	0.2478 / 0.2505	0	H, π- π	0	0	2
E	0.2471 / 0.2510	1	None	1	0	0
F	0.2480 / 0.2525	1	None	1	0	0

Table 2-10 Selection of pose for norfluoxetine based on a quality metric
The quality metric is the sum of the density fit (0= large parts of ligand out of density, 1= some ligand out of density, 2= all ligand in density) and bond score (bond expected with protein molecules, one bond = 1 point), minus the geometric constraint score (0= unrestrained ligand conformation, 1= restrained) and the clash score (0= no clash, 1= few minor clashes, 2= major clashes). The top table shows the result for R-norfluoxetine, while the bottom table shows the result for S-fluoxetine. Highlighted in green are the ligand poses that have been selected.

The binding mode of brominated fluoxetine is slightly shifted when compared with that of norfluoxetine (Figure 2-21). It is likely that this change is due to the presence of a large bromine atom driving the position of binding. In particular, as noted in Section 2.2.3 and Figure 2-18, a pocket within the binding site perfectly accommodates a bromine atom, and this may modify the binding mode slightly. To accommodate the resulting shift in ligand positioning, Leu^{320} is flipped to a different rotamer.

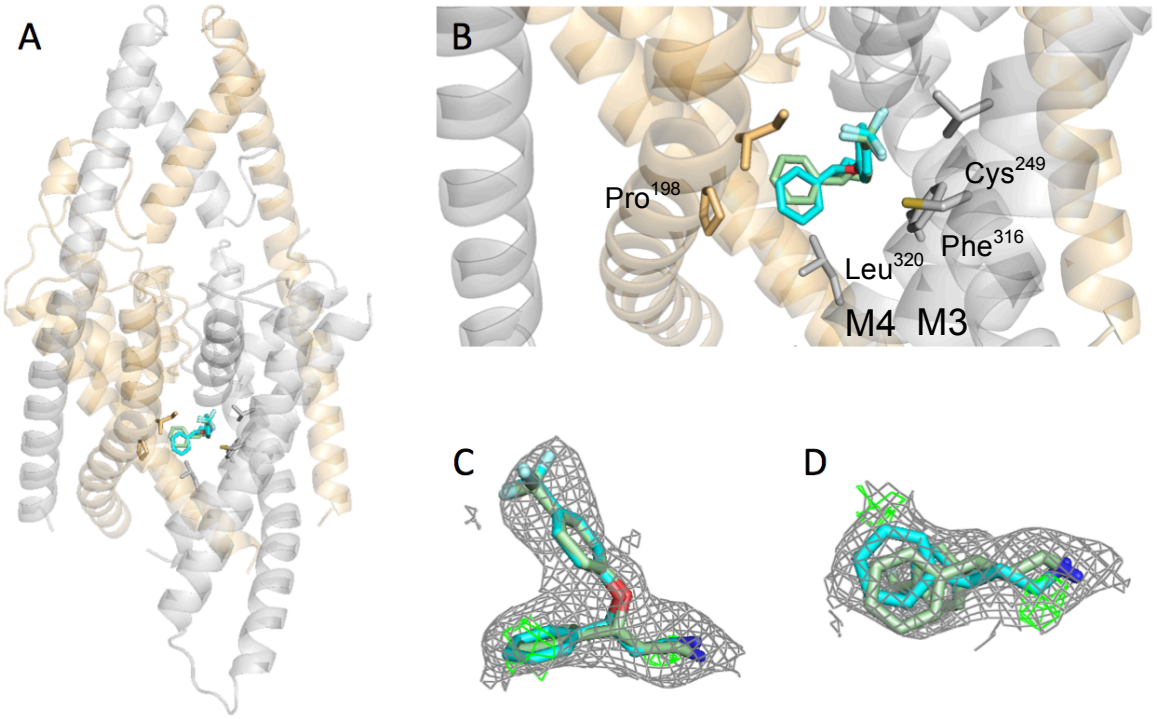

Figure 2-20 Dual Refinement of R and S-norfluoxetine bound to TREK-2

R (Green) and S (Cyan) norfluoxetine were refined simultaneously with occupancies of 0.5 within the fenestration of TREK-2 (A). The two enantiomers refine to similar positions (B), and the RESOLVE density modified BUSTER density (grey, $2mF_o$-DF_c 1σ; green mF_o-DF_c 3σ) agrees well with this model of ligand binding (C).

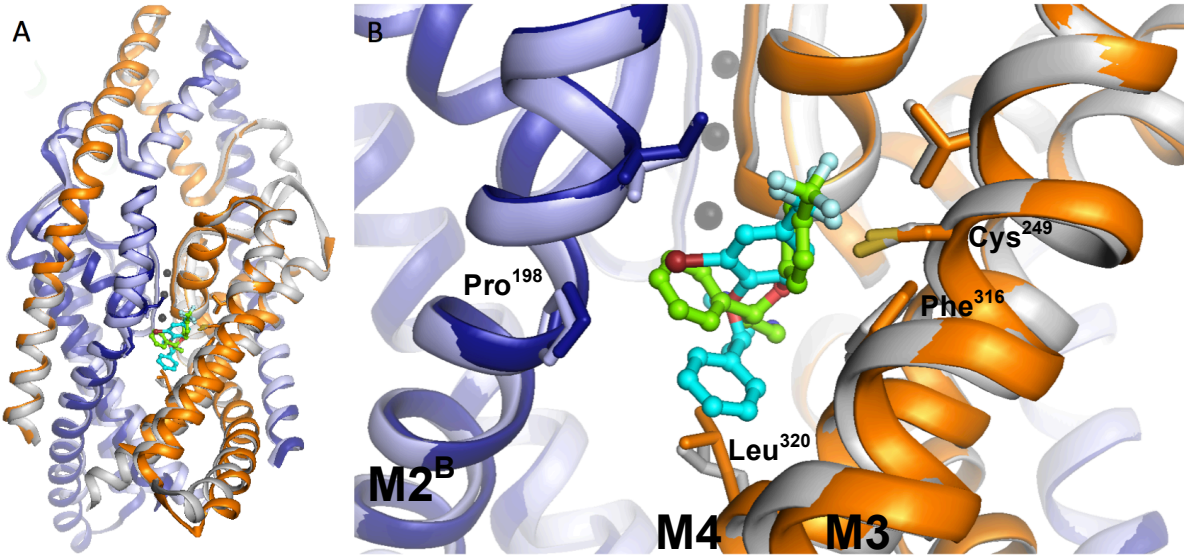

Figure 2-21 Comparison of the binding modes of BF-1 and norfluoxetine

The overall structure of TREK-2 (A) in the presence of norfluoxetine (A chain orange and B chain dark blue) is similar to that observed for BF-3 (A chain grey, B chain light blue) is almost identical. However, the binding mode of R-BF-1 (cyan sticks) is shifted slightly right when compared with R-norfluoxetine (green sticks), (B)

.

2.2.5 Co-crystallisation with potential covalent Inhibitor

There is a non-bonded cysteine side chain (Cys^{249}, M3) within the fluoxetine binding site that is not utilised for specific interactions with the ligand. This could be utilised to design a more potent or specific inhibitor of TREK-2. A fluoxetine derivative that binds directly to the cysteine could produce a covalent inhibitor of TREK channels. To this end the compound CovF was designed with and synthesised by Melissa D'Ascenzio from the Target Discovery Institute, Oxford. This Racemic compound is an acrylamide derivative. Cys^{249} should act as a nucleophile to give 1,4 Michael addition to the α,β unsaturated amide in CovF, leading to a covalent linkage (Figure 2-22).

	Derivative	Salt	Smiles String	Compound Structure
Fluoxetine	R or S Chirally Pure	HCl	**R:**CNCC[C@H](c1ccccc1)Oc1ccc(cc1)C(F)(F)F.[Cl] **S:**CNCC[C@@H](c1ccccc1)Oc1ccc(cc1)C(F)(F)F.[Cl]	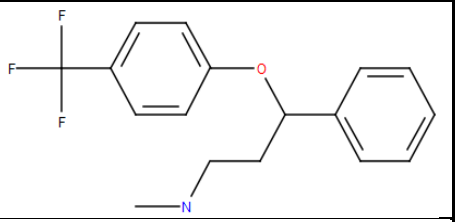
	Covalent Fluoxetine (CovF) racemic	HCl	N(/C(=C/SCC(N)C(=O)O)[O-])C1C=CC(=CC=1)OC(CC[N+]C)C(C=CC=C1)=C1	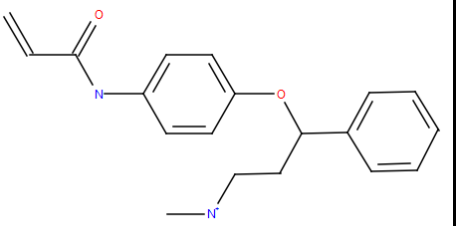

Table 2-11 Design of a covalent inhibitor for TREK-2, CovF

To investigate whether the compound was able to form a covalent bond with the protein mass spectrometry was employed. If the compound forms a covalent bond with the protein the molecular weight should be shifted by the mass of the compound. A time-series was therefore completed with 5:1 molar ratio of CovF to protein molecules. For all time points tested no covalent adducts could be detected (Figure 2-23). It is possible that the ligand enters the pocket but fails to form a covalent bond with the cysteine due to the conditions within the pocket or the specific binding mode of the ligand. Co-crystal trials were therefore instigated.

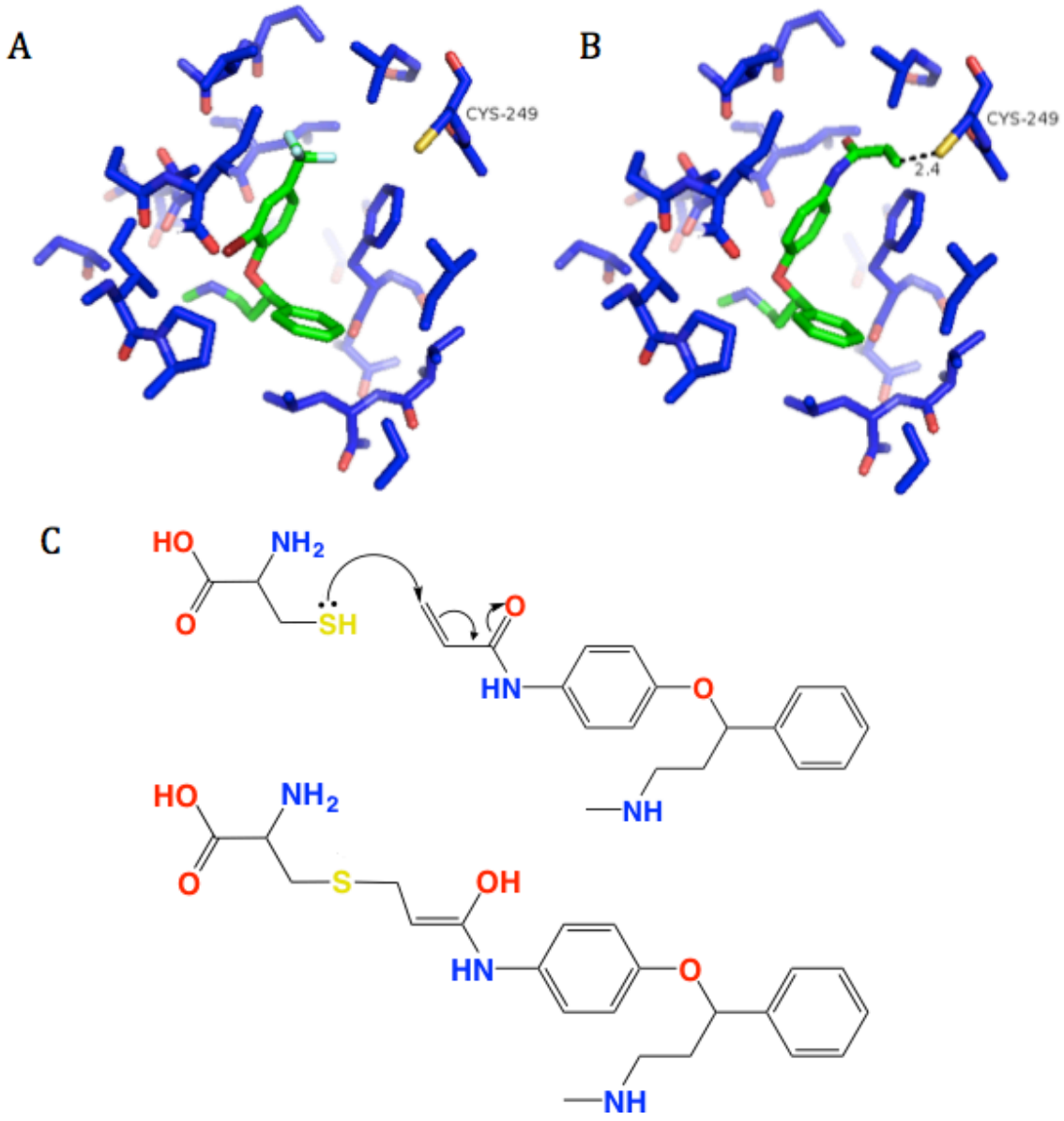

Figure 2-22 Design of a covalent TREK-2 inhibitor

The fluoxetine derivative CovF (B) has been designed to covalently bond to Cys^{249} (M3). It can be modelled into the fenestration based on the BF1 binding mode (A), providing a 2.4Å gap between the molecule and the sulphur atom of the cysteine. A carbon-sulphur bond is around 1.8 Å in length. The cysteine sulphur binds to the the α,β unsaturated amide in CovF via nucleophillic attack (C).

Although co-crystals of TREK-2 were grown in the presence of 5-10mM CovF, collection of a dataset with resolution 3.7 x 3.7x 4.1Å revealed no ligand density within the fenestration. Presence of the ligand did however promote formation of the down state of TREK-2 while inhibiting formation of up state crystals. This indicates that the ligand may be interacting with the protein or alternatively it may be influencing the crystallisation of TREK-2 in another way.

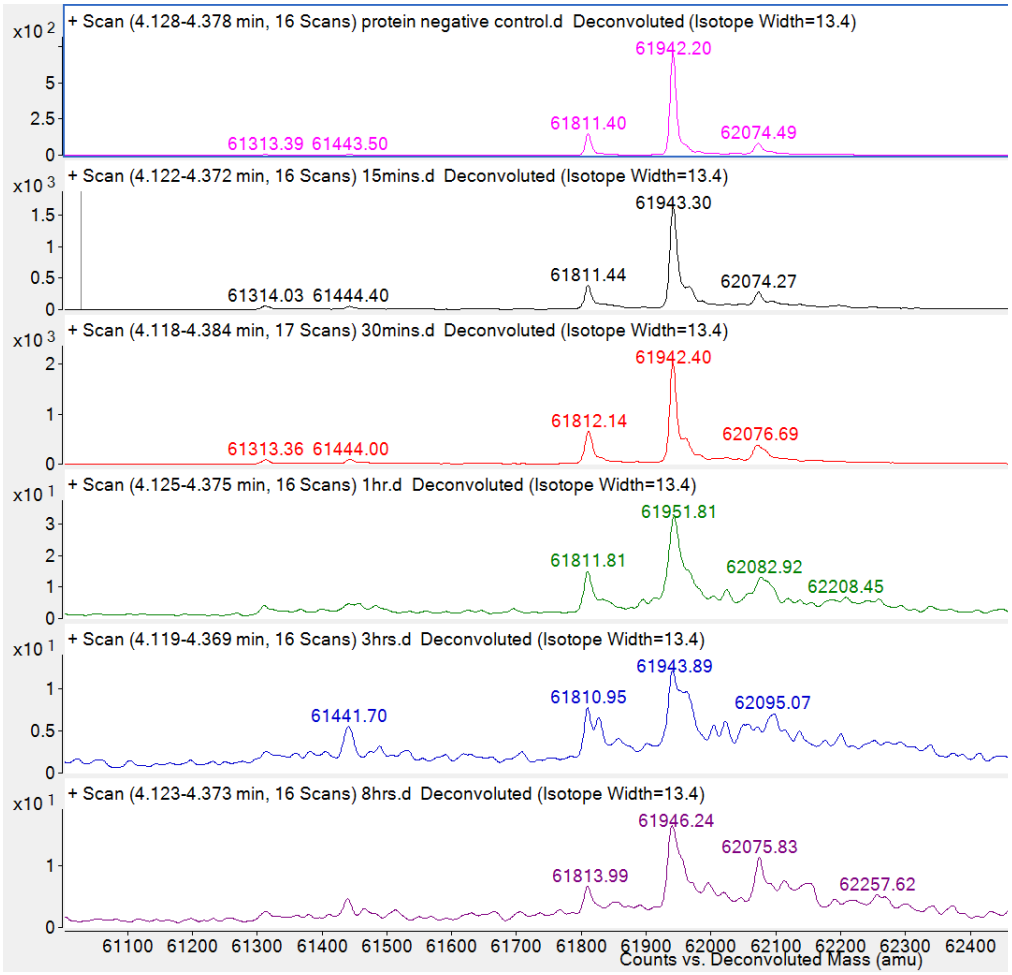

Figure 2-23 De-convoluted mass spectra of TREK-2 incubated with CovF

Three main peaks are evident; 62074 Da corresponds to the TREK-2 dimer. 61811Da corresponds to the dimer with loss of one methionine per chain. 61950Da corresponds to the dimer with loss of a single methionine. The mass spectra observed at time points 0.25, 0.5, 1, 3 and 8 hours incubation does not differ from that observed without compound in a way that is consistent with covalent binding of a ligand (an expected mass shift of 415.15Da). There is therefore no evidence for the covalent binding of CovF to TREK-2.

2.2.6 Binding Assays

A thermo-stability assay was used to estimate the approximate affinity of fluoxetine and the brominated fluoxetine derivatives for the purified, detergent solubilised, TREK-2 crystal construct protein. N-[4-(7-diethylamino-4-methyl-3-coumarinyl)phenyl]maleimide (CPM) is a fluorescent dye that covalently binds to exposed cysteine. The protein was gradually heated and unfolded in response to this heating. Buried cysteines became exposed, allowing the CPM dye to bind and fluoresce[146]. If a compound binds it thermostabilises the protein, slowing unfolding. The method assumes that binding will always influence thermostability.

The stability of a protein in response to heating is measured as a melting temperature T_m, the temperature at which 50% of the protein is unfolded. A compound that thermostabilises the protein will alter the melting curve of the protein, changing the T_m. The difference in melting temperatures between the sample with and without compound gives a thermal shift ΔT_m- the degree to which addition of the compound thermostabilises the protein. Titration experiments can be done with the compound to determine the concentration required to cause a half maximal thermal shift. This can be used to compare relative binding affinities of compounds to a protein. In this experiment I aimed to detect whether brominating of fluoxetine influences it's binding to TREK-2.

Exploratory experiments indicated that the addition of high concentrations of fluoxetine did not lead to a significant T_m shift. There are several possible reasons for this result. First, the compound does not bind to the protein. Given binding is observed in crystallization this explanation is unlikely. Second, the compound may bind to TREK-2 but not cause a shift in the stability. Purified TREK-2 is very stable ($T_m \approx 72°C$) and it is possible that it is difficult to further increase thermostability of such a stable protein.

These results were mirrored with brominated fluoxetine. Addition of the brominated fluoxetine derivative BF-1, for which the co-crystal structure with TREK-2 was solved, produced no significant shift in T_m. However, patch-clamping experiments carried out by a

collaborator (Conor McClenaghan) on full length TREK-2 indicate that BF-1 inhibits TREK-2 with a similar efficacy to both fluoxetine and norfluoxetine[75].

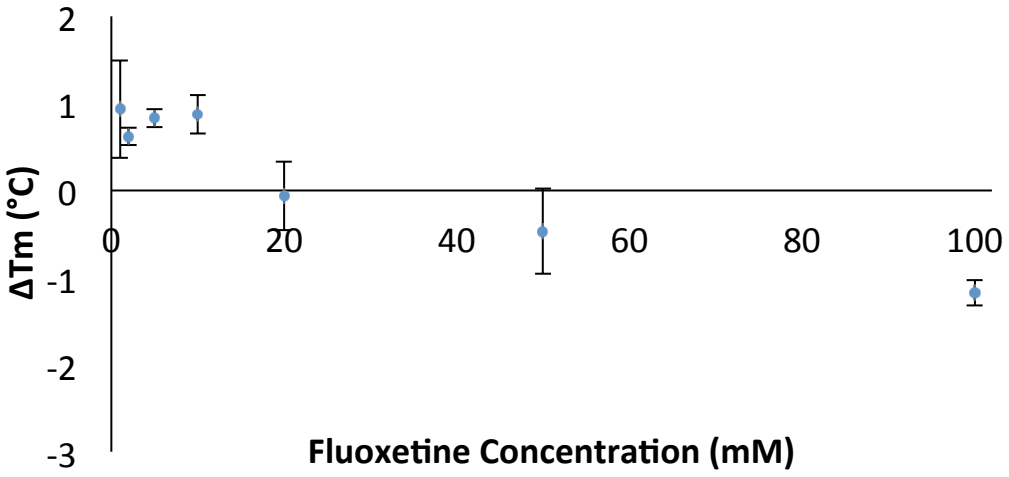

Figure 2-24 Thermostabilisation of TREK-2 by fluoxetine in a CPM dye assay.
These data show the shift in melting temperature (ΔT_m), measured by the CPM dye assay, of purified TREK-2 protein when adding increasing concentrations of fluoxetine. Data is averaged over 9 single data points, which are taken from three individual protein samples. Errors shown are standard errors of the mean value.

2.3 Discussion

2.3.1 Determination of the Prozac binding site in TREK-2

This work demonstrates the binding site of fluoxetine derivatives in TREK-2. This binding site lies in the fenestration connecting the membrane with the inner vestibule beneath the selectivity filter. The location of this binding site was confirmed with three different fluoxetine derivatives, BF-1, BF-3 and norfluoxetine. Although it has been suggested that the K2P channel fenestration may be a binding site for lipids[65], this work represents the first definitive evidence that compounds can bind within this hydrophobic pocket. Fenestrations have also been observed in other ion channels[30]; a similar strategy could be employed to determine if these were also drug binding sites.

Fluoxetine is a weak binder to TREK channels, with an IC_{50} of ~20μM. This is reflected well by the few specific interactions that the drug forms with the protein. Since the equilibrium dissociation constant K_d is directly related to the enthalpy change ($\Delta H, \text{joules per mole}$) of binding;

$$\Delta H - T\Delta S = RT \ln K_d \qquad \textbf{Equation 2-5}$$

[where T is the temperature (Kelvin) ΔS the entropy change of the system (Joules per Kelvin per Mole) and R the ideal gas constant 8.31 Joules per Kelvin per Mole], few specific interactions would mean a less negative enthalpy change and thus a small dissociation constant. This would result in a lowered IC_{50}. A lack of specific interactions may allow the ligand may adopt more than one position within the binding site. This may also explain why fluoxetine was not visible without bromine attached. This large atom may have anchored the fluoxetine to one or more of positions within the binding site.

Attempts were made to utilise features of the binding site to design higher affinity TREK inhibitors. In particular a covalent inhibitor was designed and synthesised (by Melissa

D'Ascenzio) to target the Cys^{249} residue within the pocket. However this compound did not covalently attach to the protein, as evidenced by mass spectrometry. It is possible that the addition of the unsaturated amide group to the fluoxetine inhibited it's binding. It is also possible that the compound was not reactive enough to bond with the cysteine side chain. A second more reactive, cysteine-modifying compound was designed (by Melissa D'Ascenzio) to overcome this. However, this molecule was not stable and degraded as soon as it was produced.

The crystal structures of TREK-2 with both BF-1 and BF-3 demonstrate non-equal occupancy in the binding sites through the differing significance levels of the anomalous peaks. As it is observed for both dimers within the asymmetric unit (which have different crystal contacts) it suggests that there may be negative co-operatively in binding. Cooperative binding has been demonstrated in many types of ion channels, however further data would need to be collected to confirm its presence in K2Ps.

Fluoxetine derivatives bind to both TREK-1 and TREK-2 and the binding site is likely to be conserved between these highly homologous structures. However, the literature suggests that fluoxetine does not bind to TRAAK[147]. There is no structural evidence of why this may be the case. The crystal structure of TRAAK has been solved in the down state showing fenestrations in which fluoxetine could bind. This TRAAK down state is highly homologous to the TREK-2 down state, particularly within the fluoxetine-binding pocket. This observation has been complemented with electrophysiological data (Conor McClenaghan, personal communication) suggesting that norfluoxetine does indeed inhibit TRAAK.

2.3.2 Insight into K2P gating mechanisms

These data provide functional insights into the existing TREK-2 structures. Apo TREK-2 has been crystallised in two states: up and down. These states were also observed in other K2Ps including TRAAK (published at the same time as the work presented here). The

binding site for the TREK-2 inhibitor fluoxetine is only present in the down state of the channel. It is therefore proposed that fluoxetine inhibits TREK-2 by stabilising a low conductivity down state of the protein. This is in agreement with the finding that the down state of TREK-2 has just three potassium ions within the selectivity filter. There is however no indication of how the movement of the M2, 3 and 4 helices is linked to gating within the filter.

These observations can be combined to propose a state-diagram for K2P channel gating (Figure 2-25). The channel can convert between the up (blue) and down (orange) states, and inhibitors such as norfluoxetine (red ligand) promote the down state of the channel. In TREK-2, crystal structures demonstrate that the down state can be less conductive, i.e. have a lower activity, than the upstate. However, as the filter may also gate independently of helical movement, it is possible that the lower activity up state and higher activity down state may exist. These states would be consistent with observations in TRAAK that a down state structure (4WFE) can have all four filter potassium sites occupied (a higher activity down state).

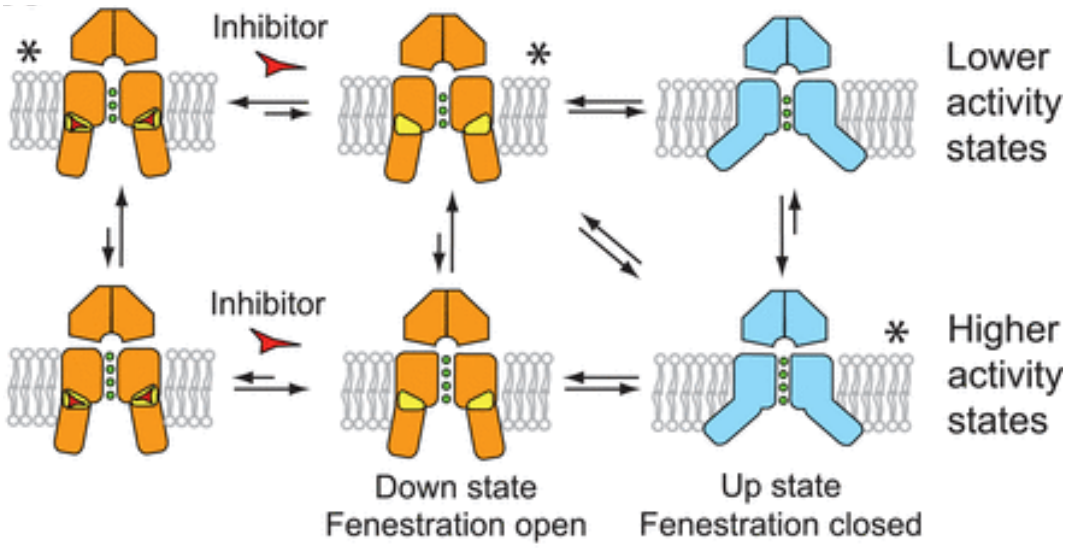

Figure 2-25 Gating model for K2P channels
Figure adapted from Dong *et. al*[75]. Reproduced with permission from AAAS.

This proposed common mechanism for the gating of K2Ps is corroborated by electrophysiological evidence. When activated by stretch or Arachidonic Acid, TREK-2 displays a reduced sensitivity to norfluoxetine. The activated channel is therefore likely to be in the up state. This is consistent with the finding that the TREK-2 up state has four potassium ions within the selectivity filter.

This data also suggests how molecules that interact with the C-terminal regulatory domain (CTD) may influence channel gating. Molecules that interact with this domain are thought to lead to channel gating through coordinated association and dissociation of this domain with the inner leaflet of the membrane. As this domain is attached directly to M4, this movement would lead to movement in the transmembrane helices and thus channel gating.

2.3.3 Integration with recently published work on K2P Channel gating

After the data presented in this chapter were analysed and the Dong *et al.*[75] paper in which these results were included was submitted (August 2014, co-authored by me), two further papers were published on the gating mechanisms of K2P channels. These papers suggest two competing theories on the functional relevance of the K2P channel up and down state. Below I will describe the major results of these two papers and demonstrate how the gating model presented in this work can reconcile the apparently disparate results.

The first paper, published by Brohawn *et al.*[76] on 4th December 2014, suggests that the down state of TREK-2 is a low conductivity state while the upstate is a higher conductivity state. The authors engineered a disulphide bond into TRAAK to hold M4 and M2 together (I159C, R284C), and prevent the fenestration from opening. They found that this mutant had increased current, and therefore verified that the up (fenestration closed) state was the conductive state. This is in agreement with the model presented in this thesis.

Brohawn *et al.*[76] suggest that downward movement of the M4 helix helical may lead to reduced conductivity by allowing lipids to block ion flow. The lipid may enter through the fenestrations of the down state and physically inhibit ion flow by obstructing binding to the cavity site. This is supported by the presence of elongated lipid-like density that is present when the fenestrations are open (down state). Elongated electron density has been observed in down state crystal structures of TWIK-1, TRAAK and TREK-2, and has been modelled as lipid in most of these structures. However, definitive evidence of the molecular source of this electron density is lacking. Furthermore, it has been suggested that lipid molecules within the cell membrane would not be long enough to reach in to the fenestrations to cause an obstruction.

The second paper, published by Lolicato *et al.*[77] on the 17th December 2014, suggests that the down state may instead by the functionally active state, while the up state has lower conductivity. Lolicato *et al.* solved the crystal structures of two TRAAK mutants (G124I and W262S) designed to investigate the interaction between M4 and the pore helix[77]. G124I lies in the part of the P1 pore helix that contacts M4. W262S lies in the side of M4 that interacts with P1. Both mutations are activatory. While these mutations have only minimal structural affects on the proximal regions of the channel, they appear to affect the conformation of the distal intracellular region M4. In both mutants M4 appears straighter than in previous TRAAK structures, due to movement around the Gly^{148} hinge point. The M4 shift observed in these mutants was large (23-27° compared with TRAAK) and lead to a ~8.3Å shift in the C-terminus of M4. The helix also twisted counter-clockwise slightly (when viewed from N-terminus). Activatory mutations in the pore-region of the channel are therefore linked to movements in the intracellular part of M4.

This suggests a mechanism by which movement of the C-terminus of M4 can be linked to channel gating. However, functionally this result disagrees with those of Dong *et al.*[75] and Brohawn *et al.*[76], since it suggests that straightening and un-bending of TM4 leads to channel activation rather than channel inhibition.

The gating mechanism proposed in this thesis (Figure 2-25) reconciles both of these apparently disparate results. Agreeing with the findings of Brohawn *et al.*[76] this data suggests that the down state is the lower conductivity of the two states. However, since it may be possible for the selectivity filter to gate via C-type filter gating independently of helical movement, activatory mutations made close to the selectivity filter would not necessarily impose a constraint on movement on M4. This would allow the down state to exist in an activated channel.

2.4 Conclusions

The results presented here demonstrate that the binding site of two fluoxetine derivatives (brominated fluoxetine and norfluoxetine) is within the fenestrations of a down state channel. Since fluoxetine is a state-dependent inhibitor, this results in a reduced conductivity channel with the S1 potassium site unoccupied. In contrast the higher activity up state of the channel has four potassium sites while the fenestrations are closed, occluding the inhibitor binding site.

When combined with data from other TREK-2 structures, this allows formation of a gating model for K2P channels. In this model, downwards movement of M4 and the outwards movement of M2/3 result in a lower conductivity state that can be stabilised by inhibitors. However, the filter may also gate independently of helical movement resulting in a low conductivity up state. The data presented here do not provide an indication of how helical movements are linked to gating.

2.5 Methods

2.5.1 Purification of TREK-2 protein

TREK-2 protein was purified as described by Dong *et al.*[75]. TREK-2 (KCNK10C) was cloned from the Mammalian Gene Collection (MGC:104160, IMAGE: 30915621, BC075021) and truncated on the N and C termini to contain residues Gly^{67} to Glu^{340}. On the C-terminus of the protein, a Tobacco Etch Virus cleavage site preceded a 10-Histidine and FLAG tag for purification. The resulting construct was cloned into a DH10Bac E.*Coli* and transfected into sf9 insect cells to produce baculovirus. After two rounds of amplification, the virus was used to infect sf9 cells in sf900II (Life Technologies) media for protein production (5mls virus per 1L of 4 x 10^6 cells/ml). After 65 hours incubation, the cells were harvested at 900g for 15 minutes and washed with phosphate buffered saline.

	Cell Re-suspension Buffer (CRB)	Cell Re-suspension Buffer + Protease Inhibitors (CRB +PI)	Wash Buffer (WB)	Elution Buffer (EB)	Gel Filtration Buffer (GFB)
Imidazole	5mM	5mM	25mM	250mM	-
HEPES pH 7.5	50mM	50mM	50mM	50mM	20mM
Potassium Chloride	200mM	200mM	200mM	200mM	200mM
Octyl Glucose Neopentyl Glycol (OGNG)	0.18% w/v	-	0.18% w/v	0.18% w/v	0.12% w/v
Cholesterol Hemi-Succinate (CHS)	0.018% w/v	-	0.018% w/v	0.018% w/v	0.012% w/v
Protease Inhibitors (Roche)	-	1 Tablet per 50ml	-	-	-

Table 2-12 Buffers used in the purification of TREK-2
The critical micelle concentration of OGNG is ~0.06% w/v. Purification is carried out with 3x CMC, and 2x CMC is used in the gel filtration buffer to reduce the detergent concentration present in crystallisation.

The cells were then re-suspended in 50ml CRB+PI per litre of cell culture. Cells were lysed with two passes through a C5 EmulsFlex homogeniser (Aventis) cooled to 4 °C. The remainder of protein purification was carried out at 4 °C. Octyl Glucose Neopentyl Glycol (OGNG) was added to the lysate at 1%, along with 0.1% Cholesterol Hemi-succinate (CHS, Sigma). The protein was solubilised in the detergent by rotation for one hour. Cell debris were removed by centrifugation at 35, 000g for one hour.

Solubilised protein was purified by metal affinity chromatography using the histidine tag. 1ml of a slurry of 50% TALON Co^{2+} resin (Clontech), pre-equilibrated with CRB buffer, was added to the sample for each litre of cell culture. The sample was rotated for 1 hour to allow the histidine Tag to bind the TALON. The TALON was then collected on a chromatography column (Crystal Cruz, Santa Cruz Biotechnology) and washed with 10 column volumes of wash buffer (WB) before being eluted with EB containing 500mM imidazole, to displace the protein from the column. The sample was then desalted using a PD10 column into CRB. PNGaseF (His-tagged) was added at a 1:10 w/w enzyme: protein ratio to remove glycosylation from the protein. TEV protease (His-tagged) was also added at the same ratio to cleave the protein tag. The protein was incubated overnight.

A reverse TALON purification was used to remove remaining protein contaminants and His-tagged enzymes from the protein sample. 1ml of a slurry of 50% TALON, pre-equilibrated with CRB buffer, was added to the sample per 5mg of protein recorded using 280nm absorbance. The sample was rotated for one hour. TALON was collected on a column and washed with one column volume of CRB to ensure all protein was collected in the flow through. The sample was concentrated using a 30kDa cut off PES concentrator (Vivaspin) to around 10mg/ml and centrifuged at 20,000g for 20 minutes to remove precipitate.

Size exclusion chromatography was then carried out to separate protein species. A Superose 6 10/300 GL column (GE Healthcare) was equilibrated with 50ml of GFB. Sample was loaded onto the column and eluted over 1.5 column volumes. The peaks corresponding to TREK-2 dimer were combined and concentrated to 10-20mg/ml before being flash frozen in liquid nitrogen.

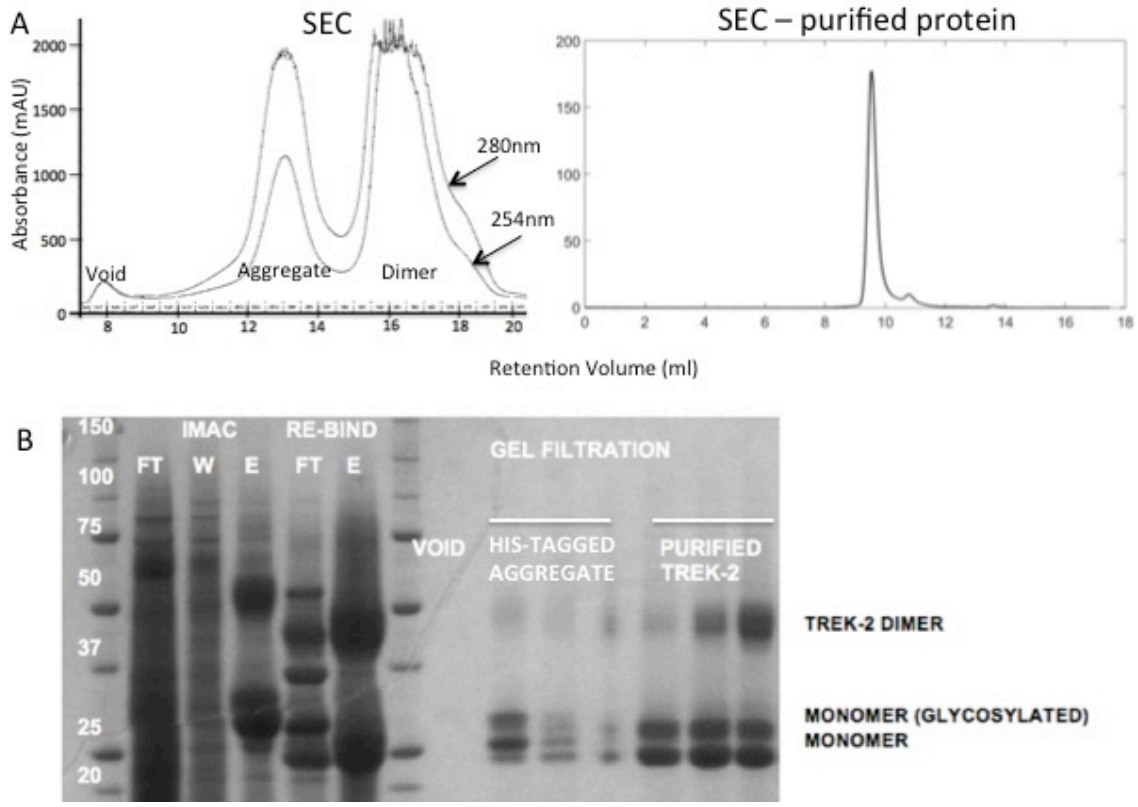

Figure 2-26 Purification of TREK-2

A) SEC profiles of TREK-2 protein during purification (left, Superose-6 10/300 column), and after purification (Shodex HPLC 15ml column) B) Coomassie stained reducing SDS PAGE gel. Standard is shown in kDa. TALON flow through (FT) and elute (E) are shown for the first (IMAC) and second (REBIND) metal affinity chromatography columns. Purified TREK-2 protein has a dimer band and two monomer bands corresponding to protein with and without glycosylation, indicating that PNGaseF did not effectively remove all glycosylation.

2.5.2 Co-crystallisation of TREK-2 in vapour diffusion

Stock solution of compounds was made at 50-100mM in solvent (Ethanol, DMSO, Gel Filtration Buffer or de-ionised water). Compound was added to 10-11mg/ml protein to give a final concentration between 1-10mM and the sample was incubated for ~ 3 hours at 4 °C before crystallisation screening.

Crystallisation screens were made using an MPII liquid handling robot. Sitting drop vapour diffusion crystallisation trials were set up using a Mosquito crystallisation robot (TTP Labtech) into 96x3 well plates (SwissCI). The 3 wells contained 200nl droplets set up at 2:1,1:1 and 1:2 protein: crystallisation solution ratios. Plates were sealed and placed into a Minstrel imaging incubator at 4 °C and inspected over six weeks for crystal growth. Most crystals grew in 1-2 weeks.

	KCNK10C-SUPER-z001	2	3	4	5	6	7	8	9	10	11	12
A	0.1M HEPES pH 7 0.1M AmForm 15% PEE 15/4 0.001M CDCL	0.1M HEPES pH 7 0.1M AmForm 17% PEE 15/4 0.001M CDCL	0.1M HEPES pH 7 0.1M AmForm 19% PEE 15/4 0.001M CDCL	0.1M HEPES pH 7 0.1M AmForm 21% PEE 15/4 0.001M CDCL	0.1M HEPES pH 7 0.1M AmForm 23% PEE 15/4 0.001M CDCL	0.1M HEPES pH 7 0.1M AmForm 25% PEE 15/4 0.001M CDCL	0.1M HEPES pH 7 0.1M AmForm 27% PEE 15/4 0.001M CDCL	0.1M HEPES pH 7 0.1M AmForm 29% PEE 15/4 0.001M CDCL	0.1M HEPES pH 7 0.1M AmForm 31% PEE 15/4 0.001M CDCL	0.1M HEPES pH 7 0.1M AmForm 33% PEE 15/4 0.001M CDCL	0.1M HEPES pH 7 0.1M AmForm 35% PEE 15/4 0.001M CDCL	0.1M HEPES pH 7 0.1M AmForm 37% PEE 15/4 0.001M CDCL
B	0.1M HEPES pH 7 0.1M AmForm 15% PEE 15/4	0.1M HEPES pH 7 0.1M AmForm 17% PEE 15/4	0.1M HEPES pH 7 0.1M AmForm 19% PEE 15/4	0.1M HEPES pH 7 0.1M AmForm 21% PEE 15/4	0.1M HEPES pH 7 0.1M AmForm 23% PEE 15/4	0.1M HEPES pH 7 0.1M AmForm 25% PEE 15/4	0.1M HEPES pH 7 0.1M AmForm 27% PEE 15/4	0.1M HEPES pH 7 0.1M AmForm 29% PEE 15/4	0.1M HEPES pH 7 0.1M AmForm 31% PEE 15/4	0.1M HEPES pH 7 0.1M AmForm 33% PEE 15/4	0.1M HEPES pH 7 0.1M AmForm 35% PEE 15/4	0.1M HEPES pH 7 0.1M AmForm 37% PEE 15/4
C	0.1M tris pH 7.5 0.001M CDCL 23% PEG400	0.1M tris pH 7.5 0.001M CDCL 24% PEG400	0.1M tris pH 7.5 0.001M CDCL 25% PEG400	0.1M tris pH 7.5 0.001M CDCL 26% PEG400	0.1M tris pH 7.5 0.001M CDCL 27% PEG400	0.1M tris pH 7.5 0.001M CDCL 28% PEG400	0.1M tris pH 7.5 0.001M CDCL 29% PEG400	0.1M tris pH 7.5 0.001M CDCL 30% PEG400	0.1M tris pH 7.5 0.001M CDCL 31% PEG400	0.1M tris pH 7.5 0.001M CDCL 32% PEG400	0.1M tris pH 7.5 0.001M CDCL 33% PEG400	0.1M tris pH 7.5 0.001M CDCL 34% PEG400
D	0.1M MES pH 6.5 0.05M MgCl 0.001M CDCL 12% PEGm500	0.1M MES pH 6.5 0.05M MgCl 0.001M CDCL 15% PEGm500	0.1M MES pH 6.5 0.05M MgCl 0.001M CDCL 18% PEGm500	0.1M MES pH 6.5 0.05M MgCl 0.001M CDCL 21% PEGm500	0.1M MES pH 6.5 0.05M MgCl 0.001M CDCL 24% PEGm500	0.1M MES pH 6.5 0.05M MgCl 0.001M CDCL 27% PEGm500	0.1M MES pH 6.5 0.001M CDCL 12% PEGm500	0.1M MES pH 6.5 0.001M CDCL 15% PEGm500	0.1M MES pH 6.5 0.001M CDCL 18% PEGm500	0.1M MES pH 6.5 0.001M CDCL 21% PEGm500	0.1M MES pH 6.5 0.001M CDCL 24% PEGm500	0.1M MES pH 6.5 0.001M CDCL 27% PEGm500
E	0.1M MES pH 6.5 0.05M MgCl 0.001M CDCL 12% PEGm350	0.1M MES pH 6.5 0.05M MgCl 0.001M CDCL 15% PEGm350	0.1M MES pH 6.5 0.05M MgCl 0.001M CDCL 18% PEGm350	0.1M MES pH 6.5 0.05M MgCl 0.001M CDCL 21% PEGm350	0.1M MES pH 6.5 0.05M MgCl 0.001M CDCL 24% PEGm350	0.1M MES pH 6.5 0.05M MgCl 0.001M CDCL 27% PEGm350	0.1M MES pH 6.5 0.001M CDCL 12% PEGm350	0.1M MES pH 6.5 0.001M CDCL 15% PEGm350	0.1M MES pH 6.5 0.001M CDCL 18% PEGm350	0.1M MES pH 6.5 0.001M CDCL 21% PEGm350	0.1M MES pH 6.5 0.001M CDCL 24% PEGm350	0.1M MES pH 6.5 0.001M CDCL 27% PEGm350
F	0.1M cacodylate pH 0.001M CDCL 10% PEG1.5K	0.1M cacodylate pH 0.001M CDCL 14% PEG1.5K	0.1M cacodylate pH 0.001M CDCL 18% PEG1.5K	0.1M cacodylate pH 0.001M CDCL 20% PEG1.5K	0.1M cacodylate pH 0.001M CDCL 22% PEG1.5K	0.1M cacodylate pH 0.001M CDCL 24% PEG1.5K	0.1M cacodylate pH 0.001M CDCL 10% PEG1.5K	0.1M cacodylate pH 14% PEG1.5K	0.1M cacodylate pH 18% PEG1.5K	0.1M cacodylate pH 20% PEG1.5K	0.1M cacodylate pH 22% PEG1.5K	0.1M cacodylate pH 24% PEG1.5K
G	0.1M tris pH 8 15% PEGm350	0.1M tris pH 8 17% PEGm350	0.1M tris pH 8 20% PEGm350	0.1M tris pH 8 22% PEGm350	0.1M tris pH 8 25% PEGm350	0.1M tris pH 8 27% PEGm350	0.1M tris pH 8 15% PEGm500	0.1M tris pH 8 17% PEGm500	0.1M tris pH 8 20% PEGm500	0.1M tris pH 8 22% PEGm500	0.1M tris pH 8 25% PEGm500	0.1M tris pH 8 27% PEGm500
H	0.1M tris pH 8 0.002M ZnSO 10% JEF2003	0.1M tris pH 8 0.002M ZnSO 14% JEF2003	0.1M tris pH 8 0.002M ZnSO 18% JEF2003	0.1M tris pH 8 0.002M ZnSO 22% JEF2003	0.1M tris pH 8 0.002M ZnSO 26% JEF2003	0.1M tris pH 8 0.002M ZnSO 28% JEF2003	0M HEPES pH 7 0.002M ZnSO 10% JEF2003	0M HEPES pH 7 0.002M ZnSO 14% JEF2003	0M HEPES pH 7 0.002M ZnSO 18% JEF2003	0M HEPES pH 7 0.002M ZnSO 22% JEF2003	0M HEPES pH 7 0.002M ZnSO 26% JEF2003	0M HEPES pH 7 0.002M ZnSO 28% JEF2003

Figure 2-27 KCNK10C-SUPER screen design

This screen was designed to replicate known crystallisation conditions of TREK-2.

2.5.3 Seeding

Plate morphology crystals were harvested from conditions containing 0.1M MES pH6.5; 1mM $CdCl_2$; 50mM $MgCl_2$; 20% PEE 15/4 and stabilised in solution containing an additional 15% PEE 15/4; 0.2% OGNG; 0.02% CHS; 0.2M KCl. They were then vortexed for 2 seconds followed by ten seconds on ice to prevent heating. This process was repeated for 5 minutes to produce a seed stock. This stock was then diluted in series to 1:50, 1:100, 1:500 and 1:1000 in the stabilising solution. 20nL of these seeds were added to the 96 well CI pates containing 150nL sitting drops with 2:1 protein: crystallisation solution ratios. The final drop volume was 170nl.

2.5.4 Data Collection

Data were collected at the Diamond Light Source synchrotron beam line I24. Fluorescence scans were run to determine the fluorescence emission edge for the bromine. CHOOCH[148] was then used to estimate the anomalous scattering factors. Collection wavelengths were selected that maximised anomalous differences in Friedel Pairs, while being sufficiently far from the absorption edge that small fluctuations in beam wavelength would not cause loss of anomalous signal.

Data collection strategies were guided by iMOSFLM[149]. A set of three test images taken 45 degree apart were used to index the data and to suggest parameters for data collection. For standard datasets, rotation angles were selected to give a minimum multiplicity of 3. For anomalous data, parameters were selected to give anomalous multiplicity of 3. The total dose was selected based on a test used to determine the onset of radiation damage in a typical crystal.

For anomalous data, two types of dataset were collected. Very high multiplicity but low dose datasets aimed to produce accurate anomalous differences without radiation damage to the

carbon-bromine bond within the compound. High dose datasets allowed collection of higher resolution reflections, however may have lead to radiation damage of the compound.

2.5.5 Structure Determination

Building of low-resolution datasets is time consuming, so it was necessary to screen for datasets that contained bromine anomalous signal. Auto processed data from the XIA-2[150] pipeline run at Diamond was phased using PHASER-MR[151]. CAD[152] was used to append these phases onto the auto-reduced data, and this was Fourier transformed in FFT[152] to produce an anomalous map. Presence of cadmium peaks within the helical cap domains acted as positive controls for map generation. If further anomalous peaks were present, the data set was selected for further processing.

In order to ensure optimal data processing, all data were re-processed using the XIA-2 pipeline. Data were processed at several resolutions to determine the data resolution. The variance of R_{merge} with image number was used to reject bad image frames and radiation damage. XIA-2 was run using XDS[153] for data reduction. Indexing was found to be more successful when using all images. The point group was selected by Pointless and data were merged with constant scales using Aimless. $CC_{1/2}$ and $I/\sigma > 2$ values[154] were used to determine resolution cut offs. As the data were anisotropic, the highest resolution crystallographic direction was used to determine the resolution cut-off for the data. C-truncate[152,155] was run before R-free flags (5%) were generated. For the orthorhombic space group, the R-free flags of the first dataset (BF-1, 4XDL) were used for later datasets.

It was observed that F^+ and F^- were reduced to F within C-truncate. For datasets where anomalous signal was important, it was necessary to stop this from happening. Therefore the XIA-2 AIMLESS[152,154] output (scaled and merged.mtz) was manually run through C-TRUNCATE (specifying to separate Friedel Pairs), and R-free flags were added using CAD.

For all datasets, PHASER molecular replacement was used to phase the structure. The search models used were 4BW5, 4XDJ and a TREK-2 model with M4 deleted from the hinge Gly^{312} onwards (based on 4BW5) were independently used as search models. Matthew's coefficient analysis using the CCP4 program Matthews[156] was used to determine the number of molecules to search for in the asymmetric unit. To reduce the effect of model bias, prime and switch[120] (PHENIX[157]) maps were calculated using the PHASER output results. These maps clearly showed that all of the structures determined here were in the down state.

Model building proceeded in coot[158]. The maps used for building were PHASER σ_A-weighted $2F_o$-F_c and F_o-F_c, prime and switch (both poly-Alanine and full models) and B-factor sharpened PHASER maps. Rigid body refinement of segments of M2, M3 and M4 were used to correctly position the alpha helical backbone into the density. Side chains for which there was no density, or for which the side chain rotamer was not clear, were removed. Parts of the molecule for which poor density existed (for example the M3-P2 loops) were removed from the model. The model was then refined using BUSTER[159] with TLS restraints by chain.

Subsequent rounds of refinement utilised BUSTER maps in lieu of PHASER maps for model building. PHENIX RESOLVE[119] was used to generate density modified averaged BUSTER maps that were also used for model building. Protein side chains and backbone were built into un-modelled electron density using coot. The resulting model was re-refined in BUSTER, for further model building/ refinement cycles.

The model building was considered finished when R_{work}/R_{free} factors stabilised, all modelable electron density was accounted for, and the structure agreed with geometric constraints (assessed by MolProbity[160]).

	4XDL (deposited)	BF-3
Data Collection		
Space Group	$P2_12_12_1$	$P2_12_12_1$
Unit cell dimensions *a*, *b*, *c* (Å)	101.71, 109.84, 166.74	103.90, 108.6,0 171.23
α, β, γ (o)	90, 90, 90	90, 90, 90
Resolution [Å]	3.5 (3.50-3.59)[1]	3.5 (3.5-3.63)[1]
Resolution limits [Å][2]	3.55, 3.5 ,3.91 (3.50,3.50,3.82) [2]	3.50, 3.65, 3.93 (3.50, 2.50, 3.87)[2]
Nominal Resolution [Å][3]	3.64	3.63
Total reflections	275680	331788
Unique reflections	24216	24998
Redundancy	11.4 (11.2) [1]	13.3 (13.3)[1]
Completeness [%]	99.9 (100) [1]	99.9 (99.9)[1]
*R*meas	0.097 (1.934) [1]	0.104 (2.185)[1]
$CC_{1/2}$	0.999 (0.553) [1]	1.000 (0.601)[1]
$I / \sigma I$	7.5 (1.5) [1]	16.36 (1.53)[1]
Refinement		
Resolution (Å)	35-3.50	40-3.5
No. reflections (free)	24155 (1217)	24998 (1259)
*R*work / *R*free	23.52 / 26.33	26.21 / 28.53
No. atoms		
Protein	7474	6247
Other	92	53
B-factors (Å^2)		
Protein	157	146
Other	169	133.80
R.m.s. deviations		
Bond lengths (Å)	0.009	0.020
Bond angles (°)	0.93	1.70

1. Values in brackets for the highest resolution shell
2. Resolution limits (h,k,l) for Mean $I / \sigma I > 2$; *in brackets are values for* $CC_{1/2} > 0.5$

Nominal resolution is where mean $I / \sigma I > 2$ *for the whole dataset (including all directions)*

Table 2-13 Dataset statistics for 4XDL and BF-3

2.5.6 Ligand Modelling

In order to ensure that the ligand density was as clear as possible, ligand modelling did not begin until a model of the protein had been completed. Geometric constraint dictionaries (.cif files) were generated using the GRADE webserver[161]. Fused planes were used to ensure aromatic rings were kept planar during refinement. Dictionaries were generated separately for the R and S enantiomers of the ligands. Ligand building strategies differed for ligands with (BF1) and without (Norfluoxetine) attached Bromines.

Brominated Ligands: BF-1

For BF-1, the location of the bromine peak was used as an anchor point to begin building the ligand. Phases from the refined protein model were used to generate more accurate anomalous density maps. The resulting peaks were used to guide ligand modelling.

BF-1 was initially built into the density next to Phe^{316}, as this density was the best out of all the fenestrations. BUSTER and PHENIX RESOLVE maps were used for ligand modelling. The methyl fluorinated ring of the ligand, which was covalently attached to the bromine, could be positioned in just one way within the density. The rest of the ligand could be placed in one of two poses; both of these were refined. The best pose was decided based on fit to density, protein clashes and geometric constraints. As the position of the aliphatic chain and pendant phenyl ring could not be uniquely defined, 4XDL was deposited with only the methyl-fluorinated ring built.

Norfluoxetine

This ligand had no anchor point, so there were 6 possible poses in which the ligand could be modelled into the density. All six poses were modelled into BUSTER and PHENIX RESOLVE electron density maps. Poses were ranked based on their fit to density, clashes with the protein, bonds formed and geometric constraints. While the methyl-fluorinated ring stacked with Phe^{216}, the location of the other parts of the molecule differed between the R and S enantiomers. Dual refinement with occupancy of 0.5 for each enantiomer was therefore carried out.

2.5.7 Mass Spectrometry

Intact mass spectrometry was used to assess whether ligands could covalently bind to TREK-2. The ligand CovF was dissolved to 50mM in both GFB and Methanol. This was added to 300µL 1mg/ml TREK-2 protein at a molar ratio of 5:1 (~800µM). At each time step (0,0.25, 0.5, 1, 3 and 8 hours), 50µL of sample was removed and TCEP was added to 1mM

to prevent further reaction. Each sample was run on a Agilent 6530 QTOF mass spectrometer with an in-line C18 Chromolith column.

Data were analysed using Quantitative Analysis software (Mass Hunter). Sections of the chromatogram corresponding to protein were de-convoluted between 1500-3000 m/z and mass of 18-80kDa. Signal to noise cut offs were reduced to a ratio of 3 to increase detection sensitivity.

2.5.8 CPM Dye Assay

Protein was diluted to 1mg/ml wit GFB. Fluoxetine was diluted to each of the 8 required the required assay concentrations (0-200μM) using GF. For each compound concentration, 95μL of fluoxetine solution was added to 11μL of 1mg/ml protein to give the final assay concentration of 0.1mg/ml TREK-2. This gave a total volume of 106μL solution per compound concentration; enough volume for four repeats for each concentration (25μL required per data point). This was mixed with the pipette, and incubated on ice for 1 hour to allow the compound to bind.

A 4mg/ml CPM dye stock was made in DMSO, and this was diluted 1:200 in GFB. 10μL of diluted CPM dye was then added to each well and mixed thoroughly. The solutions were then pipetted out into a 96-well plate (Thermo Scientific AB-0700 PCR plates) as shown in Table 2-14.

	Columns 1-4 Fluoxetine + TREK-2	Columns 5-8 Compound only controls	Columns 9-12 Positive Controls (TREK-2 + 100uM Norfluoxetine)
A	1uM	1uM	
B	2uM	2uM	
C	5uM	5uM	
D	10uM	10uM	
E	20uM	20uM	
F	50uM	50uM	
G	100uM	100uM	
H	0uM (control)	0uM (control)	

Table 2-14 Layout of a CPM-dye assay plate

The assay was performed with an Agilent Mx3005P Quantitative PCR system with a fluorescence detector and ANS filter set. The temperature of the plate was raised from 25°C to 95°C (1°C per minute) and the resulting fluorescence recorded with MxPro MX3005P Version 4.10 (Stratagene) software.

Data were processed as follows. The background signal (CPM dye and compound without protein, columns 5-8 in Table 2-14) was subtracted from all measurements. The data were then imported into Graph Pad Prism 6.0. The melting curves were fitted with Boltzmann Sigmoidal distributions to extract melting temperatures (equal to the temperature of the half-maximal response). Average values were taken over the four triplicates to determine the average melting temperatures for each compound concentration.

Chapter 3 Co-crystallisation of TREK-2 with activators

3.1 Introduction

3.1.1 Mechanism of activation in TREK

TREK-2 is a polymodal channel activated by a broad range of stimuli including stretch, acidification, volatile anaesthetics, poly-unsaturated fatty acids (PUFAs) and small molecule pharmacological agents such as Riluzole. Based on the state diagram presented in Chapter 3, there are three structural mechanisms through which TREK channels could be activated (Figure 3-1):

A. Stabilisation of the up state of the protein. This state is thought to have higher activity due to the presence of 4 K^+ ions within the selectivity filter. Stabilising this state may therefore activate the channel. This corresponds to structure A on the state diagram.

B. Modification of the down state to from an activated down state. For example an activator may bind in the same site as fluoxetine, but lead to a different affect on the selectivity filter. This corresponds to structure B on the state diagram.

C. A novel high-activity state that has not yet been observed with crystallography. This may involve different movements of the helices, or interactions with the cap domain. It may be completely independent of helix movement. This structure is not yet on the state diagram.

Electrophysiological recordings on TREK-2 channels provide evidence for structural mechanism A. In these experiments, channels were first activated using Arachidonic Acid (AA) or stretch. The state dependant inhibitor norfluoxetine[131] was then applied to the

activated channels. It was found that the activated channels were less sensitive to this inhibitor. In an inverse experiment, norfluoxetine inhibited channels displayed slowed activation by stretch or AA[75]. The up state of the protein may be stabilised, burying the norfluoxetine binding site and thus preventing channel inhibition.

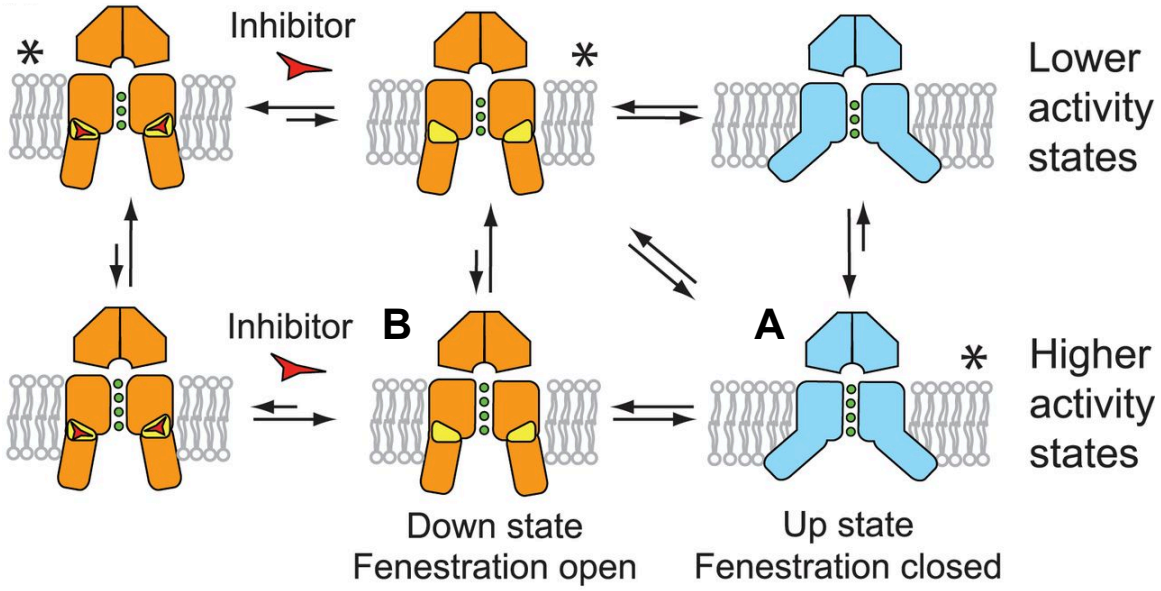

Figure 3-1 The possible structural states of an activated TREK channel
TREK-2 may be activated by C-type gating independent of the state of the helices. Otherwise, it may bind and stabilise the up state (A), or bind to the down state and modify it to become high conductivity (B). Figure from Dong *et al.* 2015[75]. Reproduced with permission from the AAAS.

However, it is unlikely that all TREK channel activators work through the same mechanism. For example channels activated by intracellular acidification do not display reduced sensitivity to norfluoxetine inhibition. This indicates that intracellular pH does not activate the channel through the same mechanism as stretch or AA[75]. The channel may instead be activated through alternative structural mechanisms (C). Finally, it may be possible that small modifications to the structure of fluoxetine may cause it to activate the channel. Since small modifications in ligand structure are unlikely to cause it to bind at a different site, activation may be due to more subtle changes in the protein structure (mechanism B).

The aim of this chapter is to determine the structure of TREK-2 in an activated state through vapour-diffusion crystallisation. In this chapter the focus is on small-molecule activation of TREK-2, since stretch activation would be difficult to achieve in crystals. In particular BL-

1249 is focused on, as it is a relatively high affinity TREK channel activator. An activator-TREK-2 complex would determine the binding site to allow for structure based activator design, as well as informing on how small molecule binding structurally couples to channel activation.

3.1.2 BL-1249 and TREK Channels

BL-1249 ((5,6,7,8-Tetrahydro-naphthalen-1-yl)-[2-(1H-tetrazol-5-yl)-phenyl]-amine) is a small molecule activator of TREK channels[162]. It was discovered by Bristol-Myers Squibb Pharmaceuticals as a potassium channel probe. It belongs to a class of clinically used compounds called fenamates that includes Flufenamic Acid (FFA) Niflumic Acid (NFA), Mefanamic Acid (MA) and Diclofenac (Figure 3-2). While most fenamates activate TREK channels[126], BL-1249 has the highest affinity. Indeed, the EC_{50} of the interaction has been measured as 8μM for TREK-1[56] while FFA, NFA and MFA are around 30 times less potent[163] (Figure 3-3).

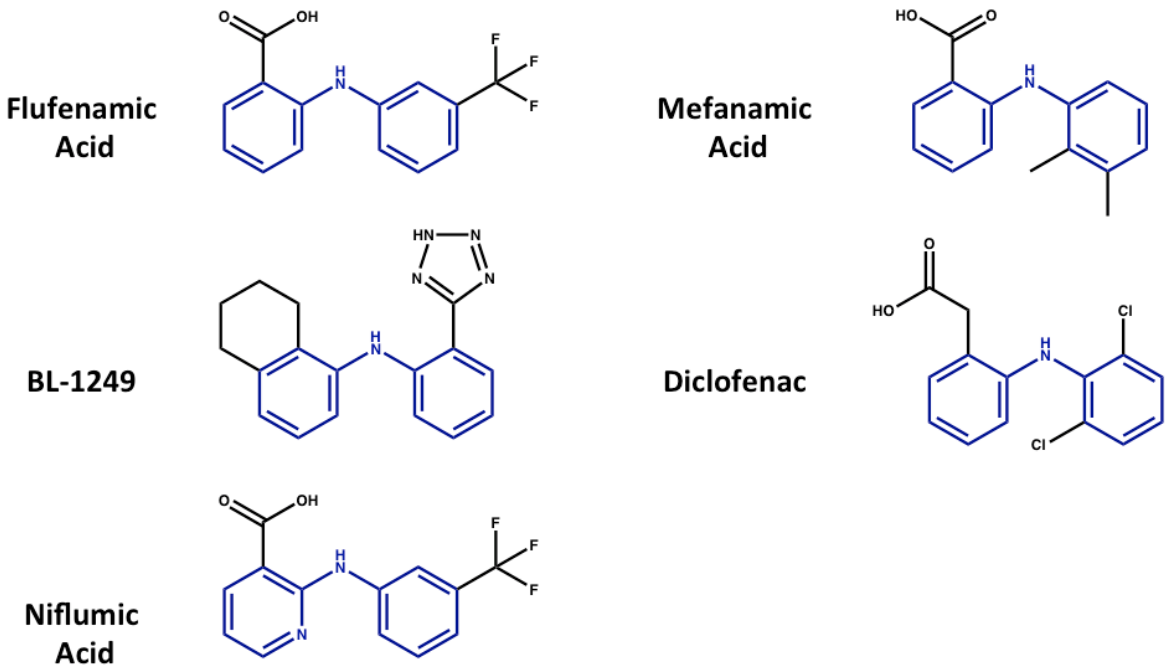

Figure 3-2 Fenamates: a class of TREK channel activators
Fenamates are used clinically as non-steroidal anti-inflammatory drugs. They share a common core structure (blue). BL-1249 was developed as a potassium channel activator, and is around 30 times more potent against TREK-1 than other fenamates.

Although the binding mode of BL-1249 is unknown studies have indicated that the intracellular N-terminus of TREK-1 is not necessary for the response. Indeed the TREK-1 isoform TREK1ΔN, which is missing the first 56 residues of the 61 residue cytoplasmic N-terminus, can be activated by fenamates[163]. Interestingly, activation also markedly increases potassium selectivity. TREK1ΔN is thought to have a collapsed selectivity filter that is sodium permeable under normal conditions[164]. Binding of BL-1249 may therefore influence the conformation of the selectivity filter (C-type gating) to increase potassium selectivity and conduction rates.

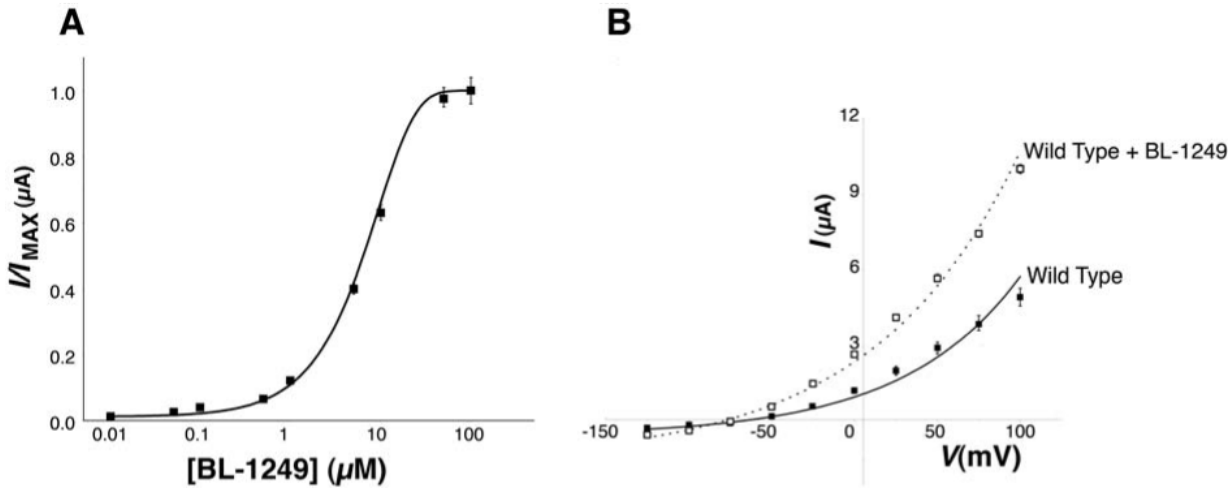

Figure 3-3 Activation of TREK-1 by BL-1249

A dose-response curve (A) determines the EC_{50} of BL-1249 against TREK-1 to be in the region of 8μM. The current voltage relationship (B) also demonstrates activation by BL-1249[56]. Reading taken from whole-cell recordings of *Xenopus* Oocytes injected with TREK-1 mRNA.

3.2 Results

3.2.1 Two-electrode voltage clap of Oocytes expressing TREK-2

Before crystallisation was attempted, two-electrode-voltage-clamp (TEVC) experiments were used to verify that the truncated crystal construct (Gly^{67}-Glu^{340}) is functionally activated by BL-1249. TEVC was carried out on Xenopus Oocytes microinjected with mRNA coding for the human TREK-2 construct (the TEV cleavage site, His-Tag or FLAG-tag were removed for this experiment). A voltage ramp protocol was applied, depolarising the membrane from -120mV to +60mV. The peak current in response to this ramp was

measured. This data was also collected for full length TREK-2, for comparison. Barium chloride (a potassium channel inhibitor[164,165]) was used to further probe the functionality of the crystallisation construct.

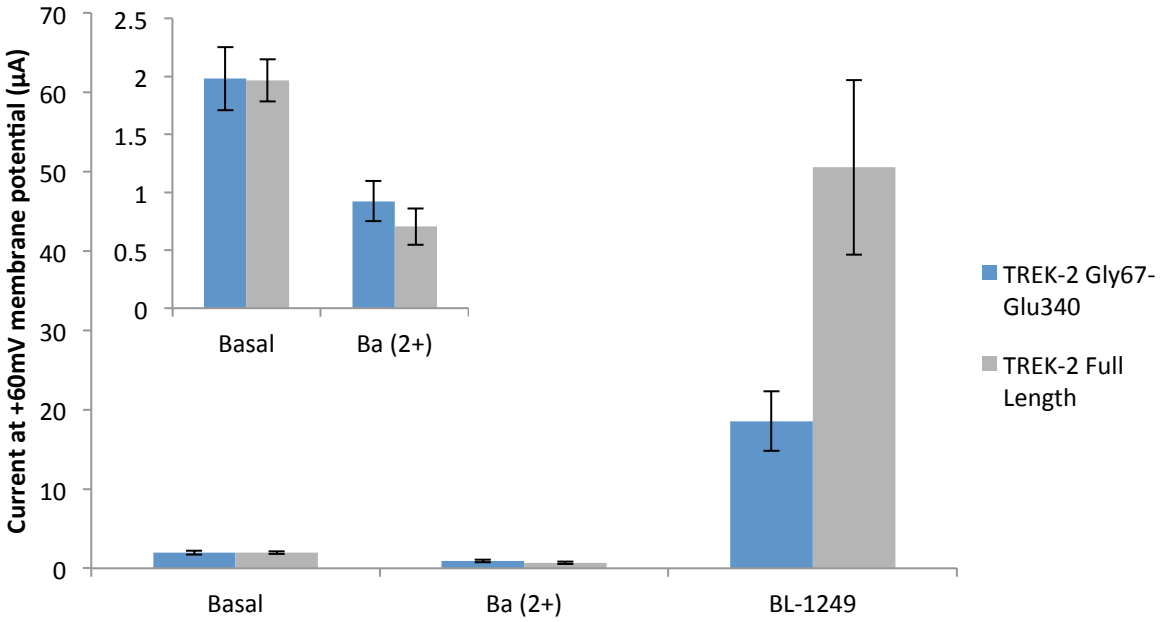

Figure 3-4 Current activation of the TREK-2 crystal construct by BL-1249
TREK-2 was expressed in Xenopus Oocytes by microinjection of cRNA. Currents were measured after a voltage ramp from -120mV to + 60mV and plotted. Oocytes were then exposed to either 10µM Barium or 10µM BL-1249 solution and after equilibration the peak current was measured again. While barium inhibited the channel (inset), BL-1249 robustly activated both the truncated and the full-length protein. Error bars show the standard error of the mean. Readings were taken across three batches of injected Oocytes. From left to right the number of measured oocytes were n = 13, 16, 6, 6, 6, 6.

Oocytes injected with truncated TREK-2 demonstrated basal currents (2.0±0.3µA) comparable with those observed for full-length protein (2.2±0.3µA). These were inhibited by 10mM barium to similar levels (truncated 0.9±0.2µA, 45% inhibition; full-length 0.9±0.1µA, 41% inhibition). While both proteins were activated by BL-1249, the response of the full-length protein was larger than that of the crystal construct (Truncated 18.5±3.7µA, 9 fold activation; Full-length 55.5±11.0µA, 25 fold activation). This is not unexpected due to the severe truncation of the protein. This may be indicative of a reduced EC_{50} against the truncated protein; this would require a dose-response curve to validate. However, BL-1249 is still able to robustly activate the truncated protein. This indicates that the compound binding is not abolished and the binding site has not been removed from the protein.

3.2.2 Co-crystallisation of BL-1249 derivatives and TREK-2

BL-1249 was derivitised with bromine (by David Pryde, Pfizer) to increase the specificity and sensitivity of ligand detection. As it is a relatively weak binder and the binding mode is unknown, compounds were produced with Br atoms in three different locations on the molecule. This means even if no ligand density is visible, the ligand could be modelled based on the locations of the bromine atoms from the anomalous map.

	Derivative	Solubility	Smiles String	Compound Structure
BL-1249	BL-1249 (BL)	ddH_2O 0-1mM Ethanol ≈50mM DMSO ≈100mM	[H]N(c1ccccc1c1nnnn1[H])c1cccc2CCCCc12	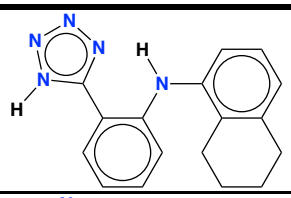
	Br-BL-1249 1 (BrBL-1)	DMSO ≈50mM	C1CCc2c(C1)cccc2Nc1ccc(cc1c1nn[nH]n1)[Br]	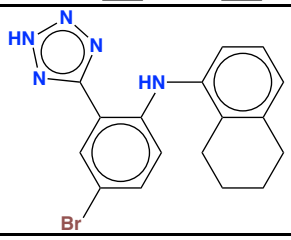
	Br-BL-1249 2 (BrBL-2)	DMSO ≈100mM	C1CCc2c(C1)cccc2Nc1cc(ccc1c1nn[nH]n1)[Br]	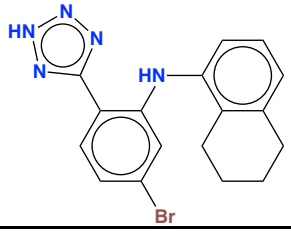
	Br-BL-1249 3 (BrBL-3)	DMSO ≈50mM	C1CCc2c(ccc(c2C1)Nc1ccccc1c1nn[nH]n1)[Br]	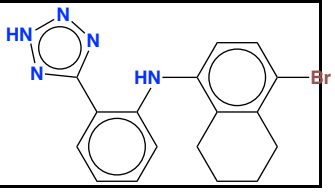

Table 3-1 BL-1249 derivatives used for TREK-2 co-crystallisation

Solubility tests with BL-1249 indicate that it is highly insoluble in water, which agrees with the compound datasheet provide by the supplier. It was soluble to ~ 100mM in DMSO and ~50mM in Ethanol. As only a small mass of compound was manufactured, a single solvent had to be selected for crystallisation testing. CPM dye assays run by another group member (Jackie Ang) indicate that while high concentrations of Ethanol (>5%) destabilised TREK-2, similar concentrations of DMSO did not. Stock solutions of compound were therefore made

in DMSO, as it does not appear to affect protein stability and can solubilise BL-1249 to a higher concentration.

Stock solutions of the compounds BrBL-1, 2 and 3 were prepared in 100% DMSO. While BrBL-2 dissolved to 100mM forming a yellow solution, BrBL-3 dissolved at 50mM to form a clear solution and BrBL-1 dissolved to 50mM forming a yellow solution. This was added to TREK-2 protein (11mg/ml) to give a final DMSO concentration of 5% (2.5mM BrBL-1, 3; 5mM BrBL-2). Vapour diffusion crystallisation was set up at 4 and 20°C using the MemGold core screen and KCNK10C-SUPER screen, containing known crystallisation conditions for TREK-2.

Two conditions produced mountable crystals. The first, MemGold-G03 (0.1M TRIS pH 8.5; 0.1M $MgCl_2$ 0.1M NaCl; 33%(v/v) PEG400) has no crystals in the control plates with apo TREK-2 protein. These crystals have an orthorhombic unit cell that has been previously seen in apo-state TREK-2 crystals. Crystals with this unit cell are generally of TREK-2 in the down state, however optimisation did not yield atomic resolution diffraction for this crystal form. The second condition was derived from MemGold-H11 (0.1M TRIS pH7.5, 1mM $CdCl_2$; 30mM $MgCl_2$; 30%(v/v) PEG400, 1% (w/v) benzamidine hydrochloride). The monoclinic unit cell and symmetry observed for MemGold-H11 corresponded to that of an already determined structure (4BW5). As this structure was solved using the same crystallisation condition it was suspected that these crystals contained up state protein similar to 4BW5.

Lattice	A (Å)	B (Å)	C (Å)	α (°)	β (°)	Y (°)
Orthorhombic	78	114	340	90	90	90
Monoclinic	96	99	106	90	91	90

Table 3-2 Unit cell parameters of TREK-2 co-crystals with a brominated BL-1249 derivative

Crystal optimisation went ahead for the MemGold-H11 condition. In order to optimise compound occupancy, crystallisation trials with higher DMSO concentrations (2.5-12mM

compound; 5-12% DMSO) were attempted. Crystals grew for all concentrations of compound. Some crystals grown at a lower compound concentrations (2.5mM) were soaked for two hours in 7.5mM compound. Higher concentrations or longer soak times reduced diffraction quality.

In order to improve diffraction quality, crystal dehydration was attempted through PEG escalation. Escalation steps of 5% were used to obtain a final concentration of 40% w/v PEG400. Modest cell shrinkage was observed in just one crystal; the observed unit cell volume was $1.04x10^6$ Å^3 compared with ~$1.1x10^6$ Å^3 for other crystals. This crystal also diffracted to a slightly higher resolution of 3.8x5 Å in test images, compared with ~5x6 Å for other crystals. This indicates that dehydration may improve diffraction quality. However, the deposited dataset 4BW5 has a unit cell volume of just $0.88x10^6$ Å^3 indicating that it is possible to shrink the cell further and potentially obtain higher resolution data.

3.2.3 X-ray data collection and processing

Datasets were collected at the DLS synchrotron for two of the three BrBL compounds. The purpose of these datasets was to determine the presence of anomalous peaks, to guide further optimisation. Initially, the Xia-2 pipeline was used for data reduction, and PHASER-MR to phase the structures. Anomalous density maps produced by FFT demonstrated no significant anomalous peaks. However, data reduced by the auto-processing pipeline FAST_DP at Diamond in combination with PHASER-MR and FFT produced a clear peak in the BrBL-2 dataset.

To discover the reason behind this discrepancy, the XDS.INP files were examined for the two processing methods. Xia-2 running in automated mode uses the Friedel's law = TRUE flag as an automatic setting. Xia-2 was also unable to detect anomalous signal in the data (due to weak signal from bromines and the likely low occupancy). In order to overcome this, data were processed manually using XDS, POINTLESS, AIMLESS, C-TRUNCATE,

CAD, PHASER-MR and FFT. The resulting anomalous maps were less noisy and in one dataset (BrBL-2) a peak could be confidently defined. This dataset is therefore discussed further below.

Derivative	Dataset No.	Maximum Resolution (Å)	Lattice	Electron Density		Crystallisation Conditions and Crystal Mounting
				Ligand	Anom	
BrBL-1	d058	3.98 x 5.12 x 6.22	monoclinic	None	Noisy / weak	**Drop**: 31% PEG400; 0.1M TRIS HCl pH 7.5; 1mM $CdCl_2$ **Compound:** 5mM, 5% DMSO **Cryo:** 33% PEG 400 **Soak:** None
BrBL-2	d059	3.86 x 4.05 x 4.80	monoclinic	None	Yes	**Drop**: 29% PEG400; 0.1M TRIS HCl pH 7.5; 1mM $CdCl_2$ **Compound:** 5mM, 5% DMSO **Cryo:** 40% PEG 400 **Soak:** None

Table 3-3 Dataset Summary: Co-crystals of TREK-2 with BL-1249 derivatives
Resolutions given are for CC1/2 >0.5, and are calculated from scaled and merged data using aimless.

3.2.4 The binding site of BL-1249 from BrBL-2 dataset

Since the datasets collected for Br-BL compounds had the same unit cell as 4BW5, it was expected that the protein would be in the up state. To confirm this, PHASER-MR was run using both up state and down state protein models for the BrBL-2 dataset. Surprisingly, it was determined that the protein was in the down state (Figure 3-5) while having identical molecular packing and crystal contacts to 4BW5 (Figure 3-6). This indicates that the up and down state in this crystal form are not imposed by crystal packing.

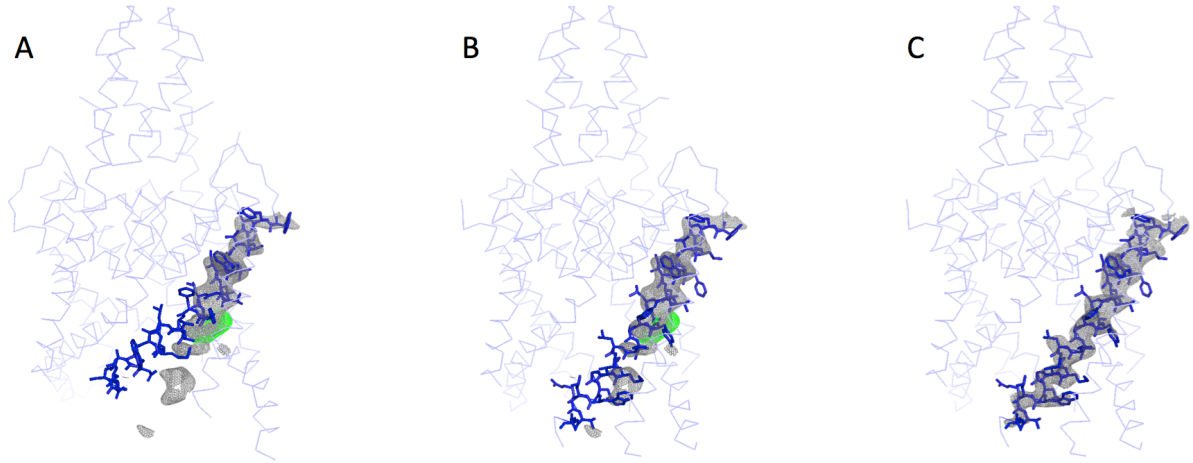

Figure 3-5 TREK-2 co-crystallises with bromo-BL1249 in a down state
Model built with a low-resolution (3.7 x 4.2 x 4.8Å) dataset of TREK-2 with a brominated BL-1249 derivative. Initial MR used a search model with M4 deleted and indicated that the protein is in a down state. Figures A and B show the PHASER-MR $2mF_o$-DF_c density (1.5σ, grey mesh) and mF_o-DF_c density (3.5σ, green mesh). Density is not consistent with the up state (A), whereas it is consistent with the down state. To confirm this, prime and switch maps were generated (C, 2.0σ grey mesh, B-factor sharpened -100$Å^2$). Note that positions of side chains are displayed for reference, and TREK-2 models shown are not complete final models. Images made in PYMOL.

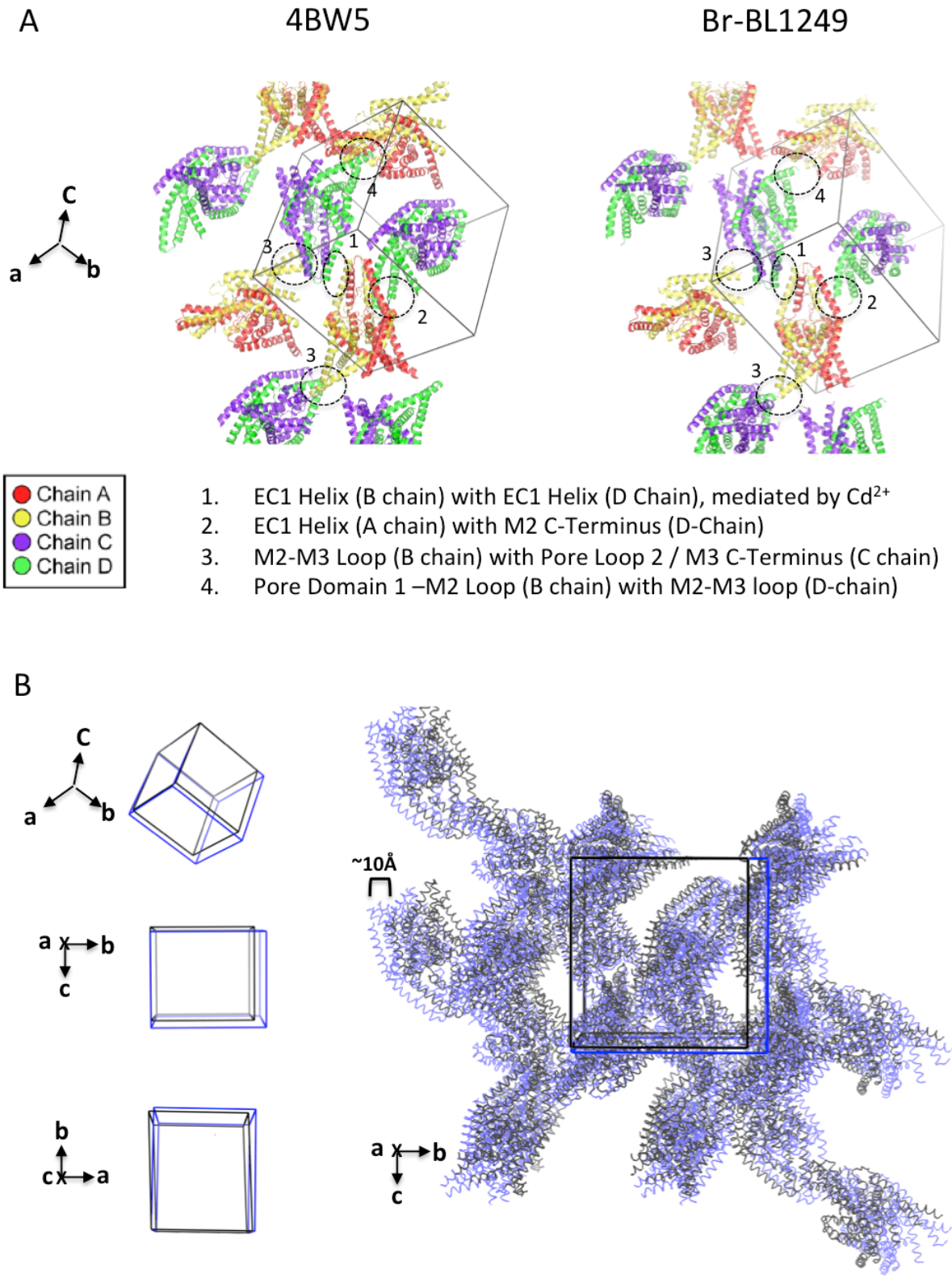

Figure 3-6 Crystal Packing in TREK-2 / BrBL-2 co-crystals

Although this dataset contained protein in the down state, it has very similar packing to the up state 4BW5 (A). Disorder in the M2-M3 loop region causes interactions 2 and 3 to be less ordered, leading to notable expansion in the unit cell along the b axis (B). Unit cells for 4BW5 are coloured black, while the expanded cell in TREK-2/Br-BL2 crystals is coloured blue. Unit cell expansion leads to an increased size in solvent channels, and an increased distance between molecules. It is possible that dehydration may lock M2-M3 loops in position, leading to robust crystal contacts and better diffraction. Images made in PYMOL and ADOBE Illustrator.

Due to the low resolution of this dataset, building of a formal model was not possible. However, the location of the helices was confirmed by refinement in their absence (BUSTER to 4Å) to avoid model bias. A final refinement with all helices in position was used to generate phases for FFT anomalous maps.

Anomalous maps were generated to locate bromine atoms. While the BrBL-1 dataset had weak peaks that were potentially in the noise, BrBL-2 had stronger peaks located close to the fenestration. When compared with the location of peaks for Br-fluoxetine (4XDL, Figure 3-7) the anomalous peak is shifted ~6.4Å to beneath Pro^{198}. This provides an indication of when Br-BL1249 may bind. However, higher resolution and Br-BL2 occupancy is necessary to model the interaction of the ligand with the protein. The low resolution of the data also prevented accurate determination of the number and position of K^+ ions in the filter. The crystal was radiation damaged during data collection, as is evident in the R-merge with image number and B-factor scaling plots. It may therefore be necessary to collect datasets at lower beam power, or from multiple crystals.

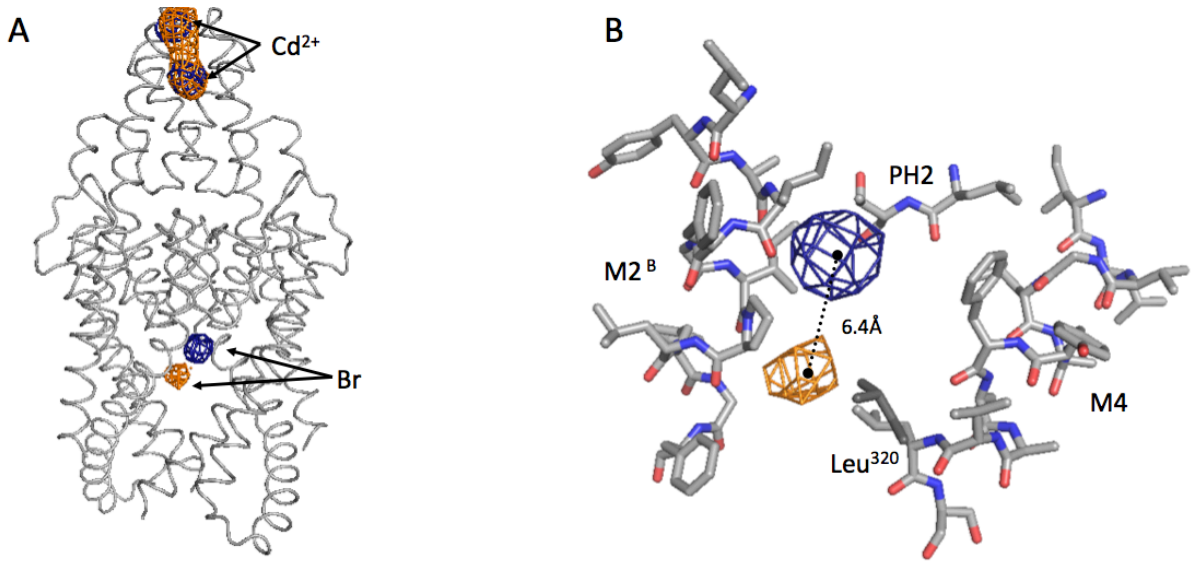

Figure 3-7 Location of Bromine Peaks within TREK-2/BrBL2 co-crystal structure
Figure shows bromine peak location for Br-Fluoxetine (4XDL, 5Å anomalous map contoured at 4σ, Blue), compared with that of Br-BL2 (8Å anomalous map contoured at 4σ, Orange,). Peaks are shown in fenestration A only. The C_α model of TREK-2/ Br-BL2 is shown in grey (A). The cadmium ions are positioned identically when compared with the Br-fluoxetine structure anomalous density. The location of these atoms was not used in molecular replacement search models, indicating that the phases of the model are roughly correct despite the low resolution of the structure and propensity for model bias at this resolution. In comparison, the location of the bromine peaks is separated by 6.4Å in the two structures (A, B). The atomic model of side chain positions is superimposed onto the C_α chain in TREK-2/Br-BL2 for demonstration purposes in B (Grey). Leu^{320} is known to be able to move between two conformations, both shown.

Fenestration	Anomalous Peak σ (8Å)
A	5.86
B	4.51
C	5.09
D	4.00

Table 3-4 Anomalous peak heights within fenestrations of TREK-2/ BrBL-2 co-crystal structure
Maps are calculated at 8Å using BUSTER refined phases. Beneath 4.5σ, some noise peaks are visible. Therefore peaks in the B and D fenestration could not be assigned with confidence.

3.2.5 Possible binding modes for BL-1249

Although no BL-1249 density was visible it is possible to suggest binding modes that are consistent with the data using bromine as a pivot point. Inspection of the protein surrounding the anomalous peak (Figure 3-8) indicates that there are two possible directions for the ligand to extend without steric clashes. Firstly, the ligand may extend into the intracellular vestibule, beneath the selectivity filter. Part of the molecule may then enter the upper part of the fenestration (fluoxetine binding site) from the vestibule. Secondly, the ligand may extend down into the lower fenestration.

Three ligand binding positions that were consistent with the data and produced no steric clashes are illustrated in Figure 3-9. The first pose (A) shows the majority of the hydrophobic molecule facing into the water filled cavity. The ligand is also in a position that is likely to obstruct the ion flow through the channel; not consistent with the functional evidence that BL-1249 is an activator. Pose A is therefore unlikely to be the correct binding mode for this ligand.

Pose B and C both have the ligand occupying the lower part of the fenestration. The nitrogen-rich tetrazol ring faces towards a water-filled cavity. This ring also faces towards Arg^{328}, a residue that is involved in a salt bridge with Asp^{209}. Meanwhile the hydrophobic naphthalene group interacts with Leu^{320}, Ile^{323}, Pro^{198} and Phe^{202}, potentially forming π-π stacks. The naphthalene group also faces towards the hydrophobic membrane. Pose B and C are similar, however pose B has better fit to the pocket. It is therefore the best estimate of ligand binding mode based on the data presented here.

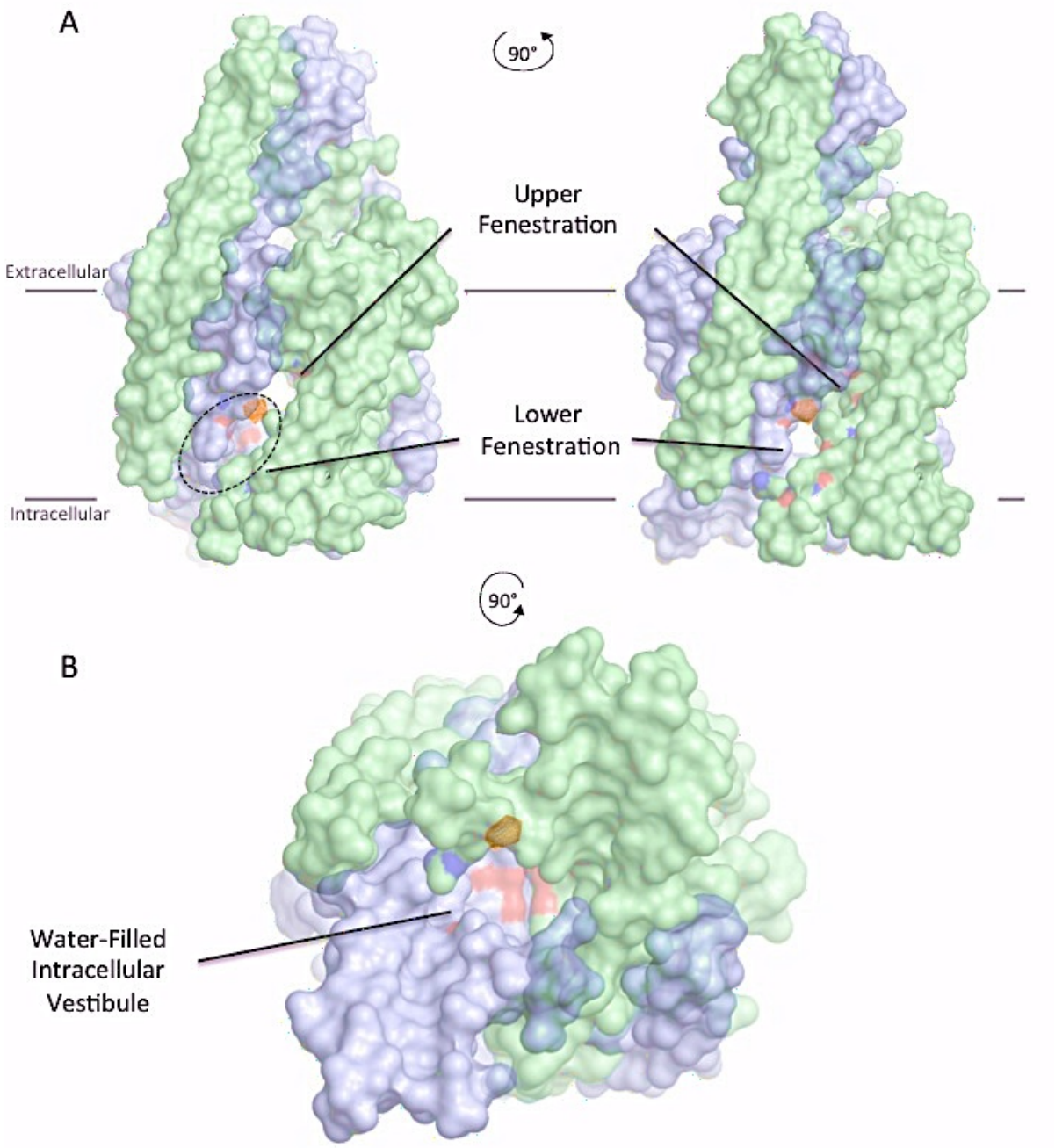

Figure 3-8 Possible pockets for brominated BL-1249 binding

The TREK-2 molecular surface (BUSTER C_α model refined to 4Å. Side chains overlaid from 4XDL for illustrative purposes) coloured by subunit. Charge is shown on the surface (blue negative, red positive) within 7Å of the anomalous peak (orange mesh, 4σ FFT anomalous map calculated to 8Å using BUSTER phases). Side views (A) show the location of the peak within the upper and lower fenestration. From the cytoplasm (B) the location of the peak is shown to be accessible from the intracellular vestibule. Image made in PYMOL.

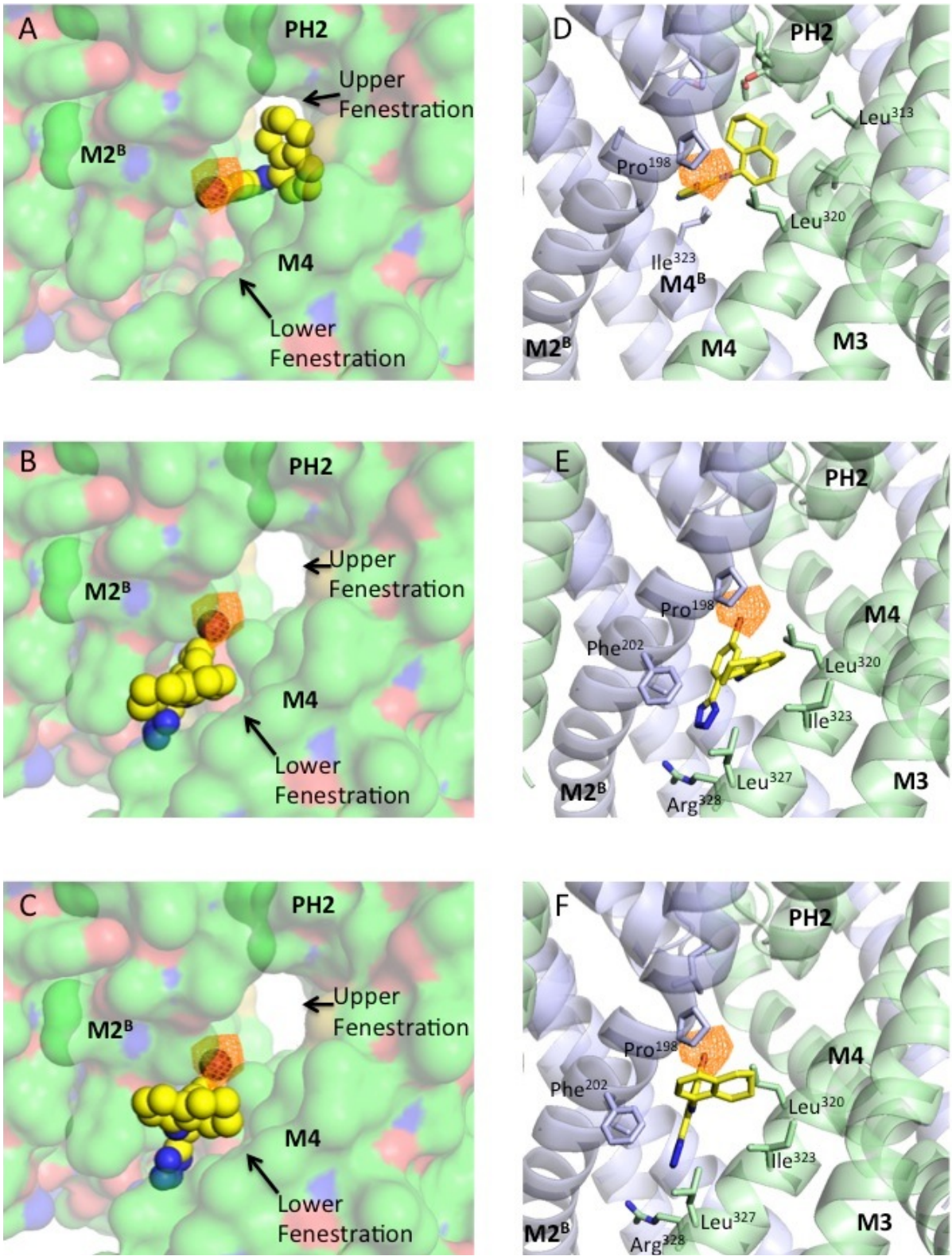

Figure 3-9 Possible binding poses for brominated BL-1249

Although no ligand density is visible for BrBL-2, potential binding poses (A-C) for the ligand can be obtained by pivoting the molecule around the bromine atom (sited at the anomalous peak, orange mesh, 4σ, 8Å map). The left hand figures show BrBL-2 bound to TREK-2 in three different poses. TREK-2 is shown surface representation coloured by electrostatic charge (blue negative, red positive). Figures D-F show the same view as A-C in cartoon representation, coloured by subunit. Residues that may interact with BrBL-2 (yellow) are shown as sticks. Images made in PYMOL.

Although it is not possible to determine the binding mode from the data presented here, these hypotheses for binding modes may be validated using orthogonal assays.

3.2.6 Binding Assays

As described in chapter 2, CPM dye assays can be used to probe the binding of ligands to purified, detergent solubilised protein. The aim of running these preliminary binding assays was two fold: firstly to determine whether BL-1249 could bind to the purified detergent solubilised protein and secondly to determine whether brominating the ligand inhibited binding. Due to the relatively small quantities of ligand available, these experiments were run at a single ligand concentration of 100μM. The experiment was run with protein in three different detergent/lipid combinations: DDM, OGNG and OGNG + CHS, as the thermostability of TREK-2 is known to vary with detergent.

In all detergent/lipid combinations, DDM purified samples produced the largest ΔT_m. For BL-1249 ΔT_m = 12.0 ± 0.3°C was observed in DDM. This compared to ΔT_m = 11.3 ± 0.3°C for BrBL-2, ΔTm = 11.6 ± 0.6°C for BrBL-3 and ΔT_m = 11.1 ± 0.4°C for BrBL-1. It would therefore appear that all brominated BL-1249 derivatives are able to thermostabilise TREK, although the relative affinities cannot be determined without a dose-response curve.

This result was mirrored in OGNG and OGNG+ CHS combinations, albeit with much smaller ΔT_m values. This may be due to the higher T_m of TREK-2 in these detergents. It is also possible that ligand binding is somewhat obscured by the OGNG-based micelle. Co-crystallisation of BL-1249 and its derivatives with DDM may therefore be something to try in the future.

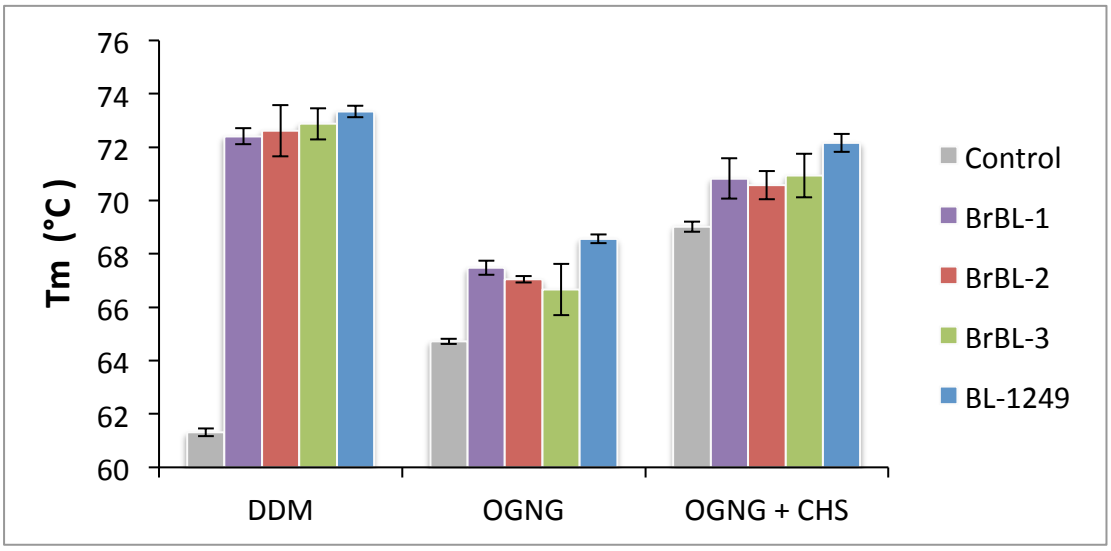

Figure 3-10 Melting temperature results for the binding of BL-1249 derivatives to TREK-2
Melting temperature (T_m in °C) was measured using 100μM of compound in a CPM dye assay. Each T_m was measured four times and an average taken. The standard error is given for the measurements.

	ΔT_m DDM	ΔT_m OGNG	ΔT_m OGNG + CHS
BL1249	12.0 ± 0.3	3.8 ± 0.2	3.1 ± 0.4
PF49	11.3 ± 0.2	2.3 ± 0.2	1.5 ± 0.6
PF50	11.6 ± 0.6	2.0 ± 1.0	1.9 ± 0.4
PF53	11.1 ± 0.4	2.8 ± 0.3	1.8 ± 0.5
Control	0.0 ± 0.2	0.0 ± 0.2	0.0 ± 0.4

Table 3-5 Thermal shift results for the binding of BL-1249 derivatives to TREK-2
The shifts in melting temperature (ΔT_m in °C) measured using 100μM of compound in a CPM dye assay. Each ΔT_m was measured four times and an average taken. The standard error is given for the measurements.

3.3 Discussion

This work demonstrates that the intracellular N and C-terminus of TREK-2 are not necessary for the activatory response to BL-1249. The residues Gly^{67}-Glu^{340} are sufficient for this response, indicating that the binding site lies within the intra-membrane or extracellular cap region of TREK-2. However, truncation of the full-length construct does lead to a reduction in the amplitude of activation from 25 fold to 9 fold. It is therefore possible that the intracellular N or C-termini are involved in the gating response to BL-1249. It is possible that truncation of the CTD may cause this effect. The CTD is thought to

associate and dissociate with the inner leaflet of the membrane leading to channel gating. Removal of sections of this domain may therefore influence response to small molecules even though they may not bind in this region.

Binding of BL-1249 and three brominated derivatives to detergent solubilised protein was demonstrated using a CPM dye assay. All BL-1249 derivatives thermostabilise the protein. Intriguingly extent of ΔT_m was dependent on the purification detergent. This may be for several reasons. The first is that TREK-2 is less thermo stable in DDM than in OGNG. The high baseline thermo stability of TREK-2 in DDM may mean that even ligand binding is not able to further stabilise the protein. However, destabilising the protein using DDM may allow the binding signal to be detected. Alternatively, it is possible that OGNG influences the protein in a way that reduces potency of ligand binding. This may occur due to the detergent obscuring the binding site, or promoting a state of the protein that the ligand does not bind to. Orthogonal binding assays for example ITC would be useful to further investigate the reason behind this detergent dependency. Attempting co-crystallisation in DDM purified protein would also be suggested by these results.

This work provides the first indication of how BL-1249 binds to TREK-2. Since the co-crystal structure of a brominated BL-1249 derivative with TREK-2 is in the down state, BL-1249 must be able to bind to this state. The location of the bromine close to the fenestration demonstrates that BL-1249 binds to the protein within this region. Further optimisation of these co-crystals, including ligand soaking, alterative BL-1249 derivatives and further dehydration experiments, may yield improved results and allow ligand density to be observed. Crystallisation in the cubic phase is utilised to try and improve ligand occupancy in the following chapter.

The preliminary results from Brominated BL-1249 compound correlate with preliminary data collected by a collaborator (Conor McClenaghan, D.Phil Thesis, Tucker Lab Oxford). Tryptic digest mass spec data with photo-activated cross-linking BL-1249 derivatives demonstrate

modification of Gly^{201}. Furthermore, the mutants F200A and L320Y significantly reduce activation by BL-1249. This is consistent with the binding site indicated by the work in this thesis.

The data presented here provides evidence for a previously unseen conformation of TREK-2 within the state diagram (Figure 3-1). This crystallographic state represents protein in the down state. However as the activator is bound to the protein this structure is likely to represent a functionally conductive channel. This could be validated by higher resolution structures allowing the occupancy of the selectivity filter to be determined. Assays to determine whether BL-1249 is a state-dependent activator would also provide insight into the functional relevance of this state.

3.4 Conclusions

The data produced here demonstrate that the movement of TM helices is not solely due to crystal packing, as structures with very similar crystal packing can be in the up or the down state. Co-crystallisation of TREK-2 with brominated BL-1249 indicates that the molecule may bind close to Pro^{198}, beneath the fluoxetine binding site. However as no ligand density was visible in the site, this ligand could not be modelled. This data indicates that it may be possible for TREK-2 to be functionally active while in the down state.

3.5 Methods

Crystallisation, crystallography and CPM dye assays are as described in section 2.

3.5.1 Electrophysiology

Sub-cloning

Both full length KCNK10C and the crystal construct KCNK10C (Gly^{67}-Glu^{340}) were sub cloned into pBF for expression in Oocytes. KCNK10 cDNA was amplified from a pFB-CT10HF-LIC (the vector used for protein production) using polymerase chain reaction.

Forward primers introduced an XbaI restriction sequence and an oocyte-compatible kozak sequence at the 5' end of KCNK10 gene. Reverse primers introduced a BglII restriction site at the 3' end of the gene. Donor vector was removed from the PCR product by Dpn1 digestion. After purification (Qiaquick PCR purification kit) KCNK10 and empty pBF vectors were digested with XBaI and BglII to create compatible sticky-ends. The digestion mixtures were gel-purified using 1% Agarose gel (Qiaquick Gel extraction kit). KCNK10 was ligated into pBF using T4 ligase. The ligated product, KCNK10-pBF, was transformed into competent DH5-alpha cells and grown in Luria Bertani (LB) media with 50µg/ml carbenicillin. DNA was purified from the transformed cells (Qiaprep Spin kit) and sequenced (source Biosiceince UK Ltd) for verification

In-vitro transcription

RNA was produced from MLu1 linearised DNA using Sp6 in-vitro transcription kits. RNA was purifidied using the Qiagen RNeasyMini Kit. RNA concentration was determined using a Nanodrop 1000 Spectrophotometer(thermo scientific).

Oocyte preparation

Xenopus oocyte ovaries were dissected and digested for 2 hours in buffer containing 2mg/ml collagenase; 83mM NaCl; 2mM KCl; 1mM MgCl2; 10mM HEPES. Healthy stage V-VI oocytes were selected manually de-folliculated. Oocytes were stored at 17.5°C in a storage solution containing 96mM NaCl; 2mM KCl; 1.8mM $CaCl_2$; 1mM $MgCl_2$; 10mM HEPES (pH7.4); 50µg/ml gentamycin; 2.5mM pyruvate. Each oocyte was injected with a total of 0.5ng RNA and incubated in storage solution at 17.5°C for 24 hours.

Electrophysiology

Membrane currents were recorded by whole-cell two-electrode voltage clamp (TEVC) using borosilicate glass electrodes filled with 3mM KCl. Currents were amplified with a Geneclamp 500 and digitised with a Digidata 1322A. Data was acquired with pClamp software. During acquisition, oocytes were perfused with bath solution containing 96mM

NaCl; 2mM KCl; 1.8mM $CaCl_2$; 2mM $MgCl_2$; 5mM HEPES (pH7.4); 10mM $BaCl_2$ or 100μM BL-1249.

Ramp protocols were performed as follows; from a holding potential of -80mV, a voltage step to -120mV was introduced for 10ms. The membrane potential was then increased linearly over 750ms to a maximum of +60mV. A voltage step returned the membrane to -80mV before the ramp was re-initiated. Recordings were continued until IV traces stabilised.

Stabilised IV traces were then plotted and the peak current (at +60mV) was determined. These values were used for data analysis.

3.5.2 Structure Determination

As Xia-2 automated processing pipeline masks weak anomalous signal, manual processing was used for these datasets. XDS[153] was used to spot find, index, integrate and scale the data. POINTLESS and AIMLESS were then used to sort and merge the data to produce a reflection file (.mtz)[154,166]. Initial phases were determined using PHASER-MR[151] with three search models; 4BW5, 4BW5 without TM4 and 4XDJ. For both structures, a single solution with sufficient TFZ was produced only using the 4XDJ model. This is likely due to the fact that the protein was in a down state. This was confirmed using prime and switch maps generated in PHENIX[157], and poly-alanine BUSTER[159] refinements (4Å, TLS restrained, NCS refinement, Jelly-body refinement) with individual TM helices omitted in the input models. Anomalous maps were generated to 8Å resolution (indicated by $CC_{1/2}^{anom}$> 0.15.) Using phases from refined poly-alanine models.

Chapter 4 Co-crystals of TREK-2 with activators in LCP

4.1 Introduction

Solving the co-crystal structure of proteins with hydrophobic ligands is challenging due to ligand solubility. Combined with low affinity, this produces low ligand occupancy in crystal structures and non-interpretable ligand density. It is therefore necessary to optimise the solubility of the compound in the crystallisation solution to ensure that occupancy in the crystal is sufficient to observe ligand density[167].

In order to overcome solubility issues small molecules may be dissolved in hydrophobic solvents such as Ethanol and DMSO or low molecular weight PEGs. Saturating solutions with solid compound may also drive the equilibrium towards binding. An alternative strategy to solubilise hydrophobic ligands is to dissolve them in lipids, and co-crystallise in lipidic cubic phase[167].

Lipidic cubic phase (LCP) crystallisation is a technique to crystallise membrane proteins after reconstitution into a lipid mixture. It is also known as *in meso* crystallisation. Upon mixing of a mono-acyl glycerol lipid with an aqueous solution of protein in detergent in a 3:2 w/w ratio at 20°C, the lipid forms a bi-continuous honeycomb structure which incorporates the protein (Figure 4-1). Upon addition of precipitant solution (typically PEG and salt), a crystal nucleates within the cubic phase. Crystal growth is thought to be facilitated by lateral diffusion of free protein molecules through lamellar conduits that suspend the crystal within the cubic phase[168].

Crystals formed within LCP provide increased surface area for crystal contacts, as neighbouring proteins can form interactions in both trans-membrane and extracellular domains. This makes cubic phase particularly useful for crystallisation of membrane proteins with scant soluble domains such as bacteriorhodopsin[169]. Because proteins can

form contacts within their hydrophobic domains, LCP crystallisation tends to produce type I crystals [170]. Type I crystals form as a stack of 2D layers of crystal. These crystals typically have a low solvent content and so tend to have better order and produce better diffraction. In comparison type II crystals typically formed by detergent solubilised proteins have contacts only between hydrophilic domains of the protein, and typically high solvent contents (Figure 4-1).

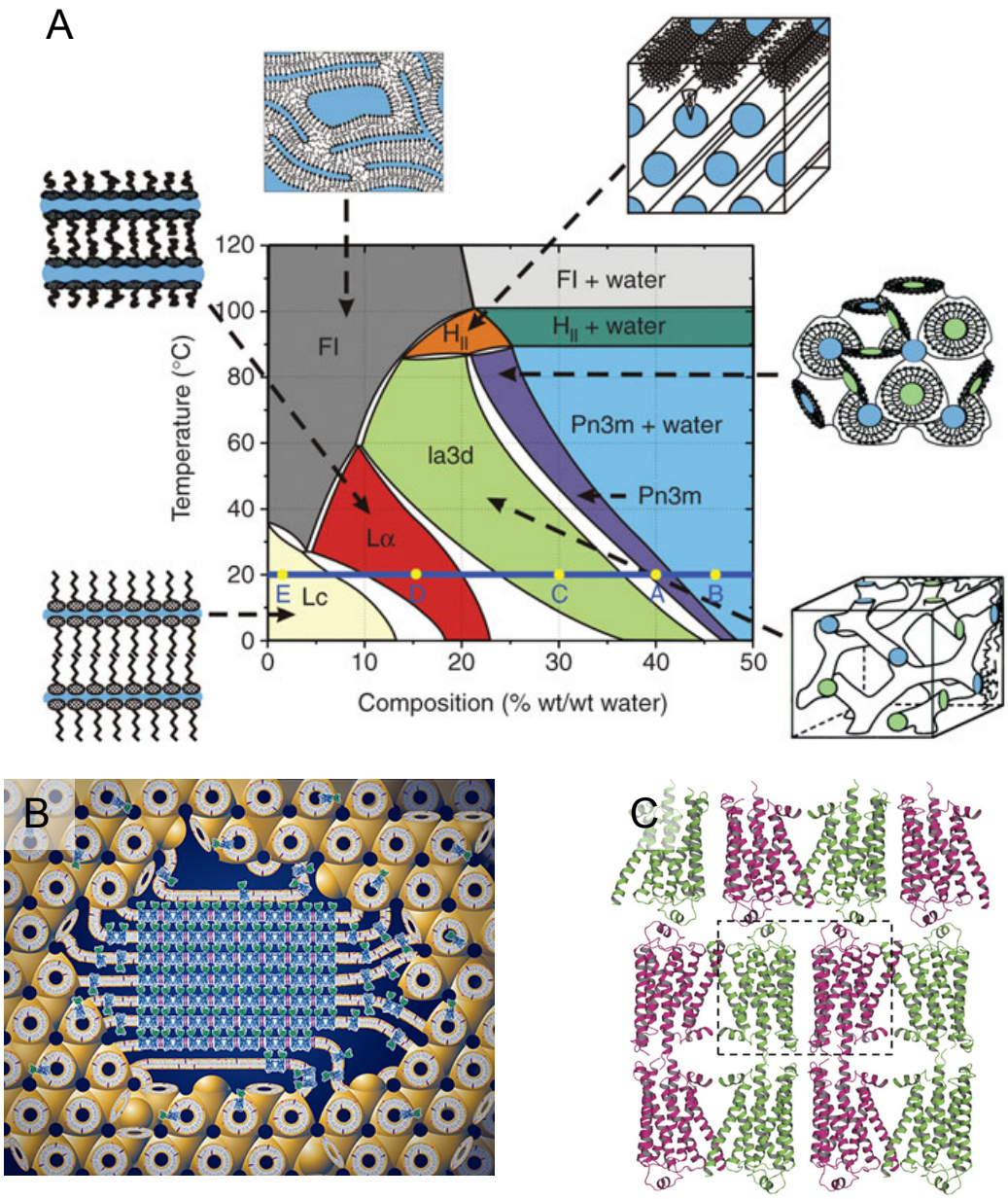

Figure 4-1 Crystallisation of membrane proteins in LCP.

A) The phase diagram for monoolein mixed with water. The cubic Pn3m phase is obtained with a composition of 40%w/w aqueous protein solution and 60%w/w Mono-Acyl Glycerol 9.9 (MAG 9.9, Monoolein) at 20°C. B) Protein crystals nucleate within the cubic phase. Crystal growth is facilitated by lateral diffusion of free proteins through lamellar conduits (Images A and B from Cherezov and Caffrey 2009[171]). C) Crystals grown in LCP display type I packing, as demonstrated by the β_1 Adrenergic Receptor (Image from Huang *et al*. 2013[172]). Images reproduced with permission from Nature.

The success of LCP as a medium for membrane protein crystallisation is exemplified in GPCRs; there are 31 GPCR structures in the PDB solved in LCP (June 2015). However, there is a notable obstacle: *In-meso* methods often produce microcrystals less than ten microns in size. Data collection therefore requires long exposure times (≈ 5s per image) on high intensity micro-focus beam lines (10^9 photons $s^{-1}\mu m^{-2}$) to achieve measurable intensities for high resolution reflections[173]. Such data collection would be time consuming, requiring merging of data from potentially hundreds of crystals, as each crystal would succumb to the effects to radiation damage before a full dataset could be collected. Even employing these extreme data collection strategies, the smallest microcrystals (<50 μm in size) may be unable to achieve the resolution required for structure building.

To overcome the problems associated with data collection from microcrystals, it was necessary to use a beam capable of much higher intensities: an X-ray free electron laser (XFEL). These high intensity beams have been in existence since 2009[174,175], however it was believed that radiation damage sustained by the crystal would prevent their use in protein crystallography. Nonetheless, multiple protein structures have been solved at the XFEL, including lysozyme[176], photosystem II[177]and several G-protein coupled receptors[173].

Radiation damage is avoided due to the pulsed nature of the XFEL. The short duration of the pulse (50fs) means that all data is collected before substantial radiation damage has time to occur[178]; the timescale for significant radiation damage is in the region of 100-200fs[179]. This allows data collection at > 3gGy; 3000 times greater than is tolerable with conventional experimental set-ups[180]. Furthermore, the high intensity of the beam (10^{12} photons in 50fs) means that atomic resolution diffraction can be achieved from crystals as small as 200nm or six unit cells across for crystals grown in aqueous mother liquor[179].

The data collection strategy at FELs is known as Serial Femtosecond Crystallography (SFX)[176]. In SFX thousands of microcrystals are injected onto a high intensity beam (10^{12} photons in 50fs) producing a single diffraction image for each crystal. After diffraction, the crystal is destroyed. It is striking to compare the type of data collected from SFX with that collected from multi-crystal synchrotron data. Liu *et al.* collected data sets for 5HT-2B receptor using both methods[173]. SFX was able to obtain a similar resolution using crystals with a volume 100 times smaller than those shot at the synchrotron. However, as it is possible to shoot each crystal only once, it was necessary to shoot 32,819 crystals to provide enough data for processing. This compared with just 17 large crystals required for synchrotron data. Although the resulting structures and dataset statistics are similar, Liu *et al.* suggest that the SFX data is more biologically relevant due to the fact it is collected at room temperature. This is reflected in the increased B-factors of the SFX structure[173].

Data collection	**5-HT$_{2B\text{-}XFEL}$**	**5-HT$_{2B\text{-}SYN}$**
Temperature, K	294[a]	100
Wavelength, Å	1.3	1.032
Beam size, µm	1.5	10
Average crystal size, µm	5 × 5 × 5	80 × 20 × 10
Number of crystals	32,819	17
Flux	$3{\cdot}10^{10}$ ph/pulse	10^{11} ph/s
Max dose per crystal, MGy	25	20
Space group	$C222_1$	$C222_1$
Unit cell, Å	61.5, 122.2, 168.5	60.57, 119.75, 170.61
Oscillation / exposure	0° / 50 fs	1.0° / 1.0-3.0 s
No. collected images	4,217,508	91
No. hits / indexed images	152,651 / 32,819	91 / 91
No. total / unique reflections	18,515,376 / 16,052	51,559 / 16,041
Resolution, Å	35 – 2.8 (2.9 – 2.8)	50 – 2.7 (2.8 – 2.7)
Completeness, %	100 (100)	90.5 (92.2)
Multiplicity	1,150 (1035.6)	3.2 (3.1)
I/σ(I)	5.9 (0.64)	8.7 (1.7)
CC* [b]	0.998 (0.74)	0.992 (0.77)
R_{split} [c] (XFEL) or R_{merge} (SYN), %	9.5 (161.9)	15.0 (91.4)
Refinement		
No. reflections / test set	16,025 / 814	15,818 / 823
R_{work} / R_{free}, %	22.7/ 27.0	22.7 / 26.6
No. atoms		
Protein	2,856	2,854
Ligand	43	43
Lipids and other	224	170
B-factors, Å^2		
Wilson B/ Overall B	115.7 /98.7	72.1 / 80.0

Figure 4-2 Comparison of 5HT-2B receptor data sets collected at the X-ray free electron laser (XFEL) and at a standard synchrotron (SYN).
Image from Liu et al. 2013[173]. Reproduced with permission from AAAS.

In this chapter I aim to use LCP to obtain a co-crystal structure of TREK-2 with BL-1249. BL-1249 is an 8µM IC_{50} (TREK-1) activator that has been shown to interact with the

crystallisation construct in Chapter 4. However it has low water solubility; dissolving it in monoolein may increase the concentration of ligand available to bind the protein. This would increase occupancy and thus the quality of electron density for bound BL-1249, allowing characterisation of the binding site and providing insights into gating mechanisms. After co-crystallising TREK-2 and BL-1249 in LCP, I optimise the crystals for SFX at the Linac Coherent Light Source (LCLS).

4.2 Crystallisation of TREK-2 with BL-1249 in Lipidic Cubic Phase

This chapter focuses on the co-crystallisation of TREK-2 with the activator BL1249, as electrophysiological and thermostability assays indicated that it could bind to the construct that was being crystallised (Section 3.2.1 and 3.2.6). Note that this BL-1249 is not brominated, since the LCLS-CXI instrument (4keV-10keV[181]) cannot achieve wavelengths suitable for Br anomalous (13.5keV) data collection. Stock solutions of 10mM BL-1249 were made in mono-acyl-glycerol 9.9 (MAG9.9, monoolein) and this was used to produce LCP with purified TREK-2. The final concentration of BL-1249 in the LCP was 6mM. The cubic phase was incubated at 20°C for three hours before crystallisation trials were set up, to allow time for the ligand to bind to the protein. LCP was set up in glass sandwich plates with commercial coarse screens.

4.2.1 Sandwich Plate Crystallisation Screening

Initial crystals were obtained from the coarse screens. After 7 days, crystals appeared in two conditions; MemGold2-B7 (28mM Sodium Chloride; 28mM Tris pH 8; 25% w/v PEG350MME) and MemGold2-H7 (70mM Tris pH 8.5; 25% w/v PEG200) conditions. These conditions did not produce crystals in the absence of BL-1249. The initial hits were similar; both low salt, Tris pH 8-8.5 and 25% low molecular weight PEG. Both conditions appeared to lie on the phase boundary between cubic and sponge phase ("soft LCP"). Crystals were ≤ 5μm in size and taken between 3 and 7 days to grow to completion (Figure 4-3).

After initial hits were identified, optimisation was carried out in sandwich plates. Optimisation aimed to grow crystals large enough for synchrotron data, or alternatively small and dense enough for SFX. Initially the parameters screened were PEG type/ concentration, buffer type/pH, ligand concentration and sodium-based salt additives. Screens were also tested with cadmium chloride as a crystallisation additive, since

cadmium is known to facilitate crystal contacts between helical cap domains in some TREK-2 crystal forms (PDB IDs 4BW5, 4XDL)[75]. These initial screens provided no evidence of crystals large enough for synchrotron data collection, so optimisation for XFEL was prioritised.

A) MemGold2 B7 (Diluted 0.7x) 28mM Sodium Chloride; 28mM Tris pH 8; 25% w/v PEG350MME

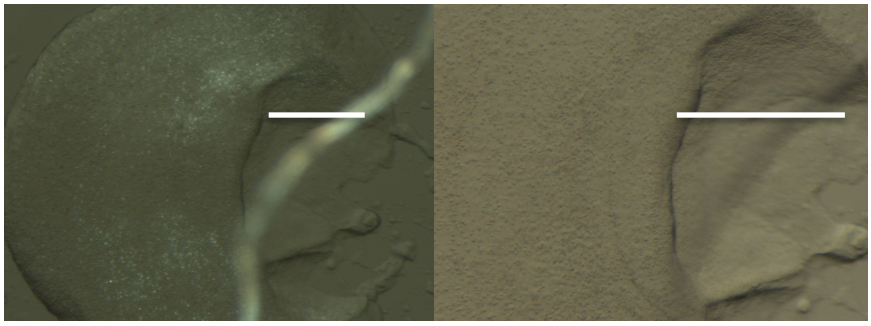

B) MemGold2 H7 (Diluted 0.7x); 70mM Tris pH 8.5; 25% w/v PEG200

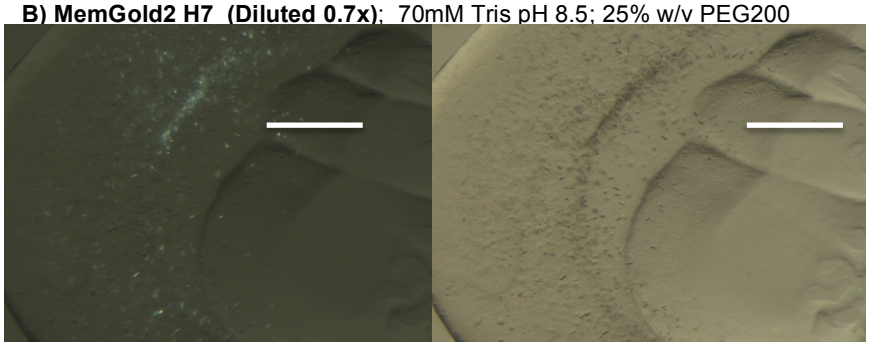

Figure 4-3 Crystals of TREK-2 in LCP from coarse screens
A,B) Initial crystals resulting from a coarse screen of TREK-2 with 6mM BL-1249. C) Crystals obtained after fine screening around the initial condition. Scale bar 200µm. Left images are viewed with cross-polariser, right images with white light.

Low molecular weight poly-ethylene glycols (LMW-PEGs) screening demonstrated microcrystals in 20-30% v/v PEG200, while other LMW-PEGs produced microcrystals in spongy phase. Spongy phase is not suitable for data collection at XFEL due to it's low viscosity; a prohibitively large sample volume would be required to maintain a constant flow of crystals through the beam given a fixed injector nozzle size. PEG200 was therefore selected as the PEG for crystallisation as it maintained the cubic phase of the Monoolein.

Buffer screening indicated that crystals could grow in Tris pH 7.5-8.5, however were larger at pH 8.5. Although data can be collected from true nano-crystals through SFX this is not possible for membrane proteins. This is because of the high scatter caused by the lipid within the crystal, leading to a high background and reduced signal to noise ratio on the

detector. It is therefore desirable to produce crystals as large as possible (5-20μM) without blocking the 50μM nozzle. Tris pH 8.5 was therefore selected as the buffer for crystallisation to produce larger crystals.

Increasing the concentration of BL-1249 within the LCP from 6mM to 10mM promoted the formation of sponge phase and reduced the frequency of crystals. The crystal density is pivotal for XFEL experiments; it must be optimised to around 10^6 crystals per millilitre of cubic phase. In an ideal experiment each laser pulse would it a single crystal. A density that is too low will lead to many empty images and long data collection times while necessitating large sample volumes. However, excessively high crystal density will lead to multiple crystals being shot in each pulse, and multiple patterns being visible on each image. 6mM BL-1249 was therefore selected as 10mM compound produced crystal densities that were too low for SFX data collection.

Sodium-based salt additives inhibited crystallisation within the cubic phase, so were removed from the condition. Cadmium chloride also appeared to inhibit crystallisation, so was removed from the condition.

After initial screening, the base condition was defined as 0.1M Tris pH 8.5 and 20-30% v/v PEG200, with 6mM BL-1249 and 30mg/ml TREK-2 in monoolein LCP. Crystals produced from initial rounds of optimisation were screened at Diamond's I24 micro-focus beam line. The resulting crystals diffracted to between 8.5 and 25 Å at 2.0x 10^{12} photons per second with 1s exposure times (Figure 4-4). The diffraction patterns could not be indexed using XDS or iMOSFLM. Diamond's auto-processing pipelines were also unable to index the crystals.

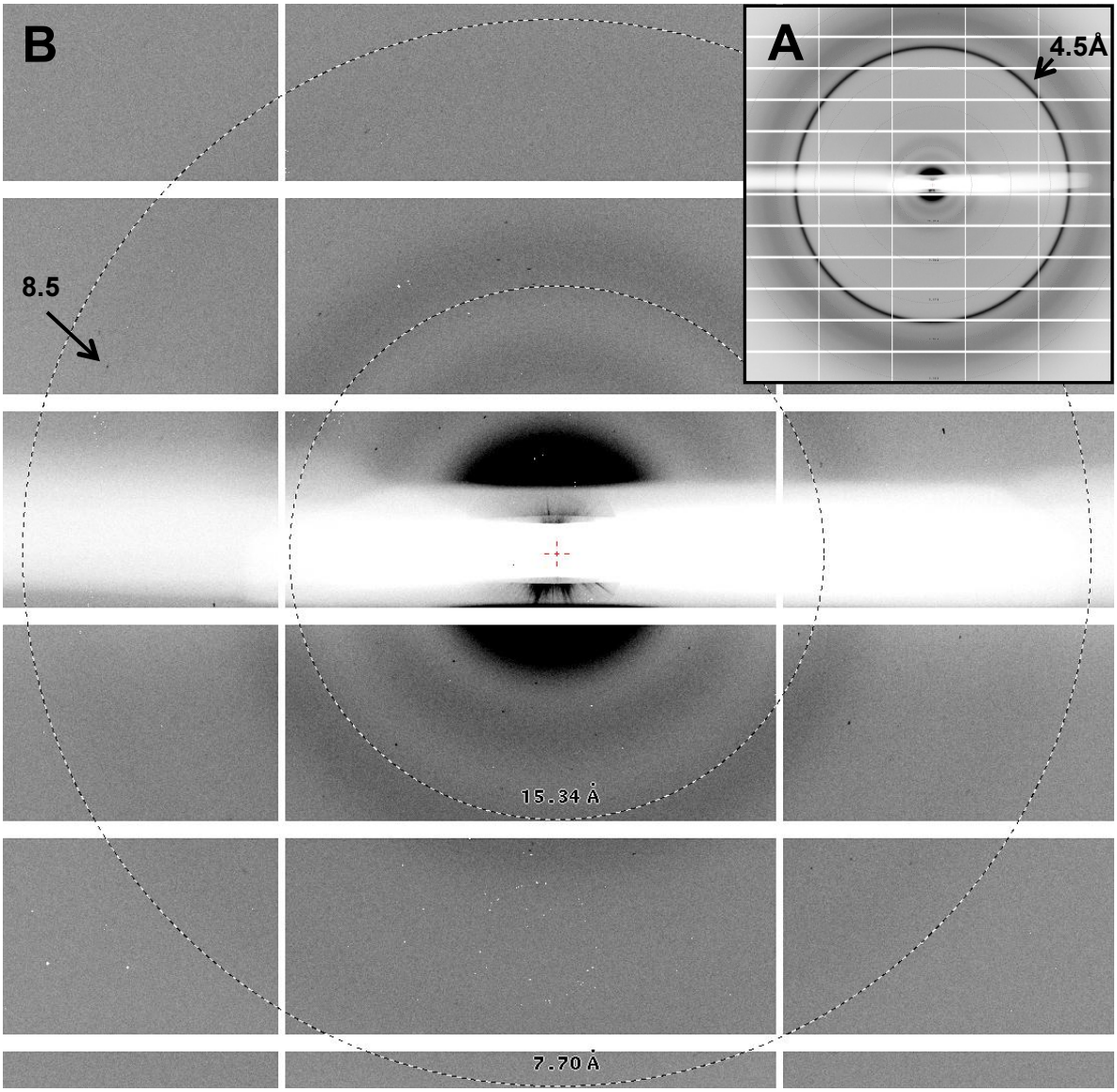

Figure 4-4 Syncrotron diffraction images of TREK-2 crystals in Lipidic Cubic Phase

Diffraction images of a TREK-2 crystal (KCNK10C-x1337) grown in lipidic cubic phase with 6mM BL-1249. Images were collected at Diamond I24 with a 1s exposure and the detector edge at 3.5Å resolution. A) The full detector image shows a ring at 4.48Å due to the Monoolein B) A single image demonstrating 8.5Å diffraction.

Salt additives were then screened (Figure 4-5). This is a common strategy in LCP crystallisation, as the presence of salt can determine whether protein is able to migrate within the cubic phase[168,182]. Salt screening was carried out using an in-house salt-additive screen (Ashley Pike, unpublished) enriched with potassium salts. KCl and KNO_3 up to 50mM did not inhibit crystal growth. However, crystals with KCl were larger. Large rod shaped crystals 150x20µm in size also grew in the presence of 50mM potassium citrate ($C_6H_5K_3O_7$). A similar citrate based condition previously yielded crystals in the absence of

BL-1249. These apo-state crystals had been extensively optimised by a post-doc (Yin Dong) and failed to produce high-resolution diffraction. Therefore potassium citrate wasn't pursued as an additive.

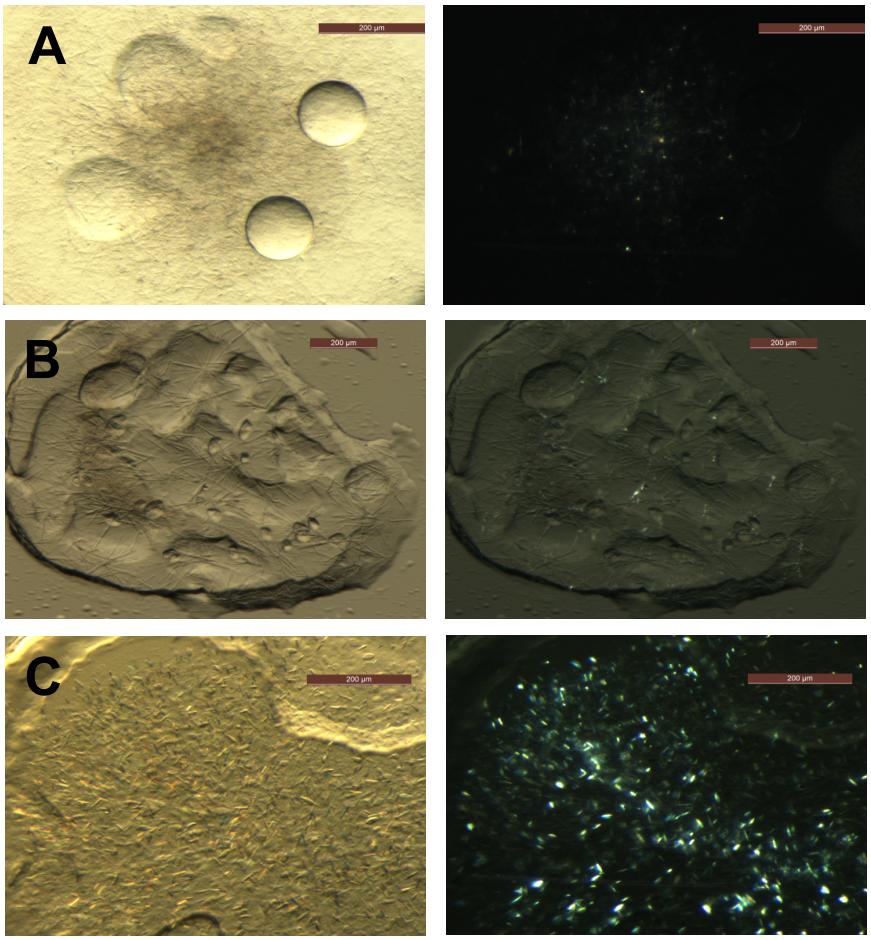

Figure 4-5 Salt additive screening of TREK-2 crystals in LCP
Scale bar 200µm. The base condition is 28-32% PEG200 and 0.1M Tris pH 8.5. Left hand images are white light, while right hand images are viewed with a cross-polariser (protein crystals are bi-refringent so show up white). A) Microcrystals <5µm in size grow in the presence of 25-50mM potassium nitrate. B) Large crystals 150 x 10µm grow in the presence of 25-50mM potassium citrate tribasic C) microcrystals 30 x 5 µm grow in the presence of 25-50mM KCl. Scale bars 200µm.

Protein concentration was then screened at 15, 30, 45 and 60mg/ml. This was carried out to determine the protein concentration required for optimum crystal density, as a high density (10^6 per ml) of crystals is required for SFX to ensure that the beam hits crystals rather than empty LCP. Furthermore, optimisation of protein concentration could reduce protein precipitation within the drop, increasing the protein available for crystal growth. 15mg/ml protein produced few crystals, while 60mg/ml produced large amounts of precipitate. 30 mg/ml TREK-2 produced microcrystals around 30x5µm in size, while 45 mg/ml produced crystals <5 µm in size. 30mg/ml was therefore selected as the best protein concentration.

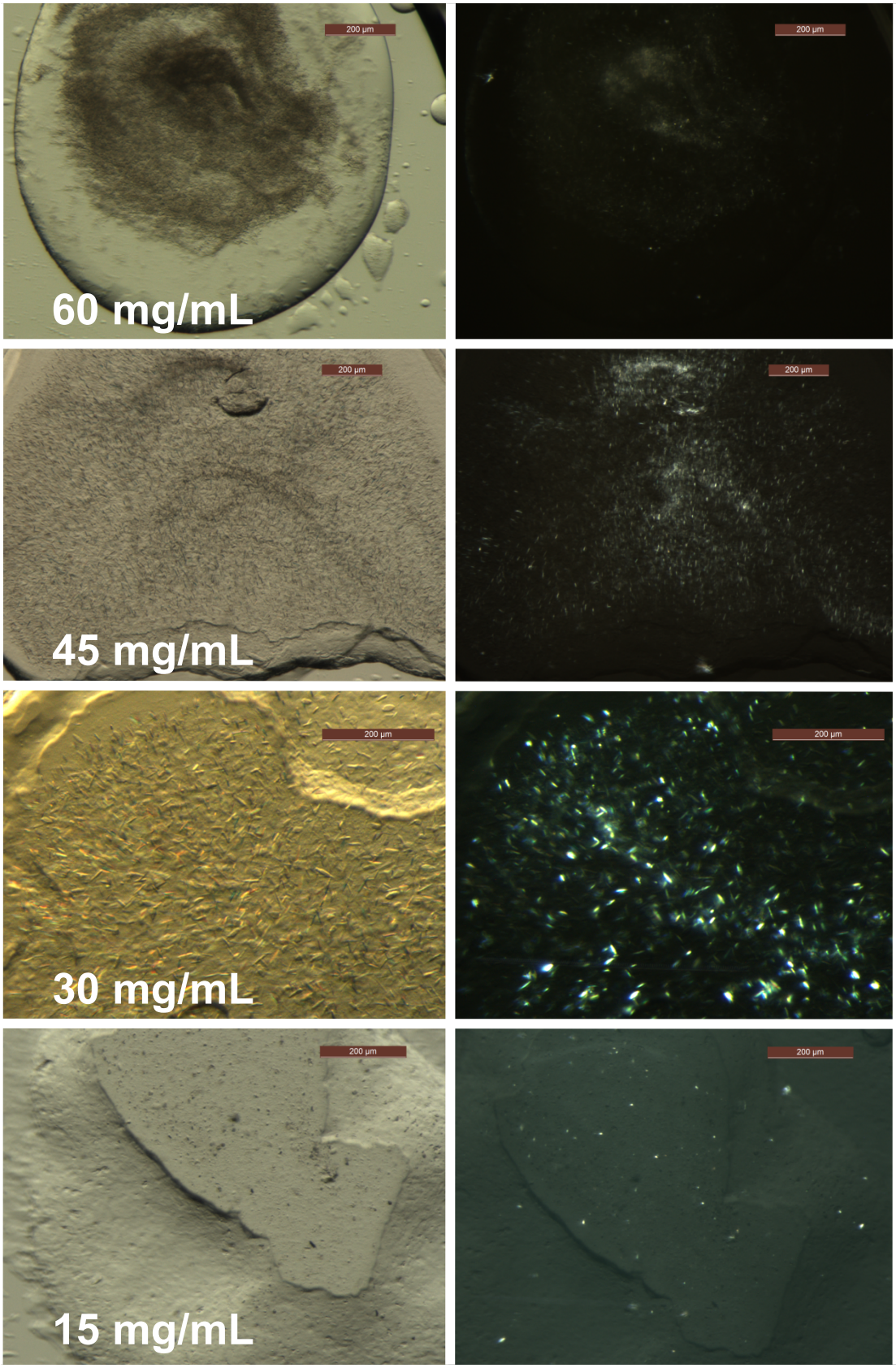

Figure 4-6 Screening protein concentration for TREK-2 crystals in Lipidic Cubic Phase

Left hand pictures are under white light, right hand pictures are taken using a cross-polariser. While high concentrations produce microcrystals in spongy phase, low concentrations produce few nucleations. 20mg/ml is therefore the best concentration for crystallisation. Scale bar 200µm.

The final condition as a result of screening in 96 well plates used 30mg/ml protein with 6mM BL-1249 in Monoolein LCP. The crystallisation conditions consisted of 20-30% PEG200, 0.1M Tris pH 8.0-9.0 and 0-50mM KCl. In these conditions crystals grow to a size of 30x5µm in 7 days. In order to screen samples at the free electron laser, it is necessary to produce sample volumes of around 50µL, depending on the hit rate. It was therefore necessary to produce the crystals in a large volume of LCP. This is usually done by crystallisation within syringes, and is discussed in the following section.

4.2.2 In-syringe crystallisation

It is not possible to use sandwich plates for data collection since it requires in the region of 50µL of sample. To produce these large volumes required for data collection at the LCLS, in-syringe crystallisation has been used[183]. In this method ~5µL of pre-formed LCP is injected into the body of a syringe containing ~20µL crystallisation solution. The syringe is then thoroughly sealed and incubated. After crystal growth, crystallisation solution is evacuated and the LCP from several crystallisation syringes is combined to make a larger sample.

The lead condition from sandwich plates was used as a basis for screening in syringes. Concentrations of crystallisation components were varied in syringes, as the kinetics of crystallisation are known to differ when going from plates to syringes. In syringes, crystals were obtained after 5-7 days. Crystals grew in a lipidic mesophase that was on the phase boundary between cubic and sponge (Figure 4-8). As this boundary typically changed by about 1% PEG with each experiment, it was necessary to set up a PEG gradient with each batch of syringes.

A total of 310 crystallisation syringes were set up in order to optimise crystals for data collection. Variables tested included concentration of KCl and Tris, as reduced evaporation with respect to sandwich plates may necessitate higher precipitant concentrations in

syringes. Batch IDs for all crystallisation components (protein purification, ligand, buffer, salt) were also tested, as they may be a cause for variability in crystallisation.

The conditions that produced crystals in syringes were not identical to those in sandwich plates. Screening the concentrations of components of the crystallisation solutions indicated that crystallisation required a higher concentration of PEG 200 (crystals grew over a range of 35-40% PEG200, compared with 20-30 in plates) and a higher concentration of potassium chloride (at least 25mM was necessary to produce crystals of sufficient size for data collection).

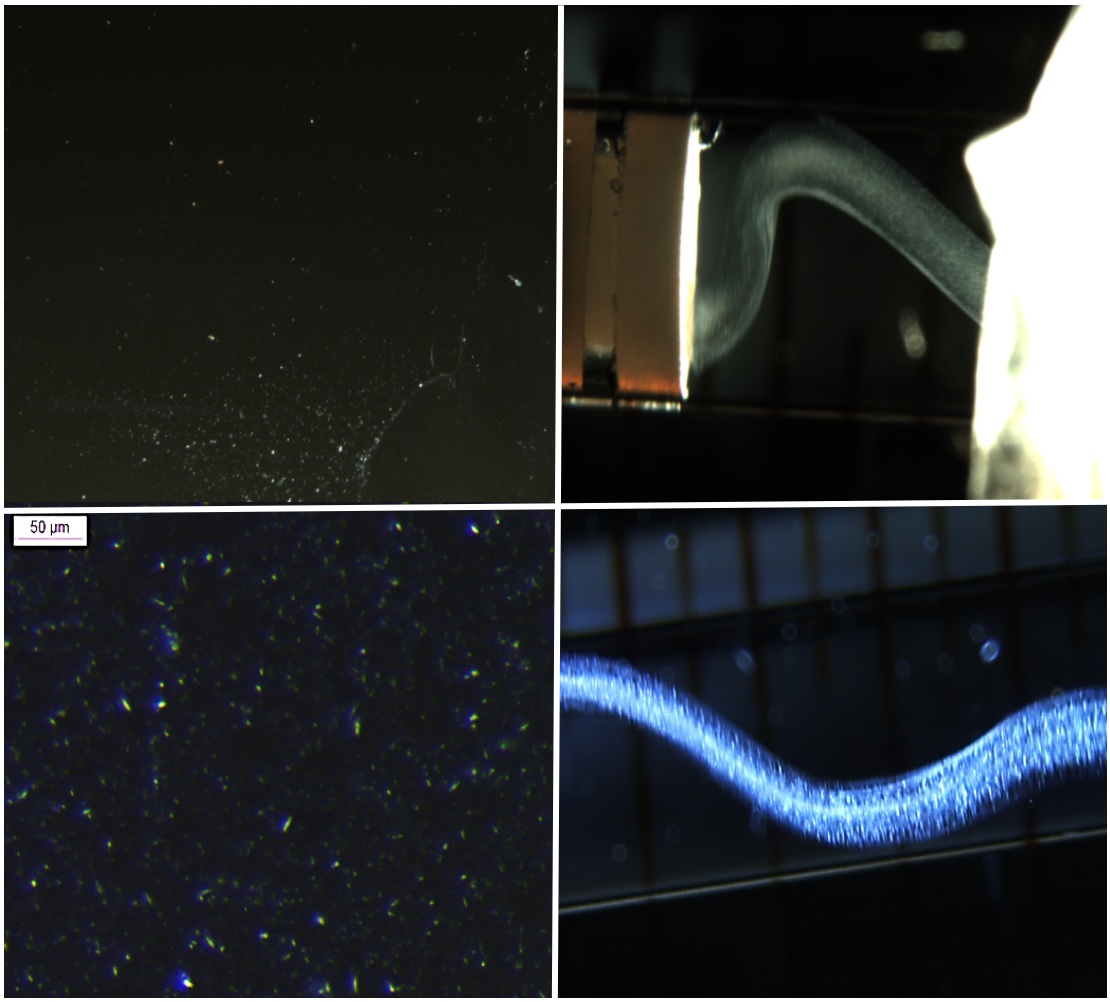

Figure 4-7 Variability in crystallisation of TREK-2 in syringes
Pictured are two syringes (right) containing identical crystallisation solution. Images on the left show what these samples on a slide under a microscope. Both sets of images are viewed with a polariser; crystals show up white. A) The majority of syringes produced hazes of sub-micron crystals B) A small proportion of syringes produced rod shaped crystals of dimensions 5x1 microns. These crystals were combined for data collection at LCLS. Samples were then combined at shot data collected at the LCLS-CXI instrument.

Crystallisation in syringes was variable with often differing results (Figure 4-7) despite consistent crystals in 96-well plates set up as positive controls. The majority of syringes containing crystals produced sub-micron crystals that were not suitable for data collection. Reliability did not improve with screening of crystallisation components, different protein purifications, or different lipid batches. Since the crystals grow on the phase boundary between sponge and cubic (Figure 4-8), it is possible that batch to batch variation in LCP had a large effect on crystallisation.

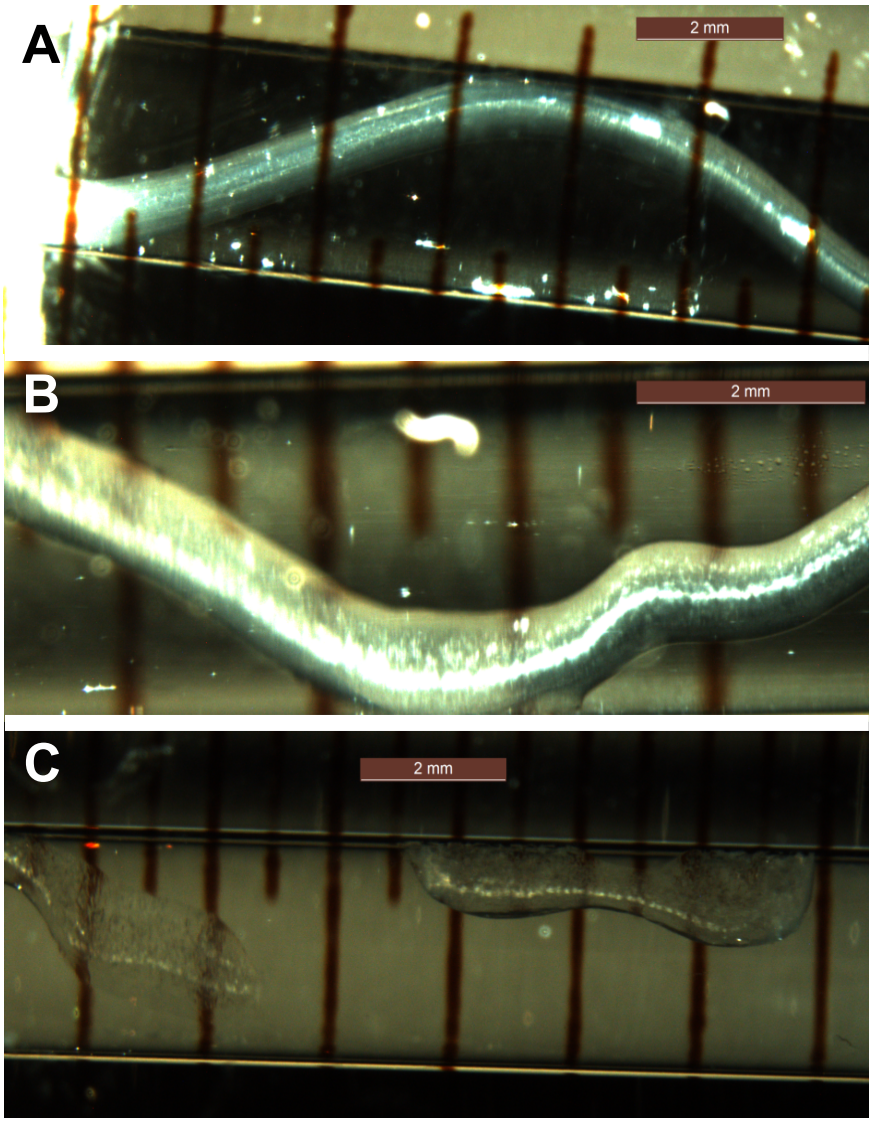

Figure 4-8 TREK-2 crystals grow on the boundary between lipdic cubic and spongy phase. A) Cubic phase with few crystals B) "soft" LCP with a high crystal density C) spongy phase. Scale bar 2mm.

Samples selected for data collection were viewed using second order nonlinear optical imaging of chiral crystals (SONICC, provided by Chelsie Conrad, Arizona State University). This system can improve signal to noise ratio in crystal images by a factor of 8000 in crystals embedded in LCP[184]. This means it is often able to detect crystals that are not visible under bright light due to the background scatter of the cubic phase. The Rock Imager also provided Bright-Field (white-light) ad UV fluorescence images for comparison. These imaging methods were unable to detect TREK-2 crystals within a sample that provided protein diffraction when jetted onto the FEL beam (Figure 4-9).

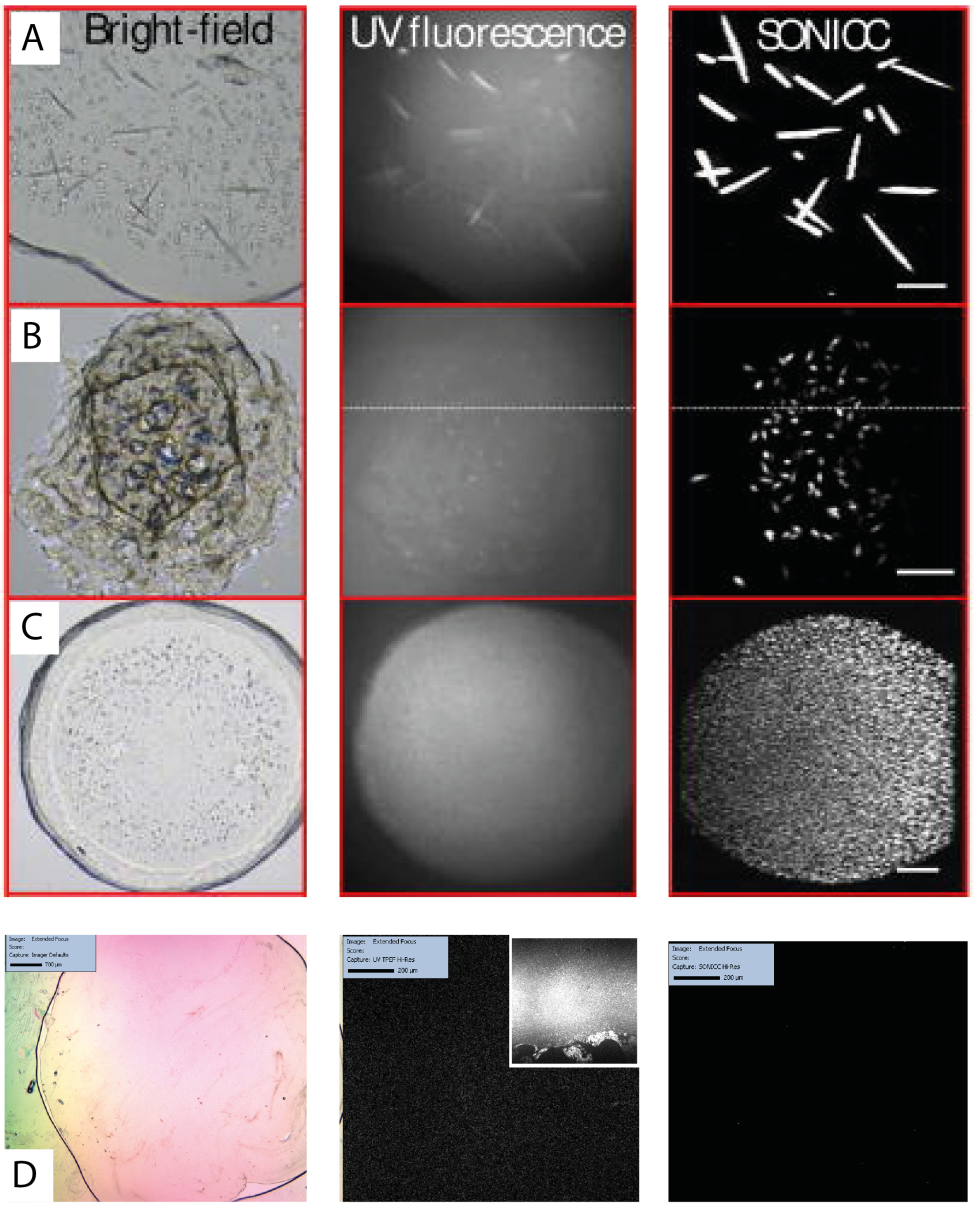

Figure 4-9 White Light, U-V Fluorescence and SONICC imaging of TREK-2 crystals
The white light (Bright Field), U-V fluorescence and SONICC images are shown for TREK-2 crystals (D), with three other samples containing crystals (A-C, taken from Kissock et al. 2010[184] with permission from ACS) for reference. The TREK-2 crystals are not visible under SONICC, U-V or bright field microscopy. Instead they must be detected using a microscope fitted with a cross-polariser.

4.3 Serial Femtosecond Crystallography of TREK-2 crystals

4.3.1 Diffraction images

Samples were prepared a week in advance and shipped to LCLS-CXI instrument. An initial set of samples was shipped for data collection by colleagues (Yin Dong, Ashley Pike, Liz Carpenter). Of twenty 5μL samples shipped, three syringes were suitable for data collection. These samples were combined with 2μL of MAG 7.9 to reduce formation of lamellar phase, and placed into the injection apparatus. A total of around 15μL of LCP was jetted into the beam through a 50μm nozzle with a viscous flow rate of 0.235μL per second. Jet integrity was maintained with a co-flowing stream of He gas at 110 PSI. The beam operated at 9.49keV (1.306Å) at 120Hz with a 42fs pulse length. A CSPAD segmented detector positioned at 108mm from the beam collected a total of 357,288 images, of which a total of 11,624 were crystal hits (3.3%). Crystal hits produced images ranging in resolution from 30 - 3Å. Some of the crystals produced split or streaky diffraction patterns. Finally a dark current (no sample) was collected for calibration of the detector. A second set of samples was shipped six months later while I was present. However these samples had weak diffraction so data collection did not proceed. What follows below is a description of data obtained at the first LCLS trip.

4.3.2 Data sorting and pre-processing

Pre-processing of the XTC format diffraction images was preformed using CHEETAH[185] software. The aim of pre-processing is to assemble diffraction images by combining detector readouts with known detector geometries, correct the images for background scatter and detector abnormalities, identify Bragg peaks within the corrected images and thus determine which images result from protein diffraction.

A dark-current stream of 7,431 images (collected with beam but without sample) allowed subtraction of the background photon count from each image. Images were then sorted into hit (had protein diffraction) or miss classes, based on input peak detection parameters. These peak detection parameters had to be optimised to produce accurate results; too sensitive and all images were classed as hits, but too stringent and real hits were labelled as misses. In order to assess whether the images are correctly sorted powder diffraction patterns, summations of the intensities across all images in the class, were created for the hit and miss classes. For the final peak detection parameters (Hit finder algorithm 8; minimum signal to noise 6:1; 20< Number peaks < 5000; 2< pixels per spot <20) the hit class contained protein powder diffraction rings, while the miss class contained few protein rings, meaning hits were accurately detected (Figure 4-10). Pre-processing output is a folder of HDF5 format files each containing a separate diffraction hit image and peak list.

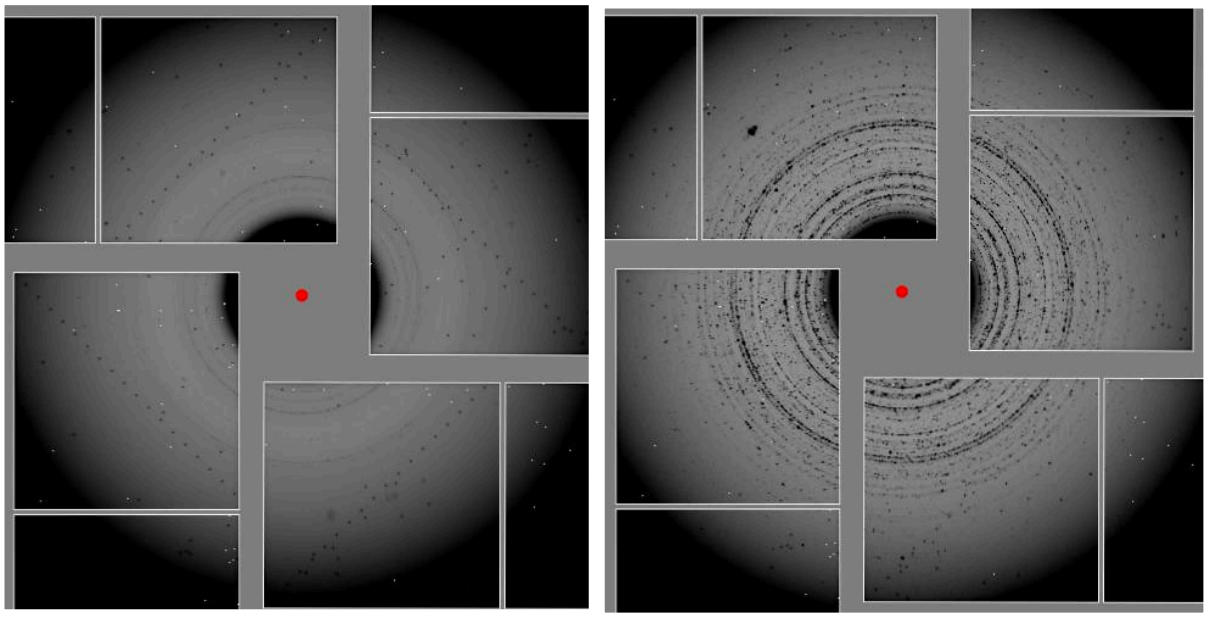

Figure 4-10 Powder diffraction images of SFX data
Cheetah used spot finding algorithms to find frames which contained protein diffraction (hits) and separate them from frames without diffraction (misses). Powder diffractions from the two groups demonstrate that the hit finding parameters were correct, as the hits have protein powder rings, while the misses contain few rings.

The hit class of diffraction patterns were then visually inspected to estimate resolution and diffraction quality. Histograms of the resolution of the images (radius in which 80% of Bragg peaks fall) indicate that there are two types of images within the dataset (Figure 4-11). This was observed for all four samples for which data was collected (Figure 4-12). Furthermore,

Bragg peaks appeared to be split or streaky in the majority of the images across all four samples.

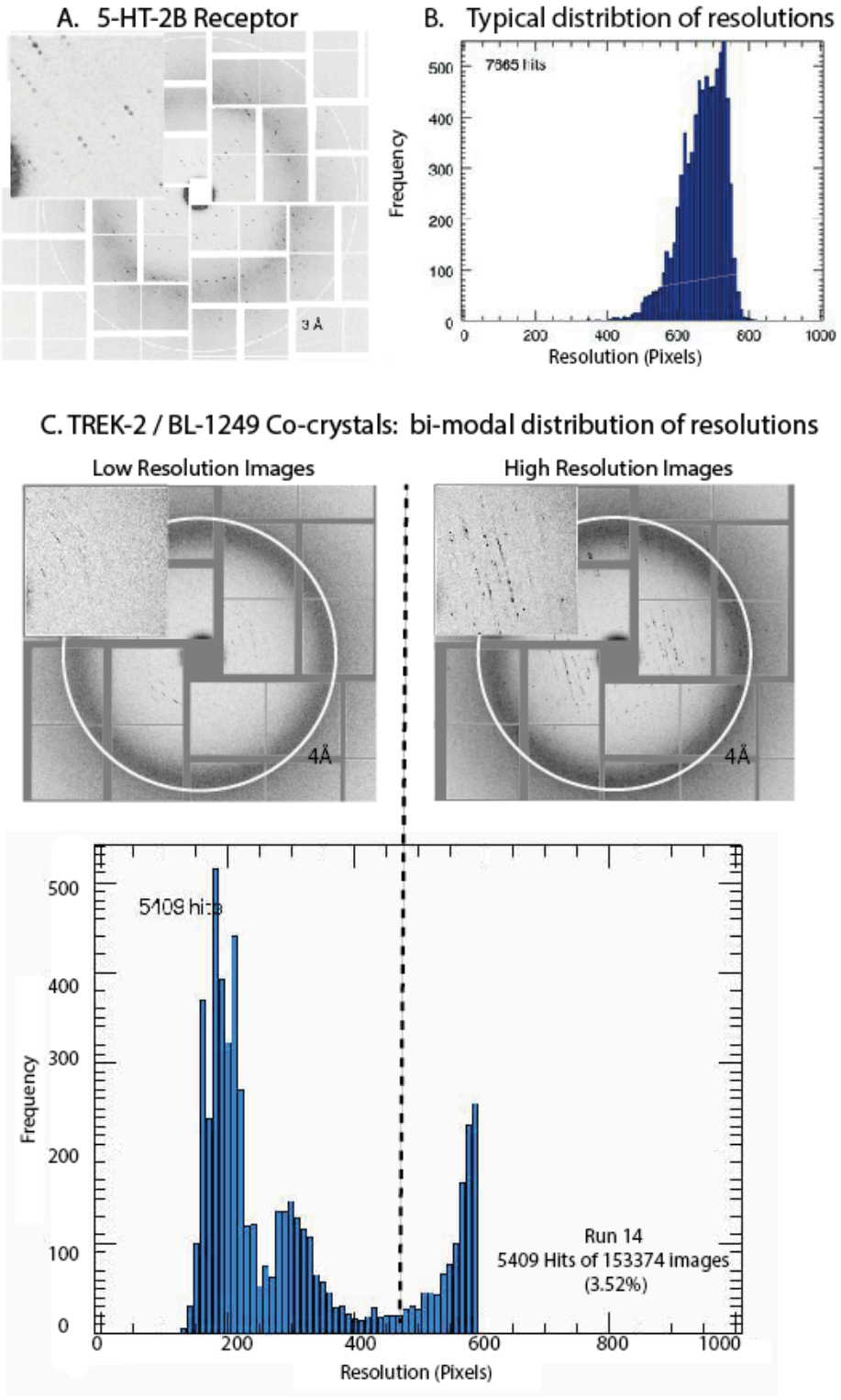

Figure 4-11 Diffraction from TREK-2 microcrystals at the LCLS

Typical diffraction images from the 5-HT_{2B} receptor[186] (A) and typical distributions of images resolutions[185] (B) are shown for reference. Images from the TREK-2 dataset (C) show a bi-modal distribution of resolutions. The majority of images are low resolution, while a smaller number diffract to beyond 4Å. A close-up of diffraction spots is shown inset. TREK-2 diffraction spots are streaky or spit when compared with an ideal dataset (A). Image C taken from Liu et. Al.[173] with permission from AAAS.

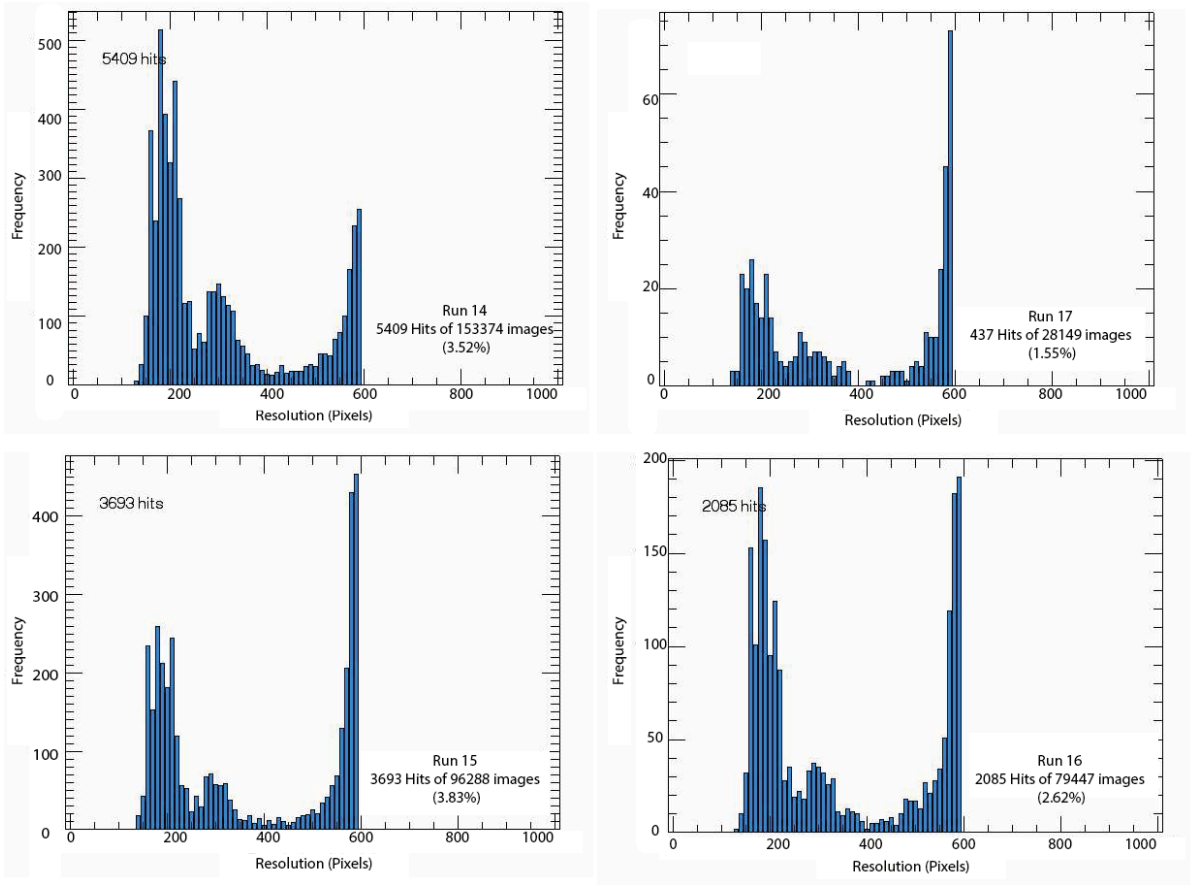

Figure 4-12 Histogram of image resolutions for TREK-2 LCP data

Distribution of image resolutions within the TREK-2/ BL-1249 crystal diffraction data. Shown are the histograms for all four runs (one run is one sample injected onto the beam). All four samples show bi-modal distributions of image resolution.

4.3.3 Space group determination

Hit HDF5 files can then be used for data reduction (indexing and integration) in the software suite crystFEL[187]. Individual images were indexed using the crystFEL program Indexamajig. Peak locations were given within the HDF5 files, as located by CHEETAH, Initially, all crystal-hit images were passed to Indexamajig for indexing using MOSFLM and DIRAX. Of those images, 69.7 % were indexed. Indexing solutions produced a broad spectrum of unit cell parameters (Figure 4-13). Inspection of the images indicated this might be due to the variable image quality.

In order to overcome problems indexing data with variable image quality, images were pre-sorted before re-indexing. Crystal hit images were sorted (framesorter) to ensure they

contained greater than 100 Bragg peaks. These images were then viewed manually to reject highly split crystals, leaving 53 images. However, a large proportion of the images could not be indexed (60.3%), and those that could did not produce a single set of unit cell parameters (Figure 4-13).

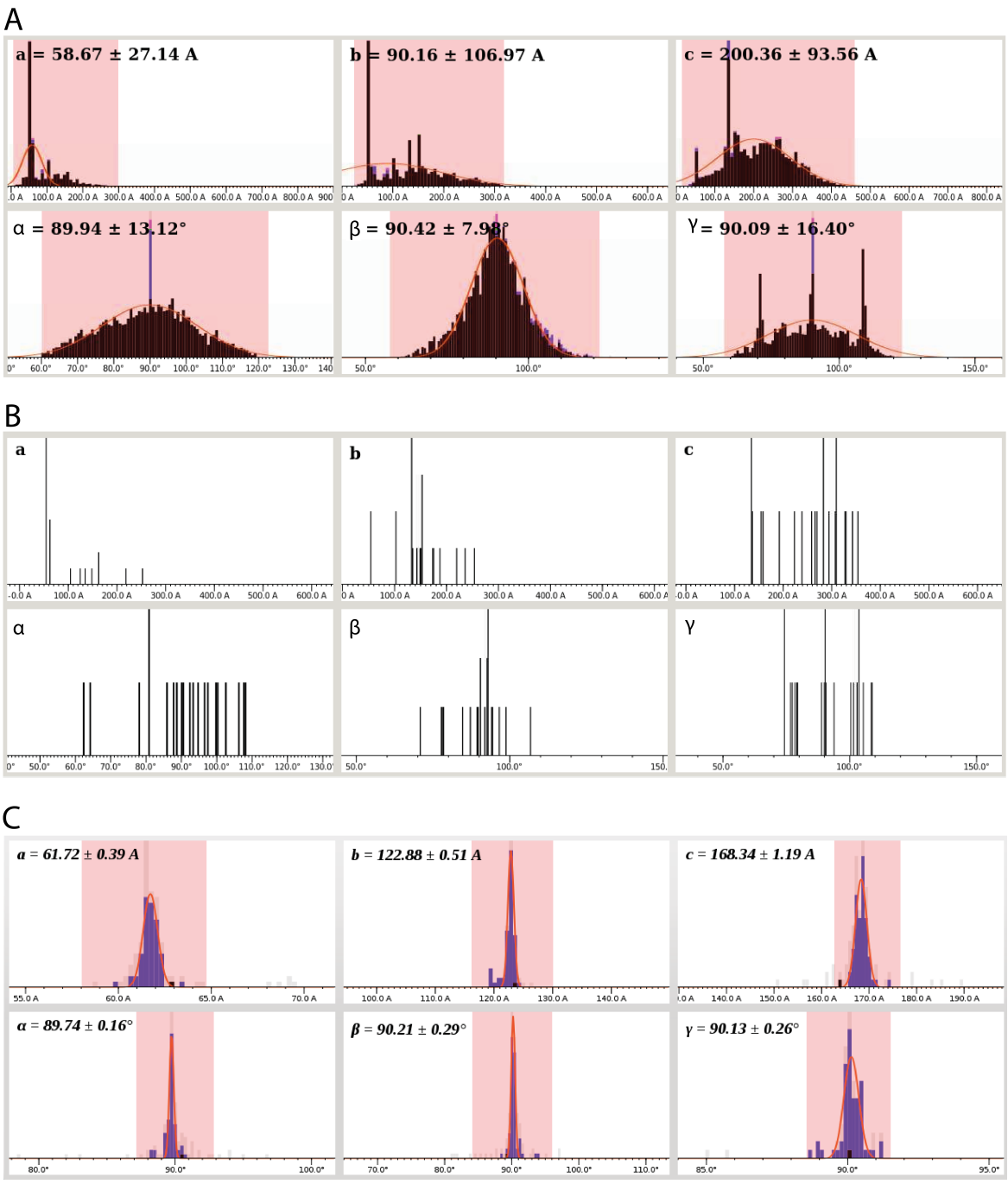

Figure 4-13 Histograms of unit cell parameters for individual SFX images
These histograms show unit cell parameters derived from MOSFLM and DIRAX indexing of individual XFEL images. When processing all TREK-2 images and fitting a Gaussian to the histogram, the unit cell parameters cannot be assigned with confidence due to the broad distributions (A). Pre-selection of images with more than 100 Bragg peaks does not improve this (B). Distribution of unit cell parameters for the 5-HT_{2B} receptor (reproduced from Liu et. Al.[186] with permission from AAAS) is shown for reference (C).

4.4 Discussion

Crystallising protein with hydrophobic ligands is known to be challenging[188,189]. Methods to solubilise hydrophobic ligands include dissolving in organic solvents and placing solid compound into crystallisation drops. Here it is demonstrated that hydrophobic ligands may be solubilised in Monoolein to increase the concentration in the crystallisation solution. This method was suggested by Caffery and Cherezov[190] and may be a useful tactic for typically hydrophobic membrane protein ligands in particular ligands that may access binding sites via the membrane, such as lipids.

Co-crystals of TREK-2 were optimised in sandwich plates and then mixed with MAG 7.9 before being injected onto the XFEL beam at the LCLS. Of 357,288 images collected, 11,624 contained protein diffraction. This is a sub optimal hit rate (3.3%; 20% is optimal), as too few hits means that a dataset will take too long to collect compared with allocated beam time. However, too many hits and you get multiple diffraction patterns in each image which may be difficult to de-convolute. The sample would therefore benefit from increased crystal density.

Of the images containing diffraction most diffracted to only a low resolution, with ~10% diffracting to between 3 and 4Å. Inspection of the sample demonstrates that most of the crystals are small (5-20μm) with a small fraction growing at a larger size (~30μm). This may be the cause of the variable resolutions observed in the diffraction data. To overcome this it would be necessary to continue fine-tuning optimisation of crystals within syringes to produce a homogenous sample of larger crystals. Alternatively, it is possible that the diffraction is strongly anisotropic and the high-resolution diffraction comes from a single crystallographic direction. Although this may improve with optimisation, it is likely an alternative crystal form would need to be sought.

It is also possible that the quality of diffraction was reduced by the addition of MAG7.9 to the sample before data collection. If protein crystals are grown in monoolein (MAG 9.9) and shot at full beam on the free electron laser, the detector will be damaged due to strong powder diffraction rings from the lipid. Lipid rings arise due to the vacuum in the chamber (10^{-3} Torr, to reduce X-ray scatter) causing evaporative cooling of the cubic phase. The cubic phase transitions into lamellar crystalline (L_c), which causes strong powder diffraction rings on the detector leading to detector damage. This may be avoided by either dramatically reducing or X-ray intensity or by preventing formation of the L_c phase. In this experiment the lipid MAG 7.9 was added to the prepared sample and mixed until clear. Addition of MAG 7.9 inhibits formation of L_c [183]. However, the sheer forces resulting from mixing the crystals combined with the change of lipidic environment may have reduced the diffraction quality of the TREK-2 crystals.

Eliminating the need to mix MAG 7.9 with TREK-2 crystals may improve the diffraction quality. This could be achieved in two ways. First, the crystals could be grown in lipidic cubic phase consisting purely of MAG 7.9, or a mix of MAG 7.9 and Monoolein. Alternatively, sample delivery methods could be improved to avoid the need to add MAG 7.9 to Monoolein. Wierstall *et al.*[191] note that by changing the co-flowing gas stream that focuses the LCP jet towards the X-Ray beam from He to N_2, the formation of L_c can be inhibited. Full data sets can therefore be collected without the need for post-growth mixing of crystals with MAG 7.9.

Diffraction images could not be indexed. This is likely to be due to the split and swirly nature of the diffraction. It is possible that the streakiness may be due to mixing with MAG 7.9. However, the splitting may well be intrinsic to the crystal. To overcome this it may be necessary to further investigate crystallisation additives to optimise these crystals.

This experiment utilised BL-1249 without Br modification. Br-BL1249 was not used, as LCLS operating wavelengths do not cover the Br anomalous absorption edge. However,

covalent modification of BL-1249 with atoms whose elemental absorption edges lie within the energies achievable by LCLS could be attached to BL1249. For example, Iodine has an anomalous signal of 10 electrons at around 5keV[192] for the L_1 edge, an energy that lies in the centre of LCLS capabilities[181].

This work re-affirms the niche for SFX as a strategy for data collection from LCP crystals. Optimisation failed to yield crystals large enough for data collection at the synchrotron. This was exemplified by the test images taken at the synchrotron, which despite a large flux (≈ $2x10^{12}$ photons per second) and long exposure times (1-5s) was able to yield just 8Å diffraction.

However it also highlights some difficulties in sample optimisation. Initial crystals could be rapidly optimised in high-throughput by using 96-well glass sandwich plates to screen crystallisation parameters. The conditions that were optimised in sandwich plates did not produce crystals in syringe crystallisation, the method currently used to produce the large sample volumes required for a full SFX dataset. In general, high PEG and salt concentrations were required to obtain crystals in syringes when compared with those in sandwich plates. This may be due to differing rates of evaporation between the to methods; sandwich plates may dry out more quickly due to large surface area to volume ratios of the small drops, or due to the limitations on effective sealing of the plates. Evaporation may also occur between LCP dispensation and plate sealing, although this is minimised by keeping he plate in a humidity chamber.

In order to improve the correlation between the high throughput screening in sandwich plates and low throughput screening in syringes, it may be necessary to further optimise parameters such as size of LCP bolus and volume of crystallisation solution used in LCP sandwich plates. Preliminary experiments were carried out to investigate the effect of the size of the LCP bolus on crystallisation in sandwich plates. However, this did not result in

greater correlation between sandwich plate and syringe crystallisation. Further investigation into these parameters is therefore necessary.

This experiment also highlights the difficulties in determining suitable samples for SFX data collection. This requires accurate and rapid selection of successful crystallisation conditions. The use of cross-polarisers to determine bi-refringence has been particularly useful for observation of microcrystals in this work. SONICC-UV can also be used to verify the presence of crystals. However, as demonstrated in this work, some protein crystals may not be visible with these methods. SONICC is also known to fail in detection of high symmetry crystals.

Once crystals have been detected, optimisation of the crystals for good quality diffraction is challenging. Screening at even a microfocus beam line does not appear to allow discrimination between good and bad samples; in this work samples with <3Å diffraction at XFEL diffracted poorly (8Å) at a third generation synchrotron. Although this may be able to differentiate between non-diffracting and diffracting samples, it may not be useful to discriminate between samples that may diffract to 2-4 Å for example. Current strategies involve producing numerous samples in different crystallisation conditions for screening at PCS time at the CXI instrument at LCLS, prior to data collection. This time is currently very limited, but as more XFEL instruments come online in the future, screening of samples should become easier.

4.5 Conclusions

Here, I present diffraction data collected from TREK-2 crystals grown in lipidic cubic phase in the presence of the small molecule activator BL-1249. Further optimisation and data collection is necessary to obtain a full dataset and determine the binding site of the ligand.

This work demonstrates that lipidic cubic phase may be used to co-crystallise membrane proteins with hydrophobic ligands. This may be of particular interest where ligands are known or suspected to act on a protein via the membrane.

However, this work also demonstrates the challenges faced in producing crystals in the lipidic cubic phase. Notably demonstrates that large crystals may be difficult to produce. To overcome this a serial femtosecond crystallography approach may be used. However, this approach is not without its difficulties. In particular detection of microcrystals, triage of crystals at synchrotron beam lines, and reproduction of large volumes of crystals from initial hits in high through-put screens are challenges when using this method.

4.6 Materials and Methods

4.6.1 Reconstitution of purified TREK-2 into LCP

Preparation of protein sample: Detergent solubilised TREK-2 (KCNK10C) was purified as described in section 2.5.1and concentrated to 60mg/ml (30kDa PES concentrator, Vivaspin). As concentrated protein had detergent concentrations around 5% w/v (Tested with a colorimetric assay[193] by Annamaria Tessitore) it was diluted in GFB (Chapter 3) without detergent to obtain the concentration required for crystallisation (15,30,45, or 60mg/ml). This minimised the final detergent concentration, as high detergent concentrations are known to affect the phase diagram of monoolein[194].

Preparation of Monoolein: Monoolein (1-oleoyl-rac-glycerol; MAG 9.9; Nu Chek Prep M-239) was warmed to 42°C. (5,6,7,8-Tetrahydro-naphthalen-1-yl)-[2-(1H-tetrazol-5-yl)-phenyl]-amine (BL-1249; Sigma-Aldrich CAS 18200-13-0) powder was added to the solution to a final concentration of 10mM. Solution was vortexed every 60 seconds until the ligand was completely dissolved. Stock solution was filtered through a 5µm centrifugal filter

(Millipore Ultrafree-MC SV, UFC30SV00) to remove solid particles that may block the injector nozzle during data collection. Samples were stored in 50µL aliquots at -20°C. Before use, an aliquot was heated to 42°C and vortexed thoroughly.

Preparation of Lipidic Cubic Phase: Lipid and protein were mixed in a 2:1 v/v ratio using the following protocol. Two 100µL gas-tight syringes (Hamilton Gastight Model 1710; 7656-01) were cleaned thoroughly with methanol and lens tissue, followed by an air-duster. The required volume of detergent-solubilised protein was pipetted into a syringe. A gastight syringe coupler (Formulatrix; SK 209526) was screwed on to the syringe. Gentle pressure was applied to the syringe plunger to remove air contained within the syringe coupler. When protein solution emerged at the end of the coupler, the plunger was retracted slightly to prevent loss of protein solution.

A second syringe was placed on top of a heat set at 42°C to warm, along with the prepared monoolein. The appropriate volume of monoolein was pipetted into the warmed syringe and air bubbles were removed by rapidly pushing the plunger up and down. The two syringes were then combined via the coupler and the solution mixed by pushing alternatively on the plungers of either syringe. The solution turned transparent and glassy after less than one minute of mixing. Mixing was continued for approximately 5 minutes to ensure homogeneity in the sample.

Para-film was wrapped around the syringe coupler to prevent dehydration of the resulting Lipidic Cubic Phase. The coupled syringe were then placed in a 20°C incubator for three hours, to allow the BL-1249 to bind to the protein.

4.6.2 High throughput screening in sandwich plates

After incubation, the cubic phase was pushed into a single syringe, and the coupling device removed. A dispensing needle was the attached to the syringe. The syringe was then placed on a crystallisation robot (Moquito-LCP) with a humidity control chamber, pre-equilibrated to 70% humidity. The robot aliquoted 50nL boli of LCP on to glass 96-well sandwich plates (Marienfield GmBH; CAT 0890003). 800nL of screen was added to the LCP bolus. Commercial screens were used (MemGold, MemGold2, MemSysStart; Molecular Dimensions) at 0.7x dilution, as undiluted screens are known to destabilise LCP[195]. The plates were thoroughly sealed and placed in a 20°C incubator.

Plates were monitored over a 14-day period for crystal growth. Drops containing crystals were detected by birefringence using a cross polariser mounted on a microscope (Leica M205)

4.6.3 In-syringe crystallisation screening

To produce large volumes of sample for data collection, it was necessary to crystallise TREK-2 in syringes. Cubic phase was prepared as described in section 6.4.1. 60µL of crystallisation solution was then drawn into a 100µL gas-tight Hamilton syringe. 5µL of cubic phase was then manually dispensed through a needle into the crystallisation solution. Syringes were thoroughly sealed using parafilm and stored in airtight zip-lock bags with damp cloths to maintain high levels of humidity. Samples were monitored over a period of 1-2 weeks for crystal growth using a cross-polariser attached to a microscope.

4.6.4 Sample preparation for data collection

Crystal growth and sample selection: Samples intended for data collection were prepared as described in 6.4.3. Sample syringes were produced in triplicate, to ensure enough material for a single run (15µL) at the XFEL. Test syringes containing 2µL of cubic phase

and 20μL crystallisation solution were set up for each set of syringes. The sample in the test syringes was inspected in a cover slip to determine which sets of syringes were suitable for data collection. In this way, samples with a high crystal density were selected for data collection.

Combining syringes for data collection: In order to produce the 15μL required for a single run at the XFEL, triplicates of syringes were combined. Crystallisation solution was removed from syringes by gently pushing the plunger while viewing the sample under a microscope. This caused the LCP to gather at the top of each syringe. Syringe couplers were used to combine the three samples into a singe syringe.

Adding MAG7.9 to the sample: To prevent formation of lipid rings on the detector, 1-(7Z-hexadecenoyl)-rac-glycerol (MAG 7.9, Avanti Polar Lipids, 850534) was added to the sample as follows. MAG 7.9 was melted on a heat block at 45°C with an empty syringe. 2μL of MAG 7.9 was slowly pipetted into the warm syringe, and air bubbles were removed. The syringe was then attached to the sample syringe using a syringe coupler. The sample was mixed until clear by applying gentle pressure to the syringe plungers alternately.

4.6.5 Data collection at LCLS-CXI instrument

Data were collected at the LCLS-CXI instrument at the Stanford Linear Accelerator Centre (SLAC) National Laboratory in Menlo Park, U.S.A. Samples were combined to make 15 μL sample volume, and 2μL of MAG 7.9 was added. Sample was loaded into an injector of 50μm nozzle (as described by Weierstall *et. Al.* [191]) and jetted onto the beam with parameters as in Table 4-1.

The data presented here were collected by a collaborative team of scientists running the LCLS-CXI instrument during the run cxig4314 in November 2014. Preparing samples were Liz Carpenter, Ashley Pike and Yin Dong. Operating the beam was Andy Quila, while Nadia Zatespin Cornelius Gati, Shibom Basu and Tom Grant provided support with data analysis.

Uwe Weierstall and Daniel James ran the sample injector. Further support and advice was provided by Petra Fromme, Tom White, Garrett Nelson, Chelsie Conrad, Jessie Coe and Vadim Cherezov.

Further TREK-2 crystals were screened on a second run of the CXI instrument (data not presented here) in April 2015. Preparing samples were Liz Carpenter, Ashley Pike, Yin Dong and Alexandra Mackenzie with help and advice from Chelsie Conrad. Operating the beam was Mark Hunter, while Nadia Zatespin provided support with data analysis. Garrett Nelson ran the sample injector.

Data Collection Parameters for TREK-2 at LCLS-CXI Instrument	
Crystallisation Solution	30mg/ml (967μM of monomer) TREK-2 ; 6mM BL-1249 ; 0.1M TRIS pH 8.5; 36-37% PEG200
Sample Volume	15μL
Number of Images	357,288
Number of Hits	11,624 (3.3%)
Maximum Resolution	3-4Å
Nozzle diameter	50μm
Distance between images	16.64μm
Jet Speed	19.97mm/s
Viscous Flow Rate	0.235μL/s
Gas Pressure (He)	110 PSI
Pressure on Liquid	17 PSI
Beam Energy	9.49keV (1.306Å)
Pulse Frequency	120Hz
Pulse Length	42fs
Pulse Energy	1.39mJ
Beam Transmission	8%

Table 4-1 Data collection parameters for Serial Femtosecond Crystallography data

4.6.6 Data analysis with CrystFEL and Cheetah

Streams of data (XTC files) generated at the XFEL were initially analysed with CHEETAH[185] 2015.3. CHEETAH was provided with geometry file that mapped the layout of pixels on the csPAD detector. Dark current (XTC streams without sample) was first analysed to allow CEETAH to calibrate and correct detector pixels. Bragg peaks with a six fold signal to noise ratio and an area between 2 and 20 pixels were identified. Frames were identified as hits if they contained between 20 and 5000 such Bragg peaks. CHEETAH provided each hit image in HDF5 format (containing peak locations and intensities) as well as powder diffraction images.

Hits as determined by CHEETAH were then indexed using Indexamajig in crystFEL 0.5.4[196]. Images were processed using both MOSFLM and DIRAX. Output of Indexamajig was viewed using the cell explorer tool within crystFEL.

Chapter 5 Concluding Remarks

The results presented here provide insight into the binding of an inhibitor (fluoxetine) and an activator (BL-1249) to the K2P channel TREK-2.

The binding site of two fluoxetine derivatives (brominated fluoxetine and norfluoxetine) are determined to be within the fenestrations of a down state channel with it's S1 potassium site unoccupied. In contrast, the up state of the channel has four potassium sites while the fenestrations are closed, occluding the inhibitor-binding site. This implies that the down-state has a lower activity.

Co-crystallisation of TREK-2 with brominated BL-1249 indicates that the molecule may bind close to Pro^{198}, beneath the fluoxetine binding site. However as no ligand density was visible in the site this ligand could not be modelled. This data indicates that it may be possible for TREK-2 to be functionally active while in the down state.

When combined with data from other TREK-2 structures, this allows formation of a gating model for K2P channels. In this model, downwards movement of M4 and the outwards movement of M2/3 result in a lower conductivity state that can be stabilised by inhibitors. However, the down state may also become activated through C-type gating or binding of activators.

Future studies may aim to determine the structural mechanisms linking ligand binding and helical movements to channel gating.

Chapter 6 References

1. Alberts, B. *Molecular Biology of the Cell: Reference edition, Volume 1*. (Garland Science, 2008).
2. Luckey, M. *Membrane Structural Biology: With Biochemical and Biophysical Foundations*. (Cambridge University Press, 2008).
3. Krogh, A., Larsson, B., von Heijne, G. & Sonnhammer, E. L. Predicting transmembrane protein topology with a hidden Markov model: application to complete genomes. *J. Mol. Biol.* **305,** 567–80 (2001).
4. Overington, J. P., Al-Lazikani, B. & Hopkins, A. L. How many drug targets are there? *Nat. Rev. Drug Discov.* **5,** 993–6 (2006).
5. Gadsby, D. C. Ion channels versus ion pumps: the principal difference, in principle. *Nat. Rev. Mol. Cell Biol.* **10,** 344–52 (2009).
6. Miller, P. S. & Aricescu, A. R. Crystal structure of a human GABAA receptor. *Nature* **512,** 270–5 (2014).
7. Janovjak, H., Szobota, S., Wyart, C., Trauner, D. & Isacoff, E. Y. A light-gated, potassium-selective glutamate receptor for the optical inhibition of neuronal firing. *Nat. Neurosci.* **13,** 1027–1032 (2010).
8. Haswell, E. S., Phillips, R. & Rees, D. C. Mechanosensitive channels: what can they do and how do they do it? *Structure* **19,** 1356–69 (2011).
9. Shen, B., Wong, C. O., Lau, O. C., Woo, T., Bai, S., Huang, Y. & Yao, X. Plasma membrane mechanical stress activates TRPC5 channels. *PLoS One* **10,** e0122227 (2015).
10. Catterall, W. A. Ion channel voltage sensors: structure, function, and pathophysiology. *Neuron* **67,** 915–28 (2010).
11. Wemmie, J. A., Taugher, R. J. & Kreple, C. J. Acid-sensing ion channels in pain and disease. *Nat. Rev. Neurosci.* **14,** 461–71 (2013).
12. Sherwood, T. W., Frey, E. N. & Askwith, C. C. Structure and activity of the acid-sensing ion channels. *Am. J. Physiol. Cell Physiol.* **303,** C699–710 (2012).
13. Nagel, G., Szellas, T., Huhn, W., Kateriya, S., Adeishvili, N., Berthold, P., Ollig, D., Hegemann, P. & Bamberg, E. Channelrhodopsin-2, a directly light-gated cation-selective membrane channel. *Proc. Natl. Acad. Sci. U. S. A.* **100,** 13940–13945 (2003).
14. Huang, W. C., Xiao, S., Huang, F., Harfe, B. D., Jan, Y. N. & Jan, L. Y. Calcium-activated chloride channels (CaCCs) regulate action potential and synaptic response in hippocampal neurons. *Neuron* **74,** 179–92 (2012).
15. Cao, E., Cordero-Morales, J. F., Liu, B., Qin, F. & Julius, D. TRPV1 channels are intrinsically heat sensitive and negatively regulated by phosphoinositide lipids. *Neuron* **77,** 667–79 (2013).
16. Dudev, T. & Lim, C. Ion selectivity strategies of sodium channel selectivity filters. *Acc. Chem. Res.* **47,** 3580–7 (2014).
17. Owsianik, G., Talavera, K., Voets, T. & Nilius, B. Permeation and selectivity of TRP channels. *Annu. Rev. Physiol.* **68,** 685–717 (2006).
18. Mowrey, D., Chen, Q., Liang, Y., Liang, J., Xu, Y. & Tang, P. Signal transduction pathways in the pentameric ligand-gated ion channels. *PLoS One* **8,** e64326 (2013).
19. Schroeder, J. I. & Hedrich, R. Involvement of ion channels and active transport in osmoregulation and signaling of higher plant cells. *Trends Biochem. Sci.* **14,** 187–92 (1989).
20. Schwab, A., Fabian, A., Hanley, P. J. & Stock, C. Role of ion channels and transporters in cell migration. *Physiol. Rev.* **92,** 1865–913 (2012).
21. Doyle, D. A., Morais Cabral, J., Pfuetzner, R. A., Kuo, A., Gulbis, J. M., Cohen, S. L., Chait, B. T. & MacKinnon, R. The structure of the potassium channel: molecular basis of K+ conduction and selectivity. *Science* **280,** 69–77 (1998).
22. Rupp, B. *Biomolecular Crystallography: Principles, Practice, and Application to Structural Biology*. (Garland Science, 2010).
23. Giacovazzo, C., Monaco, H. L., Artioli, G., Viterbo, D., Milanesio, M., Gilli, G., Gilli, P., Zanotti,

G., Ferraris, G. & Catti, M. *Fundamentals of Crystallography*. (OUP Oxford, 2011).

24. Rhodes, G. *Crystallography Made Crystal Clear: A Guide for Users of Macromolecular Models*. (Academic Press, 2010).

25. Jiang, Y., Lee, A., Chen, J., Cadene, M., Chait, B. T. & MacKinnon, R. Crystal structure and mechanism of a calcium-gated potassium channel. *Nature* **417,** 515–22 (2002).

26. Jiang, Y., Lee, A., Chen, J., Ruta, V., Cadene, M., Chait, B. T. & MacKinnon, R. X-ray structure of a voltage-dependent K+ channel. *Nature* **423,** 33–41 (2003).

27. Kuo, A., Gulbis, J. M., Antcliff, J. F., Rahman, T., Lowe, E. D., Zimmer, J., Cuthbertson, J., Ashcroft, F. M., Ezaki, T. & Doyle, D. A. Crystal structure of the potassium channel KirBac1.1 in the closed state. *Science* **300,** 1922–6 (2003).

28. Nishida, M. & MacKinnon, R. Structural basis of inward rectification: cytoplasmic pore of the G protein-gated inward rectifier GIRK1 at 1.8 A resolution. *Cell* **111,** 957–65 (2002).

29. Zhou, Y., Morais-Cabral, J. H., Kaufman, A. & MacKinnon, R. Chemistry of ion coordination and hydration revealed by a K+ channel-Fab complex at 2.0 A resolution. *Nature* **414,** 43–8 (2001).

30. Payandeh, J., Scheuer, T., Zheng, N. & Catterall, W. A. The crystal structure of a voltage-gated sodium channel. *Nature* **475,** 353–358 (2011).

31. McCusker, E. C., Bagnéris, C., Naylor, C. E., Cole, A. R., D'Avanzo, N., Nichols, C. G. & Wallace, B. A. Structure of a bacterial voltage-gated sodium channel pore reveals mechanisms of opening and closing. *Nat. Commun.* **3,** 1102 (2012).

32. Shi, N., Ye, S., Alam, A., Chen, L. & Jiang, Y. Atomic structure of a Na+- and K+-conducting channel. *Nature* **440,** 570–4 (2006).

33. Moiseenkova-Bell, V. Y., Stanciu, L. A., Serysheva, I. I., Tobe, B. J. & Wensel, T. G. Structure of TRPV1 channel revealed by electron cryomicroscopy. *Proc. Natl. Acad. Sci. U. S. A.* **105,** 7451–5 (2008).

34. Kew, J. & Davies, C. *Ion Channels: From Structure to Function*. (2010).

35. Alexander, S. P. H., Benson, H. E., Faccenda, E., Pawson, A. J., Sharman, J. L., Catterall, W. A., Spedding, M., Peters, J. A. & Harmar, A. J. The concise guide to Pharmacology 2013/14: ion channels. *Br. J. Pharmacol.* **170,** 1607–51 (2013).

36. Littleton, J. T. & Ganetzky, B. Ion channels and synaptic organization: analysis of the Drosophila genome. *Neuron* **26,** 35–43 (2000).

37. Hille, B. *Ionic Channels of Excitable Membranes*. (Mass., 1992).

38. Battefeld, A., Tran, B. T., Gavrilis, J., Cooper, E. C. & Kole, M. H. P. Heteromeric Kv7.2/7.3 channels differentially regulate action potential initiation and conduction in neocortical myelinated axons. *J. Neurosci.* **34,** 3719–32 (2014).

39. Liu, P. W. & Bean, B. P. Kv2 channel regulation of action potential repolarization and firing patterns in superior cervical ganglion neurons and hippocampal CA1 pyramidal neurons. *J. Neurosci.* **34,** 4991–5002 (2014).

40. McFerrin, M. B., Turner, K. L., Cuddapah, V. A. & Sontheimer, H. Differential role of IK and BK potassium channels as mediators of intrinsic and extrinsic apoptotic cell death. *Am. J. Physiol. Cell Physiol.* **303,** C1070–8 (2012).

41. Jensen, B. S., Odum, N., Jorgensen, N. K., Christophersen, P. & Olesen, S. P. Inhibition of T cell proliferation by selective block of Ca(2+)-activated K(+) channels. *Proc. Natl. Acad. Sci. U. S. A.* **96,** 10917–21 (1999).

42. Morais-Cabral, J. H., Zhou, Y. & MacKinnon, R. Energetic optimization of ion conduction rate by the K+ selectivity filter. *Nature* **414,** 37–42 (2001).

43. Derebe, M. G., Sauer, D. B., Zeng, W., Alam, A., Shi, N. & Jiang, Y. Tuning the ion selectivity of tetrameric cation channels by changing the number of ion binding sites. *Proc. Natl. Acad. Sci. U. S. A.* **108,** 598–602 (2011).

44. Furini, S. & Domene, C. Selectivity and permeation of alkali metal ions in K+-channels. *J. Mol. Biol.* **409,** 867–78 (2011).

45. Egwolf, B. & Roux, B. Ion selectivity of the KcsA channel: a perspective from multi-ion free energy landscapes. *J. Mol. Biol.* **401,** 831–42 (2010).

46. Furini, S. & Domene, C. Nonselective conduction in a mutated NaK channel with three cation-binding sites. *Biophys. J.* **103,** 2106–14 (2012).

47. Darré, L., Furini, S. & Domene, C. Permeation and dynamics of an open-activated TRPV1 channel. *J. Mol. Biol.* **427,** 537–49 (2015).

48. Bagnéris, C., Naylor, C. E., McCusker, E. C. & Wallace, B. A. Structural model of the open-closed-inactivated cycle of prokaryotic voltage-gated sodium channels. *J. Gen. Physiol.* **145,** 5–16 (2015).

49. Zhou, Y. & MacKinnon, R. The occupancy of ions in the K+ selectivity filter: charge balance and coupling of ion binding to a protein conformational change underlie high conduction rates. *J. Mol. Biol.* **333,** 965–975 (2003).

50. Bernèche, S. & Roux, B. Energetics of ion conduction through the K+ channel. *Nature* **414,** 73–7 (2001).

51. Roux, B. Ion conduction and selectivity in K(+) channels. *Annu. Rev. Biophys. Biomol. Struct.* **34,** 153–71 (2005).

52. Hummer, G. Biochemistry. Potassium ions line up. *Science* **346,** 303 (2014).

53. Köpfer, D. A., Song, C., Gruene, T., Sheldrick, G. M., Zachariae, U. & de Groot, B. L. Ion permeation in K^+ channels occurs by direct Coulomb knock-on. *Science* **346,** 352–5 (2014).

54. Cuello, L. G., Jogini, V., Cortes, D. M. & Perozo, E. Structural mechanism of C-type inactivation in K(+) channels. *Nature* **466,** 203–8 (2010).

55. Petkov, G. V. Role of potassium ion channels in detrusor smooth muscle function and dysfunction. *Nat. Rev. Urol.* **9,** 30–40 (2012).

56. Sharma, C. *Structure and Function Studies of K2P Channels, DPhil. Thesis*. (2012).

57. Honoré, E. The neuronal background K2P channels: focus on TREK1. *Nat. Rev. Neurosci.* **8,** 251–61 (2007).

58. Poulsen, H. & Nissen, P. Structural biology. The inner workings of a dynamic duo. *Science* **335,** 416–7 (2012).

59. Hodgkin, A. L. & Huxley, A. F. A quantitative description of membrane current and its application to conduction and excitation in nerve. *J. Physiol.* **117,** 500–44 (1952).

60. Ketchum, K. A., Joiner, W. J., Sellers, A. J., Kaczmarek, L. K. & Goldstein, S. A. A new family of outwardly rectifying potassium channel proteins with two pore domains in tandem. *Nature* **376,** 690–5 (1995).

61. Czempinski, K., Zimmermann, S., Ehrhardt, T. & Müller-Röber, B. New structure and function in plant K+ channels: KCO1, an outward rectifier with a steep Ca2+ dependency. *EMBO J.* **16,** 2565–75 (1997).

62. Kunkel, M. T., Johnstone, D. B., Thomas, J. H. & Salkoff, L. Mutants of a temperature-sensitive two-P domain potassium channel. *J. Neurosci.* **20,** 7517–24 (2000).

63. Goldstein, S. A., Price, L. A., Rosenthal, D. N. & Pausch, M. H. ORK1, a potassium-selective leak channel with two pore domains cloned from Drosophila melanogaster by expression in Saccharomyces cerevisiae. *Proc. Natl. Acad. Sci. U. S. A.* **93,** 13256–61 (1996).

64. Lesage, F., Guillemare, E., Fink, M., Duprat, F., Lazdunski, M., Romey, G. & Barhanin, J. TWIK-1, a ubiquitous human weakly inward rectifying K+ channel with a novel structure. *EMBO J.* **15,** 1004–11 (1996).

65. Miller, A. N. & Long, S. B. Crystal structure of the human two-pore domain potassium channel K2P1. *Science* **335,** 432–6 (2012).

66. Brohawn, S. G., del Marmol, J. & MacKinnon, R. Crystal Structure of the Human K2P TRAAK, a Lipid- and Mechano-Sensitive K+ Ion Channel. *Science (80-.).* **335,** 436–441 (2012).

67. Ma, L., Zhang, X. & Chen, H. TWIK-1 two-pore domain potassium channels change ion selectivity and conduct inward leak sodium currents in hypokalemia. *Sci. Signal.* **4,** ra37 (2011).

68. Enyedi, P. & Czirják, G. Molecular background of leak K+ currents: two-pore domain potassium channels. *Physiol. Rev.* **90,** 559–605 (2010).

69. Fink, M., Duprat, F., Lesage, F., Reyes, R., Romey, G., Heurteaux, C. & Lazdunski, M. Cloning, functional expression and brain localization of a novel unconventional outward

rectifier K+ channel. *EMBO J.* **15,** 6854–62 (1996).

70. Czirják, G. & Enyedi, P. Formation of functional heterodimers between the TASK-1 and TASK-3 two-pore domain potassium channel subunits. *J. Biol. Chem.* **277,** 5426–32 (2002).

71. Hwang, E. M., Kim, E., Yarishkin, O., Woo, D. H., Han, K.-S., Park, N., Bae, Y., Woo, J., Kim, D., Park, M., Lee, C. J. & Park, J.-Y. A disulphide-linked heterodimer of TWIK-1 and TREK-1 mediates passive conductance in astrocytes. *Nat. Commun.* **5,** 3227 (2014).

72. Poulsen, H. & Nissen, P. Structural biology. The inner workings of a dynamic duo. *Science* **335,** 416–7 (2012).

73. Long, S. B., Campbell, E. B. & Mackinnon, R. Voltage sensor of Kv1.2: structural basis of electromechanical coupling. *Science* **309,** 903–8 (2005).

74. Brohawn, S. G., Campbell, E. B. & MacKinnon, R. Domain-swapped chain connectivity and gated membrane access in a Fab-mediated crystal of the human TRAAK K+ channel. *Proc. Natl. Acad. Sci. U. S. A.* **110,** 2129–34 (2013).

75. Dong, Y. Y., Pike, A. C. W., Mackenzie, A., McClenaghan, C., Aryal, P., Dong, L., Quigley, A., Grieben, M., Goubin, S., Mukhopadhyay, S., Ruda, G. F., Clausen, M. V, Cao, L., Brennan, P. E., Burgess-Brown, N. A., Sansom, M. S. P., Tucker, S. J. & Carpenter, E. P. K2P channel gating mechanisms revealed by structures of TREK-2 and a complex with Prozac. *Science* **347,** 1256–9 (2015).

76. Brohawn, S. G., Campbell, E. B. & MacKinnon, R. Physical mechanism for gating and mechanosensitivity of the human TRAAK K+ channel. *Nature* **516,** 126–130 (2014).

77. Lolicato, M., Riegelhaupt, P. M., Arrigoni, C., Clark, K. A. & Minor, D. L. Transmembrane helix straightening and buckling underlies activation of mechanosensitive and thermosensitive K(2P) channels. *Neuron* **84,** 1198–212 (2014).

78. Maingret, F., Honoré, E., Lazdunski, M. & Patel, A. J. Molecular basis of the voltage-dependent gating of TREK-1, a mechano-sensitive K(+) channel. *Biochem. Biophys. Res. Commun.* **292,** 339–46 (2002).

79. Enyedi, P. & Czirják, G. Molecular background of leak K+ currents: two-pore domain potassium channels. *Physiol. Rev.* **90,** 559–605 (2010).

80. Bang, H., Kim, Y. & Kim, D. TREK-2, a new member of the mechanosensitive tandem-pore K+ channel family. *J. Biol. Chem.* **275,** 17412–9 (2000).

81. Lesage, F., Terrenoire, C., Romey, G. & Lazdunski, M. Human TREK2, a 2P domain mechano-sensitive K+ channel with multiple regulations by polyunsaturated fatty acids, lysophospholipids, and Gs, Gi, and Gq protein-coupled receptors. *J. Biol. Chem.* **275,** 28398–405 (2000).

82. Fink, M., Lesage, F., Duprat, F., Heurteaux, C., Reyes, R., Fosset, M. & Lazdunski, M. A neuronal two P domain K+ channel stimulated by arachidonic acid and polyunsaturated fatty acids. *EMBO J.* **17,** 3297–308 (1998).

83. Noël, J., Sandoz, G. & Lesage, F. Molecular regulations governing TREK and TRAAK channel functions. *Channels (Austin).* **5,** 402–9

84. Medhurst, A. D., Rennie, G., Chapman, C. G., Meadows, H., Duckworth, M. D., Kelsell, R. E., Gloger, I. I. & Pangalos, M. N. Distribution analysis of human two pore domain potassium channels in tissues of the central nervous system and periphery. *Brain Res. Mol. Brain Res.* **86,** 101–14 (2001).

85. Gu, W., Schlichthörl, G., Hirsch, J. R., Engels, H., Karschin, C., Karschin, A., Derst, C., Steinlein, O. K. & Daut, J. Expression pattern and functional characteristics of two novel splice variants of the two-pore-domain potassium channel TREK-2. *J. Physiol.* **539,** 657–68 (2002).

86. Kim, Y., Gnatenco, C., Bang, H. & Kim, D. Localization of TREK-2 K+ channel domains that regulate channel kinetics and sensitivity to pressure, fatty acids and pHi. *Pflugers Arch.* **442,** 952–60 (2001).

87. Patel, A. J., Honoré, E., Maingret, F., Lesage, F., Fink, M., Duprat, F. & Lazdunski, M. A mammalian two pore domain mechano-gated S-like K+ channel. *EMBO J.* **17,** 4283–90 (1998).

88. Thomas, D., Plant, L. D., Wilkens, C. M., McCrossan, Z. A. & Goldstein, S. A. N. Alternative translation initiation in rat brain yields K2P2.1 potassium channels permeable to sodium.

Neuron **58,** 859–70 (2008).

89. Simkin, D., Cavanaugh, E. J. & Kim, D. Control of the single channel conductance of K2P10.1 (TREK-2) by the amino-terminus: role of alternative translation initiation. *J. Physiol.* **586,** 5651–63 (2008).

90. Rajan, S., Preisig-Müller, R., Wischmeyer, E., Nehring, R., Hanley, P. J., Renigunta, V., Musset, B., Schlichthörl, G., Derst, C., Karschin, A. & Daut, J. Interaction with 14-3-3 proteins promotes functional expression of the potassium channels TASK-1 and TASK-3. *J. Physiol.* **545,** 13–26 (2002).

91. Heurteaux, C., Lucas, G., Guy, N., El Yacoubi, M., Thümmler, S., Peng, X.-D., Noble, F., Blondeau, N., Widmann, C., Borsotto, M., Gobbi, G., Vaugeois, J.-M., Debonnel, G. & Lazdunski, M. Deletion of the background potassium channel TREK-1 results in a depression-resistant phenotype. *Nat. Neurosci.* **9,** 1134–41 (2006).

92. Heurteaux, C., Guy, N., Laigle, C., Blondeau, N., Duprat, F., Mazzuca, M., Lang-Lazdunski, L., Widmann, C., Zanzouri, M., Romey, G. & Lazdunski, M. TREK-1, a K+ channel involved in neuroprotection and general anesthesia. *EMBO J.* **23,** 2684–95 (2004).

93. Noël, J., Zimmermann, K., Busserolles, J., Deval, E., Alloui, A., Diochot, S., Guy, N., Borsotto, M., Reeh, P., Eschalier, A. & Lazdunski, M. The mechano-activated K+ channels TRAAK and TREK-1 control both warm and cold perception. *EMBO J.* **28,** 1308–18 (2009).

94. Pereira, V., Busserolles, J., Christin, M., Devilliers, M., Poupon, L., Legha, W., Alloui, A., Aissouni, Y., Bourinet, E., Lesage, F., Eschalier, A., Lazdunski, M. & Noël, J. Role of the TREK2 potassium channel in cold and warm thermosensation and in pain perception. *Pain* **155,** 2534–44 (2014).

95. Alloui, A., Zimmermann, K., Mamet, J., Duprat, F., Noël, J., Chemin, J., Guy, N., Blondeau, N., Voilley, N., Rubat-Coudert, C., Borsotto, M., Romey, G., Heurteaux, C., Reeh, P., Eschalier, A. & Lazdunski, M. TREK-1, a K+ channel involved in polymodal pain perception. *EMBO J.* **25,** 2368–76 (2006).

96. Duprat, F., Lesage, F., Fink, M., Reyes, R., Heurteaux, C. & Lazdunski, M. TASK, a human background K+ channel to sense external pH variations near physiological pH. *EMBO J.* **16,** 5464–71 (1997).

97. Ashmole, I., Goodwin, P. A. & Stanfield, P. R. TASK-5, a novel member of the tandem pore K+ channel family. *Pflugers Arch.* **442,** 828–33 (2001).

98. Kim, Y., Bang, H. & Kim, D. TASK-3, a new member of the tandem pore K(+) channel family. *J. Biol. Chem.* **275,** 9340–7 (2000).

99. Meadows, H. J., Benham, C. D., Cairns, W., Gloger, I., Jennings, C., Medhurst, A. D., Murdock, P. & Chapman, C. G. Cloning, localisation and functional expression of the human orthologue of the TREK-1 potassium channel. *Pflugers Arch.* **439,** 714–22 (2000).

100. Kim, C. J., Cho, Y. G., Jeong, S. W., Kim, Y. S., Kim, S. Y., Nam, S. W., Lee, S. H., Yoo, N. J., Lee, J. Y. & Park, W. S. Altered expression of KCNK9 in colorectal cancers. *APMIS* **112,** 588–94 (2004).

101. Bittner, S., Budde, T., Wiendl, H. & Meuth, S. G. From the background to the spotlight: TASK channels in pathological conditions. *Brain Pathol.* **20,** 999–1009 (2010).

102. Rajan, S., Wischmeyer, E., Xin Liu, G., Preisig-Müller, R., Daut, J., Karschin, A. & Derst, C. TASK-3, a novel tandem pore domain acid-sensitive K+ channel. An extracellular histiding as pH sensor. *J. Biol. Chem.* **275,** 16650–7 (2000).

103. Ma, L., Zhang, X., Zhou, M. & Chen, H. Acid-sensitive TWIK and TASK two-pore domain potassium channels change ion selectivity and become permeable to sodium in extracellular acidification. *J. Biol. Chem.* **287,** 37145–53 (2012).

104. Talley, E. M. & Bayliss, D. A. Modulation of TASK-1 (Kcnk3) and TASK-3 (Kcnk9) Potassium Channels: VOLATILE ANESTHETICS AND NEUROTRANSMITTERS SHARE A MOLECULAR SITE OF ACTION. *J. Biol. Chem.* **277,** 17733–17742 (2002).

105. Kim, D., Cavanaugh, E. J., Kim, I. & Carroll, J. L. Heteromeric TASK-1/TASK-3 is the major oxygen-sensitive background K+ channel in rat carotid body glomus cells. *J. Physiol.* **587,** 2963–75 (2009).

106. Trapp, S., Aller, M. I., Wisden, W. & Gourine, A. V. A role for TASK-1 (KCNK3) channels in the chemosensory control of breathing. *J. Neurosci.* **28,** 8844–50 (2008).

107. Olschewski, A., Li, Y., Tang, B., Hanze, J., Eul, B., Bohle, R. M., Wilhelm, J., Morty, R. E., Brau, M. E., Weir, E. K., Kwapiszewska, G., Klepetko, W., Seeger, W. & Olschewski, H. Impact of TASK-1 in human pulmonary artery smooth muscle cells. *Circ. Res.* **98,** 1072–80 (2006).

108. Guagliardo, N. A., Yao, J., Hu, C., Schertz, E. M., Tyson, D. A., Carey, R. M., Bayliss, D. A. & Barrett, P. Q. TASK-3 channel deletion in mice recapitulates low-renin essential hypertension. *Hypertension* **59,** 999–1005 (2012).

109. Davies, L. A., Hu, C., Guagliardo, N. A., Sen, N., Chen, X., Talley, E. M., Carey, R. M., Bayliss, D. A. & Barrett, P. Q. TASK channel deletion in mice causes primary hyperaldosteronism. *Proc. Natl. Acad. Sci. U. S. A.* **105,** 2203–8 (2008).

110. Decher, N., Wemhöner, K., Rinné, S., Netter, M. F., Zuzarte, M., Aller, M. I., Kaufmann, S. G., Li, X. T., Meuth, S. G., Daut, J., Sachse, F. B. & Maier, S. K. G. Knock-out of the potassium channel TASK-1 leads to a prolonged QT interval and a disturbed QRS complex. *Cell. Physiol. Biochem.* **28,** 77–86 (2011).

111. Donner, B. C., Schullenberg, M., Geduldig, N., Hüning, A., Mersmann, J., Zacharowski, K., Kovacevic, A., Decking, U., Aller, M. I. & Schmidt, K. G. Functional role of TASK-1 in the heart: studies in TASK-1-deficient mice show prolonged cardiac repolarization and reduced heart rate variability. *Basic Res. Cardiol.* **106,** 75–87 (2011).

112. Gierten, J., Ficker, E., Bloehs, R., Schweizer, P. A., Zitron, E., Scholz, E., Karle, C., Katus, H. A. & Thomas, D. The human cardiac K2P3.1 (TASK-1) potassium leak channel is a molecular target for the class III antiarrhythmic drug amiodarone. *Naunyn. Schmiedebergs. Arch. Pharmacol.* **381,** 261–70 (2010).

113. Seyler, C., Li, J., Schweizer, P. A., Katus, H. A. & Thomas, D. Inhibition of cardiac two-pore-domain K+ (K2P) channels by the antiarrhythmic drug vernakalant--comparison with flecainide. *Eur. J. Pharmacol.* **724,** 51–7 (2014).

114. Linden, A.-M., Sandu, C., Aller, M. I., Vekovischeva, O. Y., Rosenberg, P. H., Wisden, W. & Korpi, E. R. TASK-3 knockout mice exhibit exaggerated nocturnal activity, impairments in cognitive functions, and reduced sensitivity to inhalation anesthetics. *J. Pharmacol. Exp. Ther.* **323,** 924–34 (2007).

115. Jiang, Y., Lee, A., Chen, J., Cadene, M., Chait, B. T. & MacKinnon, R. The open pore conformation of potassium channels. *Nature* **417,** 523–6 (2002).

116. Piechotta, P. L., Rapedius, M., Stansfeld, P. J., Bollepalli, M. K., Ehrlich, G., Erhlich, G., Andres-Enguix, I., Fritzenschaft, H., Decher, N., Sansom, M. S. P., Tucker, S. J. & Baukrowitz, T. The pore structure and gating mechanism of K2P channels. *EMBO J.* **30,** 3607–19 (2011).

117. Bagriantsev, S. N., Clark, K. A. & Minor, D. L. Metabolic and thermal stimuli control K(2P)2.1 (TREK-1) through modular sensory and gating domains. *EMBO J.* **31,** 3297–308 (2012).

118. Read, R. J. Improved Fourier coefficients for maps using phases from partial structures with errors. *Acta Crystallogr. Sect. A Found. Crystallogr.* **42,** 140–149 (1986).

119. Terwilliger, T. SOLVE and RESOLVE: automated structure solution, density modification and model building. *Journal of Synchrotron Radiation* **11,** 49–52 (2003).

120. Terwilliger, T. C. Using prime-and-switch phasing to reduce model bias in molecular replacement. *Acta Crystallogr. D. Biol. Crystallogr.* **60,** 2144–9 (2004).

121. Terwilliger, T. C. Using prime-and-switch phasing to reduce model bias in molecular replacement. *Acta Crystallogr. D. Biol. Crystallogr.* **60,** 2144–9 (2004).

122. Afonine, P. V, Moriarty, N. W., Mustyakimov, M., Sobolev, O. V, Terwilliger, T. C., Turk, D., Urzhumtsev, A. & Adams, P. D. FEM: feature-enhanced map. *Acta Crystallogr. D. Biol. Crystallogr.* **71,** 646–66 (2015).

123. Liu, C. & Xiong, Y. Electron density sharpening as a general technique in crystallographic studies. *J. Mol. Biol.* **426,** 980–93 (2014).

124. Gomora, J. C. & Enyeart, J. J. Dual Pharmacological Properties of a Cyclic AMP-Sensitive Potassium Channel. *J. Pharmacol. Exp. Ther.* **290,** 266–275 (1999).

125. Nayak, T. K., Harinath, S., Nama, S., Somasundaram, K. & Sikdar, S. K. Inhibition of human two-pore domain K+ channel TREK1 by local anesthetic lidocaine: negative cooperativity and half-of-sites saturation kinetics. *Mol. Pharmacol.* **76,** 903–17 (2009).

126. Takahira, M., Sakurai, M., Sakurada, N. & Sugiyama, K. Fenamates and diltiazem modulate lipid-sensitive mechano-gated 2P domain K(+) channels. *Pflugers Arch.* **451,** 474–8 (2005).

127. Duprat, F., Lesage, F., Patel, A. J., Fink, M., Romey, G. & Lazdunski, M. The neuroprotective agent riluzole activates the two P domain K(+) channels TREK-1 and TRAAK. *Mol. Pharmacol.* **57,** 906–12 (2000).

128. Minieri, L., Pivonkova, H., Caprini, M., Harantova, L., Anderova, M. & Ferroni, S. The inhibitor of volume-regulated anion channels DCPIB activates TREK potassium channels in cultured astrocytes. *Br. J. Pharmacol.* **168,** 1240–54 (2013).

129. Iceta, R., Mesonero, J. E., Aramayona, J. J. & Alcalde, A. I. Molecular characterization and intracellular regulation of the human serotonin transporter in Caco-2 cells. *J. Physiol. Pharmacol.* **57,** 119–30 (2006).

130. Gordon, J. A. & Hen, R. TREKing toward new antidepressants. *Nat. Neurosci.* **9,** 1081–3 (2006).

131. Kennard, L. E., Chumbley, J. R., Ranatunga, K. M., Armstrong, S. J., Veale, E. L. & Mathie, A. Inhibition of the human two-pore domain potassium channel, TREK-1, by fluoxetine and its metabolite norfluoxetine. *Br. J. Pharmacol.* **144,** 821–9 (2005).

132. Perlis, R. H., Moorjani, P., Fagerness, J., Purcell, S., Trivedi, M. H., Fava, M., Rush, A. J. & Smoller, J. W. Pharmacogenetic analysis of genes implicated in rodent models of antidepressant response: association of TREK1 and treatment resistance in the STAR(*)D study. *Neuropsychopharmacology* **33,** 2810–9 (2008).

133. Talkowski, M. E. *et al.* Evaluation of a susceptibility gene for schizophrenia: genotype based meta-analysis of RGS4 polymorphisms from thirteen independent samples. *Biol. Psychiatry* **60,** 152–162 (2006).

134. Congiu, C., Minelli, A., Bonvicini, C., Bortolomasi, M., Sartori, R., Maj, C., Scassellati, C., Maina, G., Trabucchi, L., Segala, M. & Gennarelli, M. The role of the potassium channel gene KCNK2 in major depressive disorder. *Psychiatry Res.* **225,** 489–92 (2015).

135. Ripke, S. *et al.* A mega-analysis of genome-wide association studies for major depressive disorder. *Mol. Psychiatry* **18,** 497–511 (2013).

136. Common genetic variation and antidepressant efficacy in major depressive disorder: a meta-analysis of three genome-wide pharmacogenetic studies. *Am. J. Psychiatry* **170,** 207–17 (2013).

137. Eckert, M., Egenberger, B., Döring, F. & Wischmeyer, E. TREK-1 isoforms generated by alternative translation initiation display different susceptibility to the antidepressant fluoxetine. *Neuropharmacology* **61,** 918–23

138. Sandoz, G., Bell, S. C. & Isacoff, E. Y. Optical probing of a dynamic membrane interaction that regulates the TREK1 channel. *Proc. Natl. Acad. Sci. U. S. A.* **108,** 2605–10 (2011).

139. Tiefenbrunn, T., Forli, S., Happer, M., Gonzalez, A., Tsai, Y., Soltis, M., Elder, J. H., Olson, A. J. & Stout, C. D. Crystallographic fragment-based drug discovery: use of a brominated fragment library targeting HIV protease. *Chem. Biol. Drug Des.* **83,** 141–8 (2014).

140. Bauman, J. D., Patel, D. & Arnold, E. Fragment screening and HIV therapeutics. *Top. Curr. Chem.* **317,** 181–200 (2012).

141. Strahs, G. & Kraut, J. Low-resolution electron-density and anomalous-scattering-density maps of Chromatium high-potential iron protein. *J. Mol. Biol.* **35,** 503–12 (1968).

142. Bagnéris, C., DeCaen, P. G., Naylor, C. E., Pryde, D. C., Nobeli, I., Clapham, D. E. & Wallace, B. A. Prokaryotic NavMs channel as a structural and functional model for eukaryotic sodium channel antagonism. *Proc. Natl. Acad. Sci. U. S. A.* **111,** 8428–33 (2014).

143. Terwilliger, T. C., Adams, P. D., Moriarty, N. W. & Cohn, J. D. Ligand identification using electron-density map correlations. *Acta Crystallogr. Sect. D Biol. Crystallogr.* **63,** 101–107 (2006).

144. Terwilliger, T. C., Klei, H., Adams, P. D., Moriarty, N. W. & Cohn, J. D. Automated ligand fitting by core-fragment fitting and extension into density. *Acta Crystallogr. D. Biol. Crystallogr.* **62,** 915–22 (2006).

145. Smart OS, Womack, TO, Sharff A, Flensburg C, Keller P, Paciorek W, Vonrhein C and Bricogne G (2014) RHOFIT, version 1.2.4 Cambridge, United Kingdom: Global Phasing Ltd.

146. Alexandrov, A. I., Mileni, M., Chien, E. Y. T., Hanson, M. A. & Stevens, R. C. Microscale fluorescent thermal stability assay for membrane proteins. *Structure* **16,** 351–9 (2008).

147. Thümmler, S., Duprat, F. & Lazdunski, M. Antipsychotics inhibit TREK but not TRAAK channels. *Biochem. Biophys. Res. Commun.* **354,** 284–9 (2007).

148. Evans, G. & Pettifer, R. F. CHOOCH : a program for deriving anomalous-scattering factors from X-ray fluorescence spectra. *J. Appl. Crystallogr.* **34,** 82–86 (2001).

149. *Evolving Methods for Macromolecular Crystallography*. **245,** (Springer Netherlands, 2007).

150. Winter, G. xia2 : an expert system for macromolecular crystallography data reduction. *J. Appl. Crystallogr.* **43,** 186–190 (2009).

151. McCoy, A. J., Grosse-Kunstleve, R. W., Adams, P. D., Winn, M. D., Storoni, L. C. & Read, R. J. Phaser crystallographic software. *J. Appl. Crystallogr.* **40,** 658–674 (2007).

152. Winn, M. D., Ballard, C. C., Cowtan, K. D., Dodson, E. J., Emsley, P., Evans, P. R., Keegan, R. M., Krissinel, E. B., Leslie, A. G. W., McCoy, A., McNicholas, S. J., Murshudov, G. N., Pannu, N. S., Potterton, E. A., Powell, H. R., Read, R. J., Vagin, A. & Wilson, K. S. Overview of the CCP4 suite and current developments. *Acta Crystallogr. D. Biol. Crystallogr.* **67,** 235–42 (2011).

153. Kabsch, W. XDS. *Acta Crystallogr. D. Biol. Crystallogr.* **66,** 125–32 (2010).

154. Evans, P. R. & Murshudov, G. N. How good are my data and what is the resolution? *Acta Crystallogr. D. Biol. Crystallogr.* **69,** 1204–14 (2013).

155. French, S. & Wilson, K. On the treatment of negative intensity observations. *Acta Crystallogr. Sect. A* **34,** 517–525 (1978).

156. Kantardjieff, K. A. & Rupp, B. Matthews coefficient probabilities: Improved estimates for unit cell contents of proteins, DNA, and protein-nucleic acid complex crystals. *Protein Sci.* **12,** 1865–71 (2003).

157. Adams, P. D., Afonine, P. V, Bunkóczi, G., Chen, V. B., Davis, I. W., Echols, N., Headd, J. J., Hung, L.-W., Kapral, G. J., Grosse-Kunstleve, R. W., McCoy, A. J., Moriarty, N. W., Oeffner, R., Read, R. J., Richardson, D. C., Richardson, J. S., Terwilliger, T. C. & Zwart, P. H. {\it PHENIX}: a comprehensive Python-based system for macromolecular structure solution. *Acta Crystallogr. Sect. D* **66,** 213–221 (2010).

158. Emsley, P. & Cowtan, K. Coot: model-building tools for molecular graphics. *Acta Crystallogr. D. Biol. Crystallogr.* **60,** 2126–32 (2004).

159. Bricogne G., Blanc E., Brandl M., Flensburg C., Keller P., P. W. & Roversi P, Sharff A., Smart O.S., Vonrhein C., W. T. O. BUSTER. *Glob. Phasing Ltd.* (2011).

160. Chen, V. B., Arendall, W. B., Headd, J. J., Keedy, D. A., Immormino, R. M., Kapral, G. J., Murray, L. W., Richardson, J. S. & Richardson, D. C. MolProbity: all-atom structure validation for macromolecular crystallography. *Acta Crystallogr. D. Biol. Crystallogr.* **66,** 12–21 (2010).

161. Smart, O. & Bricogne, G. in *Multifaceted Roles of Crystallography in Modern Drug Discovery SE - 13* 165–181 (Springer Netherlands, 2015).

162. Tertyshnikova, S., Knox, R. J., Plym, M. J., Thalody, G., Griffin, C., Neelands, T., Harden, D. G., Signor, L., Weaver, D., Myers, R. A. & Lodge, N. J. BL-1249 [(5,6,7,8-tetrahydro-naphthalen-1-yl)-[2-(1H-tetrazol-5-yl)-phenyl]-amine]: a putative potassium channel opener with bladder-relaxant properties. *J. Pharmacol. Exp. Ther.* **313,** 250–9 (2005).

163. Veale, E. L., Al-Moubarak, E., Bajaria, N., Omoto, K., Cao, L., Tucker, S. J., Stevens, E. B. & Mathie, A. Influence of the N terminus on the biophysical properties and pharmacology of TREK1 potassium channels. *Mol. Pharmacol.* **85,** 671–81 (2014).

164. Ma, X.-Y., Yu, J.-M., Zhang, S.-Z., Liu, X.-Y., Wu, B.-H., Wei, X.-L., Yan, J.-Q., Sun, H.-L., Yan, H.-T. & Zheng, J.-Q. External Ba2+ block of the two-pore domain potassium channel TREK-1 defines conformational transition in its selectivity filter. *J. Biol. Chem.* **286,** 39813–22 (2011).

165. Jiang, Y. The Barium Site in a Potassium Channel by X-Ray Crystallography. *J. Gen. Physiol.* **115,** 269–272 (2000).

166. Evans, P. Scaling and assessment of data quality. *ACTA Crystallogr. Sect. D-BIOLOGICAL Crystallogr.* **62,** 72–82 (2006).

167. *Biophysical Approaches Determining Ligand Binding to Biomolecular Targets: Detection, Measurement and Modelling*. (Royal Society of Chemistry, 2011).

168. Caffrey, M. Crystallizing membrane proteins for structure determination: use of lipidic mesophases. *Annu. Rev. Biophys.* **38,** 29–51 (2009).

169. Landau, E. M. & Rosenbusch, J. P. Lipidic cubic phases: a novel concept for the crystallization of membrane proteins. *Proc. Natl. Acad. Sci. U. S. A.* **93,** 14532–5 (1996).

170. DeLucas, L. *Membrane Protein Crystallization*. (Academic Press, 2009).

171. Caffrey, M. & Cherezov, V. Crystallizing membrane proteins using lipidic mesophases. *Nat. Protoc.* **4,** 706–31 (2009).

172. Huang, J., Chen, S., Zhang, J. J. & Huang, X.-Y. Crystal structure of oligomeric β1-adrenergic G protein-coupled receptors in ligand-free basal state. *Nat. Struct. Mol. Biol.* **20,** 419–25 (2013).

173. Liu, W. *et al.* Serial Femtosecond Crystallography of G Protein-Coupled Receptors. *Science (80-.).* **342,** 1521–1524 (2013).

174. Hand, E. X-ray free-electron lasers fire up. *Nature* **461,** 708–9 (2009).

175. Emma, P. *et al.* First lasing and operation of an ångstrom-wavelength free-electron laser. *Nat. Photonics* **4,** 641–647 (2010).

176. Boutet, S. *et al.* High-resolution protein structure determination by serial femtosecond crystallography. *Science* **337,** 362–4 (2012).

177. Kern, J. *et al.* Room temperature femtosecond X-ray diffraction of photosystem II microcrystals. *Proc. Natl. Acad. Sci. U. S. A.* **109,** 9721–6 (2012).

178. Neutze, R., Wouts, R., van der Spoel, D., Weckert, E. & Hajdu, J. Potential for biomolecular imaging with femtosecond X-ray pulses. *Nature* **406,** 752–7 (2000).

179. Chapman, H. N. *et al.* Femtosecond X-ray protein nanocrystallography. *Nature* **470,** 73–7 (2011).

180. Barty, A. *et al.* Self-terminating diffraction gates femtosecond X-ray nanocrystallography measurements. *Nat. Photonics* **6,** 35–40 (2012).

181. Boutet, S. & Williams, G. LCLS CXI Technical Specs. at <https://portal.slac.stanford.edu/sites/lcls_public/instruments/cxi/Documents/CXItechspecs.pdf>

182. Cherezov, V., Liu, J., Griffith, M., Hanson, M. A. & Stevens, R. C. LCP-FRAP Assay for Pre-Screening Membrane Proteins for in Meso Crystallization. *Cryst. Growth Des.* **8,** 4307–4315 (2008).

183. Liu, W., Ishchenko, A. & Cherezov, V. Preparation of microcrystals in lipidic cubic phase for serial femtosecond crystallography. *Nat. Protoc.* **9,** 2123–34 (2014).

184. Kissick, D. J., Gualtieri, E. J., Simpson, G. J. & Cherezov, V. Nonlinear optical imaging of integral membrane protein crystals in lipidic mesophases. *Anal. Chem.* **82,** 491–7 (2010).

185. Barty, A., Kirian, R. A., Maia, F. R. N. C., Hantke, M., Yoon, C. H., White, T. A. & Chapman, H. Cheetah: software for high-throughput reduction and analysis of serial femtosecond X-ray diffraction data. *J. Appl. Crystallogr.* **47,** 1118–1131 (2014).

186. Liu, W. *et al.* Serial Femtosecond Crystallography of G Protein-Coupled Receptors. *Science (80-.).* **342,** 1521–1524 (2013).

187. White, T. A., Kirian, R. A., Martin, A. V., Aquila, A., Nass, K., Barty, A. & Chapman, H. N. CrystFEL : a software suite for snapshot serial crystallography. *J. Appl. Crystallogr.* **45,** 335–341 (2012).

188. Hassell, A. M., An, G., Bledsoe, R. K., Bynum, J. M., Carter, H. L., Deng, S.-J. J., Gampe, R. T., Grisard, T. E., Madauss, K. P., Nolte, R. T., Rocque, W. J., Wang, L., Weaver, K. L., Williams, S. P., Wisely, G. B., Xu, R. & Shewchuk, L. M. Crystallization of protein-ligand complexes. *Acta Crystallogr. D. Biol. Crystallogr.* **63,** 72–9 (2007).

189. Jonasson, E. Correlation between ligand solubility and formation of protein-ligand complexes in X-ray crystallography. (University of Gothenburg, 2012).

190. Caffrey, M. & Cherezov, V. Crystallizing membrane proteins using lipidic mesophases. *Nat. Protoc.* **4,** 706–31 (2009).

191. Weierstall, U. *et al.* Lipidic cubic phase injector facilitates membrane protein serial femtosecond crystallography. *Nat. Commun.* **5,** 3309 (2014).

192. Rupp, B. *Biomolecular Crystallography: Principles, Practice, and Application to Structural Biology*. (Garland Science, 2009).

193. Urbani, A. & Warne, T. A colorimetric determination for glycosidic and bile salt-based detergents: applications in membrane protein research. *Anal. Biochem.* **336,** 117–24 (2005).

194. Caffrey, M. A comprehensive review of the lipid cubic phase or in meso method for crystallizing membrane and soluble proteins and complexes. *Acta Crystallogr. Sect. F, Struct. Biol. Commun.* **71,** 3–18 (2015).

195. Li, D., Shah, S. T. A. & Caffrey, M. Host Lipid and Temperature as Important Screening Variables for Crystallizing Integral Membrane Proteins in Lipidic Mesophases. Trials with Diacylglycerol Kinase. *Cryst. Growth Des.* **13,** 2846–2857 (2013).

196. White, T. A., Barty, A., Stellato, F., Holton, J. M., Kirian, R. A., Zatsepin, N. A. & Chapman, H. N. Crystallographic data processing for free-electron laser sources. *Acta Crystallogr. D. Biol. Crystallogr.* **69,** 1231–40 (2013).

Chapter 7 Abbreviations

E_m	Membrane potential (Volts)
BF	Brominated fluoxetine
BL-1249	[(5,6,7,8-Tetrahydro-naphthalen-1-yl)-[2-(1H-tetrazol-5-yl)-phenyl]-amine]
C12E8	Polyoxyethylene (8)dodecyl Ether
cAMP	Cyclic adenosine monophosphate
CHS	Cholesterol hemi-succinate
CPM	N-[4-(7-diethylamino-4-methyl-3-coumarinyl)phenyl]maleimide
CTD	Highly charged C-terminal regulatory domain
CXI	Coherent X-ray imaging
CYMAL-5	5-Cyclohexyl-1-Pentyl-β-D-Maltoside
DDM	n-Dodecyl β-D-Maltopyranoside
DLS	Diamond Light Source
DM	n-Decyl-β-D-Maltoside
DMSO	Dimethyl sulfoxide
EC	Extracellular
GHK	Goldman-Hodgkin-Katz
GPCR	G-protein coupled receptor
GWAS	Genome wide annotation studies

IC	Intracellular
IMP	Integral Membrane Protein
ITC	Isothermal calorimetry
KCNK	Gene encoding a K2P channel
KcsA	Potassium crystallographically-sited activation channel
LCLS	Linac Coherent Light Source
LCP	Lipidic cubic phase
LDAO	N, N-dimethyldodecylamine N-oxide
LMNG	Lauryl Maltose Neopentyl Glycol
LMW-PEG	Low molecular weight poly (ethylene glycol)
LSP	Lipidic spongy phase
M	Transmembrane helix
M1-P-M2	A pore-forming domain flanked by TM helices. In 3D it creates a re-entrant loop.
MAG	Mono-acyl glycerol
MES	2-(N-morpholino) ethane sulfonic acid
MME	Methyl ether
MR	Molecular replacement
NaK	Sodium/ potassium channel
NaK-CNG	Sodium/potassium channel selectivity filter mutant TVGDGNFS to TVGDTPP
NG	n-Nonyl-β-D-Glucopyranoside
OGNG	Octyl Glucose Neopentyl Glycol
P1	The first pore forming domain of a K2P channel (M1-M2)
P2	The second pore-forming domain of a K2P channel (M3-M4)
PEE	Pentaerythritol ethoxylate
PEG	Poly (ethylene glycol)
P_{Na}/P_K	Sodium permeability relative to potassium permeability
QA	Quaternary Ammonium ion
R	Ideal gas constant
rtp	Room temperature
S	Potassium binding site
SDS-PAGE	Sodium dodecyl sulphate polyacrylamide gel electrophoresis

SEC	Size exclusion chromatography
SFX	Serial femtosecond crystallography
SNP	Singe nucleotide polymorphism
SSRI	Selective serotonin re-uptake inhibitor
SYN	Synchrotron
T	Temperature (Kelvin)
TEVC	Two-electrode-voltage-clamp
TM	Transmembrane
TRIS	Tris (hydroxymethyl) aminomethane
TRP	Transient Receptor Potential channel
XFEL	X-ray free electron laser

Chapter 8 Appendices

8.1 Co-crystallisation with other ligands

In this thesis, the results for co-crystallisation of TREK-2 with brominated fluoxetine, brominated BL-1249 and norfluoxetine are presented. These results represent all compounds for which a structure was modelled and some evidence of ligand density or anomalous signal was present. However, a large number of compounds were screened that didn't fulfil these criteria. Listed here are the outcomes of all compounds screened.

Compound ID	Compound Description	Supplier	Crystal Plates	Mounted Crystals	Data sets	Outcome	SMILES
I00013a	Norfluoxetine		22	46	1	Density / resolution not improved on Yin Dong's dataset	[H]N([H])CCC(c1cccc1)Oc1ccc(cc1)C(F)(F)F
I00014a	Flufenamic acid		3	1		Poor quality crystals/ diffraction/ resolution	[H]N(c1cccc(c1)C(F)(F)F)c1ccccc1C(=O)O[H]
I00015a	Penfluridol		18	8		Poor quality crystals/ diffraction/ resolution	[H]OC1(CCN(CCCC(c2ccc(cc2)F)c2ccc(cc2)F)CC1)c1ccc(c(c1)C(F)(F)F)[Cl]
I00016a	BL1249		393	0		Poor quality crystals/ diffraction/ resolution	[H]N(c1ccccc1c1nnnn1[H])c1cccc2CCCCc12
I00017a	Fluoxetine HCl	Enzo	4	14		Poor quality crystals/ diffraction/ resolution	CNCCC(c1ccccc1)Oc1ccc(cc1)C(F)(F)F.[Cl]
I00024a	Brominated fluoxetine HCl	TDI	7	10		Poor quality crystals/ diffraction/ resolution	CNCCC(c1ccccc1)Oc1ccc(c(c1)[Br])C(F)(F)F.[Cl]
I00025a	Brominated fluoxetine HCl	TDI	10	37	2	Ligand built in thesis	CNCCC(c1ccccc1)Oc1ccc(cc1[Br])C(F)(F)F.[Cl]
I00027a	Racaemic Fluoxetine	Gian Filippo	12	42	1	No ligand density in binding site	[H]N(C(C=C)=O)c1ccc(cc1)OC(CC[N+

	Derivitive, For covalent attachment to cysteine	Ruda					]([H])([H])C)c1ccccc1.C(C(F)(F)F)([O-])=O
I00028a	Brominated fluoxetine derivitive, chirally pure	Gian Filippo Ruda	14	41	5	Bromine site described in thesis	[H][N+]([H])(C)CCC(c1ccc(cc1)[Br])Oc1ccc(cc1)C(F)(F)F.[H][Cl]
I00029a	Brominated fluoxetine, chirally pure,		2	11	1	Poor quality crystals/ diffraction/ resolution	C[N+]CCC(c1ccc(cc1)[Br])Oc1ccc(cc1)C(F)(F)F.[Cl]
I00035a	WAY 254765-A Fluoxetine derivative	David Pryde, Pfizer	4	5		Poor quality crystals/ diffraction/ resolution	C(CN1CCNCC1)C(c1ccccc1)Oc1ccc(cc1)C(F)(F)F
I00036a	WY-25969 Fluoxetine derivative	David Pryde, Pfizer	4	3		Poor quality crystals/ diffraction/ resolution	C1CNCCC1(c1ccccc1)Oc1ccc(cc1)C(F)(F)F
I00038a	UK-129282 Riluzole derivative	David Pryde, Pfizer	2	1	1	No identifiable ligand density	[H]N([H])c1nc2ccc(cc2s1)[Br]
I00039a	PF1205472(aka UK-332336) Riluzole derivative	David Pryde, Pfizer	2	3		Poor quality crystals/ diffraction/ resolution	[H]N([H])c1nc2c(cc(cc2s1)OC(F)(F)F)[Br]
I00040a	PF-4882389 Lamotrigine derivative	David Pryde, Pfizer	2	3	1	No identifiable ligand density	[H]N([H])c1c(c2cc(cc(c2[Cl])[Cl])[Br])nnc(n1)N([H])[H]
I00041a	Brominated BL-1249	David Pryde, Pfizer	5	24		Poor quality crystals/ diffraction/ resolution	C1CCc2c(C1)cccc2Nc1cc(ccc1c1nn[nH]n1)[Br]
Compound ID	**Compound Description**	**Supplier**	**Crystal Plates**	**Mounted Crystals**	**Data sets**	**Outcome**	**SMILES**
I00042a	Brominated BL-1249	David Pryde, Pfizer	5	33		Poor quality crystals/ diffraction/ resolution	C1CCc2c(C1)cccc2Nc1ccc(cc1c1nn[nH]n1)[Br]
I00043a	Brominated BL-1249	David Pryde, Pfizer	6	16	3	Anomalous peak shown in this thesis	C1CCc2c(ccc(c2C1)Nc1ccccc1c1nn[nH]n1)[Br]
K02107b	Lamotrigine	Sigma Aldrich	3	9		Poor quality crystals/ diffraction/ resolution	C(=C(N1)N)(C(C(=C([Cl])C2)[Cl])=CC=2)N=NC=1N
N11426b	R-Fluoxetine	Sigma	20	46	5	No ligand density in binding site	CNCC[C@H](c1ccccc1)Oc1ccc(cc1)C(F)(F)F.[Cl]
N11427b	S-Fluoxetine	Sigma	13	21	2	No ligand density in binding site	CNCC[C@@H](c1ccccc1)Oc1ccc(cc1)C(F)(F)F.[Cl]
N11499a	100nM TREK activator , David Pryde Pfizer	Chris Abell, Cambridge	24	13	2	No ligand density identifiable	CC(C)(C)c1cc(C=C(C#N)C#N)cc(c1O)C(C)(C)C
Z00046a	ZnCl2, zinc chloride	Sigma Aldrich	1	0		Precipitates protein heavily	[Zn]([Cl])[Cl]
Z00052b	MnCl2, manganese chloride	Sigma Aldrich	2	5	1	No clear anomalous peak	[Mn]([Cl])[Cl].O
Z00131a	Benzamidine	Sigma Aldrich	9	29	2	No identifiable ligand density	C(=N)(N)C(=CC=C1)C=C1.[Cl]
Z00156a	[Sr] strontium chloride		2	7	1	No clear anomalous peak	[Cl-].[Cl-].[93Sr++]
Z00161a	[Ba] barium chloride		2	6		Poor quality crystals/ diffraction/ resolution	[Cl-].[Cl-].[Ba++]
Z01001a	Copper (II) Chloride	Sigma	2			Precipitates protein- no crystals	[Cl-].[Cl-].[Cu++]
Z01003a	S-Norfluoxetine free base	Santa Cruz Biotech	3	0		No crystals suitable for mounting	C(CN)[C@@H](c1ccccc1)Oc1ccc(cc1)C(F)(F)F
Z01004a	R-Norfluoxetine free base	Santa Cruz Biotech	2	14	1	No ligand density in binding site	C(CN)[C@H](c1ccccc1)Oc1ccc(cc1)C(F)(F)F